Atomic layer deposition of conformal silver as an ultra-thin anti-microbial coating for orthopaedic implants

By

Zahra Golrokhi

PhD Thesis

The University of Liverpool

School of Engineering

Faculty of Science and Engineering

May 2016

Abstract

The controlled deposition of ultra-thin conformal silver nanoparticle films is of interest for applications including anti-microbial surfaces, plasmonics, catalysts and sensors. Although various techniques can produce silver films, only a limited number of techniques can offer highly conformal ultra-thin coatings on high aspect ratio surfaces and complex geometries, together with sub-nanometre control and scalability. Here we develop a self-limiting atomic layer deposition (ALD) process for the deposition of conformal metallic silver nanoparticle films.

In this study, silver films have been deposited using direct liquid injection thermal ALD with ((hexafluoroacetylacetonato) silver (I) (1,5-cyclooctadiene)) as the metal source. The ALD process has been compared and contrasted by using propan-1-ol as a co-reactant with the ALD process using tertiary butyl hydrazine as a co-reactant. A narrow ALD temperature window between 123 and 128 °C is identified for the propan-1-ol process with a nominal mass deposition rate of ~17.5 ng/cm^2/cycle. The ALD reaction mechanisms have been elucidated using in-situ quartz crystal microbalance (QCM) measurements, showing chemisorption of the silver precursor, followed by heterogeneous catalytic dehydrogenation of the alcohol to form metallic silver and an aldehyde. A significantly wider temperature window between 105 and 128 °C (23 °C) is identified for the hydrazine based process with a nominal mass deposition rate of ~20.2 ng/cm^2/cycle (a nominal growth rate of 0.18 Å/cycle). The effects of temperature, co-reactant dose and cycle number on the deposition rate and on the physico-chemical and electrical properties of the films have been systematically investigated. Under self-limiting conditions, films grown using propan-1-ol are non-conductive metallic silver with a nano-textured surface topography. The size distribution of nanoparticles is narrow under ALD conditions and the number of ALD cycles can be used to accurately control nanoparticle sizes up until neighbouring particles begin to merge. The hydrazine based process produces less textured, more film like coatings. The films are found to be metallic silver and are electrically conductive. Also, better surface adhesion was achieved with scotch tape test in hydrazine based process compared with propan-1-ol.

Silver is the most favourable metal for antimicrobial coatings due to its excellent antimicrobial activity against a wide range of microorganisms including inhibition of bacterial adhesion, broad anti-bacterial spectrum, and its tendency for being less prone to the increase of bacteria resistance compared to antibiotic.

The need for artificial implants has raised due to aging populations and obesity and resulted in the number of implant-related infections. These infections result in the implant failure, revision surgeries, pain for the patients, more hospitalisation time and also hugely increase the financial burden on health services. One of the major bacteria associated with joint replacement complications is *Staphylococcus epidermidis*, having strong biofilm forming capabilities in deep wounds and on prostheses. In order to inhibit biofilm formation on surfaces of implants we developed 3D titanium structures using the selective laser melting technique and subsequently coated them with an ultra-thin conformal layer of metallic silver nanoparticles using (ALD). Silver coated implants showed high antimicrobial effect on *S. epidermidis* by reducing it up to 2-log fold. Ultrastructural examination of human fibroblasts (HS27), keratinocytes (HaCaT), endothelium (HMVEC and HUVEC) and bone (SAOS2) cells showed robust growth on both silver coated and control Titanium implant surfaces. The study shows that a nano-layer of silver coated SLM manufactured titanium implants have significant effect in reducing the pathogenic biofilm formation while retaining their biocompatible properties, making these surface-modified implants promising candidates for clinical orthopaedic applications.

List of Publications

Golrokhi, Z., Chalker, S., Sutcliffe, C. J., & Potter, R. J. (2015). Self-limiting atomic layer deposition of conformal nano-structured silver films. *Applied Surface Science*. 364 (2016), 789–797.

Golrokhi, Z., Chalker, P., Marshall, P., & Potter, R. J. (2016). Extending the ALD temperature window of silver using tertiary butyl hydrazine as a co-reactant. *Applied Surface Science. Submitted.*

Mullin, A., Todd, N., ***Golrokhi, Z.***, Geng, H., Konerding, M., Potter, R., Sutcliffe, C., Jones, E., & Mitchell, C. (2016). Titanium implants coated with a nano-layer of silver inhibit colonization by S. epidermidis, support cell growth and promote vascularized Osseo-integration *in vivo*. *Biomaterials. Submitted.*

Geng, H., Sutcliffe, C., ***Golrokhi, Z.***, Potter, R., Mitchell, C. Mullin, A., & Todd, N. (2016). Impact of antibacterial silver coating on bone formation and osseointegration in additive manufactured titanium scaffold. *Acta Biomaterial. Submitted.*

Acknowledgments

I would like to express my gratitude to my supervisors Dr. R. Potter and Prof. P. Chalker for their support, ideas, discussions and valuable guidance. I would also like to thank Dr. P. Marshall (University of Liverpool) for his guidance and providing technical supports during my experiments.

I would like to give a massive thank to Stryker Howmedica Osteonics Company for patricianly sponsoring the work and helped me to work in collaboration with amazing people. A very special thanks goes out to Dr. C. Sutcliffe for giving me the opportunity to work with his SLM team and providing me with orthopaedic samples during my research. Also, I would like to thank Prof. E. Jones, who took the time to share his knowledge with me.

Gratitude is extended to Prof. C. Mitchell, A. Delvin and N. Todd (University of Ulster) for providing the antimicrobial results. I express my warm thanks to the academic and technical staff of the Material Science team, who help me and provided me with the facilities being required for this research.

Finally, special recognition goes out to my family, for their support, encouragement, patience and sacrifices that they made on my behalf since I was born.

Abbreviations

ALD	Atomic layer deposition
ALE	Atomic Layer Epitaxy
AFM	Atomic force microscope
Ra	Arithmetical mean roughness
CVD	Chemical vapour deposition
EDX	Energy dispersive X-ray spectroscopy
FPP	Four Point Probe
FWHM	Full-Width at Half Maximum
MFC	Mass flow controller
NP	Nano particle
PVD	Physical vapour deposition
PEALD	Plasma enhanced atomic layer deposition
QCM	Quartz crystal microbalance
SC	Solar Cell
SEM	Scanning electron microscope
SLM	Selective laser melting
TBH	Tertiary butyl hydrazine
UV	Ultraviolet
XPS	X-ray Photoelectron Spectroscopy
XRD	X-ray diffraction

Table of Contents

Chapter 1. Introduction

1.1. Introduction……2
1.2. Antimicrobial coating of orthopaedic implants……..6

Chapter 2. Literature Review

2.1. Introduction…… 11
2.2. Orthopaedic implants……....11
2.3. Materials used for implants fabrication……13
2.4. Bacterial infections of orthopaedic implants……16
2.5. Bacteria classification of implant-related infections……19
2.6. Antimicrobial coatings of orthopaedic implants……..…21
2.7. Material requirements for antimicrobial coatings……26
2.7.1. Metals……26
2.7.1.1. Silver and its antimicrobial mechanism……28
2.7.1.2. Silver nanoparticles and their antimicrobial effect……30
2.7.2. Classification of implant-related infections……..32
2.7.3. Health effects of silver coatings……32
2.8. Deposition techniques……..34
2.8.1. Physical based deposition (PVD)…… 34
2.8.2. Chemical based deposition……....36
2.8.2.1 Chemical vapour deposition (CVD)……36
2.8.3. Layer-By-Layer deposition (LBL)……37
2.9. Atomic layer deposition……...38
2.9.1. Fundamental features of ALD……...39
2.9.2. Principles of ALD……41
2.9.3. Different types of ALD……43
2.9.4. Self-limiting behaviour of ALD……44
2.9.5. Benefits and challenges of ALD……48
2.9.6. Metal precursor/co-reactant……...50

2.9.7. ALD precursor delivery methods…… 51
2.10. Silver ALD……... 56
2.11. Summary of the chapter……... 63

Chapter 3. Experimental Methods

3.1. Introduction……..... 67
3.2. Sample preparation…….... 68
3.2.1. Flat samples……. 68
3.2.2. Selective Laser Melting (SLM)……... 69
3.2.2.1. Manufacturing equipment ……... 69
3.2.3. SLM bone-implant samples…… 70
3.2.4. SLM split cube samples…….. 75
3.3. Precursor preparation……. 76
3.4. Co-reactants…….. .77
3.4.1. Propan-1-ol/Butan-1-ol…… ...77
3.4.2. Tertiary Butyl Hydrazine (TBH)…… 77
3.5. Atomic Layer Deposition…….. 78
3.5.1. Aixtron AIX 200FE……78
3.6. Material characterisation and analysis techniques…… …..... 81
3.6.1. Quartz Crystal Microbalance (QCM)……81
3.6.2. Weight gain……83
3.6.2.1. Measurement information……83
3.6.3. X-ray Diffraction (XRD)……85
3.6.4. Scanning Electron Microscope (SEM)…….. 87
3.6.4.1. Measurement information…….. 87
3.6.5. Atomic Force Microscopy (AFM)…… 88
3.6.5.1. Measurement information…… 88
3.6.6. X-ray Photoelectron Spectroscopy (XPS)……..89
3.6.7. Post growth heat treatments…….…. 90
3.6.7.1. Argon annealing……. 90
3.6.8. Adhesive testing…… 91
3.6.8.1. The scotch tape test…… 91
3.6.9. Four point probe (FPP)……. 91

Chapter 4. ALD growth of Ag thin films using alcohol-based co-reactants

4.1. Introduction……..93
4.2. Experimental procedure…….. 94
4.3. Deposition with no co-reactant……... 95
4.4. ALD with propan-1-ol as a co-reactant…….…..96
4.4.1. Growth study……....96
4.4.2. In-situ QCM study……..100
4.4.3. Composition analysis……..105
4.4.4. Microstructure study of films……. 109
4.4.5. Summary of the propan-1-ol growth study…….115
4.5. ALD with butan-1-ol as a co-reactant……116
4.5.1. Growth study……...116
4.5.2. Summary of the butan-1-ol growth study……...120

Chapter 5. ALD growth of Ag thin films using TBH as a co-reactant

5.1. Introduction……....122
5.2. ALD with tetra butyl hydrazine as a co-reactant……123
5.2.1. Experimental procedure…….. 123
5.2.2. Growth study……...124
5.2.3. Composition analysis……..130
5.3. Micro-structural study……....134
5.4. Electrical properties……. 141
5.5. Summary of the TBH growth study……. 142

Chapter 6. Titanium implants coated with a nano-layer of silver ALD for antimicrobial study

6.1. Introduction……..144
6.2. Nucleation and growth on titanium substrates…….145
6.2.1. Growth characteristics……...145
6.2.2. Micro-structural characterization of the ALD process……..149
6.3. Chemical composition of the silver NPs……..158
6.3.1. XPS spectra on titanium flat substrate……..158

6.4. Microstructure study on bone-like SLM structures……..161
6.4.1. SEM study of Ag NPs on the foam structures……...161
6.4.2. Conformal coating of porous foam structures assessed by SEM……..162
6.5. Titanium implants coated with a nano-layer of silver……..169
6.6. Growing S. epidermidis on Ti and Ti/Ag Solid samples…… 171
6.7. Human cell line adhesion on silver coated titanium structures……....173
6.8. Vascular Corrosion Casting…… 175

Chapter 7. Conclusions and Suggestions for Future Work

7.1. Conclusions…….. 179
7.2. Suggestions for Future Work……... 183

Appendix A……..185
Appendix B……...220
Appendix C……...221
Appendix D……...222
Appendix E……...224
Appendix F……...227
Appendix G……..227
Appendix H……..230
Appendix I……231
Appendix J……233
Appendix K……...234
Appendix L……...235
Appendix M…… …236
Appendix N……...237
Appendix O……...238
Appendix P……...239
Appendix Q……...240

References……241

Chapter 1

Introduction

1.1. Introduction

Atomic layer deposition (ALD), which is also known as atomic layer epitaxy (ALE), was initially introduced by Suntola and Antson in the mid 1970's in Finland to fabricate high quality luminescent ZnS and Al_2O_3 insulator for electroluminescent flat panel displays (TFEL)[1,2]. It was in the mid 1990's that ALD technology has become a commercial achievement in order to provide the requirements for high-k oxides in microelectronics due to the need for decreasing the device dimensions. Since then, a diverse range of materials have been deposited by ALD including metal oxides[3,4,5,6], metal nitrides[7,8], pure metals (e.g. Ru, Pt)[9] and metal sulphides[10]. ALD is a cyclic process developed from chemical vapour deposition (CVD) using alternating pulses of two or more gaseous precursors which are chemisorbed onto the substrate to form the desired film and eliminate unwanted reaction by-products[11]. ALD operates based on four steps including: precursor pulse, precursor purge, co-reactant pulse and co-reactant purge (Figure 1.1). Precursor molecules initially are chemisorbed onto the surface and under suitable conditions, leads to a saturative layer of surface species[12]. Once saturation has been achieved, no further adsorption can occur and hence, excess precursor remains in the gas phase, where it is readily pumped away during the subsequent purge step. The saturation behaviour of ALD results in self-limiting film growth and hence, allows deposition of conformal and uniform thin films with precise thickness control even on high aspect ratio three dimensional structures. According to the literature, no other thin film technique can produce the high conformality obtained by ALD on high aspect ratio structures[11]. A suitable co-reactant is then introduced into the chamber which reacts with the chemisorbed precursor of the surface. A second purge step is used to complete the ALD cycle, which carries away all un-reacted species and by-products, and making the surface ready for the next cycle. Not all ALD processes follow four steps using two reactants; in some cases three or more reactants are used in sequence[13].

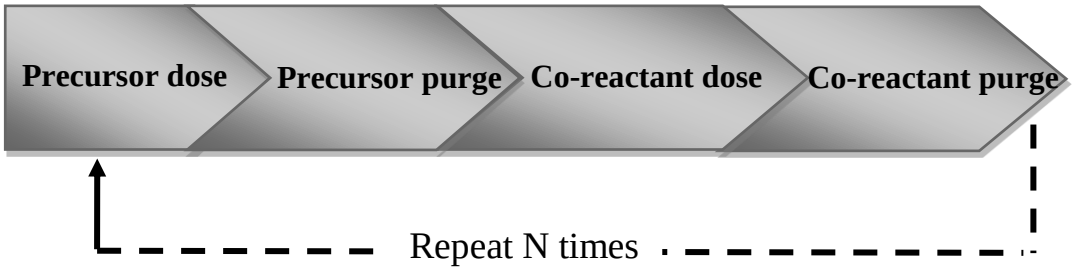

Figure 1.1: *Schematic of the ALD process to deposit thin films*

ALD can offer several key advantageous compared to other deposition techniques such as electrochemical deposition, physical vapour deposition (PVD) or chemical vapour deposition (CVD). These key advantages are including industrial scalability due to the non-directionality of the ALD processes[15], chemical selectivity (enable to deposit only on the regions with reactive surface species)[14,15], highly control of the thickness down to the Angstrom level, the ability of conformal coating on high aspect ratio structures, large area uniformity, pin-hole free film and relatively low substrate temperatures[8].

ALD films have numerous applications in both commercial and research area. Various companies such as Intel, Aixtron, Applied materials, Beneq, etc[16], use ALD technology for both commercial and research applications. ALD has become mostly an established process within the microelectronics industry and is rapidly becoming an enabling technology in an increasingly diverse range of sectors. Amongst other technology sectors, ALD is enabling significant developments in microelectronics[17], renewable energy[18], energy storage[19], food packaging[20], biomedical[21] and photonics[22]. Unique features of ALD can be highlighted in each of these applications providing new levels of performance[1]. One of the potential application of ALD is antimicrobial coating over highly porous and complex three dimensional implant structures due to its superb sub-nanometre scale thickness control and excellent conformality.

Among a diverse range of materials which have been deposited by ALD, there has only been a very limited number of published studies concerning ALD of silver so far[23,24,25,26,27,28]. The deposition of silver films with both chemical vapour deposition (CVD)[29,30,31] and physical vapour deposition (PVD)[32] has been explored over a period spanning more than 40 years exploiting, however, silver ALD has been investigated more recently for less than 10 years. At the time of doing this research, only three publications of silver ALD was reported. The limited number of researches in this area perhaps reflecting the challenge involved in developing volatile silver precursors, which are stable enough to survive vaporisation.

The ability of conformal coating of ultra-thin metallic silver nano-textured films are of significant interest for a range of applications including anti-microbial surfaces[33], plasmonic enhanced thin film PV[34], catalysts[24] and gas sensors[35]. In these applications, control over the size, shape and distribution of the nanoscale features on the surface is often critical to the functional performance of the layer. As several of these applications involve non-planar surfaces, the current work seeks to develop a thermal ALD process for the deposition of silver due to its ability in conformal coatings onto complex non-planar surfaces. This process should be controlled by self-limiting surface reactions to enable the production of highly conformal coatings onto complex three dimensional surfaces. To the best of our knowledge, only two published studies have reported on thermal ALD of silver and both leave open unanswered questions relating to the ALD temperature window and to the self-limiting nature of the processes that they describe[23,24].

The first thermal ALD study of metallic silver by Chalker et al.[24] used liquid injection ALD to demonstrate the growth of silver nanoparticles (NPs), using the organometallic precursor (hfac)Ag(1,5-COD) ((hexafluoroacetylacetonato) silver(I) (1,5-cyclooctadiene)) dissolved in a 0.1 M toluene solution. The silver adsorbate species was reduced to metallic Ag NPs using

intermittent pulses of propanol. Transmission electron microscopy reveals that the NPs deposited in the temperature range 110 ºC – 250 ºC consist of face centred cubic, facetted silver crystallites. Although this seminal paper is of great interest, it focuses more on the properties of the nanoparticles rather than on the ALD process itself and hence it does not provide evidence that the process is self-limiting.

The second thermal ALD study was done by Masango et al.[23] reported on the deposition of silver nanoparticle films using trimethylphosphine (hexafluo-roacetylacetonato) silver (I) as a silver source together with either formalin (for the AB-type process) or with trimethylaluminum and water (for the ABC-type process) as co-reactants. In their process, growth rate is defined as being self-limiting between 170 and 200 °C, however, they also observe an increase in the growth from 2 to 10 ng/cm^2/cycle as the temperature increases. This increase in growth rate together with the TGA data would appear to indicate that thermal decomposition of the silver precursor is at least partly contributing to the observed growth rate within this temperature range which is not conclusive to be truly self-limiting process. More detail is provided in chapter 2.

The current research identifies different self-limiting thermal ALD processes for the deposition of metallic silver nanoparticle films. The motivation for this research is to exploit the self-limiting property to coat complex three dimensional structures, such as biomedical implants. In the first part of the thesis the following objectives are identified:

I. Make a contribution with respect to the ALD of metallic silver thin film by finding the optimum growth conditions for self-limiting growth

II. Using different co-reactants and investigate their incorporation with silver stoichiometry

III. Systematic investigation on the effects of temperature, precursor dose, co-reactant dose and cycle number on the deposition rate and on the properties of the films. To investigate these properties, characterization tools including XRD, SEM, XPS, AFM, EDX and four point probe were used.

IV. QCM was used as an in-situ characterization technique in order to analyse the reactions involved in the ALD process

1.2. Antimicrobial coating of orthopaedic implants

Although using antibiotics have saved millions of people's life since 20th century by the discovery of penicillin by Alexander Fleming in 1928[36], the overuse of these antibiotics has started the increase of antimicrobial resistance. In 2013, Professor Dame Sally Davies (England's Chief Medical Officer) warned disastrous consequence of antimicrobial resistance (AMR)[37] which causes threatening the global public health. For instance, every year in Europe, 25000 people die due to antibiotic-resistant bacteria[38]. In the United States, deaths caused by AIDS was less than deaths caused by a single mulita-resistance bacteria[39]. There are various ways which can threat the success of antibiotics in facing bacteria and causing antibiotic treatment failure[39]. Biofilm formation is one of the most certain reason which can cause bacterial resistance to the antibiotics and hence, bacterial infection[40]. Bio-films with three dimensional structures are a biologically active matrix of cells and extra cellular substances that are irreversibly attached to live surfaces[41,42,43] and lead to survival of microbial cells up to 1000 times more protected against most antibiotics[44]. Therefore, this can cause spreading the

infections by exchanging antibiotic genes between bacteria within bio-films and consequently, increase the formation of bacterial resistant strains[45].

One of the major failure caused by antibiotics resistance and biofilm formation has occurred in implanting orthopaedic devices. Due to aging populations and obesity, the need for artificial joint replacement and orthopaedic surgeries has increased and affect millions of people around the world over the last 35 years[46]. Increasing the need of these artificial implants also rises the number of implant-related infections which is extremely resistant to systematic antibiotic treatments. Implant infection is a serious issue and can lead to additional pain, revision surgery and even death.

There is a 'race for the surface' between bacteria and host cells where they try to win the eventual fate of the implant[47,48]. Once biofilm forms, it is impossible to treat it with antibiotics and hence, lead to revision surgery. Thus, the strategies of preventing the spread of bacteria adhesion and bio-film formation on the implant surface is considered as one of the most critical and essential step in order to avoid implant-related infections[49,50].

Silver is the most favourable metal for antimicrobial coatings because of its exceptional properties including inhibition of bacterial adhesion, broad anti-bacterial spectrum, long lasting anti-bacterial effect, etc[51]. The antimicrobial effect of silver has been confirmed to work against more than 650 disease-causing microorganisms (bacteria, viruses, fungi, etc) even at low concentration[52,53] and also found to be less harmful to the human body in comparison with some organic antimicrobial species[54].

For the first time, this research attempts to investigate if silver can be employed to reduce surface colonisation by clinically relevant pathogens by ALD coating of titanium implant structures for orthopaedic applications made with the Selective Laser Melting (SLM) technique. This can offer two main benefits by providing highly conformal coating on high

aspect ratio porous structures and also by sub-nanometre scale control over the coating thickness. The sub-nanometre control is also very important as high levels of silver in the body can result in adverse side effects[55] and hence, ALD potentially offers a route to preventing this by minimising the amount of silver on the implant. In the second part of the thesis the following objectives are identified:

V. Make a contribution with respect to the ALD of metallic silver thin film on flat titanium substrate and titanium implant structures and finding the optimum growth conditions for self-limiting growth

VI. Assessing the microbial effects of silver coated orthopaedic implants for both *in vivo* and *in vitro* studies

The numbering part of this thesis is structured as follows:

Chapter 2 provides an overview of the related literature to this work from the basic principles of ALD technique and more specifically about the ALD of silver. Also in this chapter, problems associated with medical implants are discussed. In *chapter 3*, the experimental details of the ALD growth process are presented together with all other analytical methods used throughout this research.

Chapter 4 investigates the self-limiting deposition of silver using thermal ALD with a direct comparison between propam-1-ol and butan-1-ol as two different alcohol based co-reactants. *Chapter 5* presents the results and discussions of thermal ALD of silver using tertiary butyl hydrazine (TBH) and a direct comparison has been made between TBH and propan-1-ol as two different co-reactants.

In order to evaluate the effect of titanium surface on the microstructure and growth of silver thin films, *chapter 6* presented a full study on growth of silver on titanium. Also, the 3D implant structures made by SLM are used in order to investigate the anti-microbial effects of silver ALD for both *in vivo* and *in vitro* studies. The last chapter (*chapter 7*) gives overall conclusions and highlights the main findings of this research and also, provides the ideas of the potential future work.

Chapter 2

Literature Review

2.1. Introduction

This chapter provides a review of orthopaedic implants focusing on the key challenges associated with the prevention of infection. The review covers antimicrobial coatings that can be used to kill or inhibit the growth of microbes on surfaces. The review then moves to looking at thin film deposition techniques and how these may be used to coat implants. A major focus in this section is ALD which offers the potential to conformally coat high aspect ratio implants. In particular, ALD of silver nanoparticle films will be discussed, focusing mainly on their use as an anti-microbial agent with the advantages may accrue and how this will be noticed.

2.2. Orthopaedic implants

Orthopaedic implants are described as manufactured healthcare products[56] which have been used in replacement surgeries with the aim of replacing the damaged bone and joint. Increasing obesity and increasingly aging populations have resulted in the growth of artificial joint replacement and orthopaedic surgeries and affect millions of people around the world[57]. For example, in the UK, the proportion of people aged more than 85 years will increase 100% by 2031 and 300% by 2071[58]. The joint replacement process is one of the most successful interventions in medicine with good impact on life quality[59]. Knee, shoulder, hip, wrist, ankle, spine and elbow implants[59] are some examples of orthopaedic products for join replacements which have been used worldwide. In order to manufacture the orthopaedic implants, there are many different orthopaedic companies available worldwide. Figure 2.1 shows the top ten joint replacement companies around the world[60].

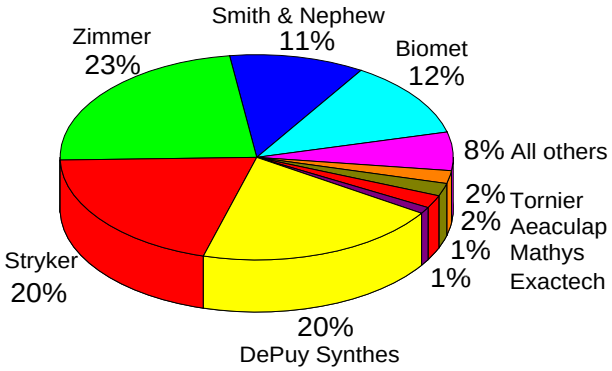

Figure 2.1: *Joint Replacement Company market (top ten)*[60]

In the US, it is expected that the demand for total hip and knee replacements will increase by 174% to 572,000 and 673% to 3.48 million procedures respectively by 2030[61]. In the UK, more than 50,000 primary hip replacement operations are taking place every year with the estimated cost of £250 million and are expected to increase up to 65,000 operations by 2026[62]. These surgeries are increasingly common in people over 50 years of age and according to the predictions, the percentage of bone disease will double by 2020 in people over 50 years of age[63]. In the UK, 35.4% of patients for implant operations are under 65 years of age, and 12.2% are under 55 years of age[64].

Regardless of the huge success in short term results of these orthopaedic implant surgeries, the long term outcomes are still suffering from several problems. Implant failure, implant loosening, implant dislocation, damaging tissue around the implant and implant infection are some reasons that can lead to revision surgery[65]. Within 15 years old of an implant, more than one third of patients need revision surgery which is an expensive and painful procedure[66]. Revision surgery also increases the risk of damage to the structural integrity of surrounding tissue as additional material is removed and even, in some cases, can lead to patient death. After revision surgery, more than 15% of patients need additional surgery, of which almost 44% need two or more additional operations[67]. Figure 2.2 shows X-ray of a knee replacement implant before the revision surgery where the primary knee replacement is unstable because of

the weekend bond (left image), and after a revision surgery where parts fit more strongly into the bones with good stability (right image)[68].

To avoid implant failure and costly revision surgery, the need to tackle the weak points of existing implants is becoming clearer. Several developments have been done in order to improve the orthopaedic implant structures including manufacturing structures with different pore morphology and size with the intention of accurate reconstruction of bone structure[69] and required nourishing to cell survival[70], progress in implant materials, implant surface coatings with biocompatible materials[71] and antimicrobial surface coatings to avoid infections[72]. The investigation of antimicrobial surface coating is of particular interest of this study.

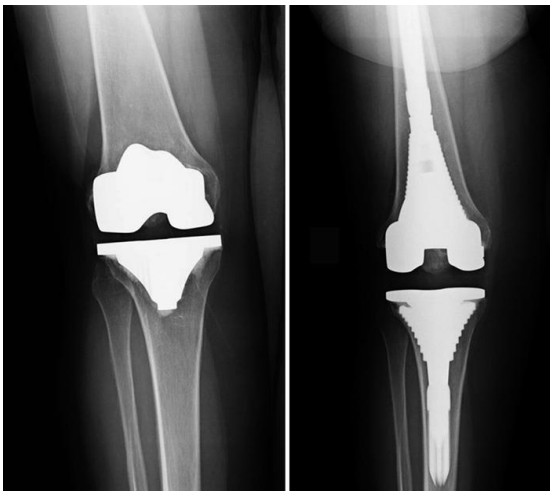

Figure2.2: *The primary knee replacement implant is unstable due to weakened bone (Left),Parts fit more securely into the bones and provide stability after revision surgery (Right)[68]*

2.3. Materials used for implants fabrication

Orthopaedic implants are most frequently fabricated from Metals, ceramics and polymers[73]. Since these devices are used as temporary, permanent or biodegradable devices, they must be able to provide suitable mechanical properties (such as ductility, toughness, wear resistance),

surface biocompatibility with the host tissue, and also possibility to be manufactured into various shapes, at relatively low cost[74,75].

"A key tenet of bone tissue engineering is the development of scaffold materials that can stimulate stem cell differentiation in the absence of chemical treatment to become osteoblasts without compromising material properties." (Dalby et al., 2007, p. 997)[76]. At present, the most common metallic biomaterials employed for the fabrication of medical devices include stainless steel, cobalt based alloys, titanium and titanium based alloys[77]. The interest in using metallic biomaterials for fabrication of medical devices is due to their high strength and resistance to fracture, which provides long-term implant performance together with the relative ease of manufacture of different shapes using existing manufacturing methods (i.e. machining, casting)[77].

Titanium and its alloys are considered as the most suitable metallic biomaterials for fabrication of orthopaedic implants[78,79]due to excellent *in-vivo* corrosion resistance (TiO_2), strong osseointegration tendency[79], and excellent biological performance[80]. Titanium alloys are of interest because of their high strength to density ratio[81].

In the early 1940s, Beaton and Davenport[82] were the first researchers who introduced titanium into the medical world by implanting it into a rat and find out no adverse reaction to titanium. Due to the bio-stability of titanium and its alloys, the number of titanium medical implants has increased more and more over time. For example, in dental implants, pure titanium has been used as the dominant material[78]. Figure 2.3 shows titanium orthopaedics medical devices for a total knee replacement (a) and a total hip replacement (b)[83,84].

Figure 2.3: *Titanium orthopaedics medical devices: (a) Total knee replacement; (b) Total hip replacement*[85,86]

To provide implant fixation to the host bone, suitable implant devices must be manufactured to supply appropriate environments for tissue development. In the past, fixing the orthopaedic implants has been achieved mostly using screws and acrylic bone cement to obtain a firm bond with the host bone, which leads to increase in the effects of stress shielding, necrosis and final failure of the implant[87]. Therefore, porous implant structures have been manufactured to provide suitable bonds with the host bone. Pore size, interconnectivity, porosity and the surface texture are the main factors that vastly influence on the cell growth and attachment into the porous devices and can lead to long term performance and stability via creating a strong physiological bond[87]. The roughness of the orthopaedic implants can help to promote the bone growth via raising the osteoblast attachments[88]. Pore dimension is a key factor in bone cells attachment to the implant surface over time and anchoring in place via the help of surrounding bone during the healing process without any extra fixation[87].

Also, a large difference in stiffness between the metallic implant and the surrounding human bone can lead to mismatch of implant-bone and eventually implant loosening due to the stress-shielding[89]. Stress-shielding can occur when implant and bone reply in a different way to applied forces[90]. By adding porosity to the implant structure the decrease in the stiffness of

implants can be obtained resulting in less stress shielding and a lower risk for implant failure, due to the fact that stiffness reduces with the square of porosity in porous materials[89].

Several manufacturing processes have been developed to fabricate porous implant structures[91,92]. Selective Laser Melting (SLM) is one of these methods which have been used for development of novel porous titanium structures for orthopaedic implants[93] with the ability of manufacturing both porous structure to provide good support for bone in growth and solid structure to supply better strength for the bone attachment. A description of the SLM methodology and its principle is available in chapter 3. This technique has the ability to produce porous parts with the optimal pore size between 100 and 700 µm, which is compatible with the natural pores in human bones and provide most effective porous implants[94]. SLM is used as a manufacturing process for fabrication of implants throughout this research.

In addition to consider all of the mentioned points, the introduction of implants in the human body is typically combined with the risk of infection, specifically for revision surgeries and the fixation of open-fractured bones[75]. Therefore, this motivates researchers to develop and investigate new methods for implants surface treatment to avoid infections or at least reduce them as low as possible, which is of particular interest of this study.

2.4. Bacterial infections of orthopaedic implants

Implant infection is a serious issue and can lead to additional pain, revision surgery and even death. Revision surgery is also very expensive and can be three to four times the initial costs for the patient and society[95] and also can result in higher morbidity. 'The Centre for Disease Control and Prevention' has stated that removal of one or two breasts results in a 2% chance of SSI (the surgical site infection), which increases to 12% when breast implants are used[96].

One of the most successful and cost-effective joint replacements is total hip replacement (THR)[97], which shows excellent clinical results, and more than 62,000 have been completed in the United Kingdom (National Joint Registry, 2014)[98]. Nevertheless, these total hip replacements have an overall rate of perioperative infection ranging from 0.5 to 2%[99], which leads to an additional cost to the NHS of £300 million each year (almost £70,000 per patient to treat)[64]. A number of reasons can increase implant-related infections, such as contamination on the surface of implant devices[100], increased operational time, existence of bacteria in the body, unclean surgical staff hands throughout the surgery, etc[101].

Bio-films are formed a result of bacteria adhesion to an implant surfaces and cause implant-related chronic infections[102]. Bio-films with three dimensional structures are a biologically active matrix of cells and extra cellular substances that are irreversibly attached to live surfaces and medical implants[41]. Figure 2.4 schematically illustrates the four major stages of bio-film formation: initial attachment, irreversible adhesion, maturation, and detachment and dispersal of bio-film cells[43]. Due to the formation of these bio-films, microbial cells can survive up to 1000 times more protected against most antibiotics[43]. Hence, this can result in spreading the infections by exchanging antibiotic genes between bacteria within bio-films and therefore, increase the formation of bacterial resistant strains[45]. The time before the bacteria firmly attach to the surface is called the window of opportunity for host cells[103] (Figure 2.4 (a)). Thus, there is a 'race for the surface' between bacteria and host cells where they try to win the eventual fate of the implant[104]. Bio-film development for bacterial cells will be difficult as soon as the host cell achieves irreversible attachments on the surface (i.e., if the host cells are the winner)[105], Figure 2.4 (b) and Figure 2.4 (c) schematically shows this process.

Bio-films are responsible for more than 80% of microbial infections in the body[106]. Therefore, the strategy of preventing initial microbial growth on the surface and hence increasing the

opportunity for host cell adhesion is one of the most important approaches towards the prevention of bio-film formation following orthopaedic implant surgery.

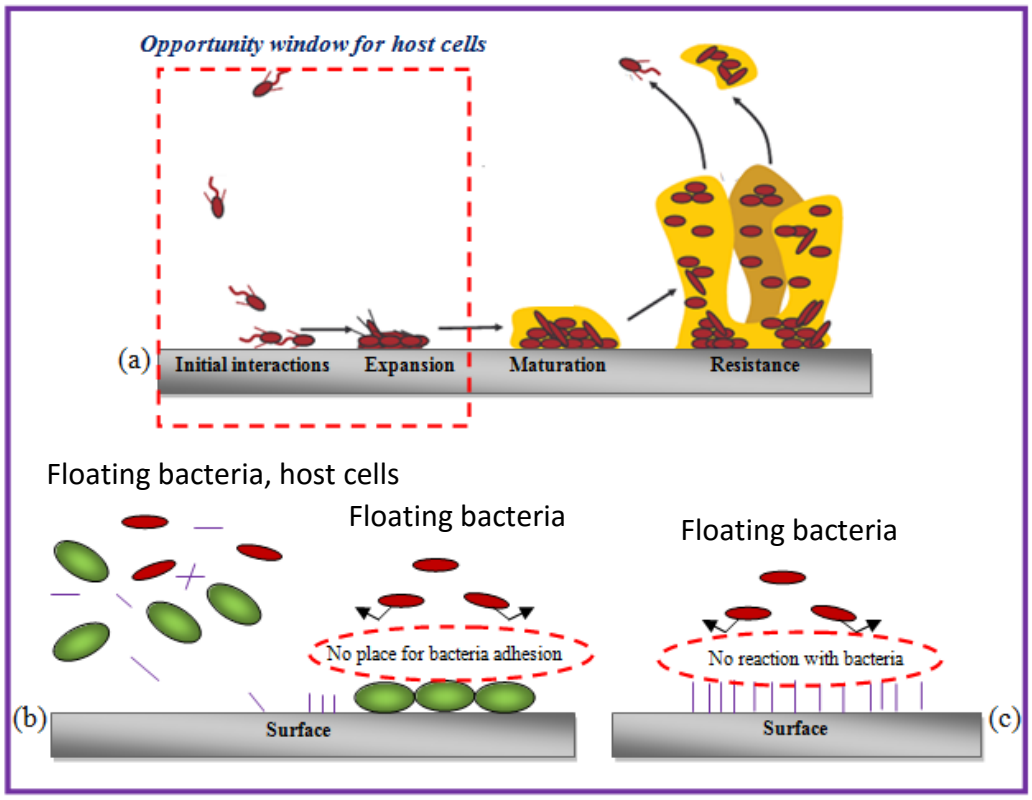

Figure 2.4: *(a) Schematic illustration of the four major stages of bio-film formation and development[43], (b) and (c) Schematic illustration for window of opportunity for host cells or local antibiotics against anti-biofilm plans[105]*

2.5. Bacteria classification of implant-related infections

Implant-related infections can happen via three routes including microbial colonisation during implantation procedure, haematogenous spreading of the pathogen to the implant or through direct spreading from an adjacent infection[107]. There are many different types of bacteria which can cause implant-related infections such as *staphylococci, Staphylococcus aureus*including *methicillin-resistant strain (MRSA), Staphylococcus epidermidis, Escherichia coli, Citrobacter, Lactobacillus, Acinetobacter, Serratiamarcescens, Klebsiellapneumoniae, P.aeruginosa, Haemophilusinfluenzae, Corynebacterium*, etc[59]. Figure 2.5 shows frequency of main types of bacteria which can cause implant-related infections. Among all these bacteria, coagulase-negative*staphylococci*, and particularly *Staphylococcus aureus* and *Staphylococcus epidermidis* are the most dominant bacteria responsible for orthopaedic implant-related infections up to two-thirds of all pathogens[108]. These pathogens are able to form strong bio-film in deep wounds and on prostheses. Very low number of these organisms (10^3 – 10^4) can cause serious infections in patients and need for revision surgeries.

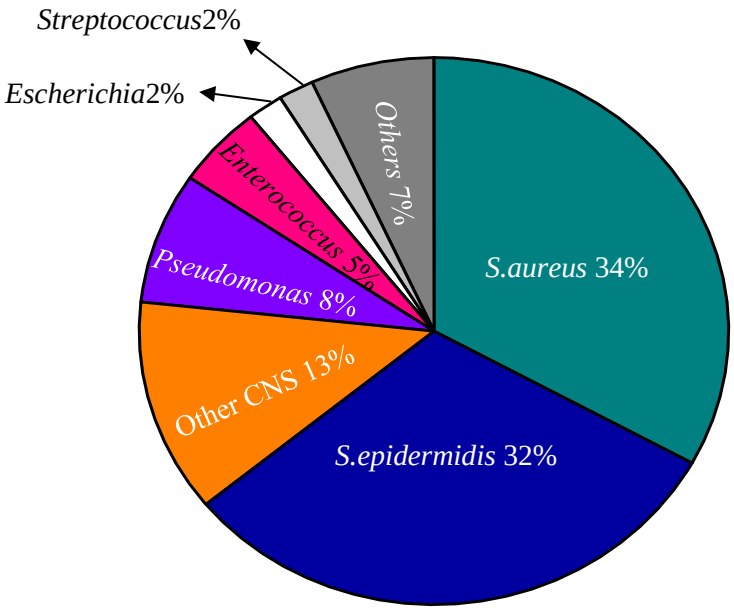

Figure 2.5: *Frequency of main types of bacteria which can cause implant-related infections*[108]

Figure 2.6 shows the X-ray of total hip replacement infection due to coagulase- negative staphylococci diagnosis. A loosening line around the stem and the cup is a sign of infection which is visible and shown by (➔). To kill the bacteria and reduce infection, using antibiotics as a systematic therapy can help, however, due to the poor accessibility to the implant site, it can lead to low drug absorption at the target part. Increasing the antibiotic doses can also result in toxicity of antibiotics in particular organs and increase in resistant bacteria and produce allergic reactions[109]. It can be imagined that some of these implant related difficulties may be solved via local delivery system of antibiotics[110]. Although local delivery system offers some advantages over using antibiotic doses such as avoiding systematic toxicity by better control of antibiotics distribution[111] and a low rate of bacterial resistance, it suffers from certain drawbacks including poor penetration into the tissues, need another operation for removal after finishing the antibiotic release, hospitalization to monitor drug levels, etc[112]. The prevention of infection has become a high priority for orthopaedic studies and motivates researchers to develop new strategy against implant infections. Therefore, antimicrobial coating of implants has been established to prevent infections of implants and to overcome some of mentioned issues.

Figure 2.6: *The X-ray of total hip replacement infection due to coagulase- negative staphylococci in 77-year-old man, [(➔) shows infection]*[113]

2.6. Antimicrobial coatings of orthopaedic implants

As it has been already discussed earlier on in this chapter, one of the worst probable outcomes of orthopaedic implants is bacterial colonization and bio-film formation on the implant-tissue interface which are extremely resistant to systematic antibiotic treatments. Microscopic images reveal that bio-films consist of microorganism in vertical structures which sometimes take the shape of tower or mushrooms[114] and they can quickly develop from the initial adhesion of bacteria to an implant surfaces and lead to implant failure. Thus, preventing bio-film formation is considered as the most critical and essential step in order to avoid implant-related infection[49,50]. As biofilm grow in a matrix form, having a not fully coated surface can also facilitate the arrival of other bacteria by providing diverse adhesion sites and develop the matrix to hold the biofilm together[115] and therefore, lead to implant failure. Figure 2.7 shows schematically the biofilm formation on fully uncoated surface (a), an antimicrobial coated surface with some uncoated parts (b) and a fully antimicrobial surface coated (c). Therefore, using methods with the ability of fully and uniform coating specifically over the high aspect ratio and complex geometries of implant structures (i.e. porous) is a significant issue that needs to be reflected.

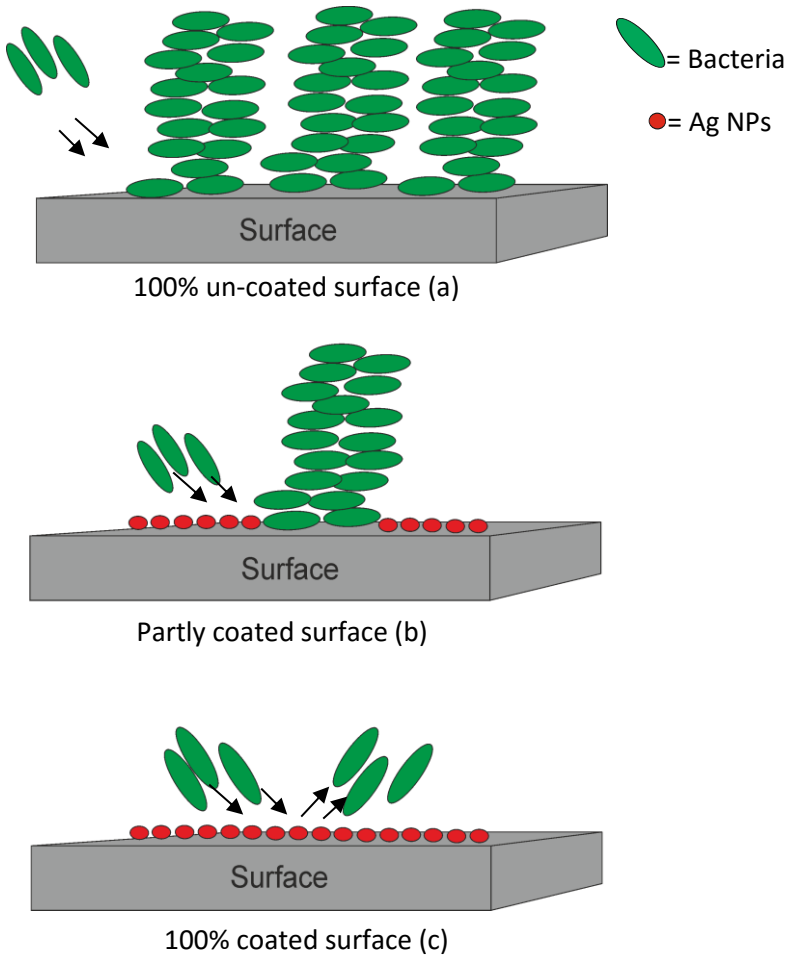

Figure 2.7: *Schematic of (a) 100% un-coated surface, (b), partly antimicrobial coated surface, (c) 100% antimicrobial coated surface*

Various investigations have been done relating to antimicrobial coating of implant surfaces with different materials[116,117,118,119,120]. In this section, methods and material requirements for antimicrobial surface coatings on orthopaedic implants have described with the aim of preventing implant-associated infections. Commonly, two different forms of implant coating have been defined, known as active coatings and passive coatings:

1) Passive surface coating:

In passive coatings, there is no releasing bactericidal agent, but the implant surfaces are designed to reduce the bacterial adhesion via surface chemistry or kill bacteria upon surface contact[121]. Therefore, surface features including surface energy, surface chemistry, surface roughness and surface conductivity play a significant role[51] in controlling the early bacterial adhesion and implant infection which resulted in the success of this type of coating. The physiochemical surface modification in passive coatings of the implant surfaces can happen in a reasonably straightforward and cost-effective ways. For instance, there is an available study showing that crystalline modification of titanium oxide layer can lead to achieving a bacterial anti-adhesive surface and decrease the bacterial attachment[122]. Another example is using ultraviolet light irradiation to enhance "spontaneous" wettability on TiO_2 in order to reduce the bacterial attachment on titanium implant surfaces[123,51,124].

In addition to the anti-adhesive coatings to the implant surfaces, there are some other studies with the focus on surface structure and design to manage and control the biological reaction by the implant surfaces. For instance, according to Singh et.al.,[125], bacteria cells preferably attached on the smooth surfaces compared with rougher surface due to the fact that rough surfaces enhance the formation of proteins clusters and therefore, proteins may perform as a passivation layer which slows down the bacteria attachments.

However, it is useful to point out that these mentioned anti-adhesive coating methods suffer some drawbacks and challenges. One of the main challenges of these methods is incapability to find a comprehensive way of treatment which can be applied to all bacteria and all surfaces. Another challenge of passive coating methods is that the success of these coatings against

bacterial adhesion is still limited and largely dependent on the bacterial types. Also, the *in vivo* efficiency of these methods against bacteria is weakly recognized and more studies and analysis are required to be able to introduce these techniques to the markets[121].

2) Active surface coating:

In active coating, on the other hand, bacteria and infection can be controlled and killed due to the coating releasing bactericidal agents like silver ions, antibiotics, antiseptics, or other organic and inorganic compounds[121]. Antimicrobial implant coating can provide some advantages such as locally controlled delivery of drugs lasting from weeks to months and increased implant longevity[126]. Active antimicrobial implant coatings must have the ability to release a controlled dose of drugs throughout the implantation time. There are various factors that can affect the time and release rate of drugs from the coated implant including homogeneity, porosity, chemical nature, coating materials and, preparation methods[127]. For example, the homogeneity and uniformity of the coating can increase the release time and stabilise the antimicrobial effect and hence, reduce the chance of bacterial colonisation[128,129].

In the future, the implant surface may be designed as a 'smart surface' which is expected to be able to be multifunctional and be responsive to different stimuli and biological tasks at the same time including the presence of bacteria[105,121]. Figure 2.8 show a rough scheme of multifunctional coated implant surface in total hip replacement. However, these kinds of coated implants are still in the early stages of progress.

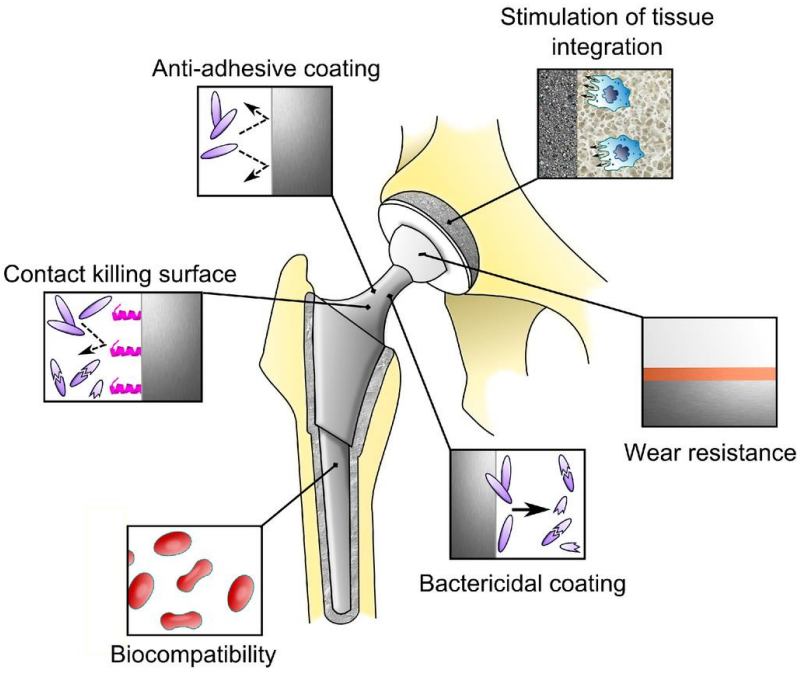

Figure 2.8: *The future scheme of multifunctional coated implant surface in total hip replacement The reaction depends on the exact capabilities of the coatings obtained throughout the manufacturing procedure*[105]

Despite all of the advantages of antimicrobial coated implants, there are still several obstacles that need to be overcome such as cytotoxicity, providing high enough coating adhesion to be able to sustain mechanical stresses during the surgical procedures, the risk of rising in bacterial resistance, provide highly uniform and homogeneous coatings even at high aspect ratio and highly textured (i.e. porous) structures to stabilise the antimicrobial effect of the coating and also avoid and minimise the chance of bacterial bio-film formation by fully coating the complex 3D implant surfaces[105].

2.7. Material requirements for antimicrobial coatings

Antimicrobial coatings must meet several requirements such as: non-toxicity in the human body, wide-spectrum activity against microorganisms, long-lasting antimicrobial effect, reasonable manufacturing cost, no unwanted long-term side effects in the body, etc[130]. Organic materials (antibiotics, anti-infective peptides, etc), metals (silver, zinc, copper, zirconium, etc) and non-metal elements (i.e. selenium) are types of materials which can be used in antimicrobial surface technologies[105].

2.7.1. Metals

Although a clear explanation of the mechanism of metallic antimicrobial materials has not yet been provided, the antimicrobial activity of the most metal coatings is related to the metallic ion or Nano form regardless of the bulk properties of the material[131]. As an example, metallic silver has no antimicrobial effects on its own and therefore it relies on releasing silver ions from the surface. The possibility can be explained as the positive charged metallic ions attached to the negatively charged bacterial cell walls and hence, lead to cell lysis and death[132]. Silver, copper and zinc show strong antimicrobial activity and have potent antimicrobial effect against broad spectrum of microorganisms[121].

In 1999, Shopsin et al. stated that there is a good possibility of using zinc oxide in medical world[133]. Antibacterial effect of zinc oxide nanoparticles have been identified versus many microorganisms including Klebsiella pneumoniae[134], Methicillin-resistant Staphylococcus aureus (MRSA)[135,136], Escherichia coli and Pseudomonas fluorescens[137]. Zinc oxide nanoparticles has shown a considerably good antimicrobial activity against Methicillin-

resistant Staphylococcus aureus (MRSA) which is one of the most important bacteria in implanted-associated infections and can lead to a large number of infections such as pneumonia, bacteraemia, surgical site infections (SSI)[133]. The coating of zinc oxide nanoparticles have important features including effective antimicrobial activity, chemical and physical stability and also high catalysis activity[133,138].

Copper is another metallic surfaces known to have good antimicrobial properties against bacteria, yeasts and viruses since ancient times[139]. It has been used in several applications such as door handles, touch plates, bed rails, call buttons, toilet seats, etc, due to its excellent contact killing mechanisms[139]. There are different available studies on titanium coated copper surfaces for exploring antimicrobial effects of medical implants[140,141,142]. Even though copper is a trace metal in the body and an important part of various enzymes, it can also cause cytotoxicity[143,142].

Although zinc and copper show good antimicrobial effects against many microorganisms, silver is the least cytotoxic[144] and the most common and effective antimicrobial coating against bacteria[145], being approximately 10 times as powerful as copper. Even though silver has a wide antimicrobial range with excellent antimicrobial activity and low toxicity[146], use of silver-coated implants stays relatively limited. As the main focus of this review is antimicrobial coating of silver and its mechanism, a more detailed report on silver and its antimicrobial mechanism will be provided in the following section.

2.7.1.1. Silver and its antimicrobial mechanism

Silver is the most favourable metal for antimicrobial coatings because of its excellent properties including inhibition of bacterial adhesion, broad anti-bacterial spectrum, long lasting anti-bacterial effect, etc[51]. There are different ways that silver can be absorbed into the human body[147], including silver-coated medical implants, dermal contact, ingestion and inhalation[148]. Due to the antimicrobial effect of silver, it has been utilised in many products in everyday life (washing machines, wound dressing, cloths containing silver, etc) since ancient times with no awareness of its working mechanism[132].

The antimicrobial effect of silver has been confirmed to work against more than 650 disease-causing microorganisms (bacteria, viruses, fungi, etc) even at low concentration and also found to be less harmful to the human body in comparison with some organic antimicrobial species[52,53]. Although silver is a heavy metal and can be tolerated better than most heavy metals in the body[149], its relative high toxicity can be a concern. For instance, there are some reports about the toxicity of silver ion on human cells in concentrations above 10mg/L[150]. The concentration level of silver must be sufficient against bacteria but not harmful for humans at the same time. In addition, some studies show that not only the concentration of silver but also its form can affect the toxicity level[151]. For example, according to Rosenman et.al.,[152] soluble silver compounds can be absorbed much more easily than metallic silver in human body and therefore, may lead to undesirable effects on human health[151].

There are a number of mechanisms which can potentially explain the antimicrobial activity of silver; however, there is no obvious and precise explanation of this mechanism[96]. It is reported that metallic silver (Ag°) has no antimicrobial effect and it's antimicrobial activity is due to the release of silver ions (Ag^{+})[130].

Figure 2.9 shows the mechanism of the antimicrobial activity of silver ions. According to available studies, the mechanism of the silver ion that produces the antimicrobial effect is due to "inactivation of membrane proteins, binding with the bacterial DNA and disrupting DNA replication, impairing the ability of ribosomes to transcribe messenger RNA into the vital proteins required by the cell to function, inactivation of the cytochrome b, and consequent bactericidal activity"[153]. Silver ions can bind to live bacteria and also to dead bacteria, blood, serum, etc, and this can result in lower antimicrobial activity of the silver ions and to them being released in an undisciplined manner[154].

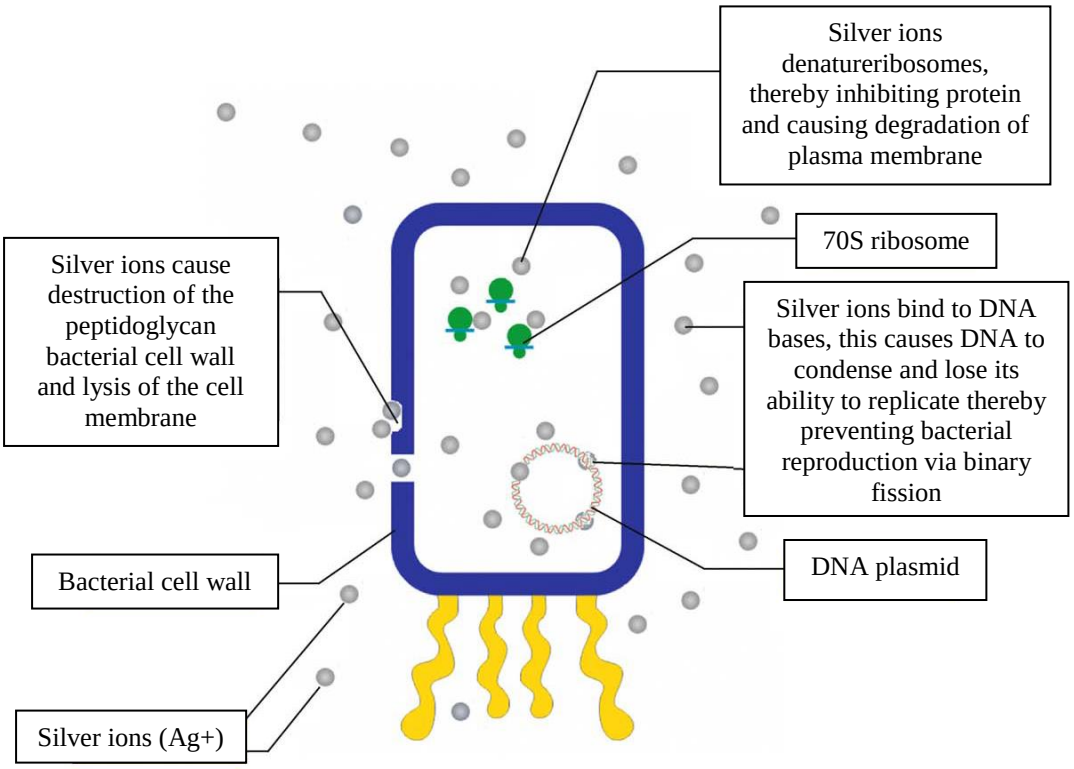

Figure 2.9: *Schematic representation of the mechanism associated with the antimicrobial behaviour of silver ions*[155].

2.7.1.2. Silver nanoparticles and their antimicrobial effect

Silver nanoparticles are clusters of silver atoms which are in the range of 1 to 100 nm in diameter size;[156] they have been used for many purposes including wound dressings, catheters, various household products[157] and bone cements[158] due to their antimicrobial activities. According to existing studies, using silver in the form of nanoparticles can result in an increase in the antimicrobial effects of the silver[159]. The increase in antimicrobial activity of silver nanoparticles compared with other forms of silver is due to the greater surface area presented for the microbes to be exposed to[160] and increases potential interactions with bacteria[161]. To investigate the exact consequences of nanoparticle size on the antimicrobial effect, nanoparticles must roughly have the same size and shape, and this is difficult to achieve with many synthesised methods. Therefore, a need for a coating technique which is able to provide uniform distributions of nanoparticles is clear.

Some theories have suggested possible ways that silver nanoparticles could affect bacteria and produce antimicrobial effect. One possible mechanism of silver nanoparticles causing antimicrobial effect is the ability of anchoring to the bacterial cell wall and penetrating it and therefore, leading to some fundamental changes in the cell membrane which can lead to death of the cell (Ag NPs contact killing lead to100% mortality against both E. coli and B. subtilis bacterial strains in 2 hours)[162]. Another possible mechanism can be explained via releasing silver ions by the silver nanoparticles and inactivating vital enzymes, damaging the cells and consequently, leading to cell death[160]. Figure 2.10 shows different mode of action of silver nanoparticles on bacteria; however, more detail studies are required to understand the exact mechanisms.

The size, shape and concentration of silver nanoparticles have a significant effect on nanoparticles activity[163]. For instance, silver nanoparticles with size smaller than <30 nm showed better antimicrobial activity compared with larger nanoparticles against *Staphylococcus aureus* and *Klebsiella pneumonia* due to the ease of penetration into bacteria[163].

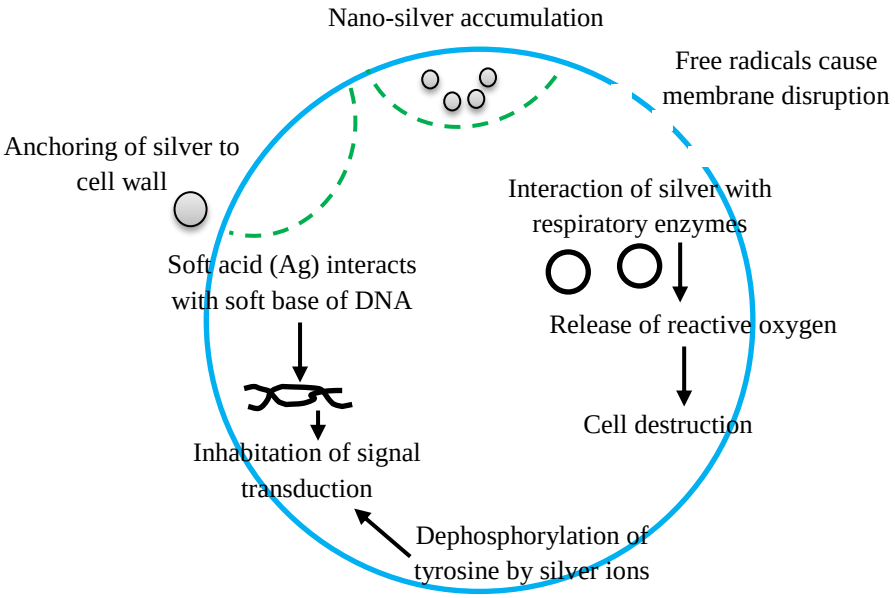

Figure 2.10: *Different mode of action of silver nanoparticles on bacteria*[160]

Silver nanoparticles have been used against both Gram-positive and Gram-negative bacteria as an antimicrobial agent[163]. Commonly, gram-negative bacteria (i.e. E.coil) appeared to be less tolerable to silver compared with gram-positive (S.aureus) and this is perhaps due to the differences in their cell wall structures. The gram-positive cell wall has several layers of peptidoglycan with strong negative charge, which may possibly stop the action of silver ions through the bacterial cell wall[163]. *Escherichia coli, S. typhi, Staphylococcus epidermidis and S. Aureus*are types of bacteria that silver nanoparticles have shown clear antimicrobial effect against them[164] *(S. aureus* and *S. epidermidis* are the most dominant bacteria responsible for orthopaedic implant-related infections).

2.7.2. Classification of implant-related infections

Sign of infection can occur during the first 3 months after surgery, referred to as early infection, usually as a result of virulent microorganisms (*e.g. Staphylococcus aureus*) with various clinical evidences such as fever, continuing local pain, erythema, edema, etc[165]. Also, symptom of infection can occur between 3-24 months after surgery, referred to as delayed infection, mostly due to low virulent microorganisms (e.g. coagulase-negative staphylococci). Nevertheless, it is difficult to distinguish the exact signs of delayed infections from aseptic failure because they are usually caused by bacterial bio-films that display little or no systematic symptoms[59]. If the infection occurs more than 2 years after surgery, it is called as late infection.

2.7.3. Health effects of silver coatings

In addition to all the positive effects of silver antimicrobial coatings, there are some possible side effects including effects of silver on human physiology, increases cytotoxicity, blood compatibility of silver coatings, etc[55,96].

a) Effects of silver on human physiology

Silver can exposed to the human body via several ways including ingestion, inhalation, skin contact, catheters, dental amalgams, etc[166]. Continual ingestion or inhalation of silver can lead to the most frequent health effects in the human body which are known as argyria (in the skin) or argyrosis (in the eyes)[151]. Although these conditions are harmless conditions, they can cause irreversible cosmetic consequences by discolouring the skin and eyes. A recent study on a patient with serious agyrosis has shown no silver

toxicity to the kidney[96]. According to several investigations, argyrosis is mostly caused by silver compounds such as silver nitrate and silver colloid solutions rather than metallic silver[167].

b) Effects of small silver particles on cytotoxicity

Although previous researches have shown low toxicity of silver ions/salts, the use of silver nanoparticles needs some investigations in order to clarify silver toxicity in NPs form as they are increasingly being used in medical devices and household products. According to some reports, silver nanoparticles change the membrane structure by attaching into it and cause damage to the cell membrane of the bacteria[168]. Studies show that bacterial properties of silver nanoparticles can significantly change according to the size and shape of the nanoparticles[169].

There are a few available *in vitro* and *in vivo* studies on the toxicity of silver nanoparticles[168,170], however, the lack of enough data relating the toxicity remained as a significant challenge and more detailed investigations need to be done before making the final conclusion on silver nanoparticles toxicity[168].

2.8. Deposition techniques

In order to have effective antimicrobial substrate coatings, deposition techniques can play an important role on the success rate of antimicrobial coated samples. These techniques should be able to fulfil a number of key requirements including strong adhesion to the implant substrate, long-term stability, control over chemistry and coating morphology, uniform and also conformal coating even on complex geometries, cost-effective process, etc[171,172]. Various methods have been used to deposit antimicrobial coating[127] including wet chemical coating (sol-gel method)[173], layer-by-layer (LBL) method[174], PVD coatings[175], CVD coatings[176,177], spray[146] and also dipping[178]. In the following section, some of these techniques will be briefly reviewed and their advantages and limitations will be highlighted. The three main categories of deposition techniques are known as mechanical (i.e. dip-coating, spray), physical (i.e. PVD, MBE) and chemical (i.e. MOCVD, Sol-Gel) techniques[179].

2.8.1. Physical based deposition (PVD)

PVD has been used in medical device industry including surgical instruments, dental instruments, and orthopaedic implants in order to deposit wear-resistant thin film coatings since the late 1980s[180]. Due to possible contamination of the film by the atmosphere, physical based deposition techniques usually need a high vacuum or ultra-high vacuum (UHV) environment. This is to provide a long mean free path of molecules, in order to help them to travel in space and not being scattered[181]. Evaporation and sputtering are the most commonly used PVD methods where atoms transferred from a liquid or solid material to be deposited onto a substrate[182]. A wide variety of substrate materials can be coated by PVD (such as metals,

polymers, ceramics, glass, etc) as well as a large number of coating materials (such as metals, alloys, semiconductors, metal oxides, carbides, nitrides, sulphides, etc)[183].

The PVD process is widely used in medical application and antimicrobial coatings as PVD can offer superior cohesion and adhesion due to ion bombardment during deposition and graded interfaces of plasma coatings[172]. Antimicrobial PVD silver coated on orthopaedic devices has been reported[184]. However, PVD methods are not able to coat complex parts and high aspect ratio structures conformally[185] as deposition is line-of-sight. This can be explained due to vapour tendency in travelling in a straight line under the high mean free path conditions and consequently, it results in poor conformality. Figure 2.11 shows a schematic of a PVD chamber and its line-of-sight deposition (blue arrows). Therefore, PVD is not a suitable technique in order to coat porous and highly textured implants with complex structures.

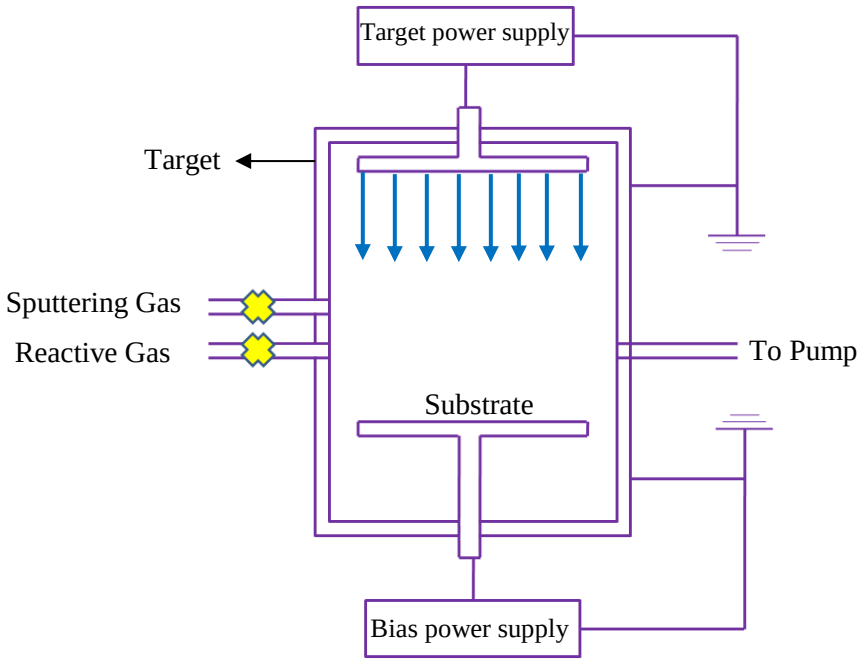

Figure 2.11: *Schematic of a PVD chamber which shows line-of-sight effect*[186]

2.8.2. Chemical based deposition

Chemical Vapour Deposition (CVD), Aerosol-Assisted Chemical Vapour Deposition (AACVD)[187] and Plasma-Enhanced Chemical Vapour Deposition (PECVD)[188] are some examples of different types of chemical based deposition methods. The appropriate reactor can be chosen depending on the application requirements for coating, substrate, precursor, morphology and thickness.

2.8.2.1 Chemical vapour deposition (CVD)

CVD is a broadly used technology which relies on the formation of solid films on a substrate by gas-phase and surface reactions[189]. CVD has been used to deposit most of the elements in the periodic table[190]. Figure 2.12 illustrates a simple schematic of the physicochemical steps in a typical CVD reaction. Evaporation, mass transport, gas phase reactions, absorption, surface diffusion and deposition are the main steps in these types of reactions.

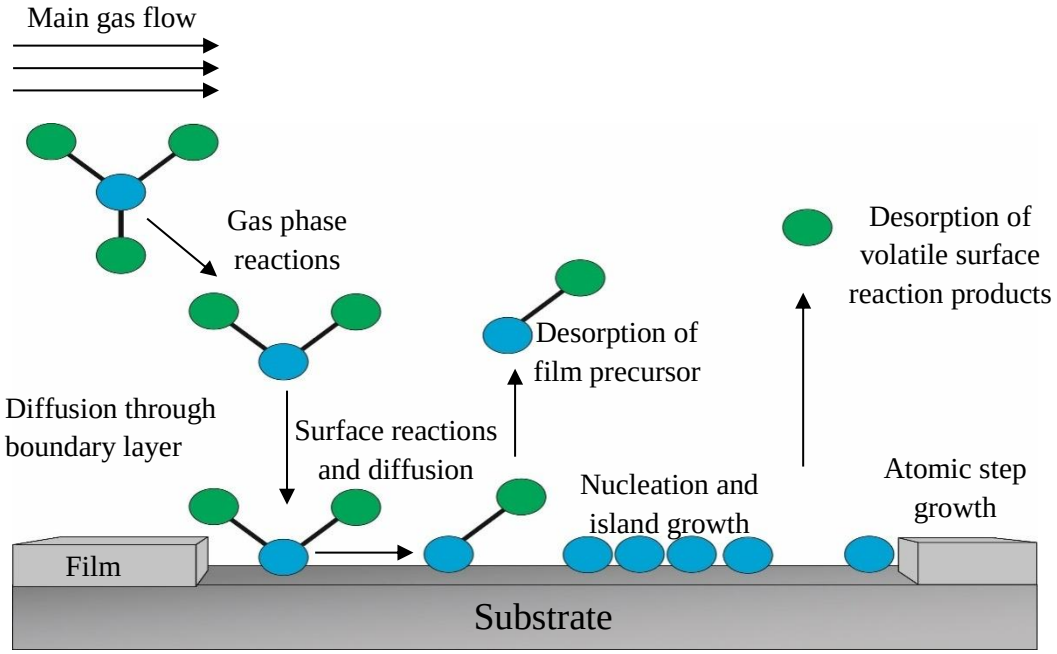

Figure 2.12: *Schematic diagram of the CVD process*[191]

A broad range of applications in thin film technology use CVD processes in areas such as microelectronics, optoelectronics, protective and decorative coatings, optical coatings, medical devices coatings, etc[191] where activation energy is typically supplied in the form of heat (thermal CVD). This can lead to some restrictions on its use as some substrates cannot withstand the heat required to react the precursors. To overcome this, a number of energy enhanced CVD processes have been developed including photo-assisted CVD and plasma-enhanced CVD. These methods enable the deposition process to take place at very low temperatures as energy to drive the reactions is provided by other sources[191,192].

CVD process can offer versatility in choosing materials (metals, oxides, nitrides and carbides and a relatively high deposition rate[185,193], however, it usually requires high process temperatures which may not be compatible with some materials (i.e. polymers)[194] and also, provides limited thickness control and conformality[195] of coating particularly over complex structures[196] due to uncontrolled chemical reactions.

2.8.3. Layer-By-Layer deposition (LBL)

LBL deposition technique is a dip-coat approach where layers are physically absorbed onto a substrate[197] and has developed since 1990s for the surface coatings[198] within the biomaterials field due to its ability to grow films on any type of substrates. Although films deposited by LBL display good thermal stability[198], it is not able to provide entirely dense and pin-hole free films[199] with the uniform coating on complex high aspect ratio structures. Therefore, a coating technique that can offer highly conformal film coverage on high aspect ratio micro-structures of implants and sub-nanometre scale control over the coating thickness is required to overcome all these mentioned challenges. In this work, we developed a coating method for orthopaedic implants by using Atomic Layer Deposition (ALD) technique.

2.9. Atomic layer deposition

Suntola and Anston in 1977 reported a rather different chemical variation of CVD called atomic layer deposition (ALD)[200], which has now become widely used in applications requiring ultra-thin films. Atomic layer deposition (ALD), also known as atomic layer epitaxy (ALE), is a cyclic growth process[201] developed from CVD. ALD is a method based on introducing pulses of the precursors onto a surface and deposition subsequently occurs via two or more surface reactions or chemisorption usually at low temperatures[202] with monolayer precision. The process relies on alternating pulses of two or more precursors with inert gas purges between them to avoid gas phase reactions[181]. As a thin film technique method, ALD can provide precise thickness control down to angstrom[11,203], highly conformal coating on complex three dimensional structures including high aspect ratio structures (such as deep trenches and narrow pores)[204], highly repeatable process and pin-hole free coatings[205].

Figure 2.13 schematically illustrates a coating comparison between PVD, CVD and ALD techniques. As is clear from the illustration, ALD can offer excellent conformality of coating on the complex structure due to its self-limiting surface reactions[206], whereas CVD shows non-uniformity over some parts of the surface and PVD shows some sections left un-coated (line-of sight effect), however, CVD shows some improvement in coating compared with PVD. Although ALD is a slow process, it can be applied to many substrates at the same time, enabling batch processing which makes it economically viable as a thin film process.

ALD has been applied in the deposition of various kinds of materials including oxides[207,208,3,209], metals[210], nitrides[211,7,212,213], carbides[214] and many others[203]. It has numerous applications including optical coatings[215,216], doping applications[217,218], catalyst[219], microelectronic industry[220,221], solar panels[222], fuel cells[202], sensors[223], etc[224].

ALD is becoming a main stream technique and has been reviewed in reasonable details in a number of sources[11,12,225,201,207]. As ALD is the main growth technique used in this current project, a reasonably detailed review will be presented in this chapter.

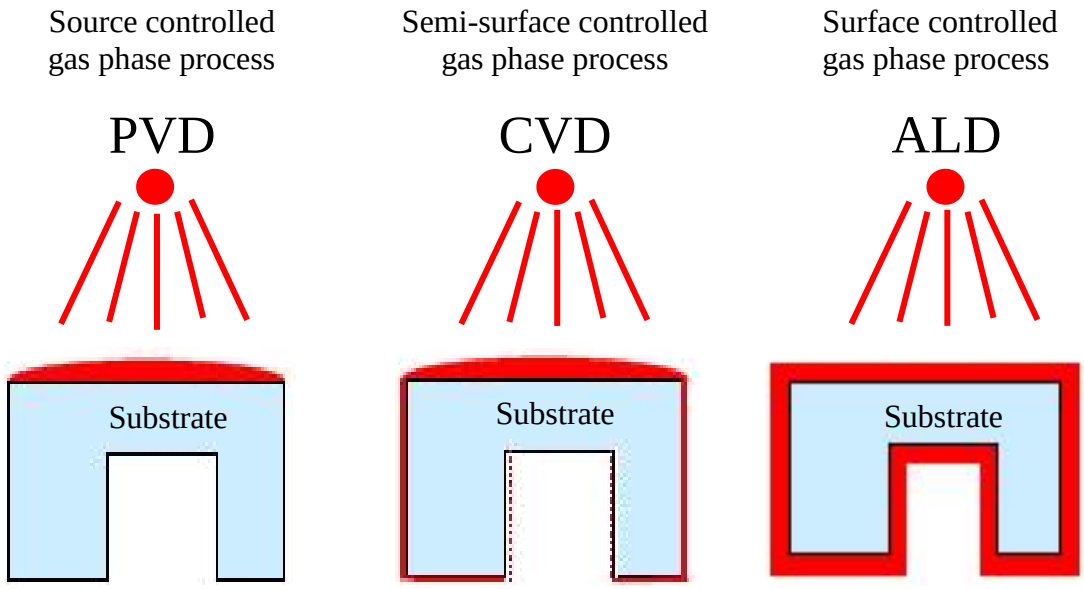

Figure 2.13: *Illustration of coating film (filled in red) on complex structures by (PVD), CVD and ALD[226].*

2.9.1. Fundamental features of ALD

The way that the coating material is arranged on the surface influences the thin film performance and this is known as a growth mode[227]. Generally, there are three basic growth modes due to competing energy terms during the ALD film deposition[228], which are recognized as: a) layer by layer growth or Frank-van der Merwe growth mode, b) island growth or the Volmer-Weber growth mode and, c) random growth mode[229] (Figure 2.14).In the 'Frank-van der Merwe' growth mode (Figure 2.14 (a)), material is preferentially deposited in un-coated areas between the existing islands from the previous ALD cycles and atoms are bonded to the substrate more strongly than each other and therefore, grows monolayer-by- monolayer (NPs-

to-substrate energy dominates). This growth mode leads to deposition of a very smooth thin film[230] and this is the most common growth mode in ALD.

In the 'Volmer-Weber' growth mode (Figure 2.14 (b)), the deposited material prefers to grow on sites where nucleation has already occurred (NPs-NPs energy dominates) and results in different shapes and sizes of islands. In the 'random deposition' mode (Figure 2.14 (c)), there is the same possibility that material will be deposited on top of all surface sites in an ALD reaction cycle. The roughness in this film growth mode is smaller than the island growth mode. There is also a possibility of mixing these modes by deposition of a layer of ALD coating and continuing to grow the islands, this growth is known as Stranski-Krastanov[230] (Figure 2.14 (d)).

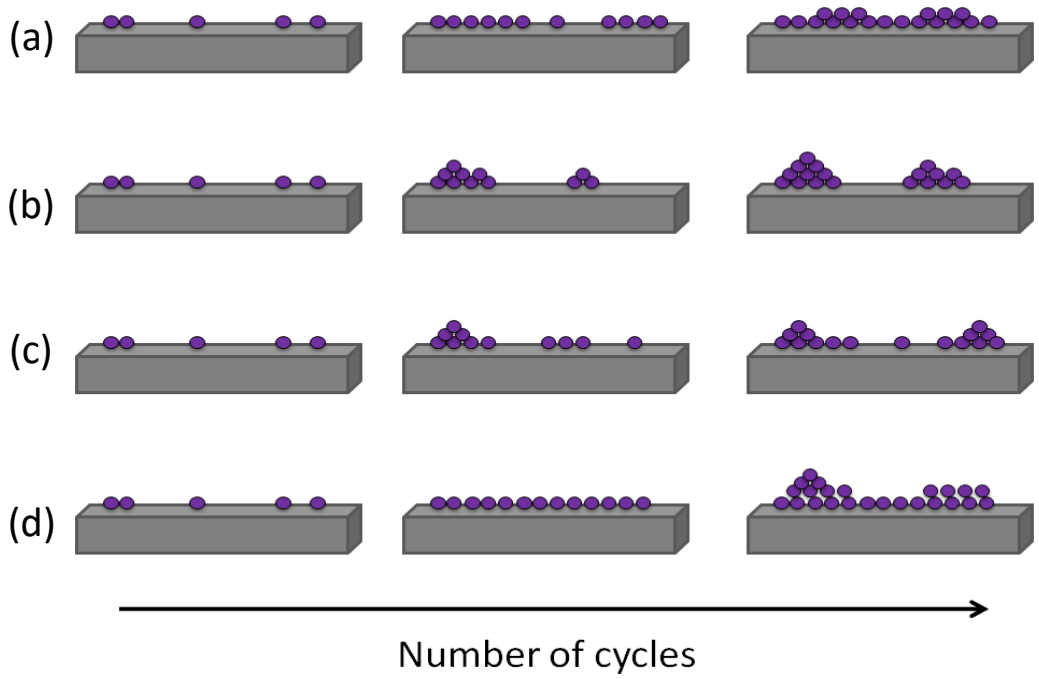

Figure 2.14: *Schematic illustration of growth modes: (a) layer-by-layer growth mode; (b) island growth mode and (c) random deposition mode, (d) Stranski-Krastanovin ALD*[231]

2.9.2. Principles of ALD

Figure 2.15 illustrates a typical cyclic surface reaction of ALD, which typically consists of four steps: 1) precursor dose, 2) precursor purge of the reaction chamber, 3) co-reactant dose and 4) co-reactant purge of the reaction chamber[232]. Depending on the desired film thickness, the ALD growth cycles can be repeated and each cycle adds a certain amount of growth (usually 0.05-0.1 nm per cycle)[233] onto the surface. The growth rate is typically measured in terms of growth per cycle (GPC)[233]. For thermal ALD, the substrate temperature is usually set and stabilized at a certain temperature (< 350°C) before starting the procedure. The temperature must be sufficient to thermally drive the surface reactions but must not cause thermal decomposition of the precursors[234].

Precursor molecules are chemisorbed onto the surface and under suitable conditions, leads to a saturative layer of surface species[12]. Once saturation has been achieved, no further adsorption can occur and hence, excess precursor remains in the gas phase, where it is readily pumped away during the subsequent purge step. Therefore, due to this surface control, the ALD process is capable of precise thickness control which is linearly proportional to the number of ALD cycles and can lead to conformal coating in large batches and even on very high aspect ratio structures[235]. A suitable co-reactant is then introduced into the chamber which reacts with the chemisorbed precursor of the surface. A second purge step is used to complete the ALD cycle, which carries away all un-reacted species and by-products, and making the surface ready for the next cycle. Not all ALD processes follow four steps using two reactants; in some cases three or more reactants are used in sequence[13].

It is worth mentioning that usually the growth rate in ALD is less than an exact monolayer per cycle and more than one cycle is needed to complete one monolayer[236], this may be due to

limited surface sites or steric hindrance of precursors. Steric hindrance occurs when each atom within a precursor molecule occupies a certain amount of space and blocking of access to a reactive site by near groups[237].

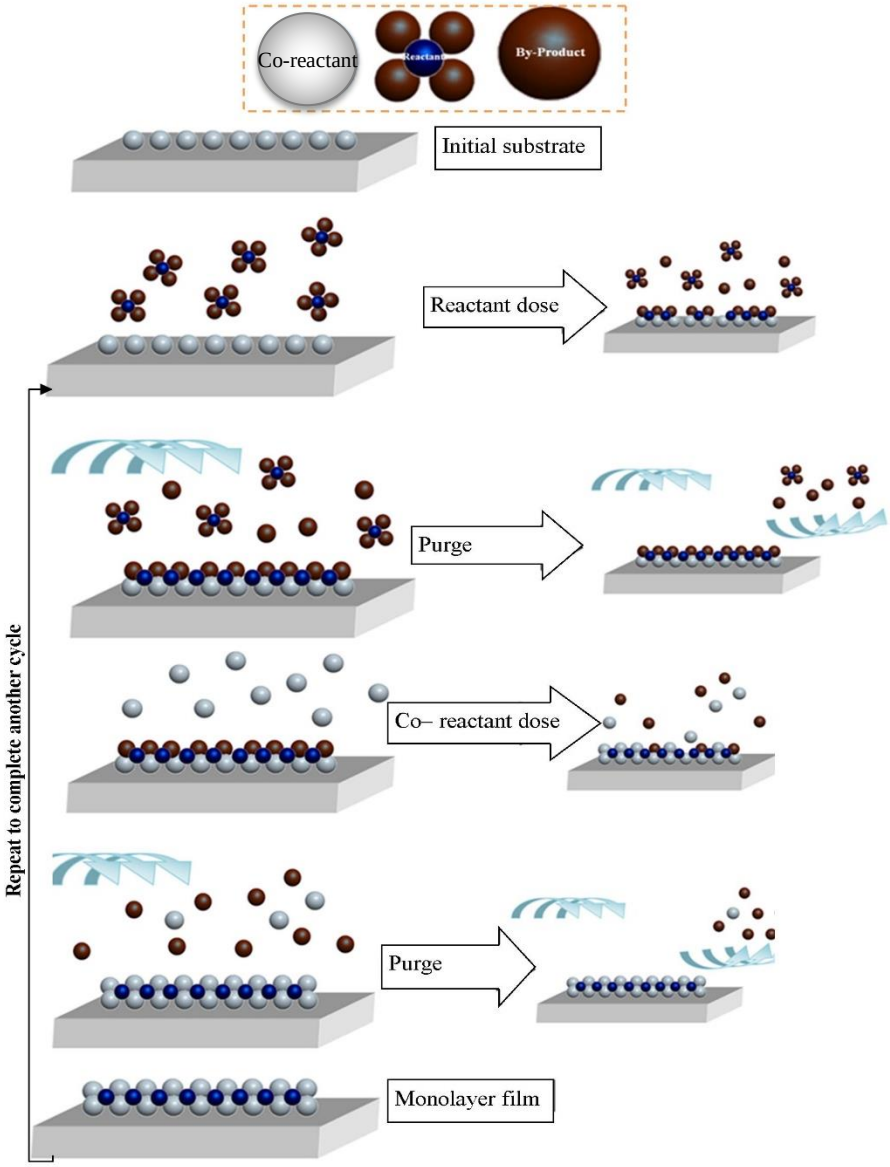

Figure 2.15: *Schematic illustration of a typical ALD process using self-limiting surface chemistry*[238]

2.9.3. Different types of ALD

Various forms of ALD have been investigated including plasma-assisted ALD (also referred to as plasma-enhanced ALD and in some cases as radical-enhanced ALD)[239], thermal or conventional ALD[207] and photo-assisted ALD[240]. Deposition aspects vary between these techniques and each of these methods can offer several merits.

For instance, plasma-enhanced ALD can provide coating at lower substrate temperatures[241,242,243], better growth rate[244,245,246], more choice of precursors[247,248] and highly controlled film composition[249,250,251] in comparison with thermal ALD. High-k dielectric layers[252,253], encapsulation[254,255] and spacer-defined double patterning[256] are some of the promising PEALD applications. Radical-enhanced ALD (REALD)[257], direct plasma-assisted ALD[258,259] and remote plasma ALD[260,261] are some of the different forms of energy enhanced ALD processes that have been used for PEALD[262,263].

In REALD method, the plasma source and the substrates are in a distant location respect to each other and therefore, only radicals are able to contact the substrate which leads to removal ion and electron on the substrates[264]. REALD can offer deposition at very low temperatures with high growth rate and was successfully used for deposition of metals (i.e. copper, silver) and oxides (i.e. tantalum oxide, aluminium oxide), however, REALD is not suitable for porous materials and high aspect ratio structures due to its high reactivity of its radicals which may lead to recombination[264].

Plasma-assisted ALD is another form of energy enhanced ALD which can also provide some potential benefits such as low growth temperature, low impurity levels, ability to deposit wide range of materials, etc[265]. However, a big challenge for plasma-assisted ALD is also inability

to produce conformal coating on high aspect ratio structures due to the possibility of recombination of radicals at the sidewalls of the structure[265].

Thermal ALD can offer some advantages over PEALD[266,267]. Thermal ALD is a well-known self-limiting technique to deposit conformal and uniform film with ultra-precise thickness control, even onto high-aspect ratio structures or porous materials. PEALD cannot produce conformal film on high aspect ratio structure as well as thermal ALD as the radicals can decompose due to collisions with surfaces; hence, PEALD is more dependent on 'line of sight'.

Similar to PEALD, photo-assisted ALD is another form of 'energy-enhanced' ALD processes and the use of light to motivate the growth is possibly thermal or photo-chemical in nature[268]. The process has been shown to use a lower temperature process compared to thermal ALD and higher growth rate[268]. However, despite the mentioned merits of this technique, very little has been published so far on photo-assisted ALD[269,240,270].

2.9.4. Self-limiting behaviour of ALD

Figure 2.16 (a) illustrates how ALD growth rate is affected by temperature and shows the key 'ALD window' where self-limiting behaviour is observed[271,272]. ALD is generally carried out within this ALD temperature window as it provides reproducible and highly uniform films in a self-limiting manner. Outside of the ALD temperature window, growth rate is affected by processes such as precursor condensation[12], insufficient reactivity[273], decomposition[246] and desorption[274]; these are summarized in Figure 2.16 (a). When the temperature is less than the ALD temperature window, condensation or insufficient energy can affect the GPC.

If precursor condensation occurs below the ALD window, results in an 'apparent' increase in growth rate, however the resulting film often contain un-reacted precursor. Alternatively, the GPC may decrease at low temperatures if there is insufficient energy to drive the chemisorption reaction of either precursor molecules or co-reactant into the substrate (low temperature can affect one or both of the 'half-reaction').

At temperatures above the ALD temperature window thermal decomposition or desorption can occur[275]. Thermal decomposition leads to CVD-like film growth and it may lead to contamination into the film with elements from precursor ligands. The GPC may also be decreased because of desorption of chemisorbed molecules on the surface.

In addition to the ALD temperature window, precursor and co-reactant pulse length play an important role in achieving a self-limiting growth rate (Figure 2.16 (b)). Increasing the precursor pulses initially results in an increase in the growth rate, however, it self-limits due to surface control reaction when the dose is sufficient to saturate the surface (all sites on the surface are already occupied when surface is saturated)[276]. This feature allows deposition of conformal and uniform thin films even on complex high aspect ratio three dimensional structures. Growing films in a self-limiting way can achieve dense and pin-hole free film, brilliant conformality on high aspect ratio structures, precise thickness control, large area uniformity and the ability to easily scale up[181]. In some cases, an ideal ALD window cannot be obtained, increasing or decreasing growth rate can occur in the saturation region because of decomposition or etching respectively. Both effect need to be minimised in order to reach self-limiting deposition.

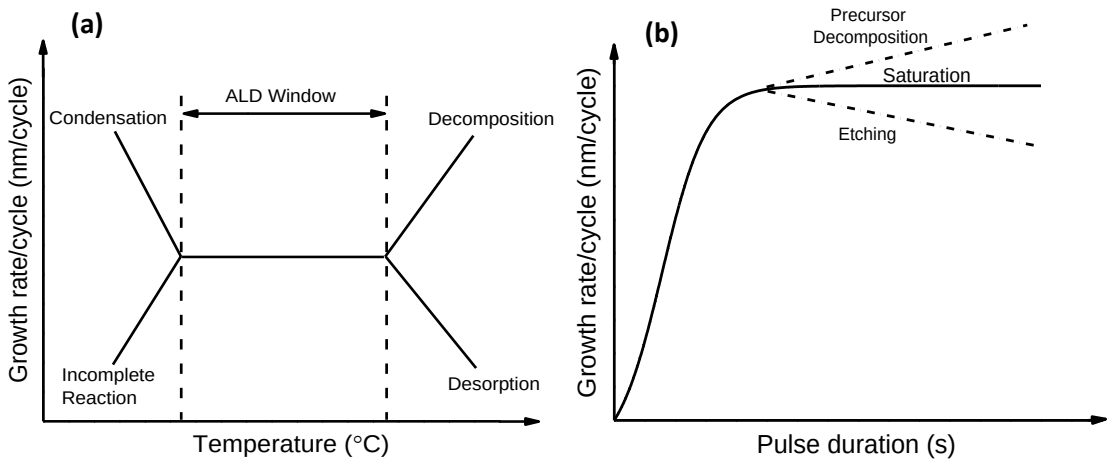

Figure 2.16: *(a) Growth rate in ALD as a function of temperature and, (b) precursor pulse duration*[277]

In addition to the ALD temperature window and precursor doses, Figure 2.17 (a) shows a linear relationship of film thickness by the number of ALD cycles, which is a good indicator to show the accurate thickness control of a self-limiting ALD process. From published data, it can be seen that noble metals grown on oxide substrates via thermal ALD show linear growth as their general tendency[278,279,280].

Although many ALD processes follow a linear trend in thickness with number of cycles, it is not uncommon to see non-linear behaviour during the initiation phase of the process, typically during the first few cycles. In many cases initial growth is enhanced due to substrate enhanced growth (Figure 2.17 (b)) or delayed due to substrate inhibited growth (Figure 2.17 (c))[277]. If the monolayer capacity on the surface is more than deposited material, the thickness shows increase in the initial phase of growth which is called substrate-enhanced growth (i.e. ALD of HfO_2 on Silicon oxide surfaces)[281]. If on the other hand, in the initial phase of the growth process, the thickness shows decrease and then increases to a constant value is called substrate-inhibited growth (i.e. the ALD of WO_3)[282].

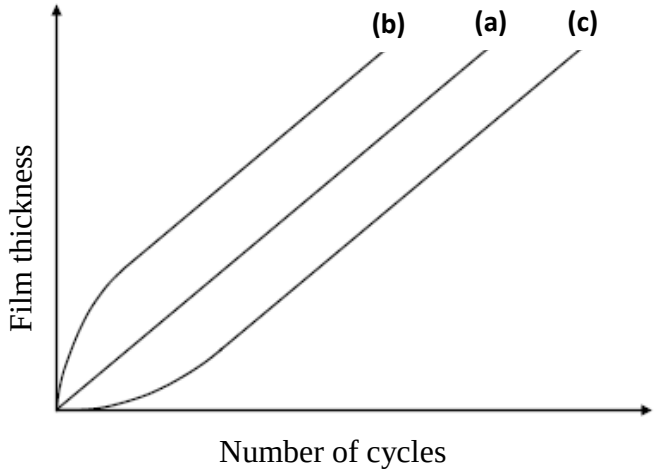

Figure 2.17: *Film thickness as a function of number of cycles a) linear growth, b) substrate-enhanced growth, c) substrate-inhibited growth*[277]

Due to the self-limiting nature of the growth, which largely gives a constant GPC, ALD is able to conformally coat complex three dimensional structures. Figure 2.18 illustrates STEM analysis of a highly conformal high-k oxide laminate coating by ALD for MIM capacitor applications with an aspect ratio of 50:1at Fraunhofer Institute for Photonic Microsystems[283]. This image is a good example of high quality and conformal coating by ALD on high aspect ratio structures. Another good example of conformal coating via ALD is a high aspect ratio of 5000:1 which has been achieved by ALD for ZnO coating on a Nano porous AA membrane by Elam.et.al.,[284,204].

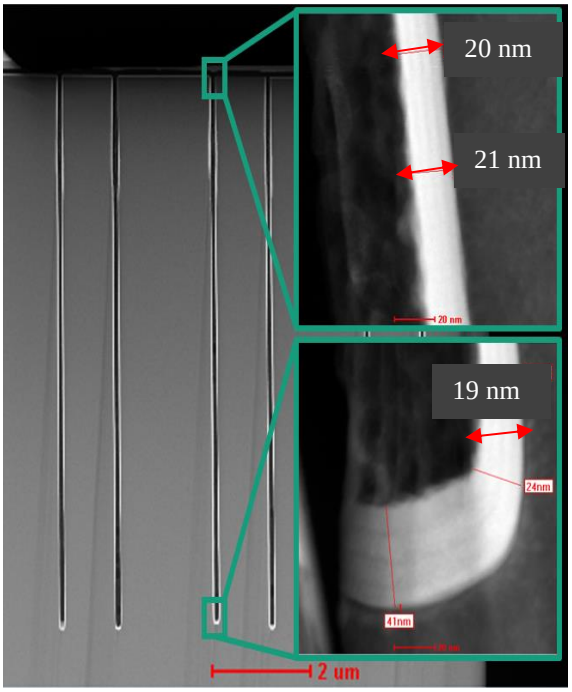

Figure 2.18: *STEM analysis of a highly conformal high-k oxide laminate coating by ALD for metal-insulator-metal (MIM) capacitor applications with an aspect ratio of 50:1*[283]

2.9.5. Benefits and challenges of ALD

The films grown by ALD methods show that ALD is a very promising technique and is already being used fora wide variety of applications (i.e. energy conversion[285], biology[286], and photonics[287]). The increased interest in deposition using ALD approach is due to several key selling points and benefits that ALD can offer. Excellent uniformity, conformality and sub-nanometre scale control over the coating thickness is achievable by ALD even on high aspect ratio structures due to its self-limiting reaction property[204]. ALD has enabled the deposition at relatively low growth temperature which is important for temperature sensitive substrates such as polymer substrates and also biochemical applications[288]. Moreover, ALD can offer some

other merits such as highly repeatable processes, scalable to batch production, good control of film composition and microstructure, etc[265].

In spite of some beneficial aspects of ALD, it is important to mention that ALD also suffers from some limitations and drawbacks[289,276].One of the most important limitations of ALD is its slow growth rate in comparison with CVD and PVD techniques. One ALD cycle regularly leads to a coating thickness in the Å range and therefore, it is not suitable for thick films application. However, as ALD is not a light-of-sight deposition technique, its slow growth rate can be compensated by up-scaling the process to large batches of substrates in one run[290].

Choosing suitable precursor with good enough volatility, reactivity and thermal stability at low temperature is another concern for using ALD method since it can limit the process. However, chemists are producing compounds to decrease the processing temperatures for many different materials (i.e. Pd, Ta, Ti, HfO_2, etc)[290,291]. Another challenge related to using ALD method is the costs of precursors which are usually very high. However, the usage amount of the precursor can be reduced by optimizing the saturation dose and therefore, decrease a large amount of precursor waste in the purging step[290].

2.9.6. Metal precursor/co-reactant

In the ALD processes, precursor chemistry is a significant factor and has been assessed in many studies[292,293]. Metal precursors in ALD depend on chemisorption of a monolayer on the surface and they can be gases, liquids or solids[294]. In the selection of a suitable metal precursor, a combination of volatility, reactivity, and thermal stability need to be considered[277] (Figure 2.19). Other metal precursor properties such as low cost, non-toxicity and ease of handling are also important to consider; however, in many cases, not all conditions are readily achievable.

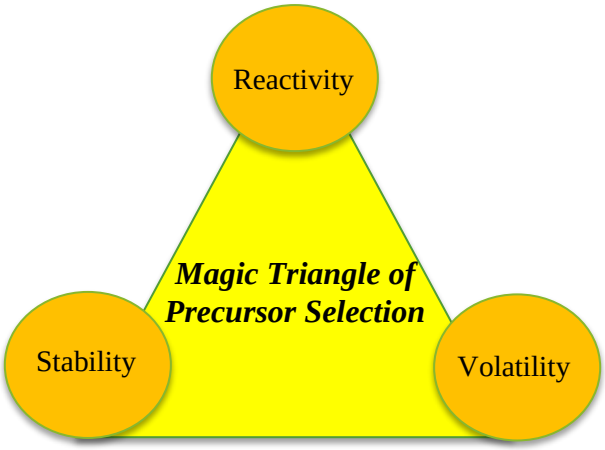

Figure 2.19: *Triangular of metal precursor requirements*[277]

In order to achieve the requirements for ALD processes, various precursors have been examined. A range of metal precursors for ALD have been developed and can be categorized as halides, -diketonates, alkoxides, alkyls, cyclopentadienyls, amides, imides, amidinates, etc[295]. There are several ALD studies showing the successful results in using β-diketonates-type precursors for deposition of metallic thin films[296,297]. This is perhaps due to the fact that the combination of noble metals (also near-noble metals) with acetylacetonate (or the related β-diketonate) ligands can provide enough volatility for an ALD precursor (i.e. using $Cu(thd)_2$ precursor for deposition of copper via ALD)[298].

In addition to the metal precursor, one or more co-reactants are typically required in the ALD process. A suitable co-reactant in an ALD processes is as significant as choosing a suitable precursor. For example, complexity in finding appropriate co-reactants has caused difficulty in ALD deposition of some metals such as copper. Thermal ALD[298], REALD and PEALD techniques[264] have been used for deposition of copper by utilizing molecular hydrogen[280], zinc vapour[299] and alcohols[300] as co-reactants respectively.

As copper and silver are both noble metals and are in the same group in the periodic table, it is expected that they have similar chemical properties and therefore, there is a good possibility to be able to use the same precursors and co-reactants for both elements. For instance, there are ALD reports on both Copper[300] and silver[24] using [hfac= hexafluoroacetylacetonate] as precursor. However, this research specifically focuses on the ALD coatings of silver and more detailed explanations will be provided in the following sections on silver ALD. Water, hydrogen peroxide, and ozone for oxygen; hydrides for chalcogens; ammonia, hydrazine, and amines for nitrogen have been used as non-metal precursors so far[207].

2.9.7. ALD precursor delivery methods

Stability and reliability in precursor delivery methods are critical factors in ALD in order to achieve success in manufacturing processes by avoiding precursor waste and minimising cost. To obtain a uniform thickness of the desired layer, precise control of the precursor dose, co-reactant dose, purge time and temperature is necessary for efficient ALD deposition. Due to the volatility of the precursor, the dosing method must be carefully selected. Any high or low temperature point in the precursor delivery line should be avoided because it could cause thermal decomposition or condensation of the precursor respectively. In some cases, ALD precursors are in solid form and they need to be changed into the gas phase via evaporation.

Additional carrier gas may be used to help precursor delivery to avoid condensation of the precursor vapour in the delivery line[277]. A number of delivery methods may be used to deliver precursors into the reactor including vapour draw, bubbling, direct liquid injection[301], vapour boost, nebulising, vapour push, aerosol assisted (AACVD), etc. All these methods will be explained briefly in this section.

Vapour draw:

When the precursors have a higher vapour pressure than the chamber pressure, they are easy to transport to the chamber using a simple vapour draw source. Basically in this method, the precursor is heated and provide vapour which can simply be sucked off and go through the reactor chamber[302] (Figure 2.20 (a)). Trimethylaluminum (TMA) and water are good examples of precursors that can be used with vapour draw[303].

Vapour boost:

Using a boost valve on the delivery system allows low vapour pressure precursors to be delivered more efficiently with the help of a gas pressurized cylinder. Low temperature ALD deposition of iron oxide is a good example where they used vapour boost system for precursor delivery[304].

Vapour push:

Using an inert push gas valve (vapour push technology) can offer a solution for low vapour pressure precursors and improve the quality of the deposited film (Figure 2.20 (b)). A comparison between the vapour push and vapour draw system for deposition of TiO_2 films

on Si (100) was made at University of Liverpool showed that better quality film with increased growth rate for vapour push system was obtained[302].

Bubbling:

Bubbling method is a conventional delivery method often used whilst the vapour pressure is insufficient to overcome the chamber pressure, but still high enough to have surface reactions[181]. In this process, an inert carrier gas (such as argon or nitrogen) is used to help carry the precursor vapour into the chamber (Figure 2.20 (c)). The actual rate of vapour transportation can be established via Equation 2.1 at a given temperature:

$$F_{liquid} = \frac{M\,(liquid)}{22.4\,l/m} \cdot \frac{Pp}{P\,(bubbler) - Pp} \cdot F_{carrier} \qquad \text{(Equation 2.1)}$$

where F_{liquid} is the mass flow rate, $F_{carrier}$ is the gas flow rate, M_{liquid} is the molecular weight of the liquid, P_p is the partial pressure of the liquid at temperature T and $P_{bubbler}$ is the total pressure in the bubbler[305]. The problem with this method often occurs in providing enough temperature to make sure that the chemical is vaporised, whilst making sure that no thermal decomposition is taking place[306]. The temperature of the precursor bubbler should be measured by an accurate and stable thermocouple to ensure the temperatures recorded are real. Any cold spot in the delivery line can lead to condensation; to avoid that happening, all the delivery line gaseous and the reactor chamber should be heated to a certain temperature (usually higher than the precursor temperature).

Direct liquid injection (DLI); Nebulising; Aerosol Assisted (AA):

To transport low volatility precursors high temperatures are needed to increase the vapour pressure, however, the thermal stability of the precursor need to be considered as this temperature rise can lead to precursor break down and decompose and hence, poor shelf life. Partial thermal decomposition of the precursor may also result in a CVD-like reaction and prevents self-limiting ALD.

Therefore, some delivery systems such as direct liquid injection, nebulising and aerosol assisted have been developed to help manage these challenges[307]. Using DLI, nebulising or AA system can lead to higher deposition quality for several reasons as; a) due to the possibility of storing the precursor at low temperature, the risk of thermal decomposition is reduced, b) flow evaporation of a 'mist' of the liquid is used and therefore, this minimised the chance of thermal breakdown while efficiently getting the precursor into the vapour phase, c) also the vapour can be provided exactly when it is needed (vapour-on-demand) and the accurate ratio can be achieved[308]. Unlike bubblers, DLI are very capable at producing vapour from liquid.

In these methods, the precursors can be stored at room temperature under an inert gas (usually Ar). Only at the time of its transportation into the vaporizer is the precursor heated to a certain temperature in the vaporizer and then transported to the deposition chamber via injectors which can be set to the pulse or continues mode[277]. However, in LIALD, the injectors are always set to the pulse mode[309]. Accurate, pure and repeatable vapours can be transported into the system by a direct liquid injection delivery method[310]. A liquid injection system has been used in this research due to the low volatility and poor thermal stability of the precursor. Figure 2.20 (d) shows a simple schematic of a direct liquid injection delivery system.

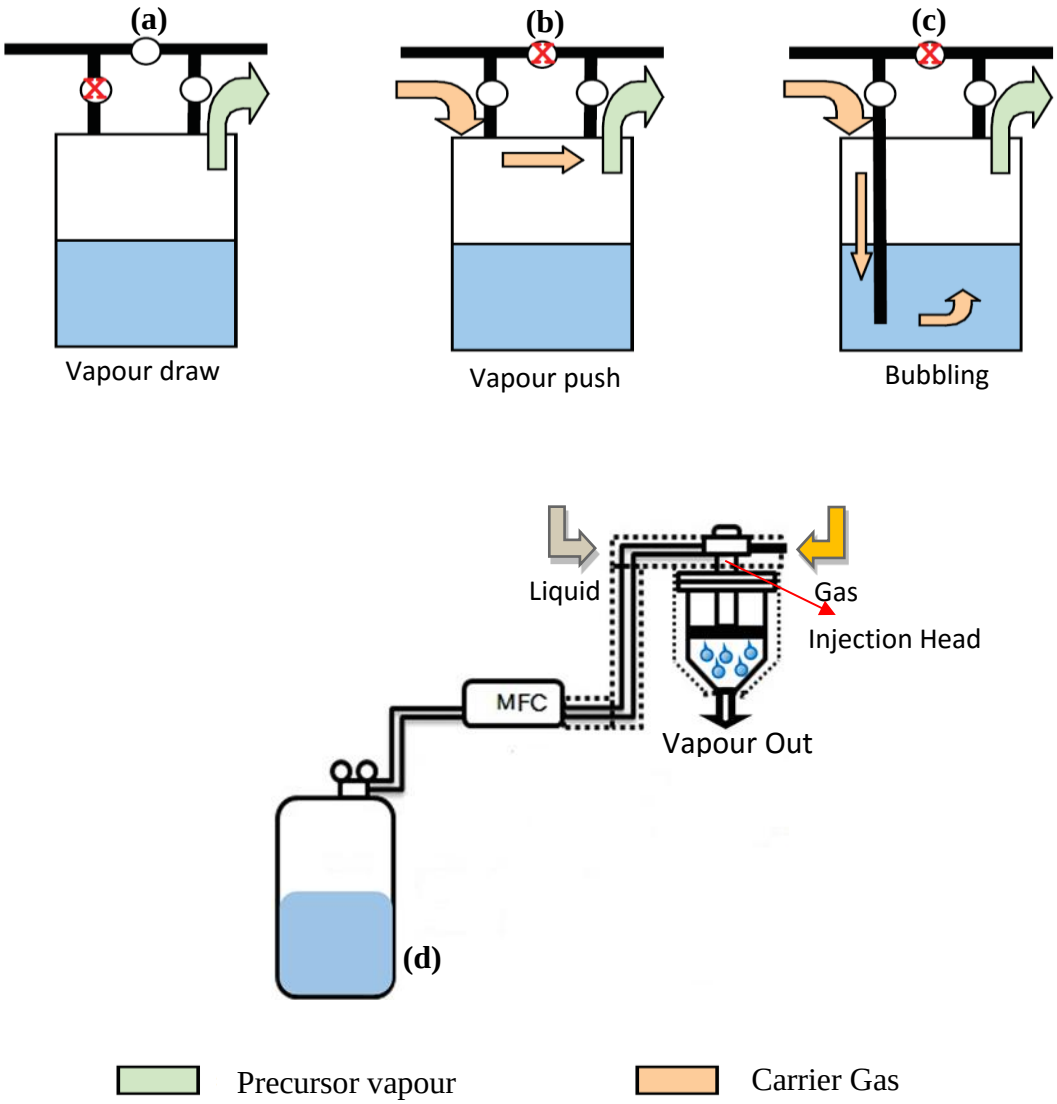

Figure 2.20: *Schematic representation of precursor transportation using a) vapour draw, b) vapour push, c) bubbling*[302]*, d) DLI*[311]

2.10. Silver ALD

Like copper and gold, silver belongs to the coinage metals[25]. Silver typically has a face centred cubic crystal structure (fcc) but the hexagonal close packed (hcp) structure has been reported for silver as well[312]. Silver has been used for many applications such as industrial applications (catalysts), electrical and electronics uses (batteries), dental and medical uses (serious burn injuries, antimicrobial coatings[313]), etc[314]. Due to the potential uses of highly conformal silver thin films in various subjects such as plasmonic devices[26], gas sensors[315], reflective mirrors[316], etc, there has been an increase in the attention paid to the ALD of silver. Silver thin films have been deposited by CVD[317,318,319,320] and PVD[321]. However, CVD deposition of silver was found to be a challenging process due to the low volatility and low thermal stability of silver precursors[322].

In recent years, deposition of silver thin films by ALD has been reported only a few times in the literature[25,26 ,24 ,23,27,28]. At the time of doing this research, only three publications of silver ALD was reported. This is largely due to the lack of appropriate volatile and stable precursors. Silver precursors that have been used in CVD are more often adducted β–diketonates and carboxylates[323]. The main barrier in using the CVD precursors for deposition of silver is limitation in the thermal stability, unlike many other ALD processes which used CVD precursors[26]. Precursors for CVD are typically activated by thermal energy to deposit the film via decomposition, whereas suitable precursors for ALD need to chemisorb on the surface as a monolayer and reach saturation. While low thermal stability in CVD precursors may be advantageous as they can readily decompose on the heated substrate to form a film, they are not suitable for ALD.

There have so far been three studies on silver thin films by plasma-enhanced atomic layer deposition (PEALD)[26], radical-enhanced atomic layer deposition (REALD)[25] and a very recent one on atmospheric pressure plasma enhanced spatial ALD[27].

In 2007, Ritala and his group published the first study on deposition of silver thin films by REALD using Phosphine-Adducted Silver Carboxylates. The precursor they chose was the most thermally stable precursor used for CVD of silver which was Ag (O_2C^tBu)(PEt_3) and hydrogen radicals as co-reactants. The silver precursor was synthesized and then characterized by mass spectroscopy (MS), nuclear magnetic resonance (NMR), thermogravimetric analysis (TGA) and infrared (IR) spectroscopy. Ag (O_2C^tBu) (PEt_3) crystals melted at low temperature and evaporated readily, which led to a good thermal stability for REALD deposition.

Silicon and glass were used as substrates and silver precursor evaporation temperature and deposition temperature were found to be 125 °C and 140 °C respectively with a growth rate of 0.12 nm per cycle. The films were found to be polycrystalline by XRD. Although conformal, uniform (even on a patterned trench substrate with an aspect ratio of 9:1) and self-limiting growth was found at 140 °C, it was limited to only one single temperature. Films with 40 nm thickness appeared to have low resistivity of 6 μΩ.cm. Furthermore, the actual film at ALD temperature was found to have a significant quantity of impurities including phosphorus (4.0 at. %), oxygen (10 at. %), hydrogen (5 at. %), and carbon (1 at. %). Figure 2.21 shows SEM images of a trench with uniform silver deposition.

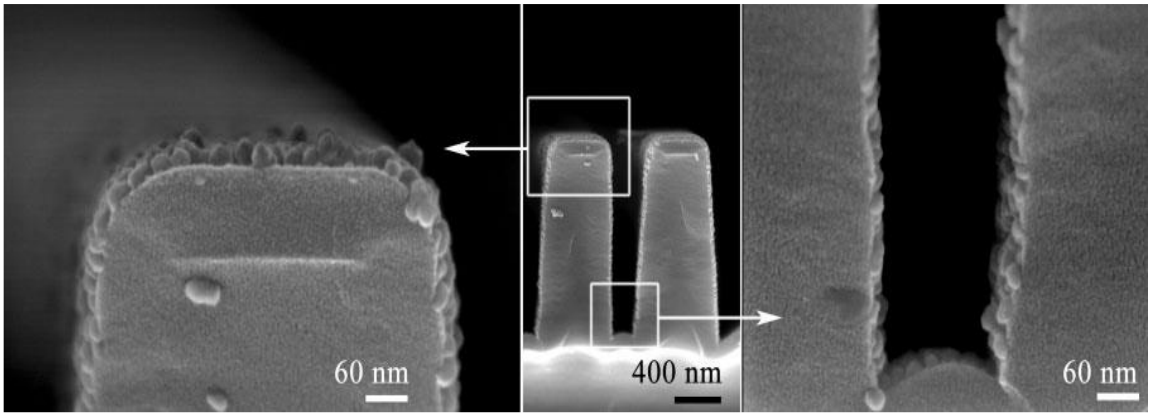

Figure 2.21: *A silver thin film deposition on a trench substrate by cross-sectional SEM images with 9:1 aspect ratio*[25]

In 2011, Ritala and his research group published another study on deposition of silver thin films by Plasma-enhanced atomic layer deposition (PEALD) on 200 mm-diameter wafers in an industrial developed reactor. They used Ag(fod)(PEt_3) (fod = 2,2-dimethyl- 6,6,7,7,8,8,8-heptafluorooctane-3,5-dionato) as a precursor with plasma-activated hydrogen as a co-reactant. An ALD temperature window was obtained between 120 to140 °C, with a growth rate of 0.03 nm per cycle.

They explained that the low growth rate of the silver films was due to the steric hindrance in the chemisorptions layer caused by bulkiness of the fod-ligand in comparison with the growth rate in the first ALD study of silver. In addition, the shorter exposure time of the plasma-activated hydrogen led to lower growth rate deposition on the substrates. This indicates that the co-reactant does not support for self-limiting growth. The resistivity of the film was 6-8 μΩ.cm with the 20 nm film thickness. In the ALD temperature window, the deposited films were found to have 85 at. % of pure silver and 15 at. % of impurities including hydrogen, carbon and oxygen. Figure 2.22 shows an SEM image of a 17 nm thick Ag film deposited at 120 °C.

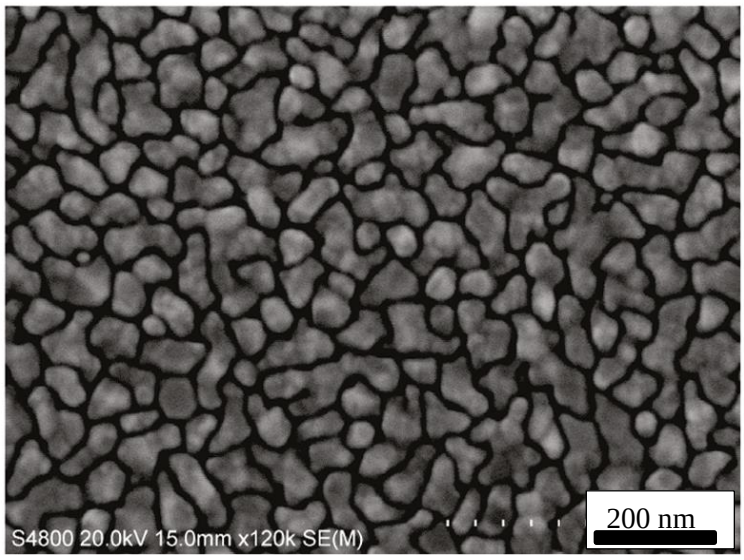

Figure 2.22: *SEM image of a 17 nm thick Ag film deposited at 120 °C temperature*[26]

In 2015, Bruele and his research team published a study on deposition of silver thin films by plasma enhanced spatial ALD using Ag(fod)(PEt_3), triethylphosphine(6,6,7,7,8,8,8-heptafluoro-2,2-dimethyl-3,5-octanedionate) silver(I), and an N_2–H_2 plasma as a co-reactant. The silver film was characterized by energy dispersive x-ray analysis (EDX) for composition analysis, high resolution scanning electron microscopy and four-point-probe to measure the resistivity. Silicon was chosen as a substrate and deposition temperature were 100 and 120 °C which revealed good purity level with a resistivity of 18 μΩ.cm[27]. They showed that silver grown as islands and the size and distribution of these islands can be controlled by different temperatures (between 100 and 120 °C) and exposure times. This process allows to control the silver film morphology accurately at all atmospheric conditions. Figure 2.23 shows SEM images of silver morphology on silicon after 2250 cycles at 100 °C (a) and 120 °C (b).

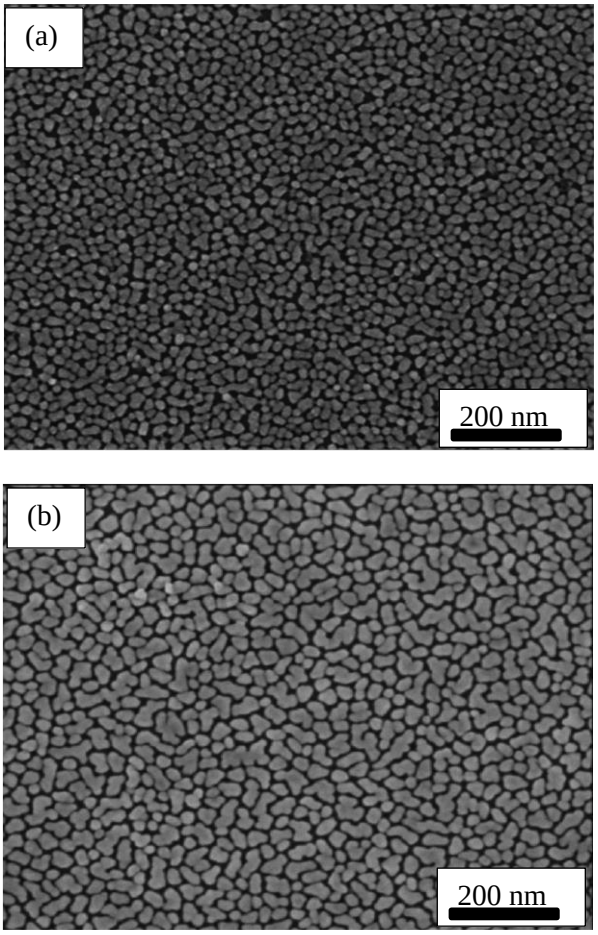

Figure 2.23: *SEM images of surface morphology of the silver films after 2250 cycles deposited at (a) 100 °C and (b) 120 °C*[27]

In addition to the three previous studies of silver thin films deposited by PEALD and REALD, two more studies have reported on thermal ALD of silver nanoparticles. In 2010, deposition of silver nanoparticles via liquid injection atomic layer deposition (LIALD) was reported by Chalker et al and developed for the potential applications in plasmonics, catalysts and analytical methods[24].

The sequential doses of (hexafluoroacetylacetonato)silver(I)(1,5-cyclooctadiene) and propan-1-ol was used at relatively low substrate temperatures (< 150 °C) to produce nanoparticle films of silver via a catalytic oxidative dehydrogenation of the metal precursor by the co-reactant. Prior to their study, the same precursor was used in MOCVD to deposit silver on a TiN adhesion layer. However, no silver films was achieved due to the fact that the precursor loses

alkene and forms [Ag(hfac)]*n* at or below the sublimation temperature and therefore, lead to insufficient volatility for CVD[319]. Hence, they realized that the same precursor can be suitable for ALD of silver. They showed in their paper the evidence for the deposition of crystalline metallic silver nanoparticles using a cyclic thermal ALD process and also presented that the particle size and distribution can be controlled by temperature and by cycle number. Figure 2.24 shows bright field and dark field TEM images of silver nanoparticles at different number of ALD cycles. Although this study was of great interest, it focused more on the properties of the nanoparticles rather than on the ALD process itself and hence it did not provide evidence that the process is self-limiting.

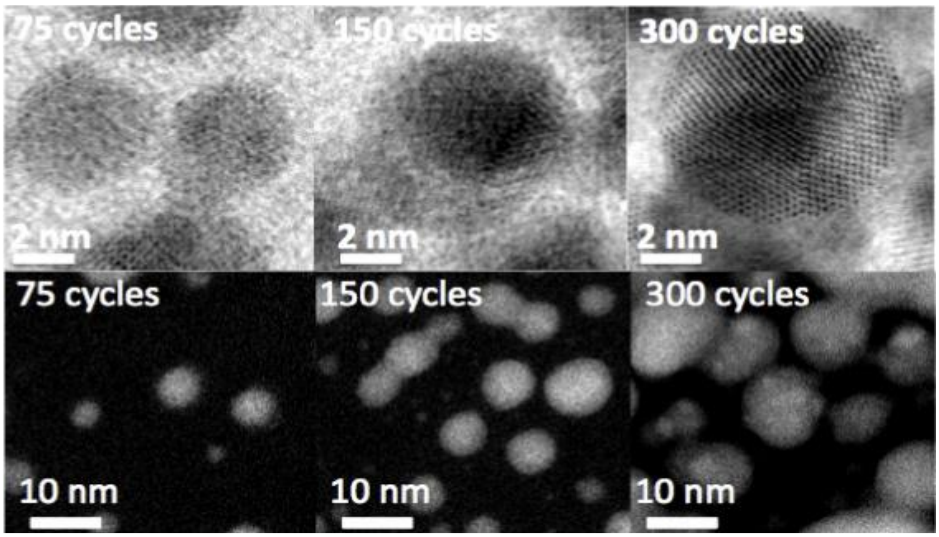

Figure 2.24: *Upper: bright field TEM images of silver nanoparticles deposited at 130 °C for various ALD cycles. Lower: corresponding high angle annular dark field TEM images*[24]

As well as the previous studies, a very recent study has been published by Masango et al[23] on the deposition of silver nanoparticle films using trimethylphosphine (hexafluoroacetylacetonato)silver(I) as a silver source together with either formalin (for the AB-type process) (Figure 2.25 (a)) or with trimethylaluminum and water (for the ABC-type process) (Figure 2.25 (b)) as co-reactants.

Masango et al used in-situ QCM to characterise the growth processes and to confirm that they were self-limiting. In their AB-type process, growth rate was defined as being self-limiting between 170 and 200 °C, however, they also observed an increase in the growth from 2 to 10 ng/cm² per cycle as the temperature increased.

This increase in growth rate together with the TGA data (presented in the supplementary information of the paper) would appear to indicate that thermal decomposition of the silver precursor is at least partly contributing to the observed growth rate within this temperature range. If a CVD-like reaction contributes to growth, then the overall ALD process is unlikely to be truly self-limiting. Although the QCM data showed a clear stepwise increase in mass with each ALD cycle, this on its own is not conclusive evidence of self-limiting ALD. To confirm that an ALD process is self-limiting really requires the effect of precursor dose on the growth to be assessed. It is perhaps worth pointing out that even CVD processes can be controlled in a stepwise fashion using short doses of precursor.

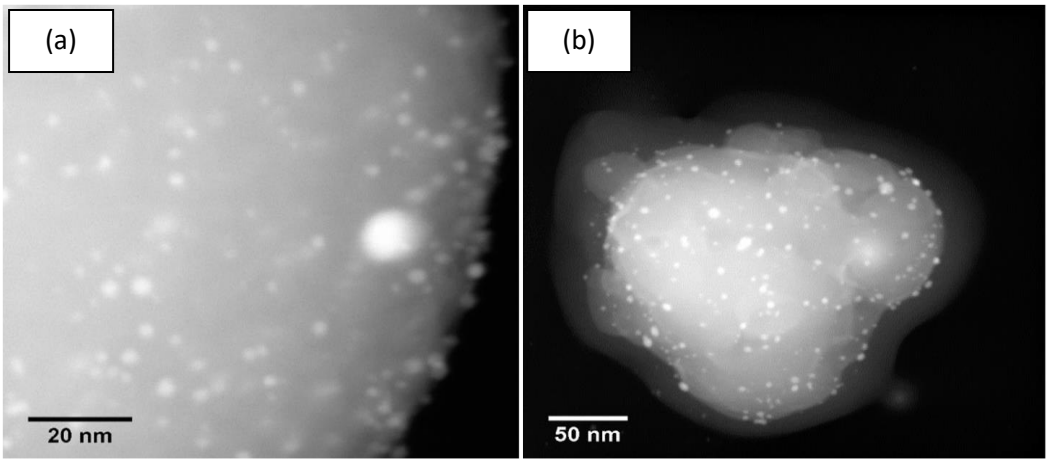

Figure 2.25: *HAADF image of as-prepared (a) 10 AB-type Ag ALD NPs on alumina-coated silica gel at 200 °C, b) Ag NPs by 20 cycles ABC-type ALD on alumina-coated silica gel at 110 °C*[23]

2.11. Summary of the chapter

Ultra-thin metallic silver nano-textured coatings are of significant interest for a range of applications including anti-microbial surfaces, plasmonic enhanced thin film PV, catalysts and gas sensors. In these applications, control over the size, shape and distribution of the nanoscale features on the surface is often critical to the functional performance of the layer. While a range of techniques, including wet chemistry, electrochemistry, chemical vapour deposition and physical vapour deposition, can readily be used to deposit nano-textured films, each has limitations when it comes to precise and repeatable nanoscale control of the coating. These techniques also have limitations when it comes to the production of highly conformal coating on complex three dimensional surfaces as might be found in biomedical implants or in non-planar semiconductor devices. One deposition technique that excels at offering highly repeatable nanoscale control over an ultra-thin film together with exceptional conformality on complex three dimensional structures and compatibility with large scale manufacturing is atomic layer deposition (ALD). The self-limiting nature of the process results in truly atomic scale control of the deposition and can produce ultra-thin films with excellent uniformity and conformity, even on large area or high aspect ratio three dimensional structures.

A diverse range of materials have been deposited by ALD including oxides, nitrides, chalcogenides as well as some metals. To date, there has only been a very limited number of published studies concerning ALD of silver; two studies relating to thermal ALD with unanswered questions relating to the ALD temperature window and to the self-limiting nature of the process, and a further four relating to plasma/radical enhanced-ALD. The limited number perhaps reflecting the challenge involved in developing volatile silver precursors, which are stable enough to survive vaporisation.

Although plasma/radical enhanced-ALD offers several potential benefits over thermal ALD, it also has limitations, particularly when it comes to coatings onto complex non-planar surfaces. Therefore, developing a thermal ALD process for self-limiting deposition of silver is necessary to enable the production of highly conformal coatings onto complex three dimensional surfaces.

Silver shows antimicrobial activity against a wide range of microorganisms and is the most favourable metal for antimicrobial coatings because of its excellent properties including inhibition of bacterial adhesion, broad anti-bacterial spectrum, and its tendency for being less prone to the increase of bacteria resistance compared to antibiotic.

Due to aging populations and obesity, the need for artificial joint replacement and orthopaedic surgeries has increased and affect millions of people around the world. Increasing the need of these artificial implants has raised the number of implant-related infections and resulted in implant failure, revision surgeries, extra pain for the patients, more hospitalisation time and also hugely increased the financial burden on health services. Therefore, there is an urgent need for preventing the spread of bacteria adhesion and bio-film formation on the implant surface and reduce colonisation of implanted titanium based biomaterials by surface modification. To modify the surface of implants to decrease the bacterial colonisation, one method is using metallic elements to coat the implant surface and silver is the most favourable metal for antimicrobial coatings due to its excellent properties identified above.

Various types of methods have been used for antimicrobial coating surfaces so far, including wet chemical coating (sol-gel method), chemical bonding of antimicrobial agents, dipping, layer-by-layer (LBL) method, spray, PVD coatings and also CVD coatings. None of these

techniques is able to provide a highly conformal, ultra-thin uniform and sub-nanometre scale control coating over the complex implant structures.

Hence, using ALD of silver for antimicrobial coating of orthopaedic implants is an advantageous method by providing two key benefits:

- Sub-nanometre scale control over the silver coating thickness as high levels of silver in the body can result in adverse side effects and therefore, ALD potentially offers a route to preventing this by minimising the amount of silver on the implant.
- Highly conformal film coverage, even on very high aspect ratio micro-structures such as the foam and solid orthopaedic implants.

Chapter 3

Experimental Methods

3.1. Introduction

This chapter describes experimental methods used in this thesis for sample preparation and characterisation. Initially, the growth technique used for films deposition is described together with details of precursor and co-reactants and other parameters involved in the coating process. Following the film growth, mass deposition was consistently measured by weight gain measurements and monitored by an in-situ Quartz Crystal Microbalance (QCM). Four point probe (FPP) has been applied to measure electrical resistivity. X-ray photoelectron spectroscopy (XPS) has been used to assess the chemical composition of the films. Scanning Electron Microscope (SEM) and Atomic Force Microscope (AFM) have been used to determine film microstructure and morphology. X-Ray Diffraction (XRD) has been employed to explore film microstructure. Selective Laser Melting (SLM) has been utilized to manufacture 3 dimensional bone-implant structures. All of the structures were fabricated by Dr. Joseph Robinson and Samuel Evans at the University of Liverpool. These experimental methods have been optimised to achieve high quality data while minimising experimental errors. For biological assessment, both *in vivo* and *in vitro* analyses have been applied. All biological studies in this thesis were conducted by Professor Christopher Mitchell, Aine Devlin and Naomi Todd at the University of Ulster and all experimental procedures for this section can be found in Appendix A.

3.2. Sample preparation

Two different form of samples were used in this research as flat samples and SLM parts which will be explained with their preparation details in the following sections.

3.2.1. Flat samples

Three types of substrate were used in each run including 75 × 25 mm standard Soda lime glass microscope slides, 30 × 30 mm n-type Si (100) wafer (Compart Technology Ltd. Virgin test grade) and 30 × 30 mm titanium sheet (Goodfellow Cambridge Ltd, 99.6% purity) to allow using different characterisation methods. The glass slides were cleaned by rinsing in isopropanol and drying using nitrogen. The glass slides were used for electrical resistivity measurements due to having non-conductive surface.

The silicon wafers were used as-supplied with no additional preparation with ~ 20 Å of native oxide on the surface. In order to obtain thickness measurements and microstructure analysis silicon wafers were employed due to its surface smoothness and well oriented grains crystalline structures. Titanium samples were cleaned by immersion in 5 % micro-90 detergent (Decon, Sussex, UK) in distilled water at 60 °C using an ultra-sonic bath (VWR, Radnor, USA) for 90 minutes, followed by rinsing in distilled water, sonication at 70 °C in distilled water for a further 90 minutes before a final rinse in distilled water. The samples were then dried at 80 °C in an oven before being used for the deposition process[324]. Titanium samples were used to investigate any change in the nucleation (size, density, etc) and mass gain of grown silver. As the application of this research is silver coated titanium implants, a detail study on titanium substrate for each run was required. After each run, all samples were wrapped with optical lens

tissues and kept in sealed plastic bags to protect them from dust, contamination or surface scratches.

3.2.2. Selective Laser Melting (SLM)

3.2.2.2. Manufacturing equipment and process condition

All of the structures including porous and solid geometries used in this research were fabricated by Dr. Joseph Robinson and Samuel Evans at the University of Liverpool using a SLM Realizer 2 - 250 (MCP, Germany). In the Appendix B, a schematic of the SLM machine as well as brief background information can be found. This equipment can build structures with a maximum height of 240 mm on a 250 × 250 mm^2 build plate. This system uses a ytterbium fibre laser with maximum power of 200 W and continuous wave with λ=1.06 μm (IPG, Germany)[87]. The build platform is joined to an elevator which is lowered after each build layer has been completed. A fresh layer of powders is then applied and levelled using a wiper blade. The laser is scanned over the powder bed using scanning mirror controlled by a computer.

To produce a fully dense parts the build speed is roughly 5 cm^3 per hour[87]. The software used in the present study was Realizer (Realizer, GmbH, Borchen, Germany) which is in charge of manipulation the CAD files. Before starting the manufacturing process by SLM, the chamber is flushed with Argon gas and the amount of residual oxygen is determined via a Rapidox 2100 gas analyser (Cambridge Sensotec Ltd., St Ives, UK). The flushing is continued until the oxygen level is under 250 ppm before the manufacture process is started. To achieve finest results in terms of the quality of the components and the speed of the process, the particle diameters of the powders is chosen between 10-75 μm.

3.2.3. SLM bone-implant samples

In this research, the materials used to manufacture the implants (porous and solid) are commercially pure grade one titanium powder (CpTi) (Sumitomo, Japan) of mean particle diameter 28.5 microns with 90% of the particles being under 45 microns produced by gas atomization. The powder layer thickness was 50 microns and laser beam diameter 80 microns, with the laser power and exposure set to produce melt spots of nominal diameter 180 microns in order to produce a wire frame structure with a nominal porosity of 65%[87].

The final implants dimensions were 2.0 mm in diameter and 1.5 mm in height for both solid and porous structures. Scaffolds were cleaned by immersion in 5% micro-90 detergent (Decon, Sussex, UK) in distilled water at 60 °C using a ultra-sonic bath (VWR, Radnor, USA) for 90 minutes for 3 times. Then, they were sonicated at 70 °C in distilled water for a further 90 minutes before two final rinses in distilled water. The structures were then dried at 80 °C in an oven overnight being ready for sintering process. The reason for cleaning the samples before sintering was to remove residual powder and avoid contaminations entering the oven.

The sintering process was carried out in a VFS HEQ 2624 vacuum furnace (Philadelphia, USA) at 1400 °C under a 5 Torr vacuum for 3 hours for both porous and solid structures. Then, samples were cooled down with backfilled argon flow in the vacuum furnace to room temperature for a period of almost 2 hours[93]. All the sintering process were carried out by Lewis Mullen at the department of advanced technology, Stryker orthopedics, New Jersey. The structures were cleaned after sintering in the same way that they were cleaned before sintering and were wrapped with optical lens tissues and kept in sealed plastic bags ready for the further steps.

Figure 3.1 demonstrates the high resolution SLM images before and after sintering. The sintering procedure can help to decrease any internal porosity and remove any small defects in the strands and also can help to merge any early developed melted powder and therefore, resulted in the development of a homogeneous and consistent macrostructure. The sinter cycle leads to smoother and more rounded parts which can decrease the free energy, with any remaining powder being merged into the parts[87].

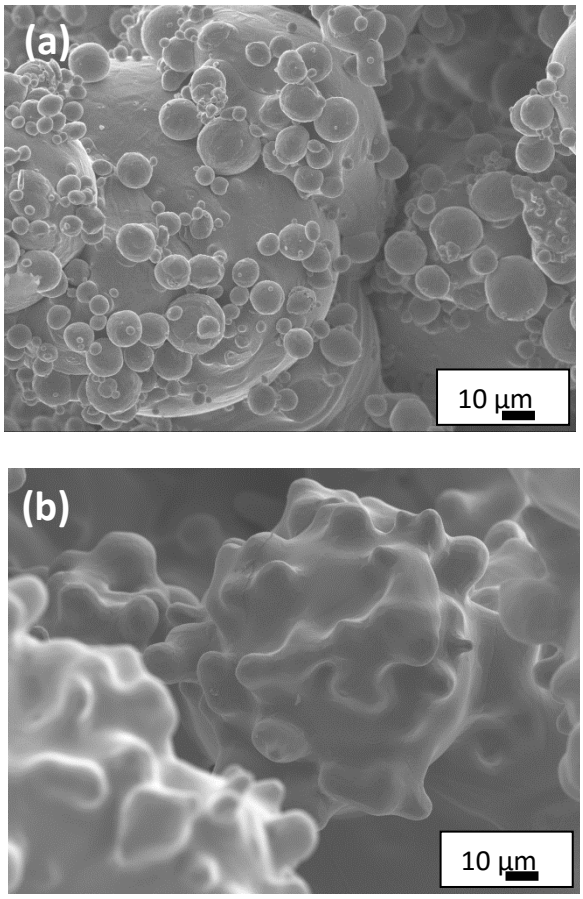

Figure 3.1: *SEM images showing the microstructure of the a) pre-sintered and b) post-sintered SLM cylindrical implants structures*

In order to mount the porous and solid samples, samples were designed with attached 5 mm tab. Figure 3.2 shows a CAD model of a solid cylindrical implant samples with the attached tab. To design 3D structures and components in this research, the software package has been utilized was Pro Engineer Wildfire 3. This package has been used to design all orthopedic

component models in this study with the ability of converting CAD files into STL format for additional changing.

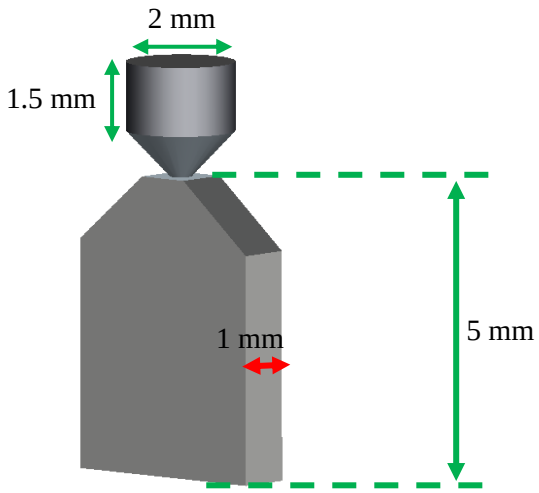

Figure 3.2: *An original CAD model file of cylindrical implant samples*

In order to design a sample holder for mounting samples in the ALD reactor a few important considerations was made. The sample holder is a key contributor to transferring the thermal energy from the graphite susceptor to the component, therefore the height of the sample holder was designed to be the same as the sample tabs which was 5 mm. The sample holder was designed with size consideration of the AIXTRON chamber and was positioned at the front part of the reactor to optimize the precursor flow throughout the samples.

The sample holder was also designed with the purpose of easy access for mounting and un-mounting samples before and after coating respectively. Due to the large amount of samples needed for this research for both in vivo and in vitro studies, the sample holder was designed to maximize the number of samples in each run while still absorbing gas flow/precursor exposure. Figure 3.3 illustrates an original CAD model file of the sample holder with dimensions of 70 × 40 × 5 mm and the maximum number of 85 cylindrical sample spaces.

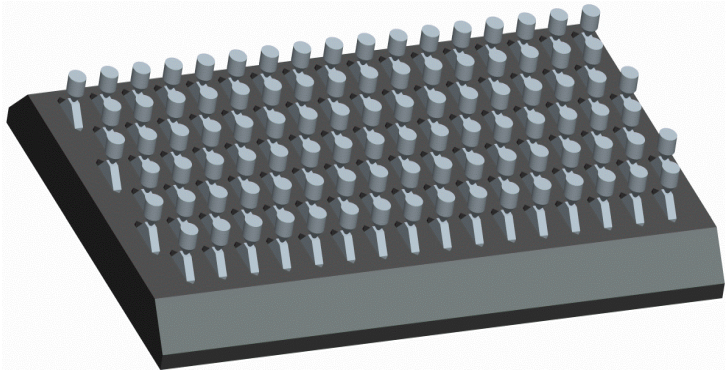

Figure 3.3: *An original CAD model file of the sample holder*

As already discussed in chapter 2, temperature has a major effect on the coatings of silver ALD and the process is very sensitive to temperature changes. Therefore, any temperature below or beyond the ALD window can lead to condensation or thermal decomposition respectively. A careful consideration of temperature variances was investigated here due to additional 5 mm height from the orthopaedic cylindrical samples to the reactor's graphite heater.

The graphite heater was adjusted until a low mass thermocouple attached to the top of one of the samples stabilized at 125 °C. The graph below (Figure 3.4) shows a study on the temperature stabilization time on the orthopaedic cylindrical sample under vacuum in the AIXTRON reactor. This study has been done to minimise any temperature effect on the coating. As it is clear from the Figure, by setting the temperature to 125 °C, the cylindrical sample temperature rises rapidly to 180 °C and then decrease slowly over time and reach to 125 °C. Therefore, to minimise any temperature effect, the 20 minutes time period for temperature stabilisation prior to the coating process was added to the AIXTRON software.

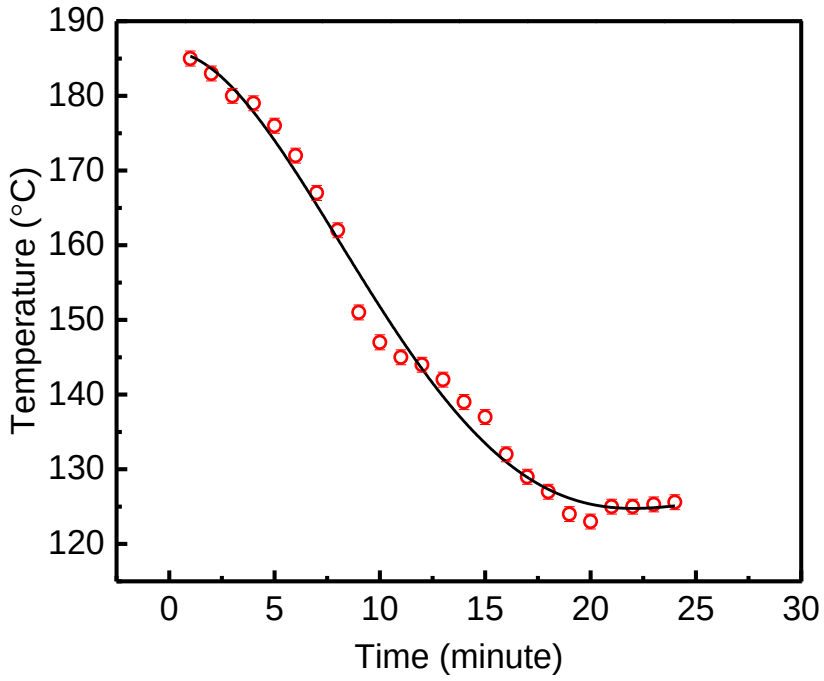

Figure 3.4: *Study on the temperature stabilization time on the orthopaedic cylindrical sample*

3.2.4. SLM split cube samples

As described in chapter 2, one of the most challenging issues associated with coating 3D structures is conformality. Self-limiting atomic layer deposition should be able to produce ultrathin and conformal films even on high aspect ratio structures[325]. To assess the conformity of the ALD coating within complex three dimensional surfaces, test structures in the form of porous titanium foam were fabricated by SLM using the randomized foams and same method as described in the section 3.2.3. 'Split cube' samples with a porosity of ~ 65% were designed to enable SEM of internal surfaces within the three dimensional structures without the need for sectioning, while might damage the coating on titanium. Each sample was made up of two 2.5 × 5 × 5 mm foam blokes tightly wired together to form 5 × 5 × 5 mm cubes.

The samples were coated using ALD with different doses of precursor. Following ALD, the two halves of the cubes were separated and SEM was used to look at the coating on the internal surfaces. Figure 3.5 shows a schematic of split cube structure showing how the sample is wired together and orientated in the ALD reactor. The triangle on top of the each split half was used as an orientation marker to identify the sample orientation with request to the flow direction.

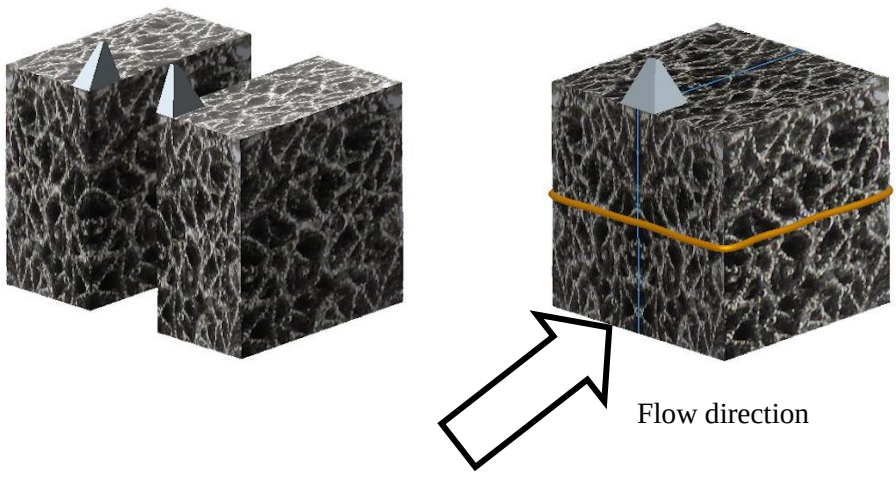

Figure 3.5: *A schematic of split cube structure showing how the sample is wired together and orientated in the ALD reactor*

3.3. Precursor preparation

A 0.1 M solution of (1, 1, 1, 5, 5, 5-hexafluoroacetylacetonate cyclooctadiene Ag (hfac) (COD)) [(hfac) Ag (1,5-COD)] ($C_{13}H_{13}AgF_6O_2$) (supplied by SAFC Hitech Ltd) in anhydrous toluene (Sigma Aldrich) was used as the silver precursor. Figure 3.6 shows chemical structure of [(hfac) Ag (1,5-COD)] molecule. Once in solution, the silver precursor is moisture and light sensitive and hence solutions were carefully prepared in a nitrogen glove box and were then stored under inert gas in the dark. The silver precursor was introduced into the reactor at a rate of 17.5 µl/s by direct liquid injection along with 200 sccm of argon (99.999 %, BOC) carrier gas. To measure the precursor rate, a flow meter sensor was installed at the inlet of the reaction chamber to monitor the precursor rate during all experiments. It helped to find out the consistency of the injector behaviour throughout the whole deposition time. Precursor delivery using direct liquid injection method was described in chapter 2.

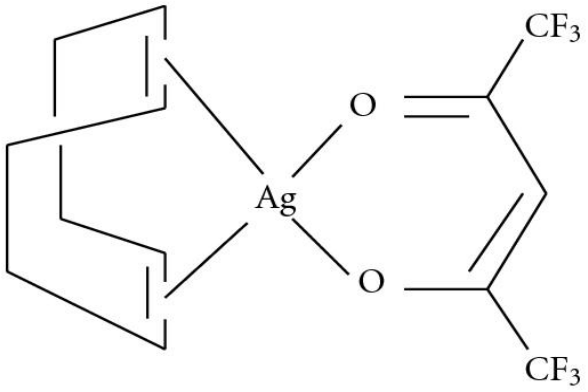

Figure 3.6: *Chemical structure of the [Ag (hfac) (COD)] molecule*[326].

3.4. Co-reactants

3.4.1. Propan-1-ol/Butan-1-ol

Propan-1-ol (HPLC grade from Fisher Scientific) and butan-1-ol (99 %, HPLC grade from Sigma Aldrich) were used as alcohol-based co-reactants. These co-reactants were introduced via vapour draw (as described in chapter 2) with a high speed ALD valve (Swagelok) to ensure accurate dosing. They were held in glass bottles at room temperature.

3.4.2. Tertiary Butyl Hydrazine (TBH)

Tertiary butyl hydrazine (98 %, HPLC grade from Sigma Aldrich) ($C_4H_{12}N_2$) was used as a highly volatile co-reactant due to its strong protonating agent compared to alcohols. The TBH was delivered into the reactor via a high speed Swagelok ALD valve (operation time of 5 ms) by a vapour draw system and held in a bubbler at room temperature[306]. At the end of each run using TBH, the chamber was cycled for 20 minutes pump/purge sequence (2 minutes pump/ 2 minutes purge) with a continuous 200 sccm Ar flow clean the reactor chamber from any residual molecules in the gas phase.

3.5. Atomic Layer Deposition

3.5.1. Aixtron AIX 200FE

All deposition in this study was carried out using direct liquid injection atomic layer deposition (LIALD) using a modified Aixtron AIX 200FE reactor. A schematic of the Aixtron AIX 200FE can be found in Appendix C. In this reactor substrates sit on a graphite heating stage which is heated using five infrared lamps and can go up to 650 °C. To control and measure the temperature, a thermocouple is embedded inside the graphite susceptor. The reactor is connected to a Jipelec TriJet® liquid precursor delivery system, which provides up to three precursor sources. The precursor is dissolved in a solvent such as anhydrous toluene, is stored at room temperature in pressurised glass containers under argon to ensure the lifetime of the precursor is maximized (normally 1200 mbar).

The precursor solution is sprayed into the heated vaporiser using an injection nozzle[327] and with a steam of argon carrier gas to help with vaporization. The liquid injection delivery method is explained in details in chapter 2. Five stage dry pumps are used to evacuate the reactor. A vacuum gauge is applied to measure the pressure of the chamber and a throttle valve is then used to control the chamber pressure. Mass flow controllers (MFCs) were used for controlling all gas flows in the reactor. To set up and control all features in the reactor the CACE software was used which lets the user change different parameters and recipes for various growth process[309].

A typical ALD cycle for silver coating in this research is shown in Figure 3.7 which can be repeated N times to form a film of N number of cycles. In this research a fixed number of 500 ALD cycles is used for the investigation of deposition rates. However, the effect of cycle number on the film growth was also investigated.

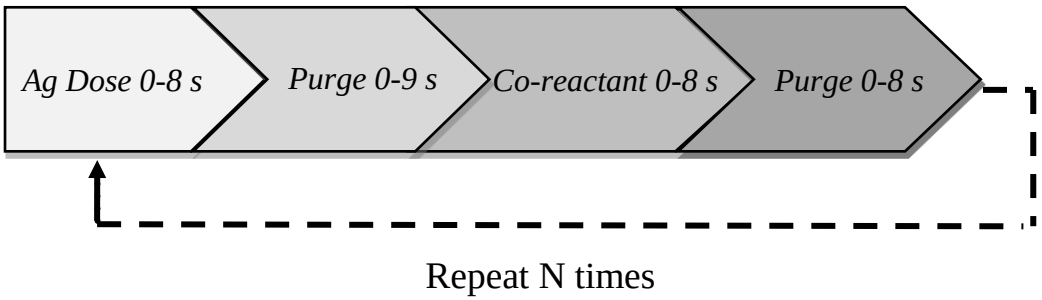

Figure 3.7: *Schematic of the ALD process to deposit Silver NPs*

Due to the effect of temperature on the ALD process, a low mass thermocouple was inserted into the chamber to enable in-situ monitoring of surface temperature under growth conditions. The measurements demonstrated that there is little fluctuation in temperature across the entire susceptor area, with the largest fluctuations of up to ± 0.3 ºC compared to the set point (Figure 3.8).

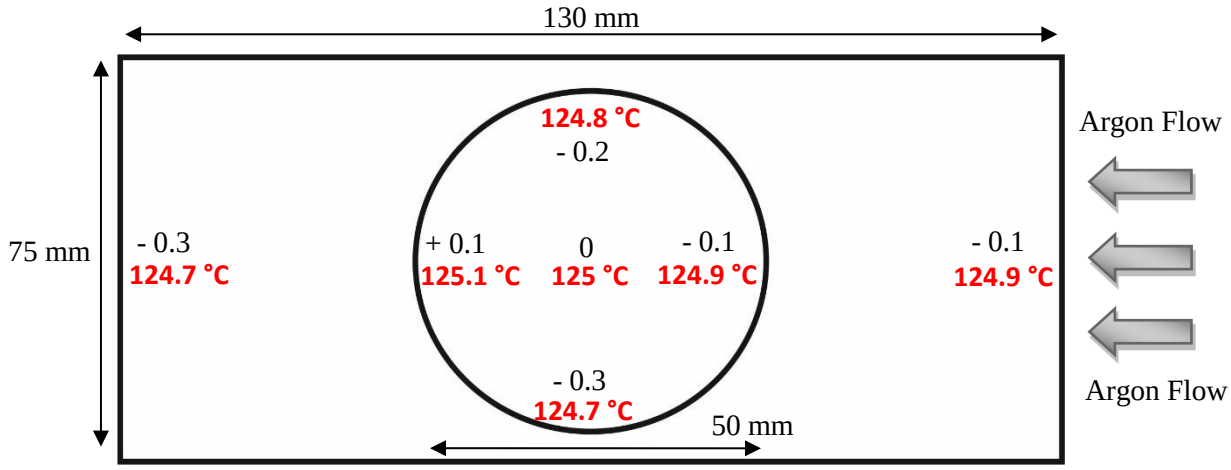

Figure 3.8: *A Schematic Illustration of Aixtron Chamber for temperature measurements across the substrate holder when heated at 125 °C.*

Growth parameters for silver deposition ALD are summarised in table 3.1 using Aixtron thermal reactor. Reactor pressure and vaporisation temperature have been chosen after several experiments to establish the most favourable conditions for the growth of (hfac) Ag (1,5-COD) in this reactor before by Paul Marshal at the University of Liverpool. Other growth parameters have all been investigated throughout this research.

Table 3.1: *Growth parameters for silver deposition using AIXTRON thermal reactor*

Precursor	(hfac) Ag (1,5-COD) 0.1M toluene solution
Co-reactant	None/propan-1-ol/butan-1-ol/tertiary butyl hydrazine
Substrate temperature (°C)	80-200
Flow rate through the precursor (sccm)	30
Vaporisation temperature (°C)	130
Flow rate of Argon through lines (sccm)	200
Reactor pressure (mbar)	5
ALD recipe	0-8s/0-8s/0-8s/0-8s

3.6. Material characterisation and analysis techniques

3.6.1. Quartz Crystal Microbalance (QCM)

A Maxtex TM - 400 deposition monitor was used in this research fitted with a custom made sensor head holder installed in the centre of the ALD reactor chamber as an in-situ mass deposition measurement. The reason for using a custom made sensor head holder was providing a good thermal contact between the quartz crystal and its holder to avoid any precursor condensation due to the high temperature sensitivity of the silver precursor. Also, a thermocouple was placed directly to the surface of the QCM to monitor the temperature accurately. Figure 3.9 shows a picture of the custom made sensor head holder used in this study. Background information about this method can be found in Appendix D.

Figure 3.9: *Picture of the custom made sensor head holder used in this study*

A Y-11° cut $GaPO_4$ high temperature crystal (0 - 460 °C) was used in this study due to its excellent thermal stability[328] with a crystal density of 3.57 g/cm³ and sheer modulus of 2.147 g/cm s² operating at resonant frequency of 6 MHz[181]. Before using the QCM to monitor the silver ALD process, initial test runs using TTIP + H_2O were carried out. The TTIP + H_2O process is well established as an ALD process and therefore provides an opportunity to test and

calibrate the QCM. A 0.1 M solution of TTIP in toluene was prepared and used for the initial testing, which was carried out at 200 °C.

Figure 3.10 shows the mass gain recorded for 19 ALD cycles with 6 s of TTIP dose and 15 s of purging Ar (200 sccm) to explore as a part of the calibration process. The long purge time was used to ensure stabilization of the QCM frequency after dosing the precursor and co-reactant. To investigate the agreement in mass gain between QCM and analytical microbalance a silicon substrate was used alongside the in-situ QCM. The mass gain achieved by analytical microbalance on silicon was 0.00016 ± 0.0001 g, whereas QCM showed 0.00028 g. This result confirms high measurements precision between two techniques.

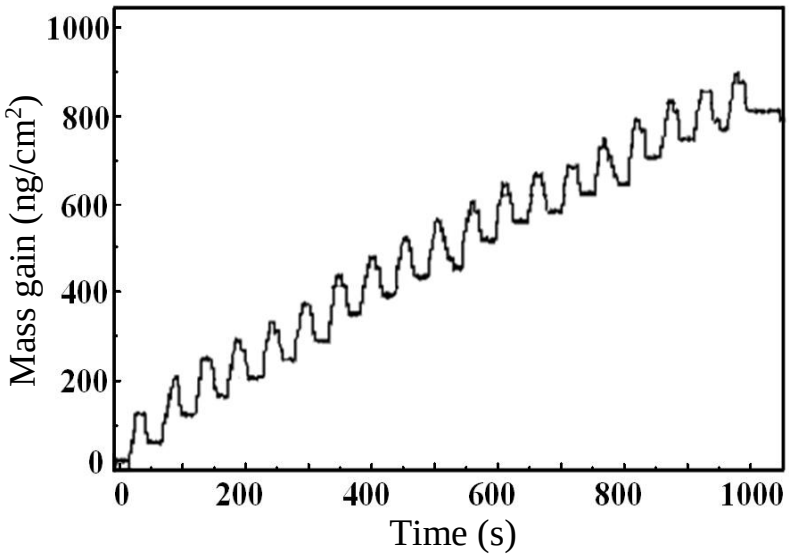

Figure 3.10: *Mass gain monitored by the QCM at 200 °C for 19 ALD cycles using (TTIP) for an Ar purge (200 sccm) of 15 s for both TTIP and H_2O*

3.6.2. Weight gain

3.6.2.1. Measurement information

To assess mass deposition rate, a Mettler Toledo XS205 analytical microbalance was used to measure mass before and after each deposition on silicon and titanium surfaces. The microbalance has high accuracy up to five decimal points[329] and the film thickness (T) can be estimated from the mass gain using equation 3.1.

$$T = \Delta M / A \times \rho \quad \text{(Eq. 3.1)}$$

Where T is the thickness (cm), ΔM is the weight gain (g), A is the surface area (cm^2), and ρ is the film density (g/cm^3). It is difficult to directly measure the film density, hence a bulk density for silver of 10.49 g/cm^3 was assumed. It is however important to note that the actual density of the deposited material may be significantly different from the bulk value, hence at best this method is just an approximation[330].

In this study, due to small deposited weight, each sample was weighted 3 times before and after the deposition to decrease errors by checking the reading stability and the balance was zeroed each time. Details of repeats of measurements have been shown in Appendix E. By avoiding the lowest and the highest measurements, the average of the other values was used to evaluate the mass gain. An uncoated 2" silicon wafer was also measured before and after the deposition as a reference sample. This sample has been measured for more than three years to check the reading stability (measured ~1200 times). Equation 3.2 was used to calculate the weight gain,

$$\Delta M = (M_{r1} + M_{s1}) - (M_{r0} + M_{s0}) \quad \text{(Eq. 3.2)}$$

M_{r0} and M_{r1} are the reference sample weight before and after deposition respectively, while M_{s0} and M_{s1} are the sample weight before and after deposition respectively[181].

This method can help to decrease the measurement shift of the microbalance at different times. Figure 3.11 illustrated 600 measurements during the study as a histogram. A measured value between 1.3666 g to 1.3667 g was obtained with the error limit of ±0.00010 g confirming the 95% reliability of the data.

Other potential errors for this technique can arise by small changes in the area of the substrates which may vary dramatically between different substrates. All the possible errors are measured and justified in the results section. Many of the films in this study go down as nanoparticles rather than as planar films, hence film thickness is of limited value. Instead of thickness, mass deposition rate is more meaningful.

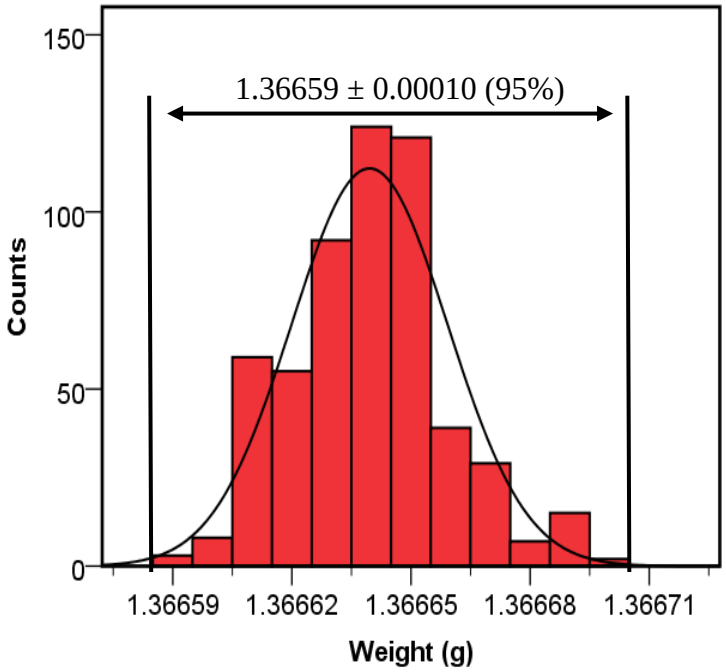

Figure 3.11: *A histogram for the measured weigh of a reference sample.*

Weight gain measurement was also used to evaluate the uniformity of the deposited film by coating 13 silicon samples (1 cm × 4 cm) across the reactor length.

3.6.3. X-ray Diffraction (XRD)

All XRD measurements throughout this work were carried out using a Rigaku Miniflex powder diffractometer with water-cooled Cu Kα x-ray source (1.54 Å wavelengths, 40 kV, 50 mA). Fundamentals about this method and the schematic of the equipment used in this research can be found in Appendix F.

By doing some preliminary studies on the samples, a range of scattering angles between 30° to 50° was chosen as the main characteristic features of silver are in this range and therefore useful information can be achieved on the phases and crystal structures. There are two more planes outside this range between 60° and 80° as (220) and (311), however, they have been avoided due to the slow scan speed for 0.01 degree per minute to improve the signal-to-noise ratio of the spectra. After applying 'Peak Search' software to remove background noise, the peak fitting with the Gaussian function was used to interpret and analysed the data to produce valuable information[331].

Figure 3.12 shows the X-ray diffraction pattern of synthesized crystalline silver nanoparticles from JCPDS database (File No. 04-0783). These standard patterns are compared with the experimental patterns to discover plane for each peak and also the phase of the specimen. The diffraction pattern of the standard patterns represents planes for (111), (200), (220) and (311) reflections of the face centred cubic (fcc) structure of metallic silver.

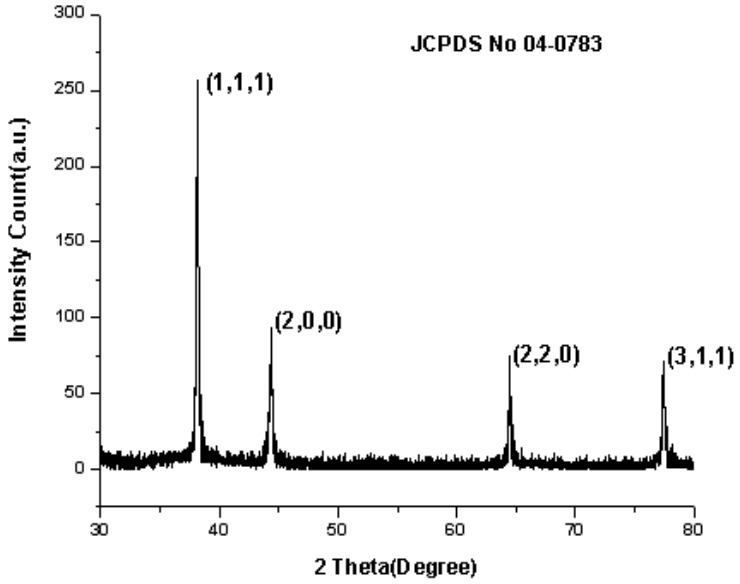

Figure 3.12: *X-ray Diffraction pattern of crystalline silver nanoparticle*[332]

The peak-fitting results showed the peak position errors between 0.01° and 0.04° together with the errors in the sample displacement for 0.01° peak shift. To conduct these errors, the same sample (15 nm thickness on silicon substrate) was mounted and scanned, then un-mounted and mounted again and this process repeated for almost 30 times. The error margins set for the three peaks are shown in Table 3.2.

Table 3.2: *Error margins set for the three silver peaks*

Plane	Peak shift (°)
(111)	± 0.02
(200)	± 0.01
(220)	± 0.04

3.6.4. Scanning Electron Microscope (SEM)

3.6.4.1. Measurement information

In this study, SEM was carried out using a JEOL JSM-7001F field emission FEG-SEM gun operated at beam energies of 15-30 KV to explore the microstructure and morphology of the film. A brief description on how SEM works can be found in Appendix G. Samples area was usually 5×5 mm^2 and was mounted on the appropriate sample stage by using double sided carbon tape with a working distance of ~10 mm.

There are a number of functions that can affect the image quality while imaging samples. Although sometimes the instrument can cause these disturbances, they mostly happen due to the inappropriate sample preparation, instrument vibration, lack of the operator skills, etc. These problems can lead to image disturbances including low quality image, noises, image deformation, lack of sharpness, etc[420]. The majority of the images in this research were produced by secondary electrons signals. However, there are a few images which have been also produced by backscattered electrons to compare and contrast the nanoparticle size differences via these two techniques.

To evaluate the individual mean particle diameters and particle distribution on the selected area, software Image J[333] and the macro Particle Size Analyser (PSA_r12)[334] were used. Each sample was analysed by randomly sampling at least four areas to ensure that the resulting data was representative of the whole. Manual measurements of particle sizes was carried out to verify the Image J analysis and also to measure irregular shaped nanoparticles.

For the hemispherical particle shape, variation of ± 3 nm in particle diameter was stablished by automatic calculations of the software. This particle size variation raised by increasing the number of cycles to ± 7 nm in particles diameter (based on the threshold level). Manual measurements of particle size was also carried out to verify the Image J analysis.

3.6.5. Atomic Force Microscopy (AFM)

3.6.5.1. Measurement information

The Bruker Multimode 8 was used to take all topographic data and measure the surface roughness of all the deposited films in this study. Schematic of the AFM and the background information are available in Appendix H. Bruker established the Scan-Asyst mode in order to develop the tapping mode technology to provide enhanced quality images for the users by removing the cantilever tuning and modifying the scanning parameters automatically[238]. Therefore, the Scan-Asyst mode using silicon nitride tips with the radius of 2-12 nm was employed for scanning all samples in this study to control scanning area, scanning speed and other scanning parameters automatically. Scans were recorded over areas from 500 nm to 10 μm^2 by employing 512 lines and with a scan frequency of 0.5 Hz. The height distribution was narrower for topographic scans over the small areas as it was anticipated.

Five different images were used from different locations on each sample to obtain the actual errors in RMS. Figure 3.13 represents a 2D topographic image of an un-coated silicon (100) substrate obtained by AFM. The surface roughness was measured to be 0.21 nm due to the vibrations during the scan. The equipment was calibrated with a reference sample (Veeco) by Tim Joyce at the University of Liverpool.

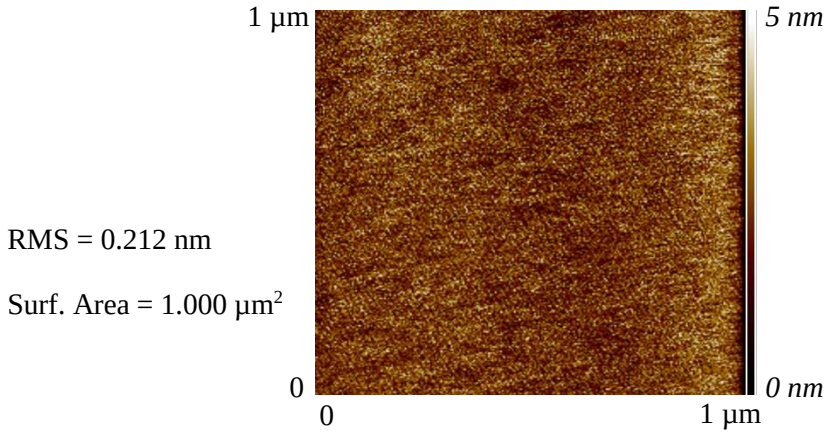

Figure 3.13: *A 2D AFM image for an un-coated silicon (100) substrate*

3.6.6. X-ray Photoelectron Spectroscopy (XPS)

The XPS measurements in this work were carried out using a FISONS VG Escalab MKII with an Al Kα x-ray source (1486.7 eV). In Appendix I, a schematic of the XPS system as well as background information can be found. Wide survey scans were carried out for each sample (BE range from 0-1200 eV) with pass energy of 50 eV alongside with narrow scans on the main elements (Ag, F, O and C) under pass energy of 20 eV and the step size of 0.1 eV. In order to compensate surface charging, all peak binding energies were calibrated to C1s peak at 285.0 eV. In this research samples were used after ALD deposition with no additional preparation with area of 1×1 cm^2 (or slightly smaller) and mostly silicon substrates which were mounted by double sided conductive tape in the sample position. Sample should always handle with gloves to avoid the oil from hands as it can contaminate the sample and also the vacuum chamber[335].

All scans are repeated twice to check for any possible damage caused by x-ray and the scan times were kept the same for collecting in all spectra. The XPS equipment is supplied with the software which can be used for peak-fitting to provide useful information such as the full width at half maximum (FWHM) value of any peak, the binding energy (BE), the ratio of two peak areas, the shape of a peak, etc[336].

3.6.7. Post growth heat treatments

3.6.7.1. Argon annealing

A Carbolite® horizontal compact tube furnace with the capability of annealing up to 1200 ºC was used to anneal silver thin films. A gas flow regulator (3L/min) was connected to an argon bottle (zero grade from BOC) which was used at the end of the furnace for providing constant argon flow while the bottle was set at 1 bar. The ramp rate was set at 5º C/min to prevent thermal shock of the ceramic tube. Before loading the sample into the furnace, the system was held for 4 hours at the set temperature to stabilise the temperature. A ceramic boat was always used to load the sample inside the furnace[309]. In order to avoid any contamination inside the tube even when it was not under operation, the tube has been kept at 300 ºC all the time. Prior to each annealing study, the argon flow was used for 10 minutes to prevent any contamination and trapped air inside the furnace. After annealing, samples were cooled to 50 °C before exposed to air. Stainless steel and anti-flame material seals were used to prevent air inside the tube furnace.

3.6.8. Adhesive testing

3.6.8.1. The scotch tape test

The adhesion of the silver film to the silicon substrate was evaluated by the Scotch tape test (Scotch® 600 transparent tape). The type of the tape and the method of stripping were kept the same for all tests. However, unfortunately achieving a 100% consistency and repeatability in this test is not possible. Although more than 200 methods are available for adhesive testing, none of these methods can provide consistency in measuring the strength of the film to the substrate[337].

3.6.9. Four point probe (FPP)

A Signatone probe head (SP4-50085TFS) and a Keithley 2400 source meter were used to perform four point probe measurements. The probe radius was 0.13 mm with 1.3 mm tip spacing and was made from tungsten carbide[238]. The specimen was placed onto the probe stage for the measurement and probes were lowered down until the stabilization on the sample surface. Four point probe values (current, range) are set and controlled via using computer software connected to the kit. The sheet resistance (Ω/square) was measured from the slope of the I-V plots and then the resistivity value was obtained (Ω.cm). In this thesis, resistivity tests were measured on the coated glass slides. The purpose of measuring resistivity was to investigate how surface morphology can effect on the resistivity by increasing the number of cycles and also using different co-reactants. Background information are provided in Appendix J.

Chapter 4

ALD growth of silver thin films using alcohol-based co-reactants

4.1. Introduction

The current chapter seeks to develop a thermal ALD process for the deposition of silver. Particular focus is given to investigating a self-limiting thermal ALD process for the deposition of metallic silver nanoparticle films. The motivation for this is to exploit the self-limiting property to coat complex three dimensional structures such as bio-medical implants. Besides, the effects of two different alcohol-based co-reactants on self-limiting behaviour of silver ALD have been investigated and a systematic comparison has been made on their growth differences. The film growth was investigated with (hfac) Ag (1,5-COD) precursor in the following schemes:

- Deposition with no co-reactant
- ALD with propan-1-ol co-reactant
- ALD with butan-1-ol co-reactant

The effects of temperature, precursor dose, different co-reactants doses and also the number of ALD cycles on the growth rates of the nano-textured films are systematically investigated using a range of in-situ and ex-situ characterisation techniques. We show that under appropriate growth conditions, it is possible to achieve self-limiting ALD with two different co-reactants used in this research and we use in-situ QCM measurements to elucidate the surface reactions involved in the process using propan-1-ol.

As microstructure plays a significant role in establishing the optical, electrical or bio-medical properties of silver thin films, hence, it is necessary to understand how it is affected by growth temperature, precursor/co-reactant doses/ different co-reactants and film thickness. AFM, SEM, and XRD have been used to investigate the microstructure of the deposited films and

revealed information on the crystallite size and surface morphology. Also, chemical composition of silver ALD was investigated using XPS at different growth conditions.

4.2. Experimental procedure

Silver films were deposited on polished virgin test grade Si(100)(Compart Technology Ltd.) by thermal ALD using a customised Aixtron customised Aixtron AIX 200FE reactor. A 0.1 M solution of ((hfac)Ag(1,5-COD)) (supplied by SAFC Hitech Ltd.) in an hydrous toluene (Sigma-Aldrich) was used as the silver precursor. Once in solution, the silver precursor is moisture and light sensitive and hence solutions were carefully prepared in a nitro-gen glove box and were then stored under inert gas in the dark. The silver precursor was introduced into the reactor at a rate of 17.5 µl/s by direct liquid injection along with 200 sccm of argon (99.999%, BOC) carrier gas. The precursor solution was volatilised using a Jipelec vaporizer set at 130 ºC (it is important to note that the precursor vapour does not actually reach 130 ºC in the vaporiser due to the flow of carrier gas). Propan-1-ol and butan-1-ol (HPLC grade from Fisher Scientific) were used as co-reactants and were introduced into the reactor as a vapour, via a Swagelok ALD valve, using a conventional vapour-draw source held at room temperature (~20 ºC). The ALD cycle was defined by sequential pulses of the two reactants separated by inert gas purges (Argon) to prevent gas phase reactions. The effects of growth temperature silver precursor dose, co-reactant dose and number of ALD cycles were all investigated. Growth was carried out at a nominal reactor pressure of 5 mbar. Samples were allowed to ‘soak’ at the set-point temperature for 20 mins prior to deposition to ensure that they reached thermal equilibrium with the graphite susceptor (a standard deviation of ±0.2 ºC was recorded in the temperature throughout the deposition period). All details are shown in Table 4.1.

Table 4.1: *ALD growth parameters for silver deposition using AIXTRON thermal reactor*

Growth condition	Value
Growth temperature	80-200 °C
Reactor pressure	5 mbar
Silver precursor	(hfac)(1,5-COD)Ag
Silver source	0.1M solution in n-Toluene
Vaporizer temperature	130 °C
Precursor delivery rate	17.5 µl/second
Argon flow rate	200 sccm
Co-reactant	Propan-1-ol/Butan-1-ol
Co-reactant delivery	Vapour draw at ~20 °C
ALD cycle	Inject 0-6 s / Purge 4 s / Co-reactant 0-6 s / Purge 0-6 s

4.3. Deposition with no co-reactant

The effect of temperature on any ALD processes is of significant importance for establishing the window in which self-limiting growth can be obtained. The temperature window of an ALD process can be affected by a number of factors, but often the most critical of these is the thermal properties of the metal precursor. To establish the thermal characteristics of the (hfac) Ag (1,5-COD), a systematic co-reactant-free growth study was carried out between 80 and 200 °C. This 'precursor-only' test used 4 s doses of the silver precursor followed by 9 s purges. The mass gain per square centimetre per cycle after 500 cycles of this process is shown in Figure 4.1.

At temperatures below ~125 °C, the mass gain is inversely proportional to temperature, which is attributed to condensation of the precursor or, more likely, the Ag(hfac) part of it (the 1,5-COD can readily dissociate from the molecule before the precursor reaches the substrate and as it is highly volatile, may be pumped away)[338]. The mass gain reaches a minimum at ~125 °C, where no detectable mass increase occurs. As the temperature increased above 125 °C, the

deposition rate increase exponentially, which is attributed to thermal decomposition of the silver precursor. To avoid thermal oxidation of the film for entire experiments, before exposing the samples to air, the reactor was always cooled to below 80 °C.

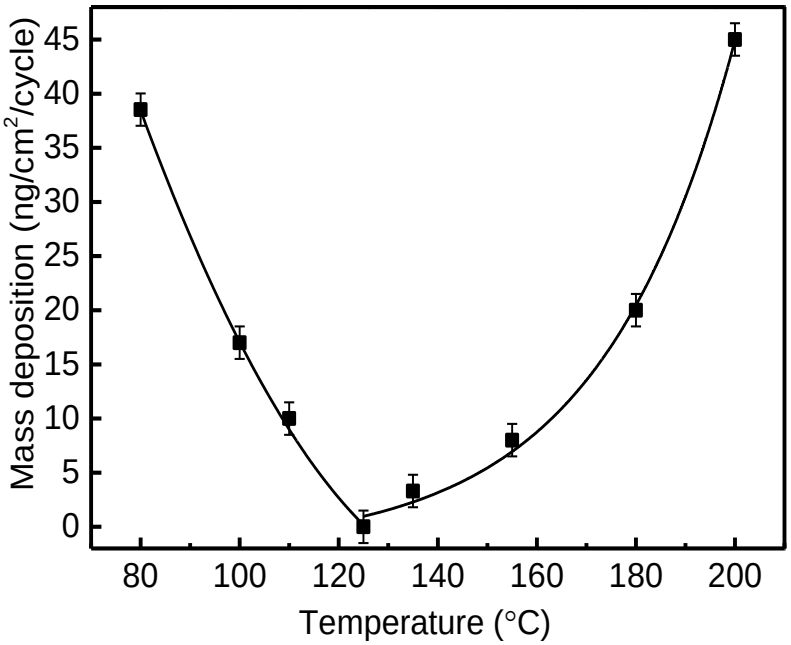

Figure 4.1: *Mass deposition as a function of substrate temperatures using 4 s doses of (hfac) Ag (1,5-COD) with no co-reactant on silicon substrate*

4.4. ALD with propan-1-ol as a co-reactant

4.4.1. Growth study

Propan-1-ol (also recognized as n-propyl alcohol, 1-propanol, and n-propanol) is an alcohol known by the molecular formula of C_3H_8O which is used as one of the co-reactant in this study. A detailed study on thermal characteristics of the (hfac) Ag (1,5-COD) between 121 and 130 °C both with 2 s doses of propan-1-ol and without co-reactant is shown in Figure 4.2. In the absence of the co-reactant, mass deposition rate is found to be zero between 123 and 128 °C.

The addition of the co-reactant causes an increase in deposition rate at all temperatures compared to the precursor only process, while retaining the same general trend.

This indicates that there is a narrow ALD temperature window between 123 and 128 °C, with a nominal deposition rate of 17 ng/cm^2 per cycle. If the coatings are initially assumed to be planar films (which is not the case, as will be discussed in the following sections), then the mass deposition data would give a nominal film thickness of ~7.9 nm for the films grown using 500 ALD cycles which corresponds to a rate of 0.16 Å/cycle (based on an assumed bulk silver density of 10.49 g/cm^3).

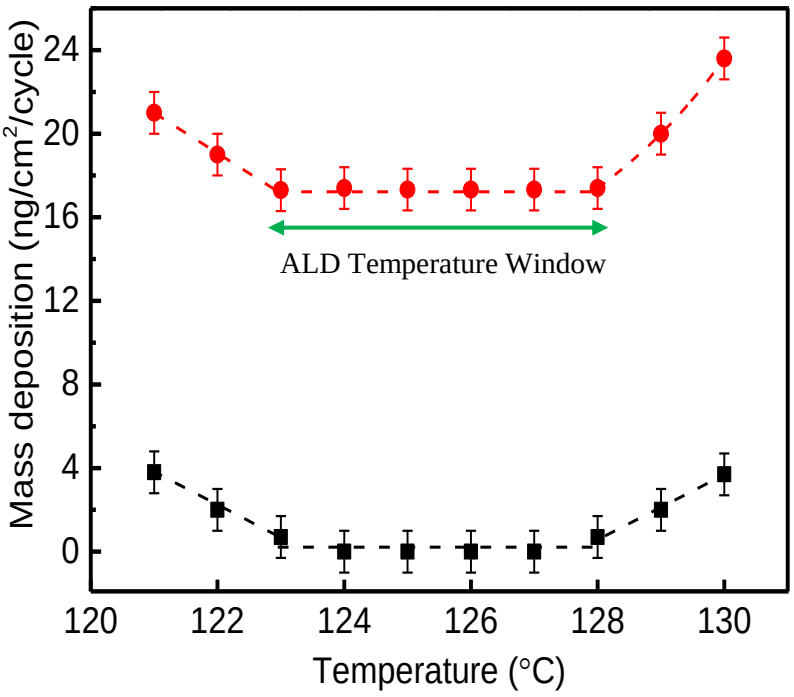

Figure 4.2: *Mass deposition as a function of substrate temperatures using 4 s doses of (hfac) Ag (1,5-COD) with detailed view of no co-reactant (squares)and with 2 s propan1-ol doses as a co-reactant (circles) per cycle.*

By definition, ALD processes should be controlled by self-limiting and saturative surface reactions, without which we would not reap many of the key benefits of this remarkable deposition approach. To establish the self-limiting characteristics of the current process, precursor and co-reactant saturation studies were carried out.

During the precursor test, the co-reactant dose was fixed at four seconds, the purge times were fixed at 4 s seconds and the cycle was repeated 500 times for each deposition run. At a growth temperature of 125 °C, the deposition initially increases with the dose, but at around two seconds, the deposition rate saturates at around 17.5 ng/cm^2 per cycle (Figure 4.3 squares). If however, the growth temperature is increased to 130 °C, which is just 2 °C above the upper limit of the ALD window, then this self-limiting behaviour is lost and the growth rate simply increases linearly with precursor dose (Figure 4.3 circles). Therefore, only slightly above the ALD temperature window, gas phase CVD-like reaction has occurred.

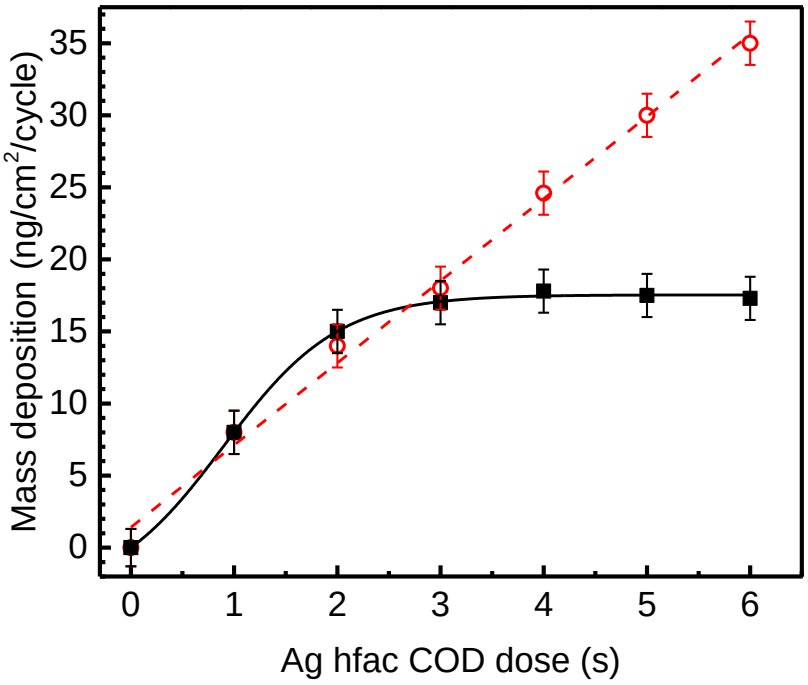

Figure 4.3: *Mass deposition as a function of a) Ag hfac COD at 125 °C (squares) and 130 °C (circles) for 500 ALD cycles.*

A similar saturation test was carried out for the co-reactant, keeping fixed the silver precursor dose fixed at four seconds. The propan-1-ol dose is also found to follow a saturative behaviour at 125 °C. The deposition rate initially increases from zero as the co-reactant dose increases, but saturation at 17.5 ng/cm^2 per cycle is achieved at approximately two seconds (Figure 4.4).

The saturative behaviour of the precursor and co-reactant at 125 °C is a clear indication that both halves of the ALD process are controlled by self-limiting surface reactions.

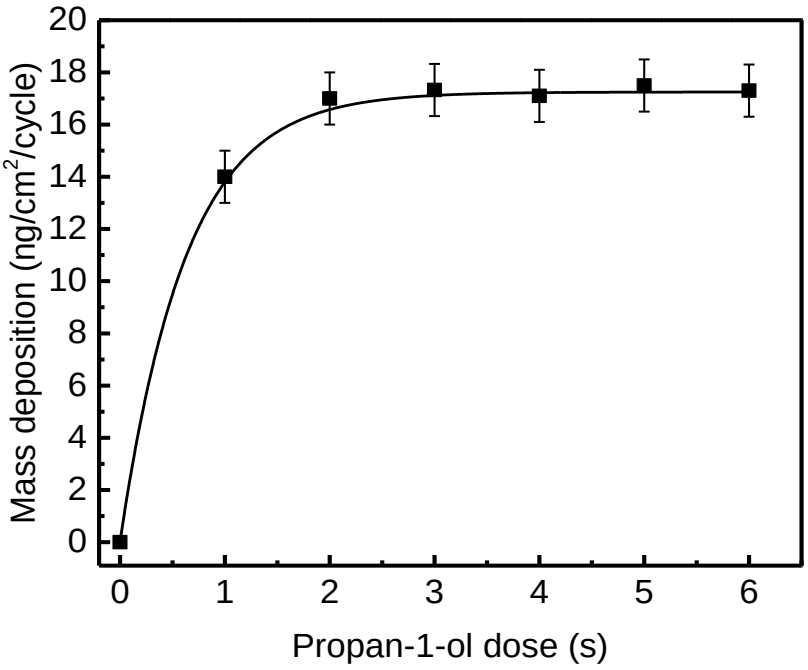

Figure 4.4: *Mass deposition as a function of propan1-ol dose at 125 °C for 500 ALD cycles.*

In addition to the ALD temperature window and precursor/co-reactant doses, mass deposition vs. number of growth cycles at 125 °C is plotted in Figure 4.5. The mass initially increases in a linear fashion between zero and 1500 cycles with a slope of 0.013 µg/cm^2/cycle. The slope then increases to 0.023 µg/cm^2/cycle above 1500 cycles. The lower initial mass deposition rate is attributed to substrate-inhibited growth, where the growth is impeded for the low number of cycles using propan-1-ol and this can occur due to the silver nanoparticles type growth on the surface rather than a continuous film. However, increasing the number of cycles may lead to change in the surface chemistry once the surface is mostly coated and silver starts growing on the already existing silver coated area, and therefore, the deposited mass increases to a constant value. The deposition of Ru or Pd films also are examples of this type of growth process[277].

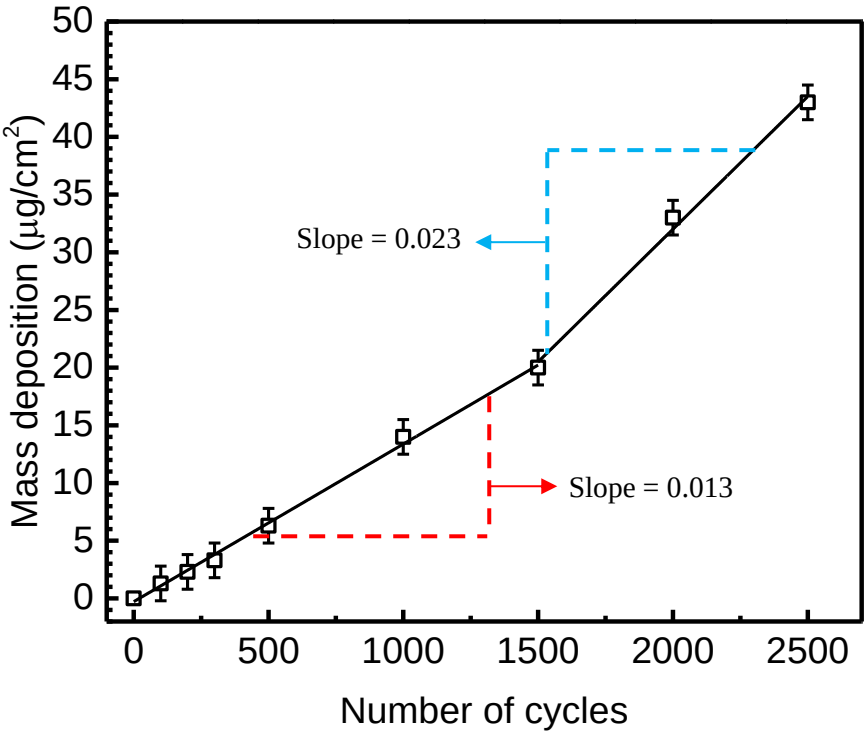

Figure 4.5: *Mass deposition per unit area as a function of ALD cycles at 125 °C on silicon with propan-1-ol dose*

4.4.2. In-situ QCM study

To elucidate the reaction mechanisms involved in the silver ALD process using propan-1-ol, *in-situ* QCM measurements were carried out under self-limiting growth conditions. Deposition was carried out at 125 °C using 6 s doses of the two reactants separated by 15 s purges. The extended purge times were used to ensure stabilization of the QCM frequency after dosing each reactant. Table 4.2 shows the main chemical groups used to deposit silver nanoparticles along with formula weight.

Table 4.2: *Chemicals used to deposit silver nanoparticles*

Chemical part	Notation	Chemical formula	Formula weight ($g.mol^{-1}$)
hexafluoroacetylacetonato	hfac	$C_5HO_2F_6$	207
silver(I)	Ag	Ag	108
1,5-cyclooctadiene	1,5-COD	C_8H_{12}	108
Propane-1-ol		C_3H_8O	60

Figure 4.6 (a) shows the QCM mass change during six cycles of the ALD process. The envelope of the QCM data indicates a linear increase in mass with the number of cycles. The total mass gain after six complete ALD cycles is ~106.2 ng/cm^2 and this give a nominal mass deposition rate of ~17.5 ng/cm^2 per cycle, which is in reasonable agreement with ex-situ mass gain measurements on Si (100).

Figure 4.6 (b) shows the average mass gain and mass loss for each ALD cycle obtained by averaging the QCM data over 6 cycles. The large mass gain, H1, at the start of the cycle coincided with the silver precursor dose and the mass loss H2 coincided with the co-reactant dose[339]. From the three mass values (H1, H2 & H3) extracted from the QCM data and the XPS film composition analysis, it is possible to propose a likely reaction scheme for the ALD process.

Within the silver precursor ((hfac) Ag (1,5-COD)), the 1,5-COD ligand helps to stabilise the precursor, however, as 1,5-COD only weakly bonds to the Ag, it can be readily dissociates when the precursor is volatilised or possibly even when the precursor is in solution[319]. The 1,5-COD is therefore expected to dissociate from the precursor before the vapour reaches the substrate and can then be readily pumped away.

This precursor pre-reaction can therefore be described by:

$$(hfac)\,Ag\,(1,5\text{-}COD)_{(g)} \rightarrow Ag\,(hfac)_{(g)} + (1,5\text{-}COD)_{(g)} \quad \textit{(Equation 4.1)}$$

Where (g) indicates gas phase species. During the first half of the ALD cycle, the Ag (hfac) intermediate (which has a formula weight of 315 $g.mol^{-1}$) is chemisorbed onto the surface. We start by considering steady state growth conditions, where the effective substrate is metallic silver with a proton termination.

After purging away the gaseous reaction by-produces and excess precursor, the surface is exposed to the alcohol co-reactant. The second 'half-reaction' of the ALD cycle is believed to proceed via heterogeneous catalytic dehydrogenation of the alcohol, which results in the formation of an aldehyde and to the reduction of the cationic silver to metallic silver[320]. This reaction is given by:

$$Ag - Ag\,(hfac)^* + CH_3CH_2CH_2OH_{(g)} \rightarrow Ag - Ag - Hx^* + Hhfac_{(g)} + CH_3CH_2CHO_{(g)}$$

(Equation 4.2)

This reaction scheme fits well with the QCM data obtained under saturature ALD growth conditions. The average values of H1 and H2 from Figure 4.6 (a) are 65 ng/cm^2 and 45 ng/cm^2 respectively, giving a ratio of the mass loss, H2, to the mass gain, H1, of ~ 66%. Hence, around two thirds of the mass gain associated with chemisorption of the silver precursor is subsequently lost due to the reaction with the co-reactant. If the reaction scheme above is correct, then the total mass gain during the first 'half-reaction' should be directly proportional to the formula weight of the Ag (hfac) adsorbate minus the formula weight of the proton. Hence the net gain should be proportional to 314 g/mol.

The QCM plot shows no sign of desorption during the purge step, hence it is reasonable to assume that the Ag (hfac) molecules remain stable following adsorption. If all of these silver molecules now react via the catalytic dehydrogenation reaction during the second 'half-reaction', then the mass loss should be directly proportional to the formula weight of the hfac leaving group minus one proton (it should be noted that QCM measurements are not accurate enough to resolve the loss or gain of very light species such as individual protons). Hence the net loss should be proportional to 206 g/mol. Based on these numbers, the ratio of the net mass loss during the second half reaction to the net mass gain is 65.6%, which is consistent with the QCM data.

The analysis discussed above assumes steady state growth conditions, where silver is being deposited on top of silver. This neglects any nucleation or initialisation reactions that may take place at the heterostructure interface between the substrate and the coating at the start of the deposition process. In many cases, it is reasonable to assume that we have a substrate that is terminated in OH groups due to exposure to air prior to the deposition. If this is the case, then the first 'half-reaction' could be described by:

$$\text{Substrate} - \text{OH}^* + (\text{hfac})\,\text{Ag}_{(g)} \rightarrow \text{Substrate} - \text{O} - \text{Ag}\,(\text{hfac})^* + \text{H}_{(g)} \qquad \textit{(Equation 4.3)}$$

Following this, it could simply be assumed that the coating process follows the steady state reactions outlined above. However, for a CVD process using the same silver precursor, Bahlawane et al[320] indicates that the bulky ligand may in fact hinder the subsequent dehydrogenation reaction with the alcohol. They go on to indicate that an initiation process involving thermal decomposition of the precursor is necessary to form metallic silver, which is able to catalyse the dehydrogenation reaction between Ag (hfac) and the alcohol.

The presence of the adsorbate Ag intermediate is able to catalyse this dehydrogenation reaction above 123 °C which accounts for the onset of the ALD growth and accounts for the rapid onset of CVD-like growth and the narrow ALD window.

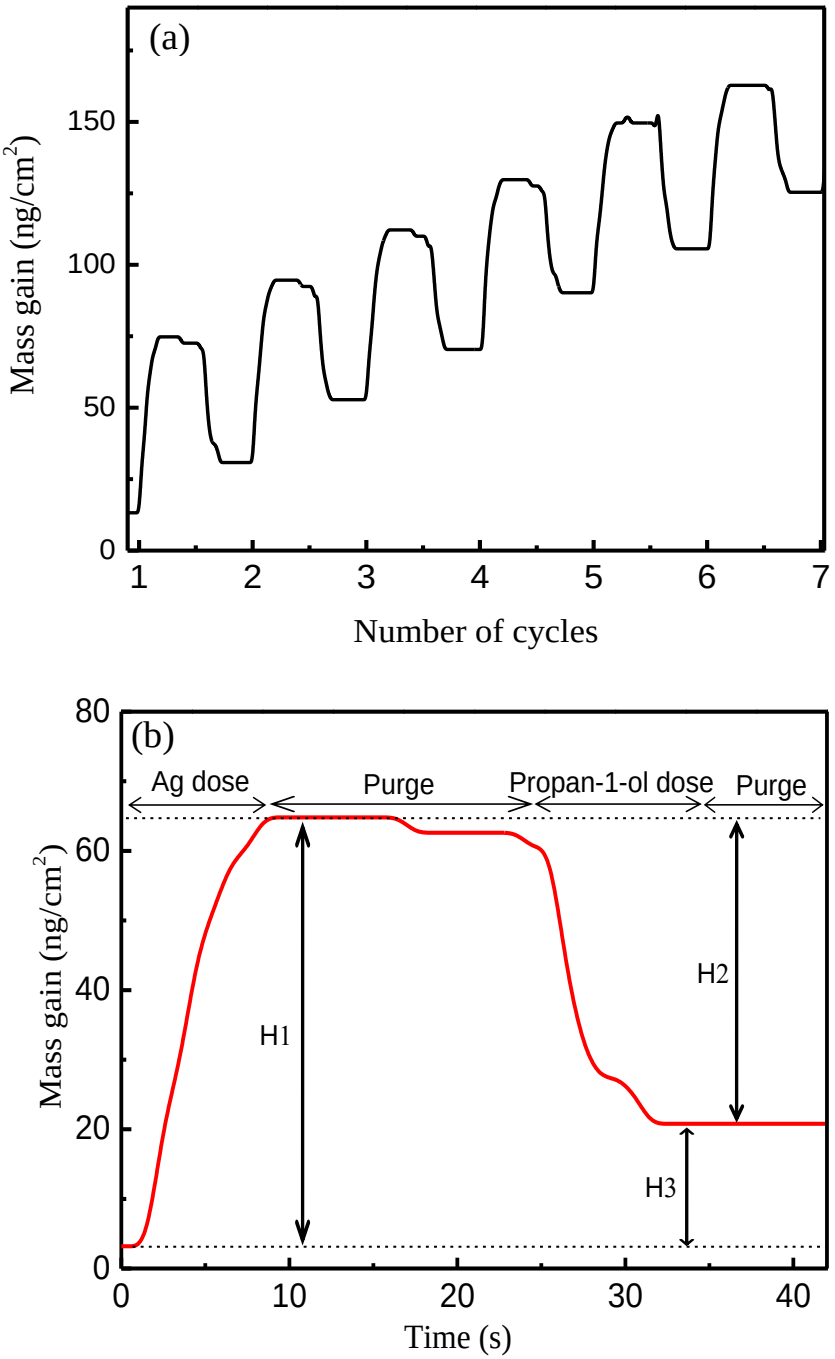

Figure 4.6: *a) QCM data for 6 cycles of Ag hfac COD based ALD at 125 °C, b) detailed view of QCM average data for one ALD cycle for 6 s - 15 s - 6 s - 15 s. (H1 = 65 ng per cm^2, H2 = 45 ng per cm^2, H3 = 20 ng per cm^2)*

4.4.3. Composition analysis

XPS was used to assess the chemical composition of films grown at different temperatures. Figure 4.7 shows a survey scan (200-700 eV) of a film deposited by ALD on Si(100) at 125 °C together with the scan of a bulk silver reference sample (99.9% silver foil, supplied by Sigma Aldrich).The XPS of the ALD film is in close agreement with the bulk silver reference sample. Both spectra show peaks relating to silver, oxygen and carbon.

Detailed XPS of the Ag3d core level region is shown in Figure 4.8. Peaks at binding energies of 368.0 and 374.0 eV are resolved, which correspond to the two spin-orbit components, $Ag3d_{5/2}$ and $Ag3d_{3/2}$ respectively. These closely match the Ag3d features for the bulk silver reference sample and are attributed to metallic silver[340]. Nano-scale texturing can influence core level binding energies by shifting them to higher energies compared to the bulk values[341,342]. This shift is only significant when the dimensions of the nano-structures fall below around ten nanometres and no such shift was observed for the ALD films.

The high resolution XPS spectra of the carbon feature reveal C1s peaks at 284.8 eV for both the ALD films and the reference sample (Figure 4.9). This peak position is associated with C-C or C-H bonds and is attributed to surface contamination rather than bulk incorporation[343]. The XPS shows similar O1s features for both the ALD films and the reference sample and is again attributed to surface adsorbates. Figure 4.10 shows high resolution O1s peak for the reference sample located at 532.4 ± 0.2 eV which is related to the non-stoichiometric near-surface oxygen atoms in carbonate ions, surface hydroxylation, adsorbed H_2O and absorbed O_2, which is correlated with OH groups at the surface[238] and was fitted with a symmetric Gaussian function. The XPS data is consistent with metallic silver films, with subsequent adsorption of atmospheric contaminants from air exposure.

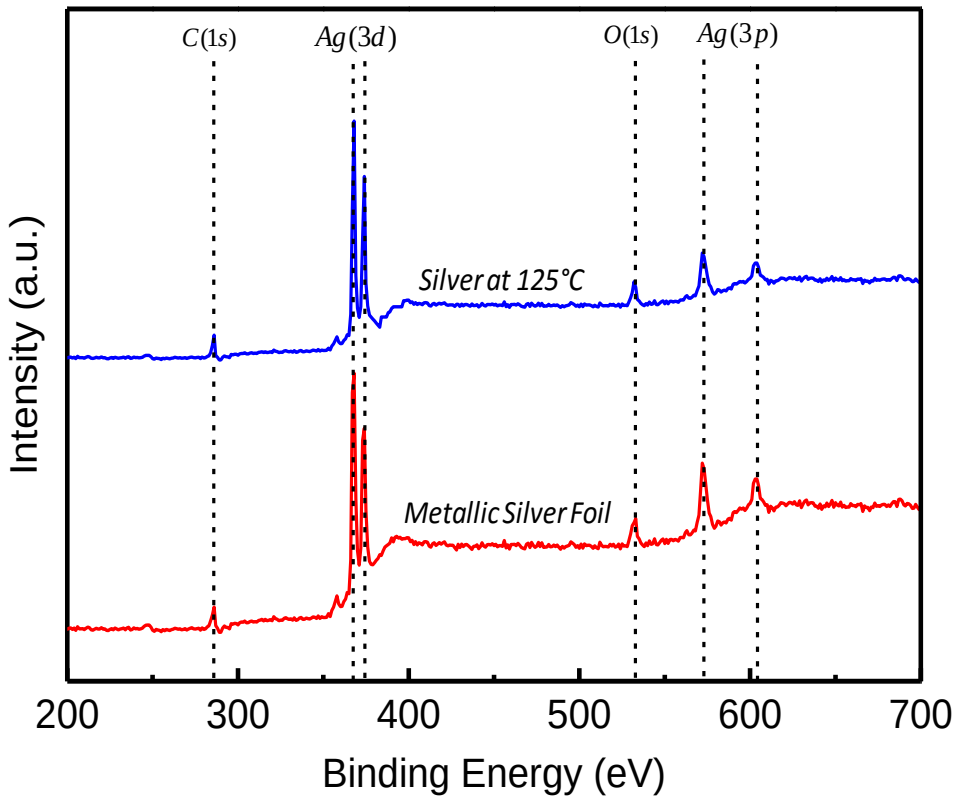

Figure 4.7: *XPS spectrum of (a) Ag bulk metal foil and (b) Ag films deposited by ALD on silicon at 125 °C.*

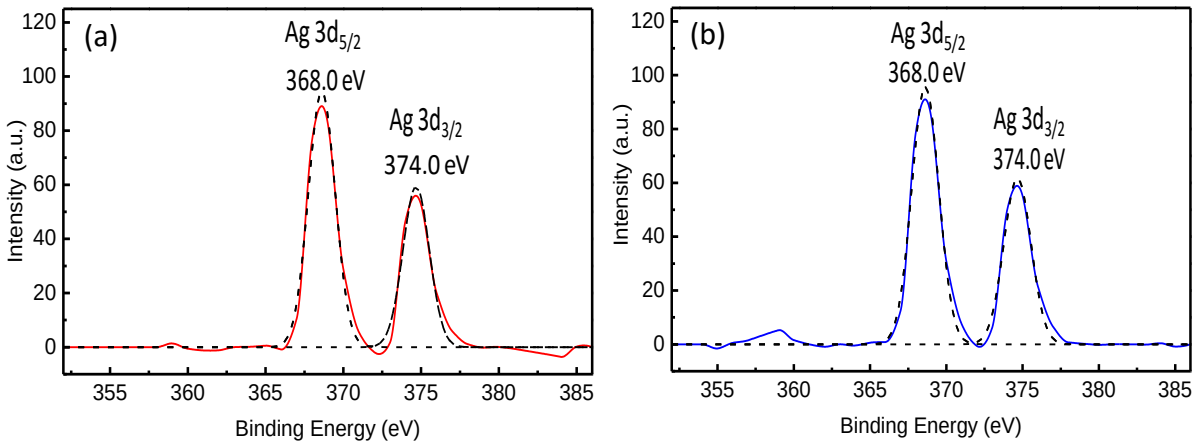

Figure 4.8: *High resolution of Ag3d XPS spectrum of silver (a) bulk metal foil and (b) Ag film deposited by ALD on silicon at 125 °C. The thin solid lines indicate the original data of XPS and the dashed curves indicate theoretically fitted curves by assuming Gaussian distribution.*

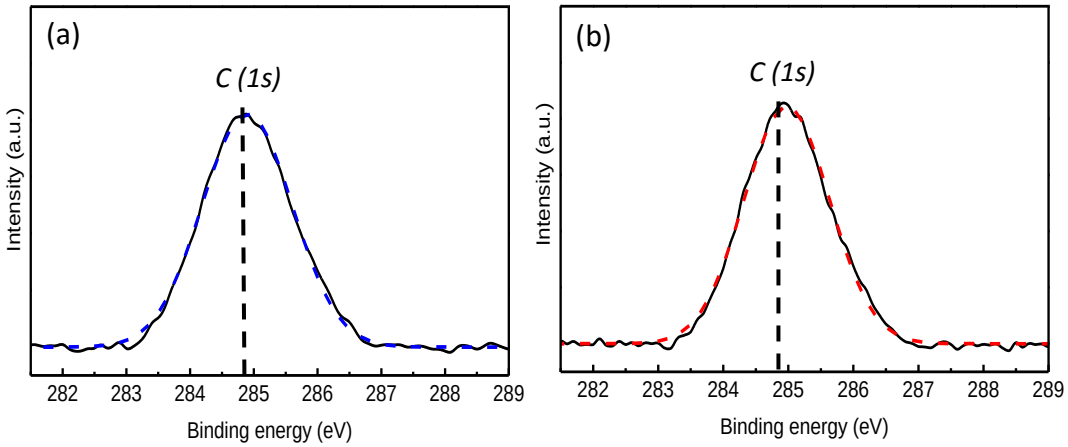

Figure 4.9: *High resolution of C (1s) XPS spectrum of (a) bulk metal foil and (b) Ag film deposited by ALD on silicon at 125 °C. The thin solid lines indicate the original data of XPS and the dashed curves indicate theoretically fitted curves by assuming Gaussian distribution.*

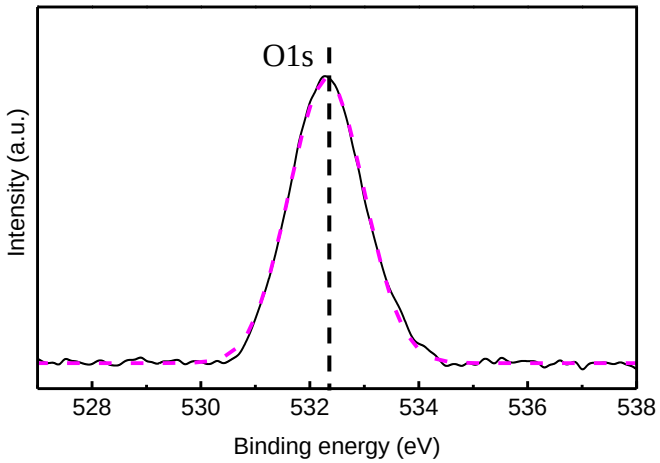

Figure 4.10: *High resolution XPS spectrum of O1s of Ag bulk metal foil*

Effective ALD processes should involve 'clean' surface reactions, which prevent ligands and reaction by-products from being incorporated into the films. Detailed XPS scans (Figure 4.11) of the films grown at temperatures between 80 and 150 °C were carried out for binding energies between 680 and 695 eV, which corresponds to the region where the F1s core level. No fluorine is detected in films deposited at or above 125°C, which provides a good indication that the ALD chemistry is proceeding cleanly within the ALD temperature window. If however, the temperature is decreased, even by 10 °C below the ALD window (115 °C), then a clear fluorine related feature is observed. The incorporation of fluorine at temperatures below the ALD growth window is attributed to insufficient energy to complete the reaction and it is likely that the $Ag^{II}(hfac)_2$ remains on the surface following the alcohol doses. Therefore, this results in increased weight gain and high levels of F contamination in the deposited film.

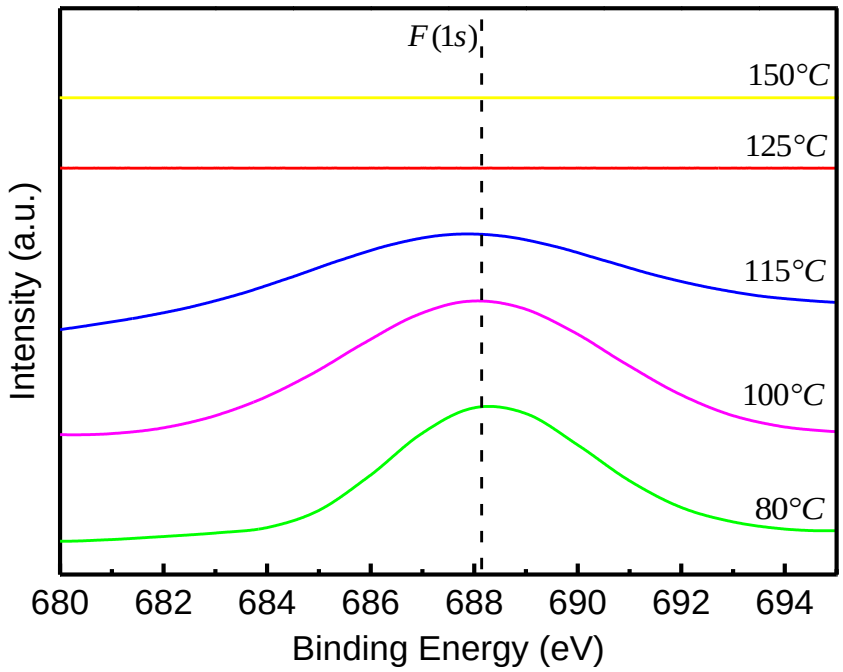

Figure 4.11: *XPS detailed regions of F1s at 80 °C, 100 °C, 115 °C, 125 °C and 150 °C from silicon substrate. Peak intensities are normalized.*

4.4.4. Microstructure study of films

XRD has been used to study the microstructure of films grown at different temperatures and the results are shown in Figure 4.12. With the exception of the lowest growth temperature (80 °C), samples show XRD peak at 38.2° and 44.4°, which are consistent with the (111) and (200) reflections of face centred cubic (fcc) metallic silver (Fm-3m) (JCPDS 04-0783). The increasing intensity of the XRD peaks with temperature (above 125°C) is attributed to film thickness. The exception to this is the film grown at 80 °C, which shows a higher mass deposition than the film deposited at 125 °C (Figure 4.12). The absence of XRD peaks together with the fluorine XPS peak in the film deposited at 80 °C is strong evidence of condensation and insufficient energy to complete the reaction. Peak width analysis using the Debye–Scherrer equation indicated average crystallite sizes of 22 nm, 35 nm and 41 nm for substrate temperature of 125 °C, 150 °C and 200 °C respectively for 500 ALD cycles.

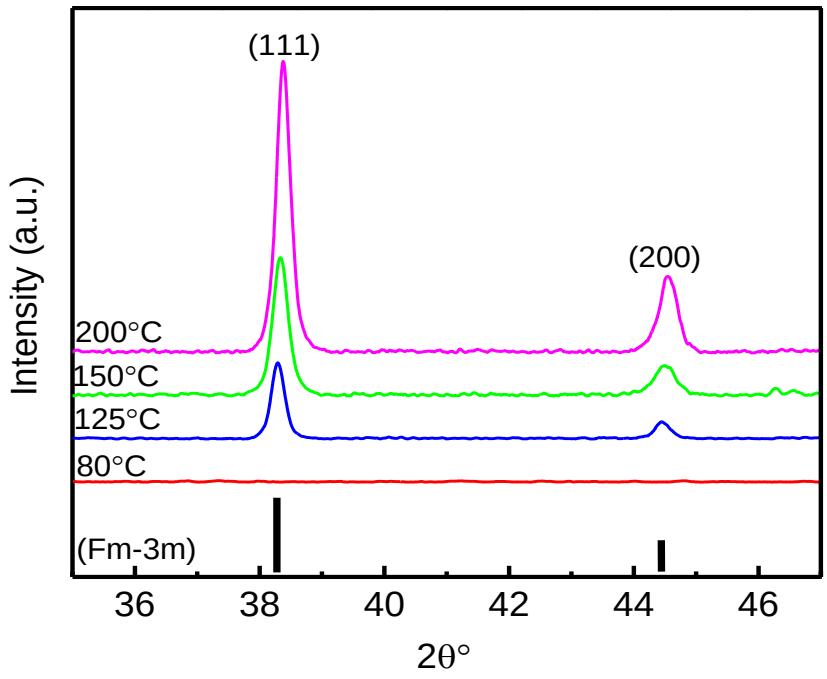

Figure 4.12: *X-ray diffraction patterns of Ag NPs deposited at various temperatures for 500 ALD cycles.*

SEM of the coatings reveals that the silver has a tendency to form as nano-particles on the surface rather than planar films by propan-1-ol doses as a co-reactant, which is in agreement with earlier study by Chalker et al[24]. The effect of silver precursor dose on the size and distribution of surface nano-structures (Figure 4.13) can be correlated with the mass deposition rate shown in section 4.3.1 (Figure 4.3) and hence to the self-limiting nature of the process. Precursor dose has little effect on the density and size distribution of the nanoparticles for dose times of 4 s or above (Figure 4.13 (c) & (d)), with only a marginal decrease in the average particle size as the dose is decreased to 2 s (Figure 4.13 (b)). However, reducing the dose time to 1 s (Figure 4.13 (a)) is seen to have a significant effect; resulting in a reduction in the density of particles, a reduction in the average size and also a broader distribution of sizes.

Under saturative growth conditions using 500 cycles, the density of particles is around 15×10^7 particles/cm², with an average particle size of ~25 nm and a standard deviation of 2.1 nm. If the precursor dose is reduced to one second (giving roughly half the saturative mass gain), then the particle density drops to 6×10^6 particles/cm², with an average particle size of ~15 nm and a standard deviation of 5.4 nm. Although this deposition process does not produce planar films, it is evident that the quasi-3D growth is still very much controlled in a self-limiting manner.

Figure 4.14 shows NPs size distribution as a function of Ag does at 125 °C for 500 ALD cycles based on SEM images. It is clear that there is a narrow size distribution under saturative growth (2-6 s dose) which is in contrast with a broad size distribution of nanoparticles below the saturation region (1 s dose).

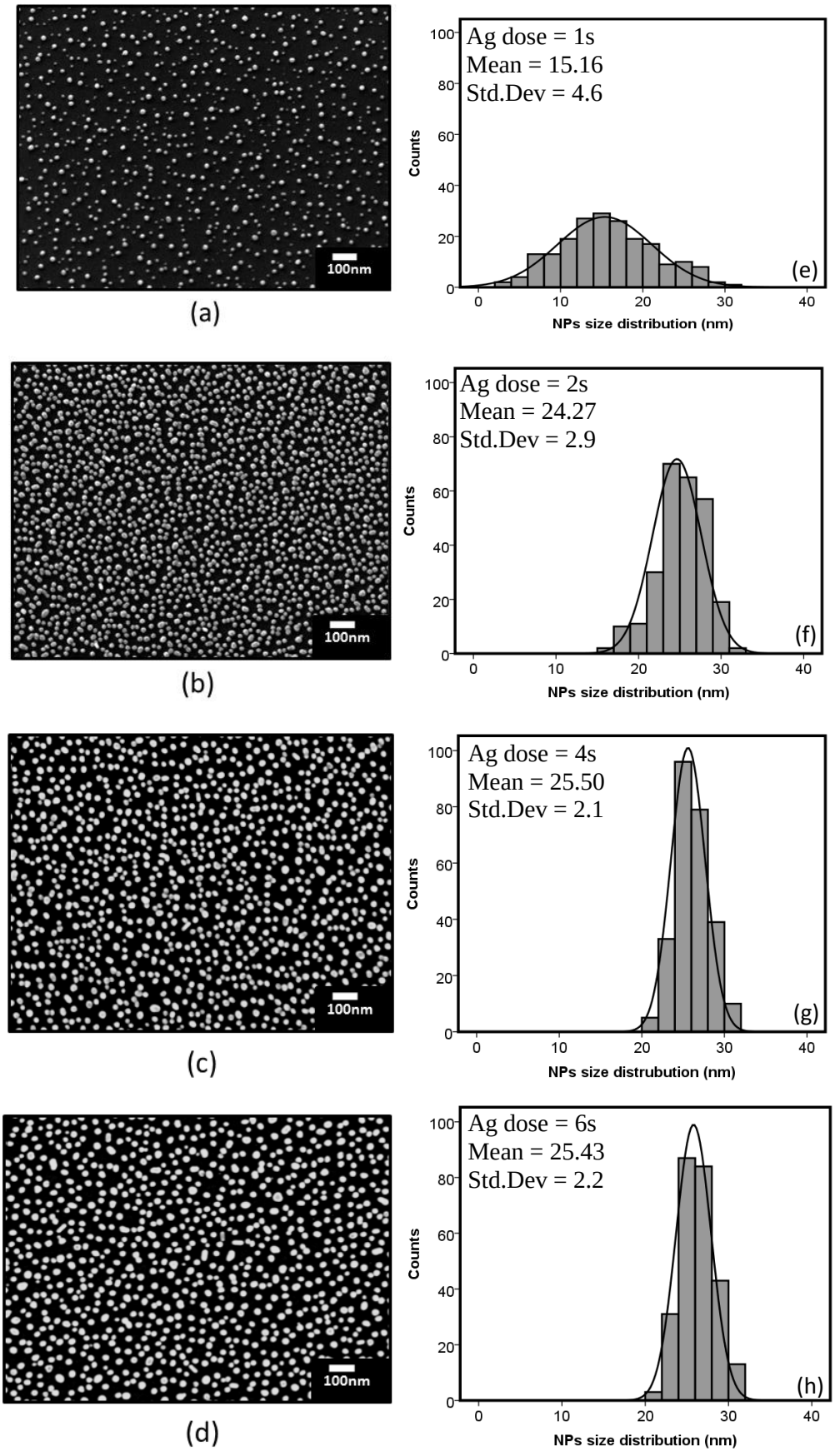

Figure 4.13: *High-resolution SEM images of ALD of silver nanoparticles as a function of Ag dose, (a) 1 s;(b) 2 s;(c) 4 s;(d) 6 s for 500 ALD cycles;(e-h)the size distribution histograms.*

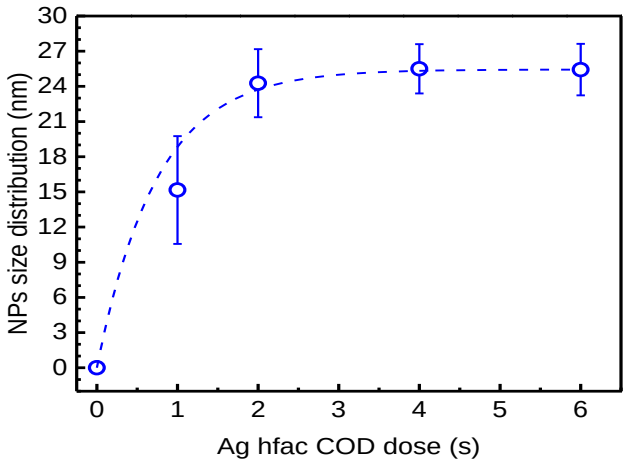

Figure 4.14: *NPs size distribution as a function of Ag does at 125 °C for 500 ALD cycles based on SEM images.*

To investigate the nucleation and growth of the silver nanoparticles in more detail, SEM was carried out on films deposited under saturative growth conditions with 4 s of propan-1-ol dose as a co-reactant between 100 and 1500 ALD cycles (Figure 4.15). The SEM images together with the corresponding histograms clearly show that increasing the number of ALD cycles from 100 to 1000 results in progressively larger hemispherical shaped particles, which retain a relatively narrow size distribution as they grow. The average size of the nanoparticles increases in a linear fashion with the number of cycles (between 0 and 1000 cycles). This implies that the nanoparticles nucleate and then grow in a homogeneous fashion during the early cycles of the ALD deposition. Additional nucleation of new nanoparticles does not appear to take place at later timeframes after the initial nucleation stage. As the number of cycles increase and the nanoparticles become bigger, nanoparticles begin to agglomerate and the particles become significantly larger and increasingly irregular in shape. The density of particles reduces and the size distribution starts to broaden as this agglomeration takes place. It is interesting to note that the average gap between neighboring nanoparticles increases as agglomeration takes place. This indicates that growing particles do not simply merge due to overlapping edges, but rather they are ‘pulled’ together and physically shift their positions inwards, presumably due to surface tension. This process is likened to ‘surface Ostwald ripening’[344,345].

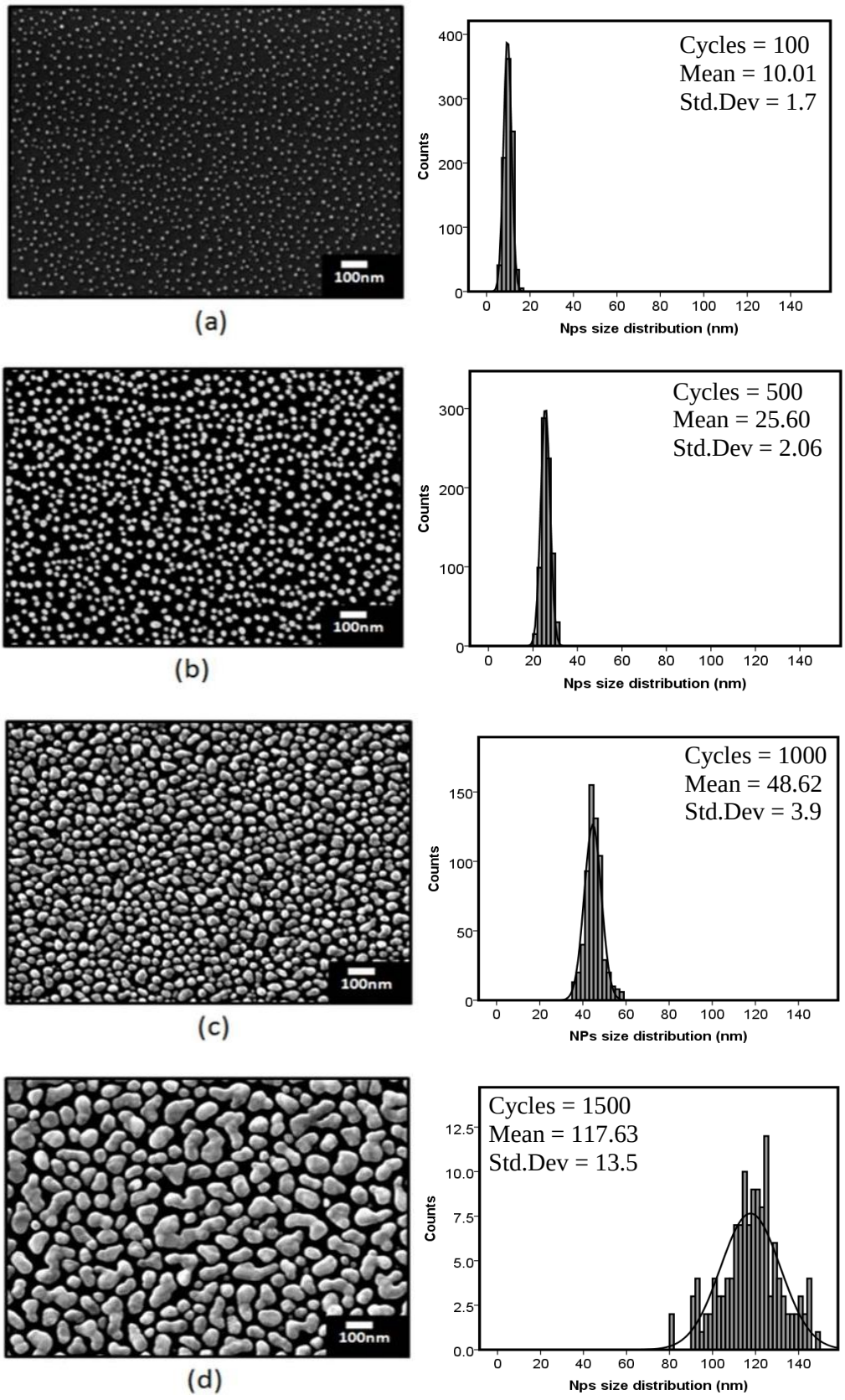

Figure 4.15: *SEM images of the surfaces at different number of ALD cycles, (a) 100; (b) 500; (c) 1000; (d) 1500 cycles; (e-h) the size distribution histograms.*

Further investigation of the SEM results is shown in Figure 4.16. The increase in the number of cycles has strong impact on the density of silver nanoparticles and also on the nanoparticles size distribution. It is clear from the graph that when the number of cycles is increased the larger nanoparticles are achieved while the density of the nanoparticles are decreased as nanoparticles begin to agglomerate.

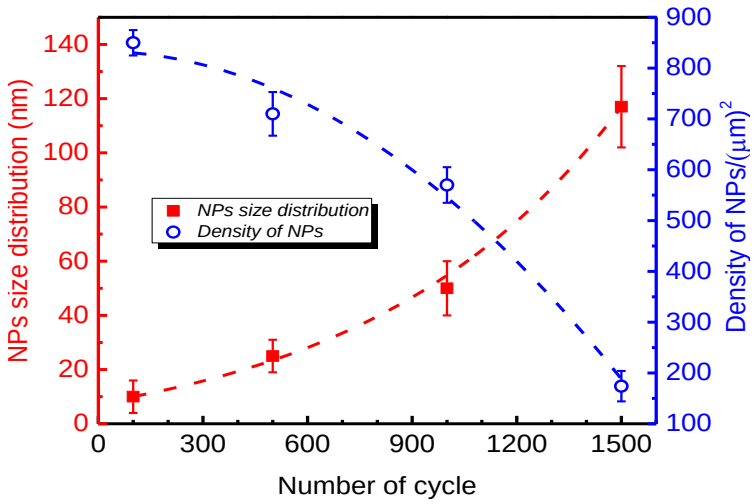

Figure 4.16: *NPs size distribution (squares) and density of NPs as a function of number of cycles at 125 °C based on SEM images.*

Figure 4.17 shows a comparison between images which are taken using secondary electrons and backscattered electrons. The grain sizes are more clearly shown in the image taking with backscattered electrons compared with secondary electrons, however, there is only ± 2 nm difference can be measured which is not a big difference and can be avoided.

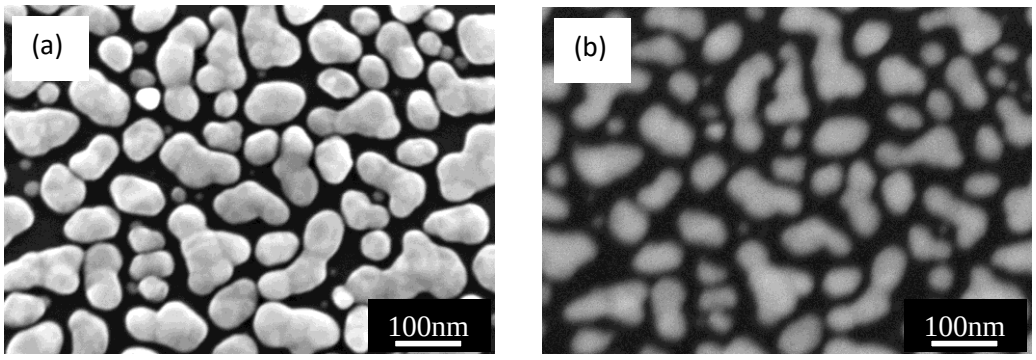

Figure 4.17: a) *SEM images of the surfaces after 1500 cycles, b) Backscattered (BS) electrons image after 1500 cycles*

4.4.5. Summary of the propan-1-ol growth study

The experiments with propan-1-ol established some encouraging results for self-limiting growth conditions for the deposition of metallic silver nanoparticle films using thermal ALD with (hfac)Ag(1,5-COD) and propan-1-ol.

A narrow ALD temperature window between 123 and 128 °C is identified and self-limiting growth is confirmed with a mass deposition of ~17.5 ng/cycle on silicon. To elucidate the reaction mechanisms involved in the silver ALD process, in-situ QCM measurements were carried out under self-limiting growth conditions. The envelope of the QCM data indicates a linear increase in mass with the number of cycles. The detailed QCM data is found to give mass changes, which are consistent with the chemisorption of Ag (hfac) followed by the formation of metallic silver via heterogeneous catalytic dehydrogenation of the propa-1-ol. Within the ALD temperature window, films are found to be crystalline metallic silver with a highly textured surface topography. The size of the nanostructures can be directly controlled using the number of ALD cycles and the coating tends towards being more film-like as features overlap and merge via a 'surface Ostwald ripening' like process.

Thermal decomposition of the silver precursor at temperatures above 128 °C results in a CVD-like contribution because of the Ag catalysed dehydrogenation of the alcohol co-reagent, nevertheless the process continues to produce metallic silver, while at temperatures below 123 °C, there is evidence of condensation of the silver precursor. However, it must be acknowledge that the ALD temperature window achieved is very narrow (123 and 128 °C), therefore, experiments were carried out with two more co-reactants (butan-1-ol and tetra butyl hydrazine) to investigate the effect of them on the growth behaviour.

4.5. ALD with butan-1-ol as a co-reactant

4.5.1. Growth study

1-Butanol (n-Butanol, Butyl alcohol)[346] with the molecular formula of CH_3 $(CH_2)_3OH$ (Figure 4.18 (a)) and molecular mass of 74.12 $g.mol^{-1}$ is an alcohol with the existence of one more Methylene (CH_2) group (longer chain) compared with propan-1-ol[347] (Figure 4.18 (b)) with molecular mass of 60.1 $g.mol^{-1}$.

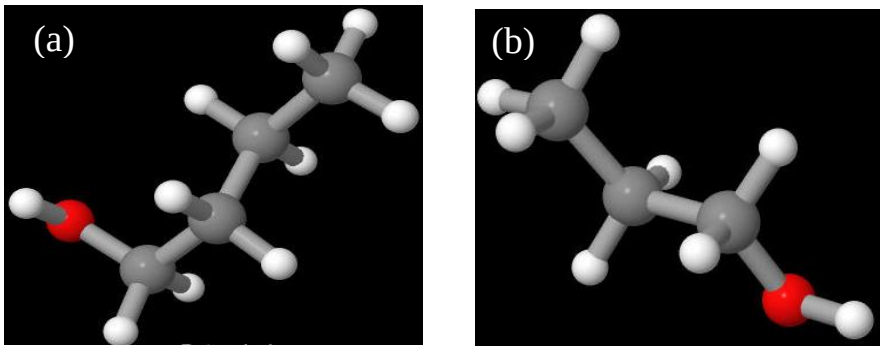

Figure 4.18: *Schematic of a) Bunat-1-ol chemical structure, b) Propan-1-ol chemical structure*[346,347]

To investigate the effect of the butan-1-ol (4 s dose) on the ALD temperature window versus propan-1-ol (4 s dose), a direct comparison is made and shown in Figure 4.19. The mass deposition rate reveals that with the influence of butan-1-ol doses, the ALD temperature follows a same narrow temperature window from 123 to 128 °C (Figure 4.19 (circles)) consistent with the previous work using propan-1-ol which resulted in obtaining the same ALD temperature range (Figure 4.19 squares). The observed similar ALD temperature window for the two co-reactants can be explained as they are both alcohols and can help to the deposition via dehydrogenation reaction and forming aldehyde as reported by Bahlawane *et al*[320] previously and also shown by QCM in this study (Figure 4.6). However, for the butan-1-ol, the

mass deposition has decreased by ~ 4 ng/cm^2/cycle within the ALD temperature window compared with propan-1-ol (17.5 ng/cm^2 per cycle) gaining a nominal deposition rate of 11.5 ng/cm^2 per cycle. Each data point has been repeated for at least 7 times. Propan-1-ol has pka value of 15.87, whereas the pka value of buta-1-ol is slightly higher for 15.92[348]. Also, the carbon chain gets longer in butan-1-ol. The increase in the non-polar carbon chain length increase the intermolecular forces significantly and therefore, more energy is required to separate the molecules[349].

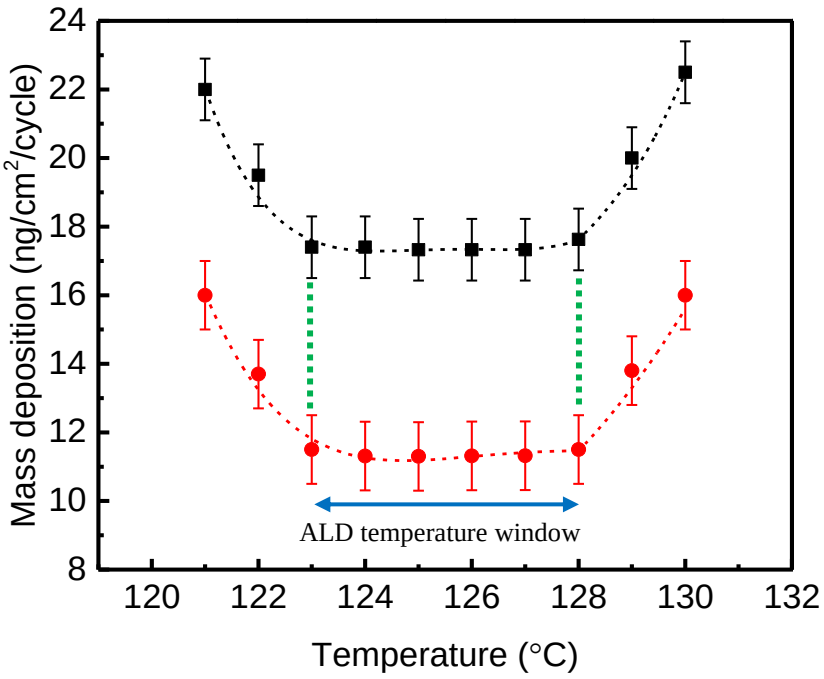

Figure 4.19: *Mass deposition as a function of substrate temperatures using 4 s dose of Ag butan-1-ol (red circles) and propan-1-ol (black squares)*

The effect of purge time was explored at 125 °C using the (hfac) Ag (1,5-COD) – purge – butan-1-ol/propan-1-ol – purge sequence of 4 s – 4 s – 4 s – t $_{purge}$, where t $_{purge}$ was changed between 1 to 6 s. The investigations further reveal that a longer purge is needed for butan-1-ol to reaches a self-limiting rate of 11.5 ng/cm^2 per cycle compared with propan-1-ol due to its longer alkane chain (Figure 4.20). The longer purge dose for butan-1-ol largely effect on the mass deposition rate from 1 s to 4 s by decreasing the deposition rate for 4 ng/cm^2/cycle before

reaches saturation (Figure 4.20) while with 2 s purge dose for propan-1-ol saturation has occurred. The extra by-products produced by butan-1-ol can block active sites by adsorbing onto the surface and causing delay in the saturation[350].

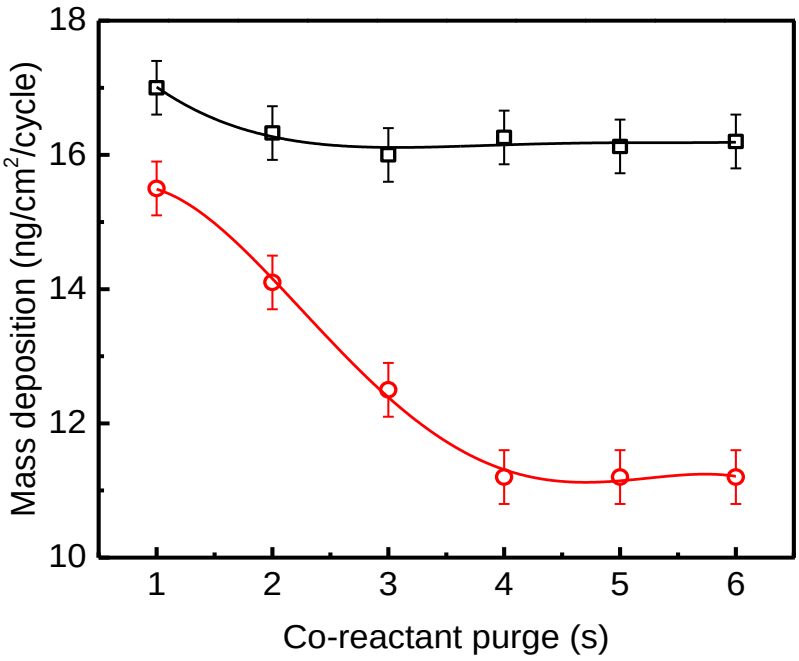

Figure 4.20: *The mass deposition rate as a function of purge time for the ALD deposition using (hfac) Ag (1,5-COD) with butan-1-ol (red circles) and propan-1-ol(black squares) at 125 °C. The (hfac) Ag (1,5-COD) – purge – butan-1-ol – purge –) order was (4 s – 4 s – 4 s – t $_{purge}$ –), where t $_{purge}$ was varied 1-6 s.*

As it has been already discussed in the literature (chapter 2), one of the main advantages of ALD over CVD process is the ability to uniformly coat over large areas. In this study, the effect of uniformity across the substrate holder was investigated using the deposition process with propan-1-ol and butan-1-ol. As the length of the sample stage is 13 cm, thirteen silicon samples with the size of 1 × 4 cm^2 were chosen and put edge by edge along the reactor length for each separate run. The uniformity across the substrate chamber using 4 s propan-1-ol doses with 4 s purge was investigated at 125 °C by measuring the mass deposition of thirteen silicon samples lengthwise the substrate. As it is shown in Figure 4.21 (black squares), deposition with propan-1-ol dose is driven by self-limiting surface reactions with the uniformity of 95 ± 1% and the

distance from the argon gas inlet does not show any effect on the uniformity. In contrast to the results with propan-1-ol, the deposition grown with 4 s dose of butan-1-ol and 4 s purge exhibited lower mass deposition in the front of the reactor for 11.8 ng/cm^2/cycle compared towards the end of the reactor for ~ 15.2 ng/cm^2/cycle. This indicates that a 4 s purge is insufficient to remove all by-products from butan-1-ol dose, leading to gas phase CVD-like reactions at the end of the reactor substrate away from the argon flow and resulting in a higher growth rate with poor uniformity of 76 ± 1% (red circles). Therefore, the experiment with butan-1-ol was repeated using 10 s purges. As it can be seen from Figure 4.21 (blue triangles), the mass deposition is driven by self-limiting surface reactions and the deposition rate is uniform across a 13 cm distance for 4 s of butan-1-ol dose and an extended purge of 10 s at 125 ºC and the uniformity improves to 96 ± 1%.

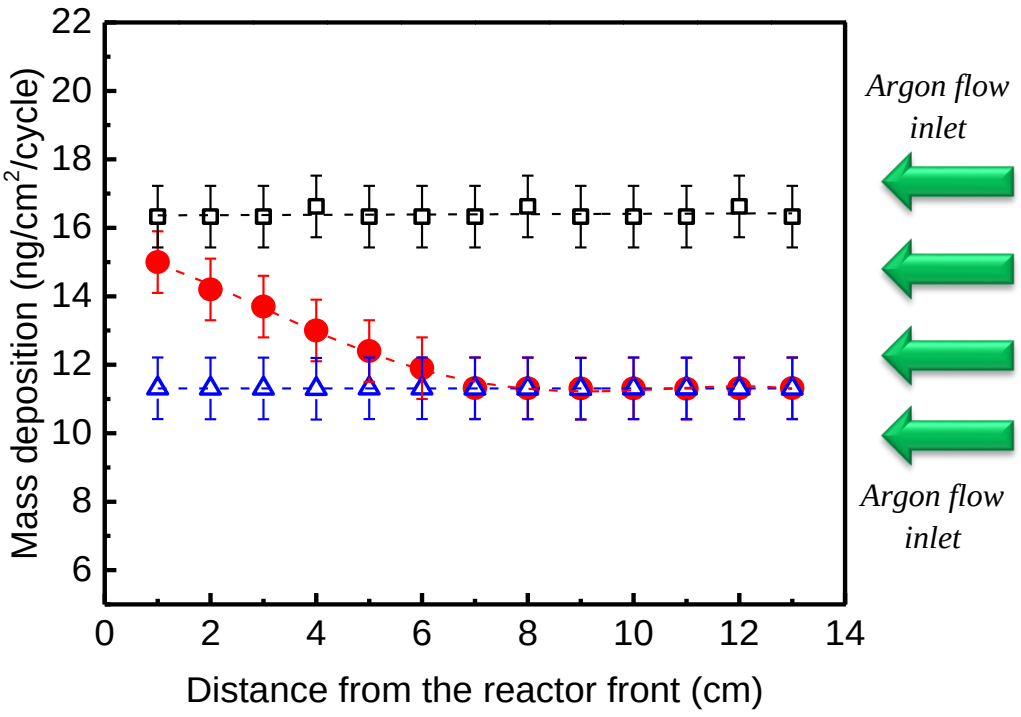

Figure 4.21: *The mass deposition measurements on silicon substrates across the 13 cm reactor chamber using silver precursor (4 s) and either pripan-1-ol dose (4 s) with 4 s purge (black squares) or butan-1-ol dose (4 s) with 4 s (red circles) and 10 s (blue triangles) purge respectively at 125 °C.*

4.5.2. Summary of the butan-1-ol growth study

Growth using butan-1-ol is very similar to growth using propan-1-ol with a similar ALD temperature window (123 to 128 °C) and slightly lower staurative growth rate of 11.5 ng/cm^2 per cycle. Self-limiting growth behaviour is achieved by butan-1-ol as well as propan-1-ol. Within the ALD temperature window, films are found to be crystalline metallic silver with nanoparticles topography. The size distribution of nanoparticles is narrow under ALD conditions and can be directly controlled using the number of ALD cycles similar to propan-1-ol. Some of the butan-1-ol data are provided in the Appendix K, L and M on page 204, 205 and 206 respectively.

Chapter 5

ALD growth of silver thin films using TBH as a co-reactant

5.1. Introduction

The current chapter seeks to develop a thermal ALD process for the deposition of silver using direct liquid injection thermal ALD with ((hexafluoroacetylacetonato) silver (I) (1,5-cyclooctadiene)) as the metal source and tertiary butyl hydrazine as a co-reactant. The effects of temperature, co-reactant dose, precursor dose and cycle number on the deposition rate and on the physico-chemical and electrical properties of the films have been systematically investigated using a range of characterisation techniques including SEM, AFM, XRD, XPS and four-point-probe.

The ALD process with TBH has also been compared and contrasted with the ALD process using propan-1-ol as a co-reactant. Therefore, the current work will analyze the ALD growth of silver using (hfac) Ag (1,5-COD) as a precursor in the following schemes:

- Effect of tertiary butyl hydrazine on growth/microstructure/composition of the deposited film
- Discussion and comparison of the ALD process of silver with TBH and propan-1-ol as two different co-reactants

5.2. ALD with tetra butyl hydrazine as a co-reactant

5.2.1. Experimental procedure

Films were deposited on Si(100) and on soda-lime glass slides using a customised Aixtron AIX 200FE reactor. A 0.1 M solution of ((hfac)Ag(1,5-COD)) (SAFC Hitech) in anhydrous toluene(Sigma Aldrich) as used as the silver source. This solution was introduced into the reactor by direct liquid injection via a Jipelec vaporiser with a set-point temperature of 130 °C. Tertiary butyl hydrazine (TBH) (98%, HPLC grade supplied by SAFC Hitech Ltd) was used as a co-reactant and was introduced into the reactor as a vapour, via a Swagelok ALD valve, using a conventional vapour-draw source held at room temperature (~20 ºC). Further details of the growth conditions are summarised in Table 5.1.

Table 5.1: *ALD growth parameters for silver deposition using AIXTRON thermal reactor*

Growth condition	Value			
Growth temperature	80-200 °C			
Reactor pressure	5 mbar			
Silver precursor	(hfac)(1,5-COD)Ag			
Silver source	0.1M solution in n-Toluene			
Vaporizertemperature	130 °C			
Precursor delivery rate	17.5 µl/second			
Argon flow rate	200 sccm			
Co-reactant	Tertiary butyl hydrazine			
Co-reactant delivery	Vapour draw at ~20 °C			
ALD cycle	Inject 0-6 s	Purge 4 s	TBH 0-0.4 s	Purge 0.5 or 4 s

5.2.2. Growth study

Considering the results and conclusions from the ALD investigations on propan-1-ol/butan-1-ol as co-reactants, tertiary butyl hydrazine (TBH) was chosen as a different co-reactant for silver ALD deposition. The potential for exploiting other reducing agents in ALD, such as hydrazines (R_1HNNHR_2 where R_1 and R_2 represent alky-substitutional for example) has been recognised[351]. An ideal hydrazine candidate would be tertiary butyl hydrazine (TBH, $C_4H_{12}N_2$) as it is a stronger protonating agent than alcohols[306]. Tertiary Butyl Hydrazine (TBH) (also known as 2-Hydrazino-2-methyl-propan, tert-Butyl-hydrazin or 1-tert-butyl-hydrazine)[352] is known by the molecular formula of $C_4H_{12}N_2$. The pKa value for TBH is 8.1[353] whereas; the pKa for both propan-1-ol and butan-1-ol is 16.1[354]. Therefore, alcohols are less acidic compared with hydrazines and so less likely to donate protons[306].

Hydrazines have been used as nitrogen sources in a number of nitride ALD studies[233,273,8] due to its superior reactivity and favourable thermo-chemistry which can lead to the relatively low deposition temperature in ALD processes[355]. However, when it comes to the ALD of silver, only one patent study has reported the deposition of silver using hydrazine as a co-reactant[351] and they showed that the growth temperature can be decreased to 60 °C with TBH from 125 °C with alcohol as a co-reactant. Although this report is of great interest, it mainly focuses on the method of forming a metal-containing film by atomic layer deposition rather than the ALD process itself, and hence, it does not provide any evidence that the process is self-limiting. In this chapter, a self-limiting thermal ALD process for the deposition of metallic silver thin films using TBH is presented for the first time and will be compared with the alcohol based silver ALD process that previously presented in the chapter 4.

The effects of deposition temperature on the ALD growth of (hfac) Ag (1,5-COD) using TBH as a co-reactant was investigated between 80 and 200 °C is shown in Figure 5.1 on silicon substrate. The mass gain per cycle was evaluated after 500 ALD cycles, using 4 s doses of (hfac) Ag (1,5-COD) and 0.2 s TBH doses as a co-reactant and 4 s purges.

The mass deposition increases with temperature between 80 °C to 105 °C before plateauing at a mass deposition rate of 20.2 ng/cm^2/cycle between 105 and 128 °C (Figure 5.2). The plateau region defines the ALD window where self-limiting growth is expected to occur. The mass gain increases at temperatures above 128 °C which is attributed to the thermal decomposition of the precursor while the decrease in mass deposition below 105 °C is attributed to insufficient thermal energy available to promote precursor chemisorption reaction at full coverage[356].

For comparison, this graph also shows growth rate data for the propan-1-ol and butan-1-ol based ALD processes from chapter 4. The ALD temperature window for both alcohol based ALD processes are from 123 to 128 °C (Figure 5.2) and therefore, using TBH as a co-reactant resulted in a significant enhancement in the width of the ALD temperature window (23 °C) between 105 and 128 °C. The mass deposition rate in the ALD temperature window is also found to be higher using TBH than propan-1-ol and butan-1-ol by ~ 3 ng/cm^2/cycle and ~ 7 ng/cm^2/cycle respectively.

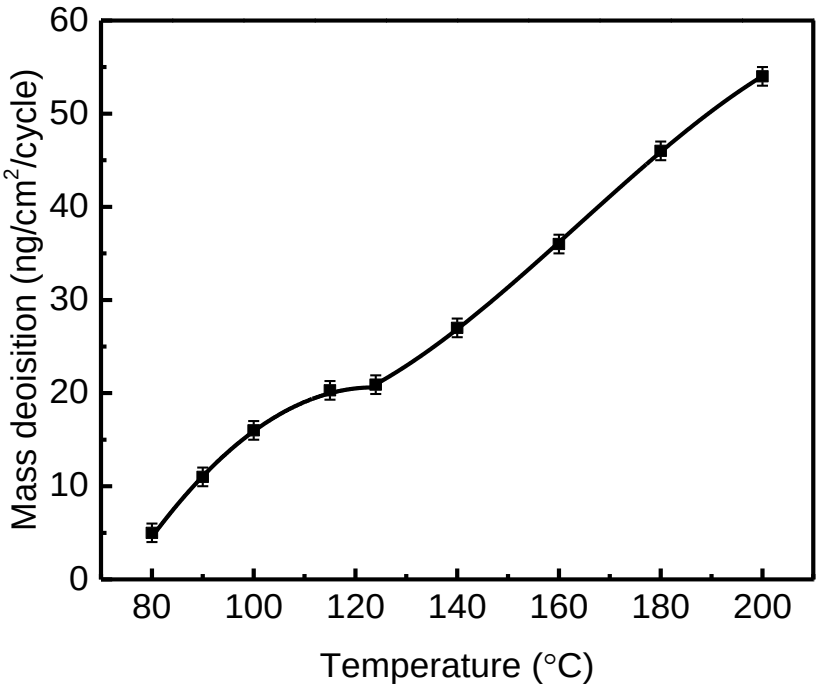

Figure 5.1: *Mass deposition as a function of substrate temperatures using 4 s dose of Ag with 0.2 s TBH as a co-reactant per cycle*

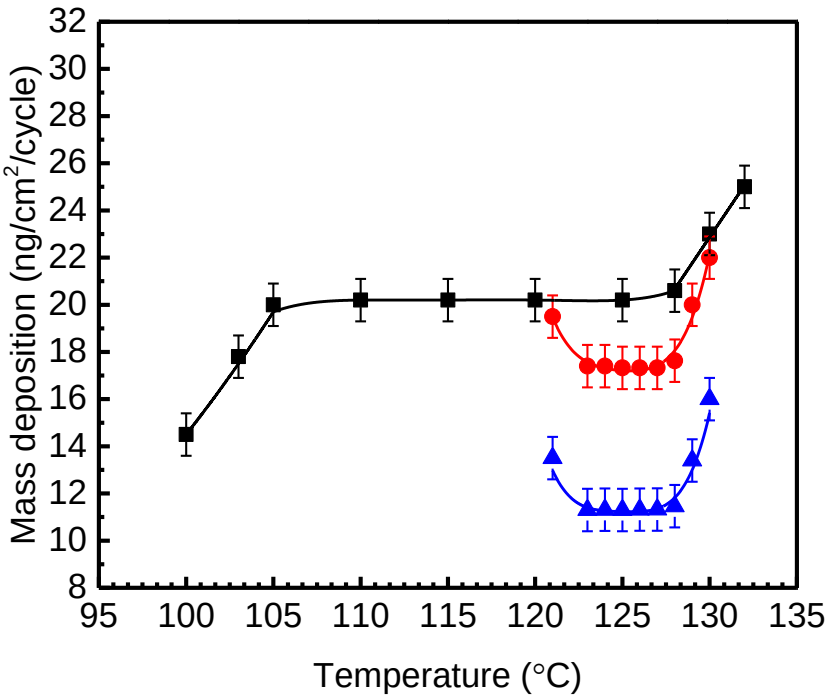

Figure 5.2: *Mass deposition as a function of substrate temperatures using 4 s doses of (hfac) Ag (1,5-COD) with 0.2 s TBH doses as a co-reactant per cycle (squares) with 4 s purges, using 4 s propan-1-ol doses (circles) and 4 s butan-1-ol doses (triangles) as a co-reactant per cycle with 4 s purges*

Within the silver precursor ((hfac)Ag(1,5-COD)), the 1,5-COD part of the silver source helps to stabilise the precursor, however, as 1,5-COD only weakly bonds to the Ag, it readily dissociates during volatilisation or possibly even when the precursor is in solution[319]. Silver coordination compounds are known to undergo oxidative reactions with hydrazines[357]. Hydrazine is a powerful reducing agent and is generally oxidized to dinitrogen by two different oxidations: (a) one-electron oxidation which generally produces a mixture of ammonia and dinitrogen; (b) four-electron oxidation which produces dinitrogen and hydrogen. Using TBH as a co-reactant, the hydrogen that is liberated from the TBH promotes the reduction of the disproportionation $Ag^{II}(hfac)_2$ product into the metallic silver film (Ag^0) and volatile H(hfac) leaving groups. The higher reactivity of hydrazine and its derivatives can be explained due to the lower dissociation energies and weak N-N bonding. The dissociation energy (E_D) of hydrazine is 297 kJ/mol[358,359] well below the dissociation energy of propan-1-ol which is 412.5±1.7kJ/mol[360].

The effects of the TBH doses were assessed at 115 °C (the middle of the ALD temperature window). Due to the high volatility of TBH, doses were chosen between 0.1 s (which is the minimum dose time allowed by the reactor control system) and 0.4 s with either 0.5 s or 2 s of purge. With a short purge for 0.5 s, the mass deposition increases from 20.2 ng/cm^2 per cycle to 23 ng/cm^2 per cycle between 0.1 to 0.4 s (Figure 5.3, circles). Therefore, this indicates that a 0.5 s purge is insufficient to remove all un-reacted chemicals from TBH dose, leading to gas phase CVD-like reactions and resulting in a higher growth rate. With a longer 2 s purge, on the other hand, the mass deposition is self-limiting with TBH doses between 0.1 s and 0.4 s at 20.2 ng/cm^2 per cycle (Figure 5.3, squares).

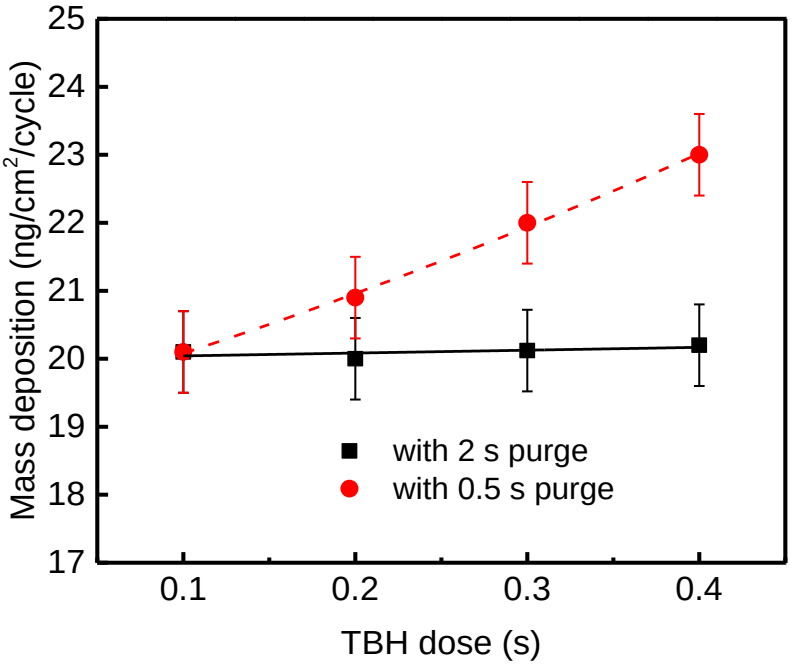

Figure 5.3: *The growth rate as a function of TBH dose at 115 °C with 4 s Ag and either 0.5 s or 2 s purge on silicon.*

The effect of (hfac) Ag (1,5-COD) dose on the deposition rate was investigated at 115 °C. The TBH dose was fixed at 0.2 seconds, the purge times were fixed at 4 s seconds and the cycle was repeated 500 times for each deposition run. The mass deposition rate initially increases with the dose, but at two seconds, it saturates at 20.2 ng/cm^2 per cycle (Figure 5.4). This saturation behaviour of the silver precursor with TBH dose is in good agreement with propan-1-ol process also shown in Figure 5.4 and therefore, it shows that both processes are controlled by saturative surface reactions. However, the saturative growth rate is lower for propan-1-ol than TBH by ~ 3 ng/cm^2/cycle.

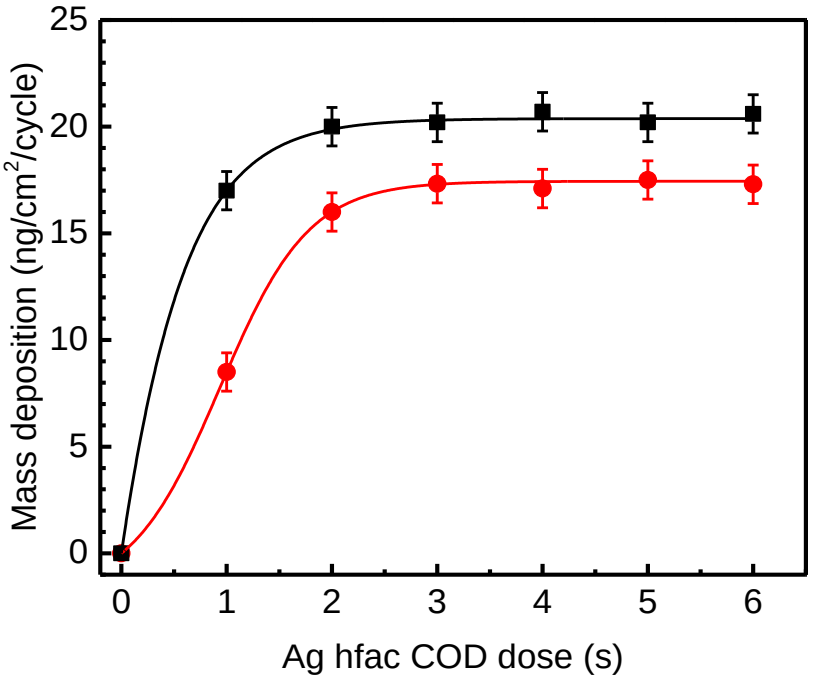

Figure 5.4: *Mass deposition as a function of a) Ag hfac COD at 115 °C (squares) with TBH dose and 125 °C (circles) for 500 ALD cycles with propan-1-ol dose on silicon*

Figure 5.5 shows the mass deposition versus the number of ALD cycles using both propan-1-ol and TBH at 125 °C and 115 °C respectively. The TBH clearly follows a linear trend going from zero mass deposition at zero cycles upwards across the full range investigated up to 2500 cycles with a slope of 0.023 µg/cm^2/cycle. In comparison, the propan-1-ol shows a linear fashion behaviour with rising number of ALD cycles with a slope of 0.013 µg/cm^2/cycle up to 1500 cycles, whereas for more than 1500 cycles, a steeper increase is obtained with the slope of 0.023 µg/cm^2/cycle. The slope of the graph with propan-1-ol after 1500 cycles is equal to the slope of the TBH graph, and therefore above 1500 cycles the growth rates are actually identical for both processes independent of the reaction involved in the process. This lower growth with propan-1-ol for low number of cycles could be explained due to differences in reaction mechanisms and higher reactivity of TBH compared with propan-1-ol which can lead to a change in surface chemistry for initial growth cycles.

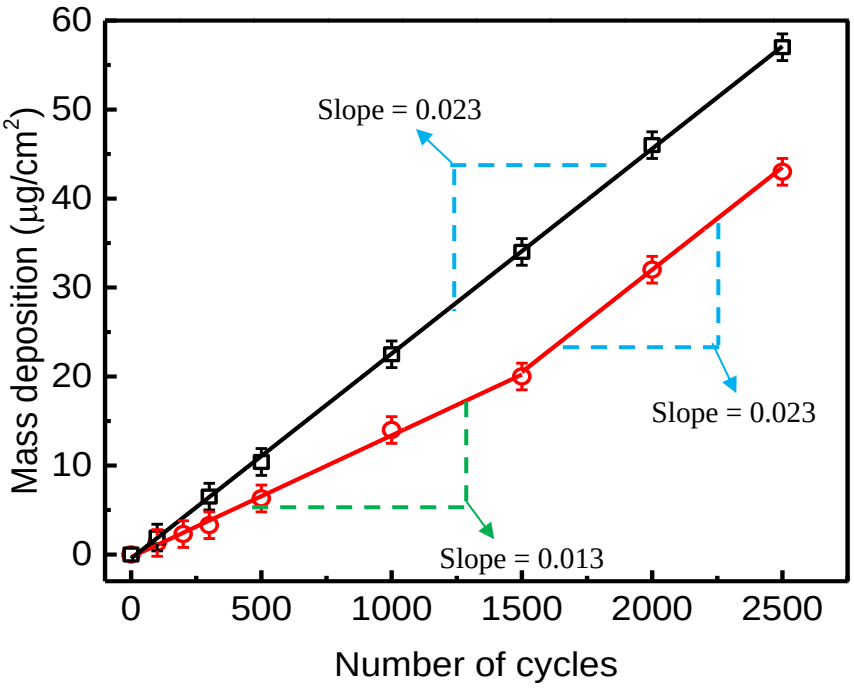

Figure 5.5: *Mass deposition per unit area as a function of number of ALD cycles at 115 °C with TBH (black squares) and at 125 °C with Propan-1-ol (red circles)*

5.2.3. Composition analysis

In order to study the chemical composition of the silver films, selected samples were analysed using XPS. Figure 5.6 shows a survey scan (200-750 eV) of films deposited on Si(100) at 115 °C using 500 cycles with 4 s of silver precursor doses, 0.2 s of TBH doses (or 4 s propan-1-ol doses) and 4 s purges. Features relating to silver, carbon and oxygen are visible on both spectra, while the fluorine feature at 688.87 eV is only detected in the sample grown using propan-1-ol as a co-reactant. The presence of the F1s features in the XPS is attributed to incomplete removal of the hfac ligands or at least fragments of it from the surface. The F1s XPS feature is only visible in films grown at temperature below the ALD-window minima. To further investigate the incorporation of fluorine, detailed XPS scans were taken for films grown using TBH at temperatures ranging from 80 to 135 °C (Figure 5.7).

No visible F1s peaks are observed at growth temperatures above 105 °C (the minima of the ALD window) indicating that the fluorine is below the detection limit of the XPS system (~1 at. %). At temperatures below 105 °C the F1s peak intensity increases almost linearly with decreasing temperature. As the mass deposition rate (Figure 5.1) for the TBH process decreases at these low growth temperatures, condensation of the silver source seems unlikely and hence the fluorine incorporation is attributed to reaction rates. At these low temperatures, there is insufficient thermal energy to fully reduce the silver precursor on the surface and hence the mass deposition rate decreases as some un-reacted precursor is left on the surface at the end of each cycle. The un-reacted precursor left on the surface at the end of one cycle may well react with the co-reactant during the subsequent cycle. The absence of the F1s feature at temperatures between 105 and 128 °C gives a good initial indication that the ALD surface reaction are 'clean' within the ALD window.

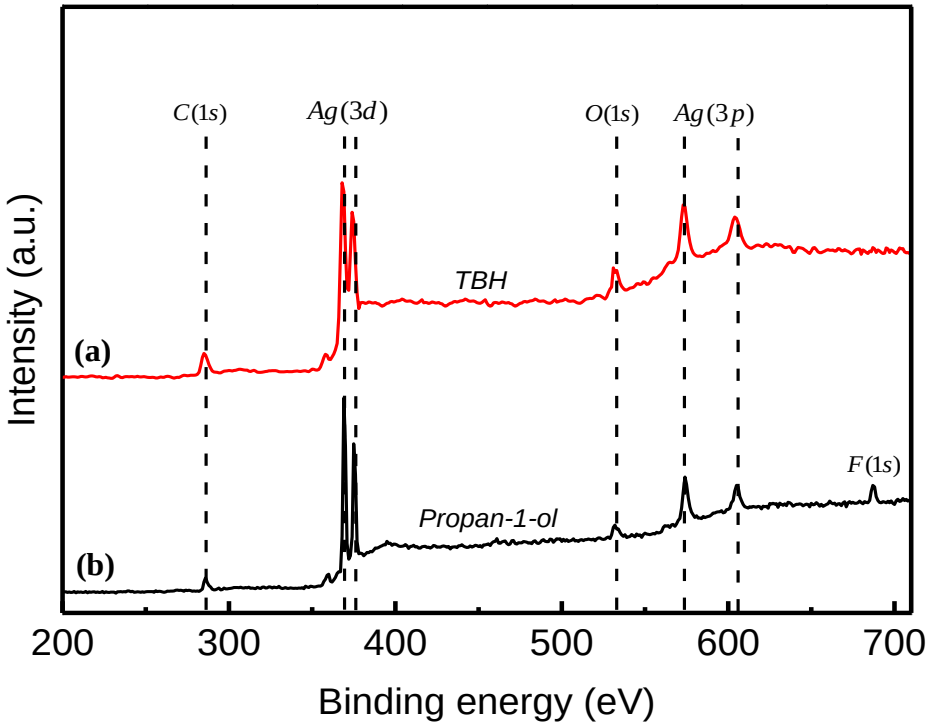

Figure 5.6: *XPS survey scan of Ag films deposited by ALD on silicon at 115 °C with (a), 0.2s of TBH dose (b), and 4 s of propan-1-ol dose as a co-reactant*

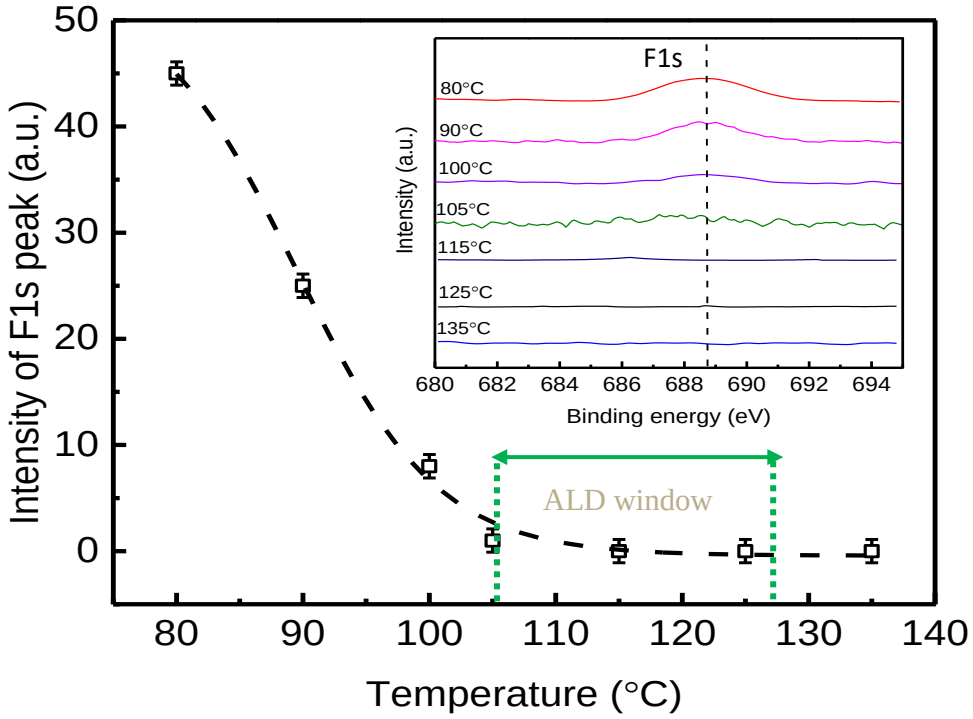

Figure 5.7: *Variation in XPS peak intensities of F1s at different temperatures with TBH dose. Peak intensities are normalised to the C1s peak.*

As it was not possible to carry out in-situ surface cleaning of samples within our XPS system, signals from atmospheric absorbates on the surface are expected to be observed. To establish the origin of the carbon and oxygen XPS features, high resolution XPS of the C1s (Figure 5.8 a), O1s (Figure 5.8 b and c) and Ag3d (Figure 5.8 d and e) features were obtained for films grown at 80 and 115 °C. The C1s peak is centred at 284.8 eV, which corresponds to C-C or C-H bonding states and is attributed to surface absorbates rather than bulk incorporation[361]. The O1s feature for the film grown at 115 °C (Figure 5.8 b) is readily fitted with a single Gaussian centred at 532.4 eV, which is consistent with oxygen in surface absorbates such as H_2O, O_2, CO_2 and CO[362]. The O1s feature for the film grown at 80 °C (Figure 5.8 c) is, however, more complex and is clearly made up of at least two peaks. A reasonable fit is obtained using two Gaussians centred at 530.3 eV and 532.4 eV, where the latter is once again attributed to surface absorbates. The peak at 530.3 eV suggests that some of the oxygen is bonded with the metal, which would be consistent with silver that is still associated with the hfac ligand.

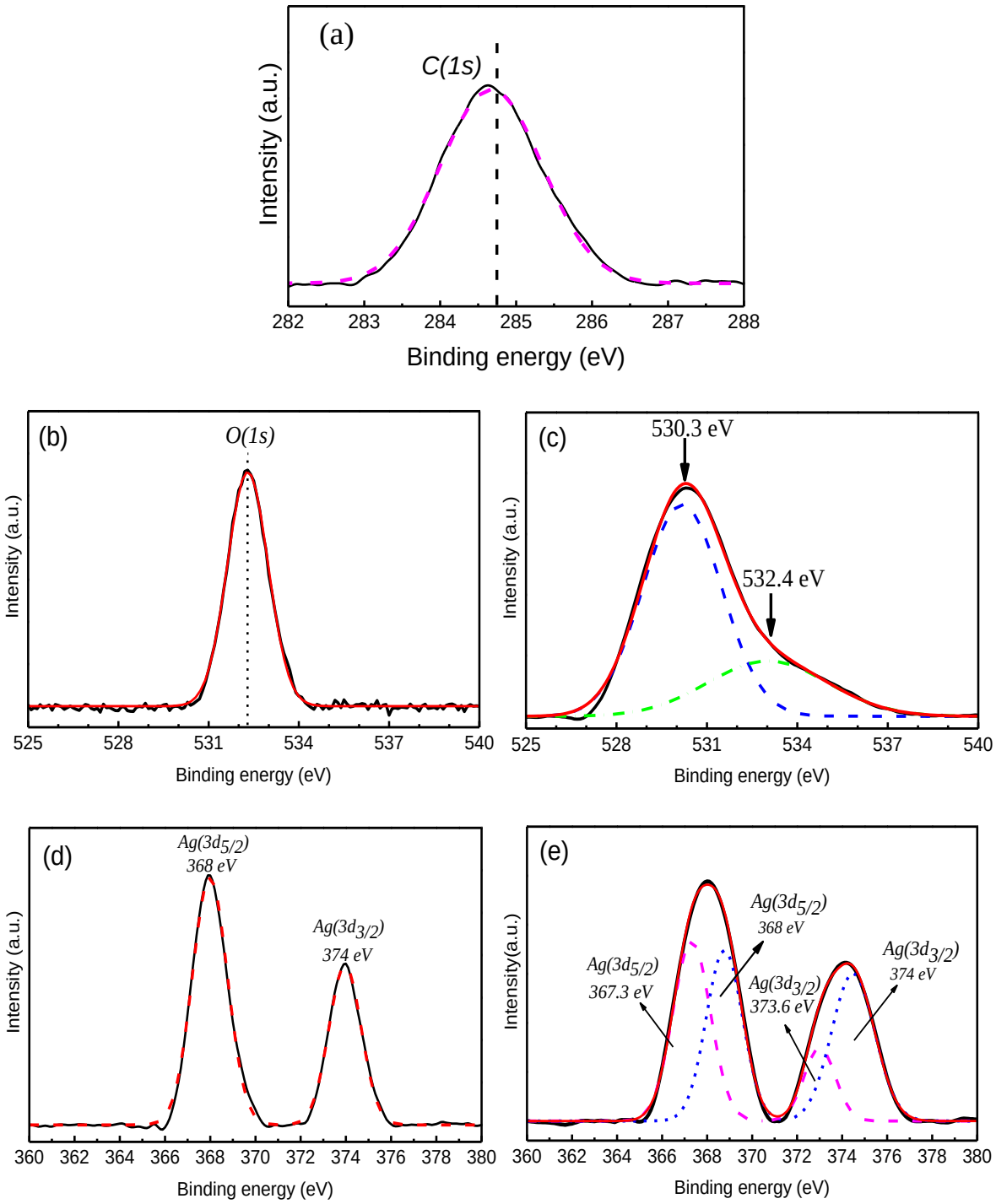

***Figure 5.8**: High resolution XPS spectrum of the C1s feature for films grown using the TBH based process at a) 115 °C and 80 °C. High resolution XPS spectrum of the O1s feature for films grown using the TBH based process at b) 115 °C and c) 80 °C. The solid lines indicate the original XPS data and the dashed curves indicate theoretically fitted curves by assuming Gaussian distribution. High resolution XPS spectrum of the Ag3d peaks for films grown using the TBH based process at d) 115 °C and e) 80 °C. The solid lines indicate the original XPS data and the dashed curves indicate theoretically fitted curves by assuming Gaussian distribution.*

For films growing in the ALD temperature window with TBH, two distinct Gaussian-like XPS peaks are observed at 368 eV ($Ag3d_{5/2}$) and 374 eV ($Ag3d_{3/2}$), which are attributed to Ag^0 species (Figure 3c), consistent with the presence of metallic silver[363,364,365]. At growth temperatures below the ALD window (Figure 3d), the $Ag3d_{5/2}$ peak becomes significantly broader and is best fitted with two Gaussians centred at 367.3 eV and 368 eV. The 367.3 eV peak is attributed to silver in the Ag-O bonding state [366,367] while the 368 eV peak is attributed to metallic silver. The XPS study shows that metallic silver is formed at all temperatures investigated, even down at 80 ^oC. While metallic silver is formed at temperatures below the window minima, the low thermal energy available results in incomplete reactions as already highlighted above. The un-reacted Ag(hfac)* species that remain on the surface at the end of one ALD cycle may act to block the chemisorptions of further Ag(hfac) species during the subsequent cycle, which could explain the observed decrease in growth rate at temperature below 105 ^oC.

5.3. Micro-structural study

The microstructure of the films grown at different substrate temperatures with TBH was studied using XRD. Figure 5.9 (a) illustrates XRD at substrate temperatures between 80 and 150 °C. Peaks at 38.2° are visible for all samples and are consistent with (111) reflection of face centred cubic (fcc) metallic silver (Fm-3m) (JCPDS 04-0783). Samples grown at temperatures between 115 and 150 °C also show (200) reflections at 44.4°. The (111) silver peak is the most intense peak in this range that shows preferential orientation of the Ag grains along the (111) crystallographic direction[368].

Further investigation of the XRD results shows that the increase in temperature has strong impact on the FWHM (Figure 5.9 (b)). By increasing the temperature from 80 to 105 °C, the film thickness increases as it has previously shown in Figure 5.1. When the film thickness increases, the FWHM of the (111) peak is reduced showing that the grain growth has occurred. At ALD temperature window, the FWHM stayed in a constant range, although the temperature increased by 23 °C from 105 to 125 °C. Again by increasing the temperature above the ALD window, a clear decrease occurs in FWHM showing growth in grain size. Figure 5.10 shows that crystallinity in the film is occurred below the ALD temperature window even at 80 °C using TBH, while no XRD peak was observed at the same temperature using propan-1-ol as a co-reactant. Therefore, this could be explained as high reactivity of TBH which requires less energy to react on the surface.

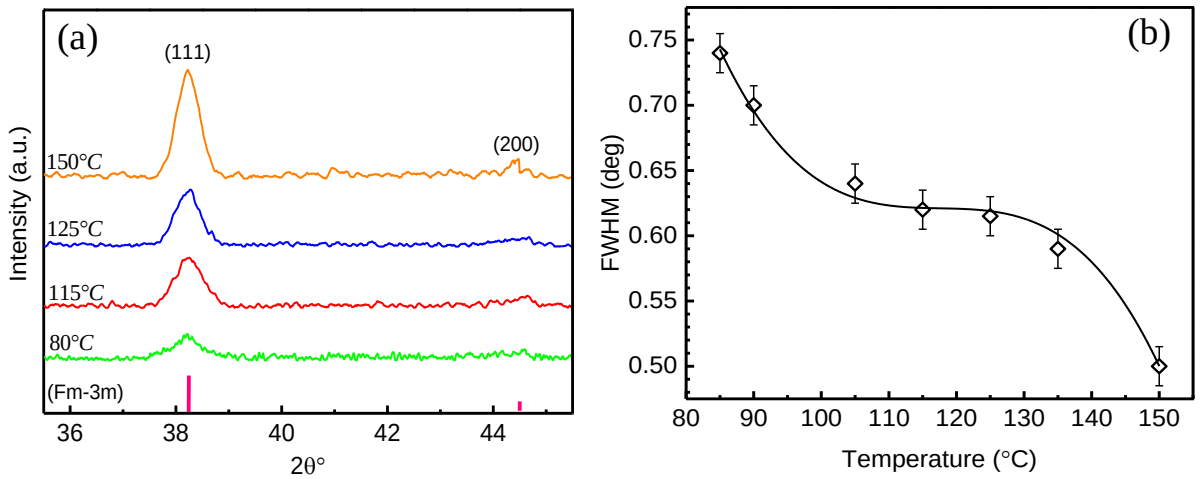

Figure 5.9: *(a) X-ray diffraction patterns of silver coatings on Silicon (100) deposited at various temperatures using 0.2 s doses of TBH with 500 ALD cycles, (b) FWHM calculated based on the temperature variations*

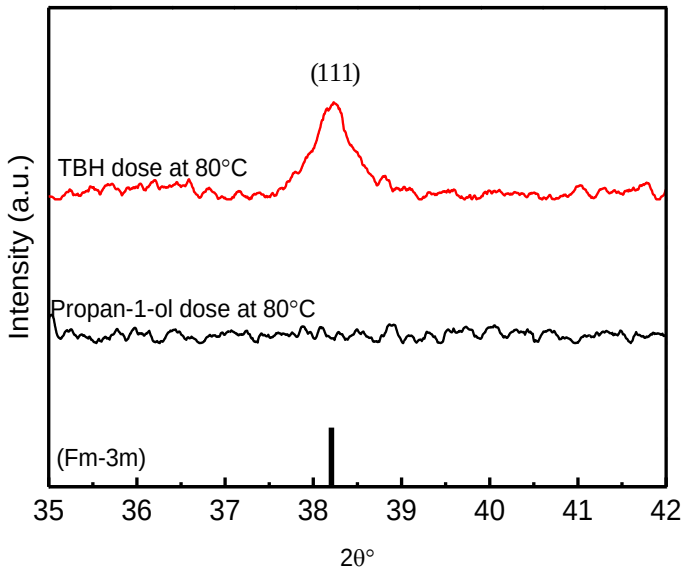

Figure 5.10: *XRD comparison of silver coatings on silicon using either propan-1-ol or TBH at 80 ºC*

To further analysis the microstructures at different growth temperatures, high resolution SEM was used. Figure 5.11 shows a set of SEM images of samples at temperatures between 105 °C and 200 °C for 500 ALD cycles, using 0.2 s of TBH dose as a co-reactant and 4 s of (hfac)Ag(1,5-COD) dose as a precursor. The same surface microstructure is observed for all samples grown within the temperature range of 105 °C and 125 °C (Figure 5.11 (a-c)).

Growth within the ALD window results in narrow distribution of nanoparticle sizes. This indicates that nanoparticles nucleate during the early stages of the process and then grow in a very controlled manner due to the self-limiting nature of the ALD process. This is in line with the XRD results when the FWHM shows a plateau region at this temperature range. Increasing the temperature to 150 °C and 200 °C results in larger grain size with a wide size distribution of nanoparticles with irregular shapes (Figure 5.11 (d-e)).

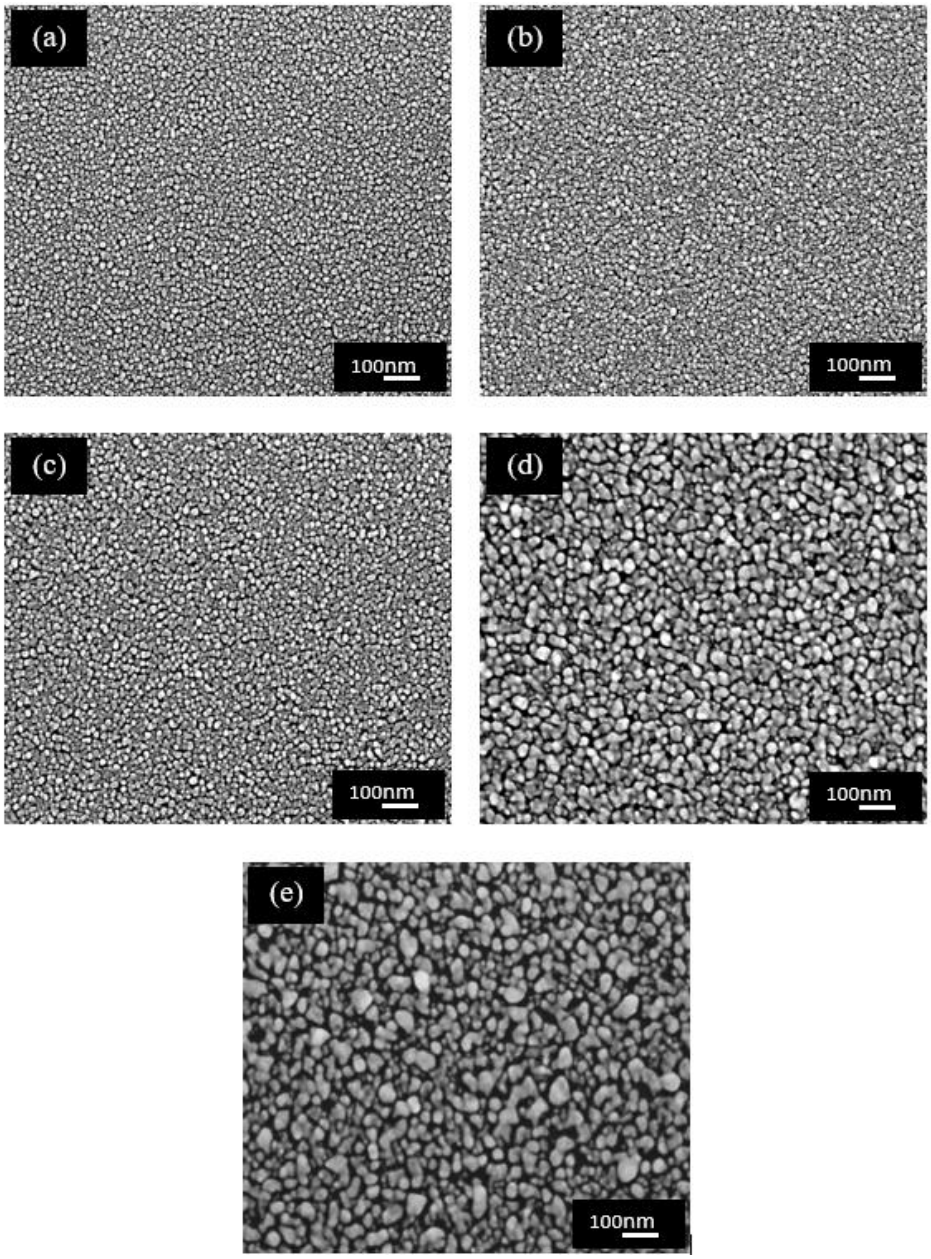

Figure 5.11: *High-resolution SEM images of ALD of silver thin films as a function of temperature, a) 105 °C, b) 115 °C, c) 125 °C, d) 150 °C, e) 200 °C for 500 ALD cycles.*

The choice of co-reactant is found to have a significant effect on the film morphology. Figure 5.12 shows example SEM images of films grown using THB at 115 °C with 500 (Figure 5.12 a), 1000 (Figure 5.12 b) and 1500 (Figure 5.12 c) cycles and also using propan-1-ol at 125 ºC with 500 (Figure 5.12 d), 1000 (Figure 5.12 e) and 1500 (Figure 5.12 f) cycles. Within the ALD window, temperature is found to have negligible effect on film morphology (Figure 5.11), hence the differences in morphology are attributed to the co-reactant itself.

As the growth rates of the two processes are different, it is perhaps best to compare films of comparable mass gains per unit area rather than cycle number. In this way, the best comparisons can be made between 500 cycles with TBH (Figure 5.12 a) and 1000 cycles with propan-1-ol (Figure 5.12 e), or between 1000 cycles with TBH (Figure 5.12 b) and 1500 cycles with propan-1-ol (Figure 5.12 f). As previously shown in chapter 4, the propan-1-ol based ALD process produces highly textured 'nano-particle' films in a Volmer-Weber[369] type growth mode (Figures 5.12 d, e & f). Silver films grown using TBH as a co-reactant (Figures 5.12 a, b & c) are also textured, however, the texturing appears significantly reduced compared to the propan-1-ol films. The TBH films appear to be almost planar, being made up of highly inner-connected platelets with narrow crevices. The growth with TBH is perhaps tending towards a Frank-van der Merwe growth mode[370]. After 1500 cycles the estimated coverage based on SEM image analysis is around 97% using TBH (compared to ~70% using propan-1-ol).

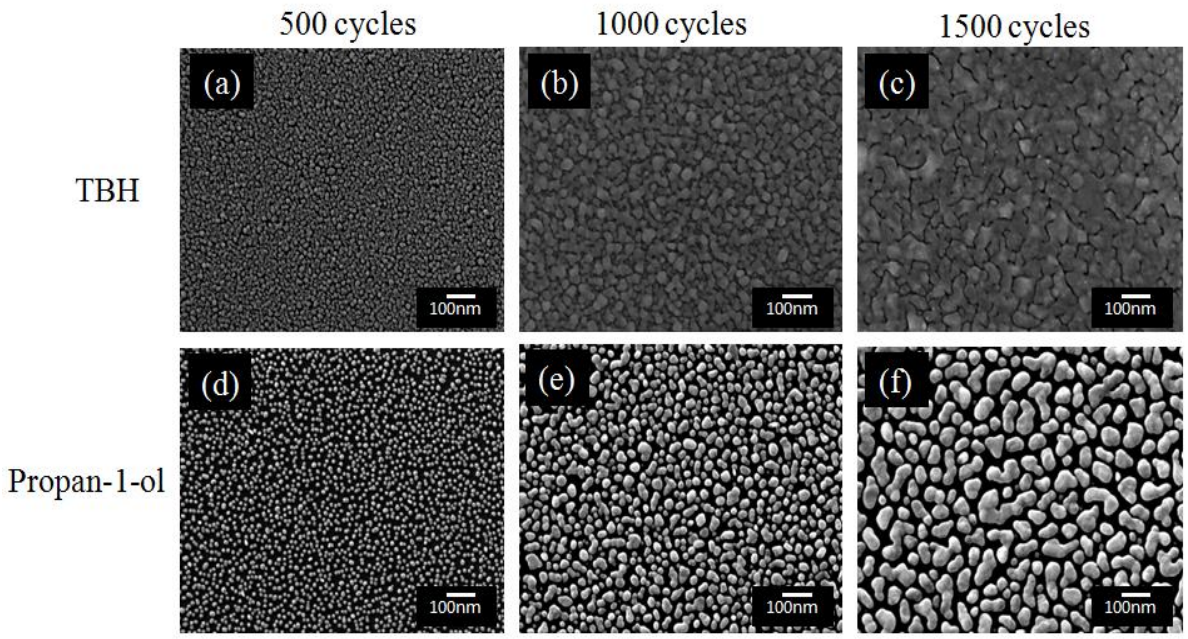

Figure 5.12: *SEM images of the surfaces at different number of ALD cycles with TBH for (a) 500 cycles [11 µg/cm^2], (b)1000 cycles [21 µg/cm^2] and (c) 1500 cycles [30 µg/cm^2], and with propan-1-ol for (d) 500 cycles [8 µg/cm^2], (e) 1000 cycle [13 µg/cm^2] and (f) 1500 cycles [19 µg/cm^2]*

The difference in film morphology achieved using different co-reactants suggests some change in the interaction between the substrate surface and the growing films. A more detailed microstructural study was made to compare the morphology of the silver using propan-1-ol and TBH as shown in TEM micrographs in Figure 5.13. In each case, the silver was deposited on SiN membranes at temperatures within the respective ALD windows for TBH and for the alcohol. The influence of the co-reagent on the growth habit, changes from a more three dimensional particulate morphology using the alcohol, to one that has a more two-dimensional platelet or island-like microstructure using the TBH. The difference in morphologies is attributed to the quite different Ag catalysed reaction for the alcohol, versus the direct surface reaction due to the decomposition of the TBH. The latter enhances surface diffusion so that growth can occur at the edges of the Ag islands, whereas the Ag catalysed propan-1-ol reaction promotes growth at the surface of the silver particles.

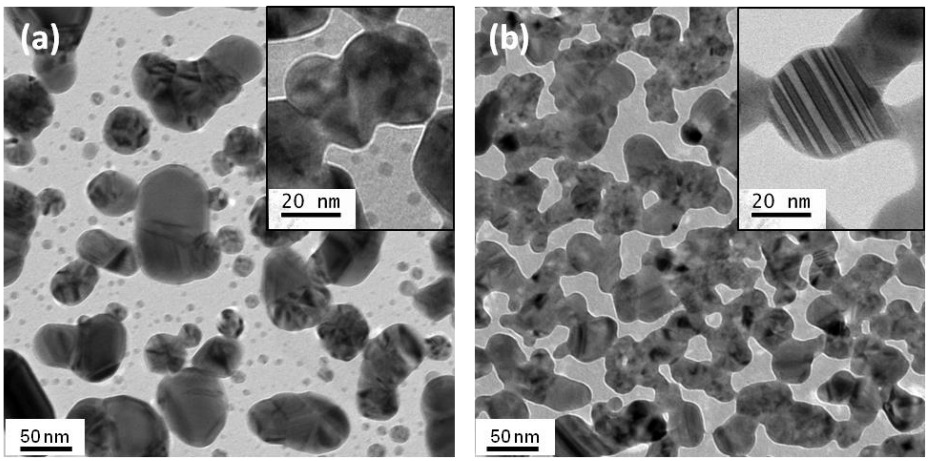

Figure 5.13: *High-resolution TEM images of ALD silver on SiN membranes for (a) propan-1-ol and (b) TBH. Inset shows detail of twinning across an individual Ag island.*

The influence of the TBH reaction with the substrate was investigated further using adhesion tests to evaluate the substrate-film bonding. Films with a nominal thickness of ~12 nm were assessed using SEM image analysis before and after the tape test (Figure 5.14). Films deposited using TBH sustain an average aerial loss of around 5%, while films deposited using propan-1-ol show significantly more damage with a loss of around 40%. While the adhesion strength was not quantitatively evaluate, it is clear that the adhesion of silver is significantly higher for films grown using TBH than propan-1-ol. As the TBH is a powerful reducing agent, it is likely that it has an effect on the substrate surface during the early deposition cycles. We suspect that the TBH helps to remove atmospheric absorbents and other contaminants on the substrate surface akin to the 'self-cleaning' observed with trimethylaluminium (TMA)[371]. The 'cleaned' surface then promotes enhanced wetting and bonding of the silver on the surface, hence producing film like growth and improved adhesion.

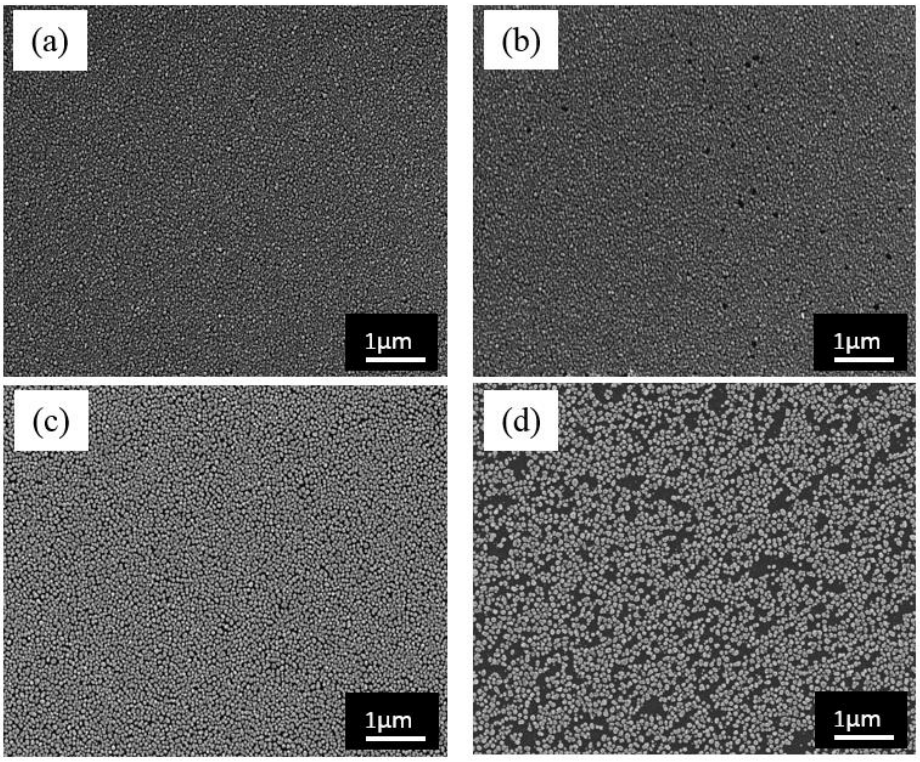

Figure 5.14: *Adhesion tape test results - SEM images of films deposited with either TBH or propan-1-ol before and after the tape test: (a) TBH before, (b) TBH after, (c) propan-1-ol before and (d) propan-1-ol after.*

5.4. Electrical properties

The electrical resistivity of films deposited on glass were investigated using four point probe measurements. Films grown using TBH at 115 ^{o}C were found to be conductive with resistivity decreasing from 0.62 Ω.cm after 500 cycles (~9 nm), to 3×10^{-4} Ω.cm after 1000 cycles (~ 18 nm) and 1×10^{-5} Ω.cm after 1500 cycles (~ 27 nm).

These values are slightly higher than best values reported for silver films grown using PE-ALD, where the lowest value of 6×10^{-6} Ω.cm for 20 nm thick film has been reported. All of the films grown using propan-1-ol were found to be insulating, even after 2000 cycles. This is attributed to the lack of interconnectivity between silver nanoparticles and, for films grown at temperatures below the ALD window, to non-metallic phases within the material.

5.5. Summary of the TBH growth study

For the first time, we have extended the ALD temperature window of silver using tertiary butyl hydrazine as a co-reactant by thermal ALD. In this study, silver films have been deposited using direct liquid injection thermal ALD with ((hexafluoroacetylacetonato)silver(I)(1,5-cyclooctadiene)) as the metal source. The ALD process has been compared and contrasted by using propan-1-ol as a co-reactant with the ALD process using tertiary butyl hydrazine as a co-reactant. A narrow ALD temperature window between 123 and 128 °C is identified for the propan-1-ol process with a nominal mass deposition rate of ~17.5 ng/cm^2/cycle. A significantly wider temperature window between 105 and 128 °C (23 °C) is identified for the hydrazine based process with a nominal mass deposition rate of ~ 20.2 ng/cm^2/cycle (a nominal growth rate of 0.18 Å/cycle). The hydrazine based process produces less textured more film like coatings and are found to shown better surface adhesion with scotch tape test compared with propan-1-ol and measurable resistivity is achieved.

Chapter 6

Titanium implants coated with a nano-layer of silver ALD for antimicrobial study

6.1. Introduction

This chapter focuses on the exploration of ALD silver on titanium and its potential application as an antimicrobial coating on complex three dimensional titanium structures developed using the selective laser melting (SLM). Titanium has been examined as a substrate and a detail investigation has been done on different conditions and morphology of silver growth on titanium. The reason of coating the 3D implant structure with silver ALD was in order to investigate the anti-microbial effects of silver ALD for both *in vivo* and *in vitro* studies. Metallic silver has been deposited using propan-1-ol as a co-reactant.

The focus is given to the film growth on titanium flat substrates and titanium three dimensional structures, how titanium can influence surface morphology, microstructure and chemical composition of the film and how it is different from silicon substrates for the same number of cycles (details in chapter 4 for silicon). Microstructure plays a central role in the anti-microbial studies for both *in vivo* and *in vitro* tests. To investigate the influence of the titanium surface on the size and density of nanoparticles, high resolution SEM, AFM and XRD were used to study different growth conditions.

In addition, detail studies have been done to determine the coating conformality within 3D SLM structures. This is the first study of the antimicrobial effect of ALD silver nanoparticles thin films. Stable and highly reproducible morphology on titanium SLM structures was achieved in this study. The microbicidal study was carried out by the Ulster group in the presence of Staphylococcus epidermidis (ATCC 35983 Methicillin Resistant), which is one of the most common causing bacteria associated with bio-medical implants. The compatibility of this silver coated modified surface was elucidated with cell adhesion. Also, *in* vivo integration of these metallic silver coated surfaces into bone defects were investigated.

6.2. Nucleation and growth on titanium substrates

6.2.1. Growth characteristics

The effect of temperature on the ALD growth rate was investigated using flat titanium substrates. Detail studies were carried out for the precursor only test and precursor with co-reactant test using 4 s doses of silver followed by 4 s purge and 4 s propan-1-ol doses followed by 4 s purges respectively between 123 and 130 °C. Figure 6.1 shows the mass gain per square centimetre per cycle.

In the absence of the co-reactant, the mass gain remains almost zero between 123 and 128 °C and rises rapidly as the temperature is increased to 130 °C, a mass deposition of ~29 ng/cm^2 cycle is achieved at 130 °C which is consistence with the study reported in chapter 4 on silicon substrate. This increase is attributed to thermal decomposition of the silver precursor. By adding the propan-1-ol as a co-reactant into the process, an increase in mass deposition is achieved between 123 and 130 °C. A nominal deposition rate of 29.6 ng/cm^2 per cycle between 123 and 128 °C is observed on titanium which is almost double the rate observed on silicon for similar condition (Figure 6.1). If the film is initially taken to be planar and a bulk density of silver (10.49 g/cm^3) is used, then a nominal film thickness of ~13 nm is obtained using 500 ALD cycles corresponding to a nominal growth rate of 0.26 Å/cycle.

It appears that silver grows faster on titanium compared with silicon (Figure 6.1). The substrate can have a critical influence on the nucleation behaviour of the film[372]. It is well known that the substrate surface properties (such as crystallinity, morphology and chemical nature of the substrate, whether it is –OH terminated or H-terminated) can play important roles on the nucleation and the microstructure of the film particularly during the initial stages of ALD deposition[373].

For instance, in 1936, Wenzel declared that increasing the surface roughness can lead to improvement of the surface wet-ability due to the chemistry of the surface[374]. Therefore, one explanation for the higher mass deposition on titanium could be the difference in surface morphology of the titanium compared with silicon and this will be discussed in more details in section 6.2.2. Another explanation may be the enhancement of the ALD growth on a metallic surface compared with semiconductor or insulator substrates[375]. This can be attributed to the electron donation from the metallic film to the chemically adsorbed precursor molecules which leads to improving the dissociation of ligands from the adsorbed precursor molecules[375]. In ALD process, the effective dissociation of ligands throughout the chemical adsorption of precursors can contribute to efficient film growth because of a reduction in steric hindrance effect[376].

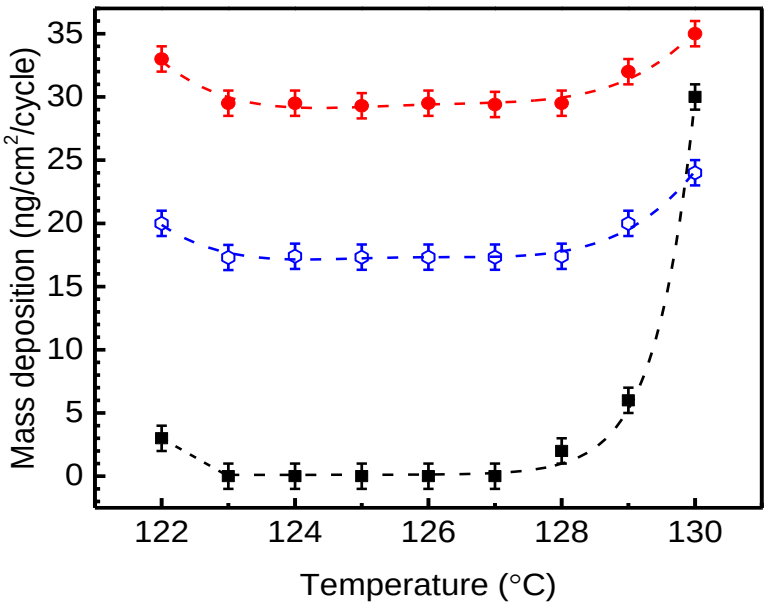

Figure 6.1: *Mass deposition as a function of substrate temperatures using 4 s doses of Ag (hfac) COD with detailed view of no co-reactant (black squares) and 4 s propan-1-ol doses as a co-reactant (red circles) per cycle on titanium foil and per cycle on silicon substrate (blue circle)*

Figure 6.2 shows a comparison on the mass deposition rate as a function of total number of growth cycles at 125 °C with saturative doses on flat titanium (black squares) and on silicon (red circles). As with other ALD process, under self-limiting conditions, a linear increase in film mass was observed on titanium with the number of ALD cycles. On silicon the initial rate of increase in mass with ALD cycles is considerably lower. However, the growth rate on silicon beyond 1500 cycles is similar to that for the titanium. It is clear that growth on silicon is affected by a 'nucleation delay' while little or no such delay is observed for growth on titanium. The growth of silver becomes independent of substrate type after 1500 cycles show that the growth is controlled by chemistry once the substrates are covered with silver. Hence, the starting surface, changes the entire deposition time until the surface is completely covered and the growth of bulk film starts. The effect of starting surface in ALD growth processes has been shown in other studies as well[377].

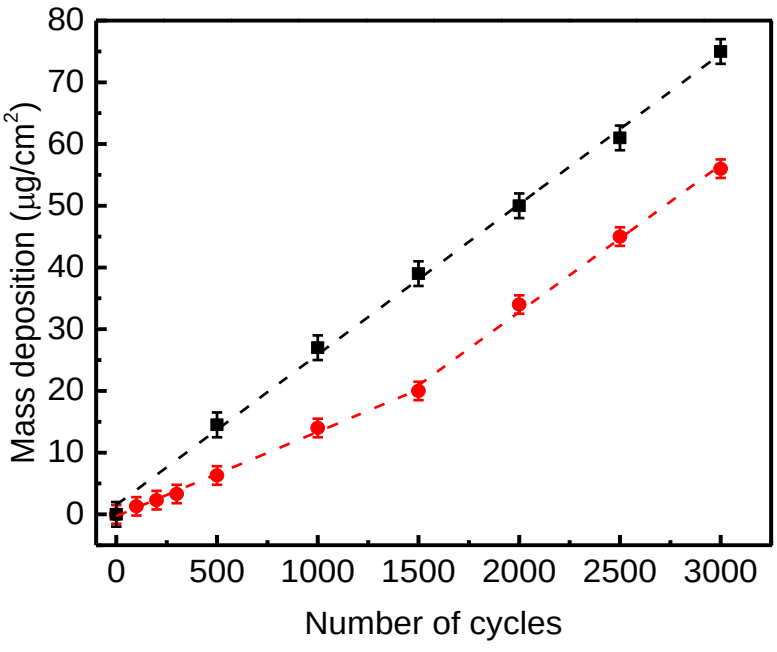

Figure 6.2: *Mass deposition per unit area as a function of ALD cycles at 125 °C on flat titanium foil (black squares) and silicon (red circles)*

To investigate the self-limiting and saturative surface reactions of Ag (hfac) COD on titanium a precursor saturation study was carried out at 125 °C. In order to do the precursor test, the co-reactant dose was fixed at four seconds, the purge times were fixed at four seconds and the cycle was repeated 500 times for each deposition run. As can be seen from Figure 6.3, the deposition initially increases with the precursor dose, however at around two seconds the deposition rate saturates at around 29.5 ng/cm^2 cycle. Therefore, the saturative behaviour of the Ag hfac COD was achieved on titanium substrate as well as silicon substrate and indicates that the ALD process is controlled by self-limiting surface reactions on both substrates.

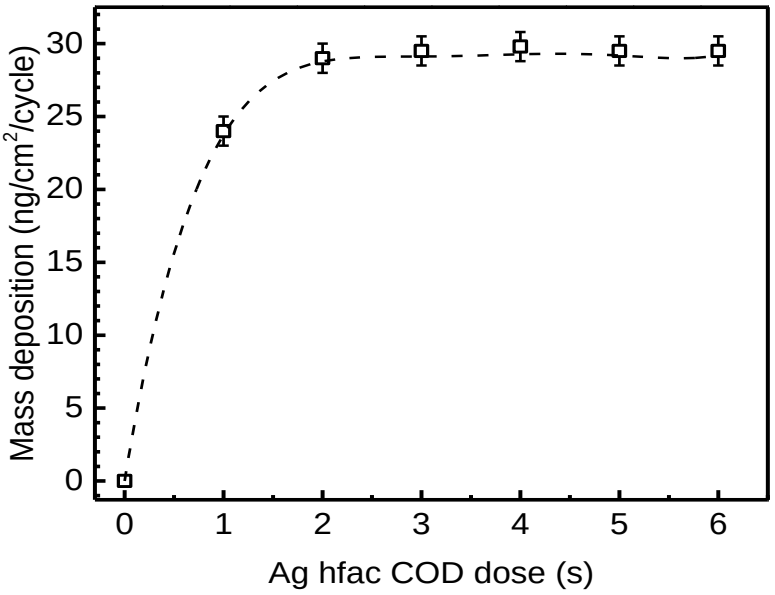

Figure 6.3: *Mass deposition as a function of Ag (hfac) COD at 125 °C for 500 ALD cycles on titanium substrates*

Under the self-limiting condition, the consistency of mass deposition on titanium was examined along the 130 mm length of the deposition zone in the reactor chamber where all parameters kept constants. Similar mass deposition occurs on titanium flat substrate between the front, centre and rear of the deposition stage (Figure 6.4) which shows that there are enough precursor throughout the reactor to saturate all surfaces.

Therefore, it is clear that self-limiting growth can be achieved throughout the reactor stage from the front edge to the end edge with Ag (hfac) COD under self-limiting condition on titanium flat substrate.

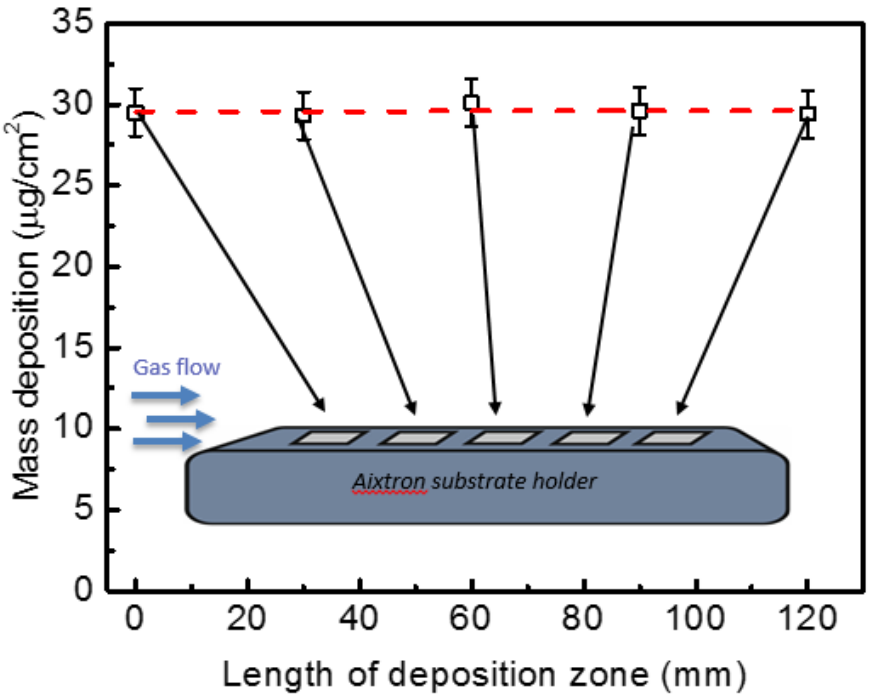

Figure 6.4: *Mass deposition along the 130 mm length deposition zone at 125 °C for 500 cycles on titanium substrates*

6.2.2. Micro-structural characterization of the ALD process

With the purpose of exploring the surface roughness of the titanium compared with the silicon, AFM studies together with SEM analysis were carried out on several uncoated substrates. Each sample was analysed by randomly sampling at least three areas to ensure that the resulting data was representative of the whole. Also, ScanAsyst mode was used for all measurements with a very low noise threshold (0.1 nm) to make sure that obtained features are the actual surface topography. Figure 6.5 shows the detailed scans (10 µm^2 and 5 µm^2) of a typical uncoated silicon and titanium substrate.

The NanoScope Analysis software was utilized to assess the root mean square (RMS) values on both titanium and silicon substrates. The RMS values were found to be 0.26 nm and 3.23 nm on silicon and titanium respectively for the scan area of 1 μm^2.

Figure 6.5 (b-d) shows the silicon surface with negligible surface features other than some vibrations during the measurement, whereas Figure 6.5 (f-h) shows titanium surface with significant valleys, features and randomly oriented ripples which are attributed to the surface fluctuation and topography and distributed across the surface. In addition to the AFM results, SEM investigations of the samples also reveal that no significant feature is observable on silicon (Figure 6.5 (a)) whereas, titanium shows visibly rougher surface with clear features (Figure 6.5 (e)).

Therefore, in addition to the substrate type effect on the growth, the larger surface roughness of the titanium substrate compared with the silicon may also have some effect in enhancing the growth of silver nanoparticles and change the initial surface nucleation on the titanium surface.

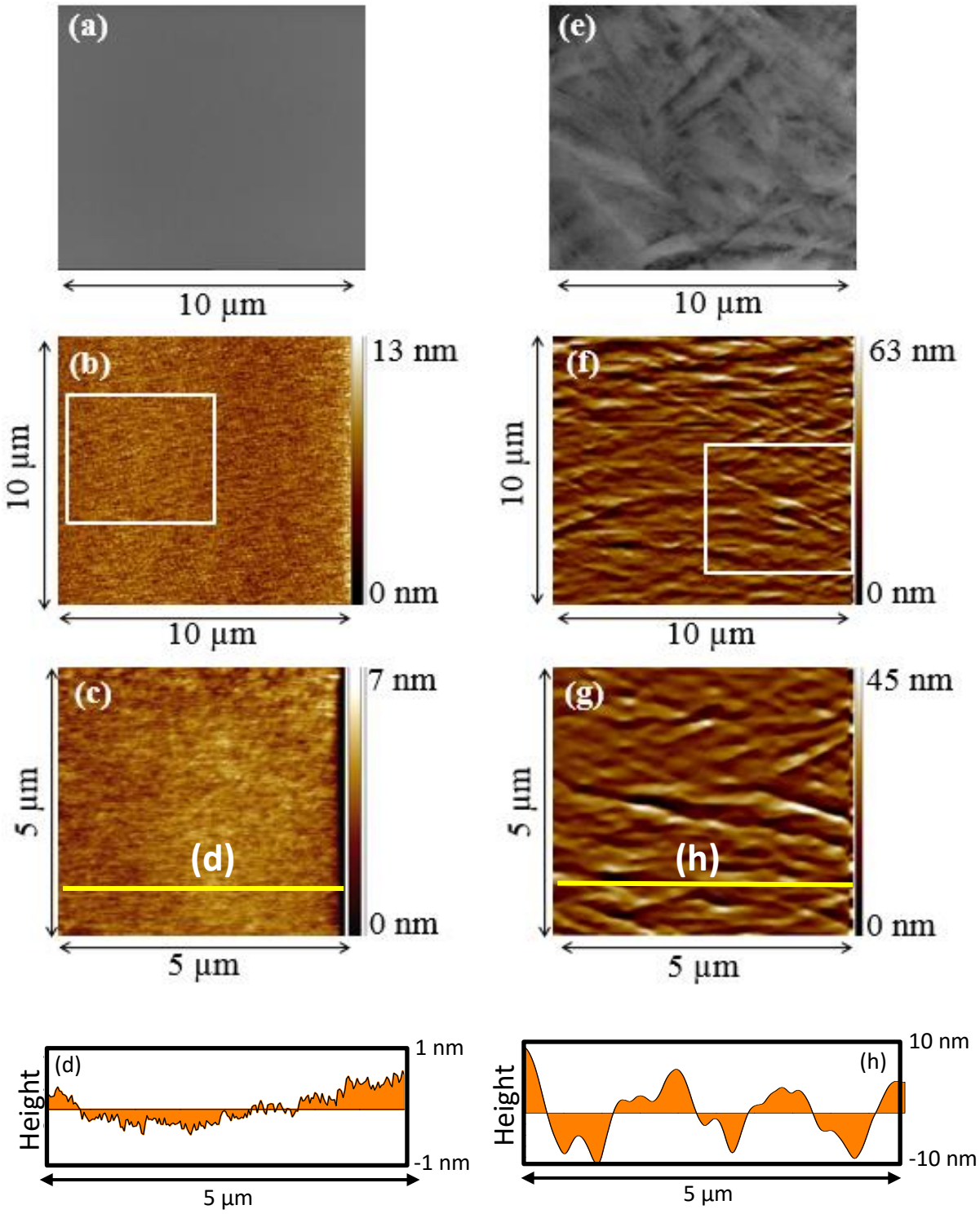

Figure 6.5: *SEM images of uncoated a) silicon and e) titanium. AFM images of uncoated b-d) silicon substrate and f-h) titanium substrate. The yellow line indicates the height changes of the surface map.*

In order to compare and contrast the microstructure of the deposited films on both substrates, AFM and SEM studies were carried out on the coated samples. Figure 6.6 indicates two dimensional and three dimensional AFM images on flat titanium and silicon substrates coated with silver at 125 °C for 500 ALD cycles. Both substrates were sampled at least four times over other scan windows and similar surface features, RMS values and comparable results were obtained which indicate that ALD silver films are conformal on both titanium and silicon substrates[378].

Figure 6.6 (a) and (e) show AFM together with SEM on silicon substrate, whereas Figure 6.6 (b) and (f) shows AFM together with SEM on titanium surface for 500 ALD cycles respectively. Islands can be observed on both substrates, which shows that silver grows in 'Volmer Weber' mode irrespective of any differences that titanium and silicon substrate can cause on the growth behavior. The AFM analysis together with SEM analysis reveal that the size and shape of the nanoparticles are different on titanium for the same number of ALD cycles compared with silicon. The average particle size distribution on the titanium is ~ 48 nm at 500 cycles, whereas the average particle size on the silicon is ~ 25 nm for the same number of cycles. This indicates that wetting and coalescence of silver nanoparticles are faster on titanium surface and lead to increase the nanoparticles size to almost twice as the nanoparticles size on the silicon for the same growth condition. This is in a good agreement with results obtained from the study of silver films grown by PEALD on different substrates[28]. This microstructural study also is in a good correlation with the higher mass deposition achieved on titanium (see Figure 6.1).

If the metal wets the oxide substrate, the $\gamma_{m/ox}$ is equal to $\gamma_{v/ox} - \gamma_{v/m}$ at equilibrium; where $\gamma_{m/ox}$ is the metal/oxide interfacial free energy, $\gamma_{v/ox}$ is the surface free energy of the clean oxide in vacuum, $\gamma_{v/m}$ is the surface free energy of the clean metal in vacuum. In this situation, a continuous metal film is formed[379].

If, on the other hand, the $\gamma_{m/ox}$ is greater than $\gamma_{v/ox} - \gamma_{v/m}$ then the metal cannot wet the oxide/vacuum interface and hence, particles are formed rather than a continuous film[380]. Hence, according to these equations, the nucleation of silver on titanium substrate with a thin naturally protective oxide layer is very difficult and results in nucleation as silver nanoparticles[379,381]. This is linked with the higher surface energy of the silver film relative to the titanium oxide substrate which resulted in forming nanoparticles to decrease the system energy.

The lack of the appropriate surface species in order to react with the metal ALD precursors is additional challenge for achieving nucleation on oxide substrates and accordingly, many ALD cycles are usually needed to detect any metal deposition on oxide substrate[381]. Also, the existing ligands in the metal precursor can bind to the oxide substrate and cause blocking the adsorption sites[382]. Therefore, this can explain the low number of publications on ALD deposition of continues thin metal films on oxide substrates[383,381].

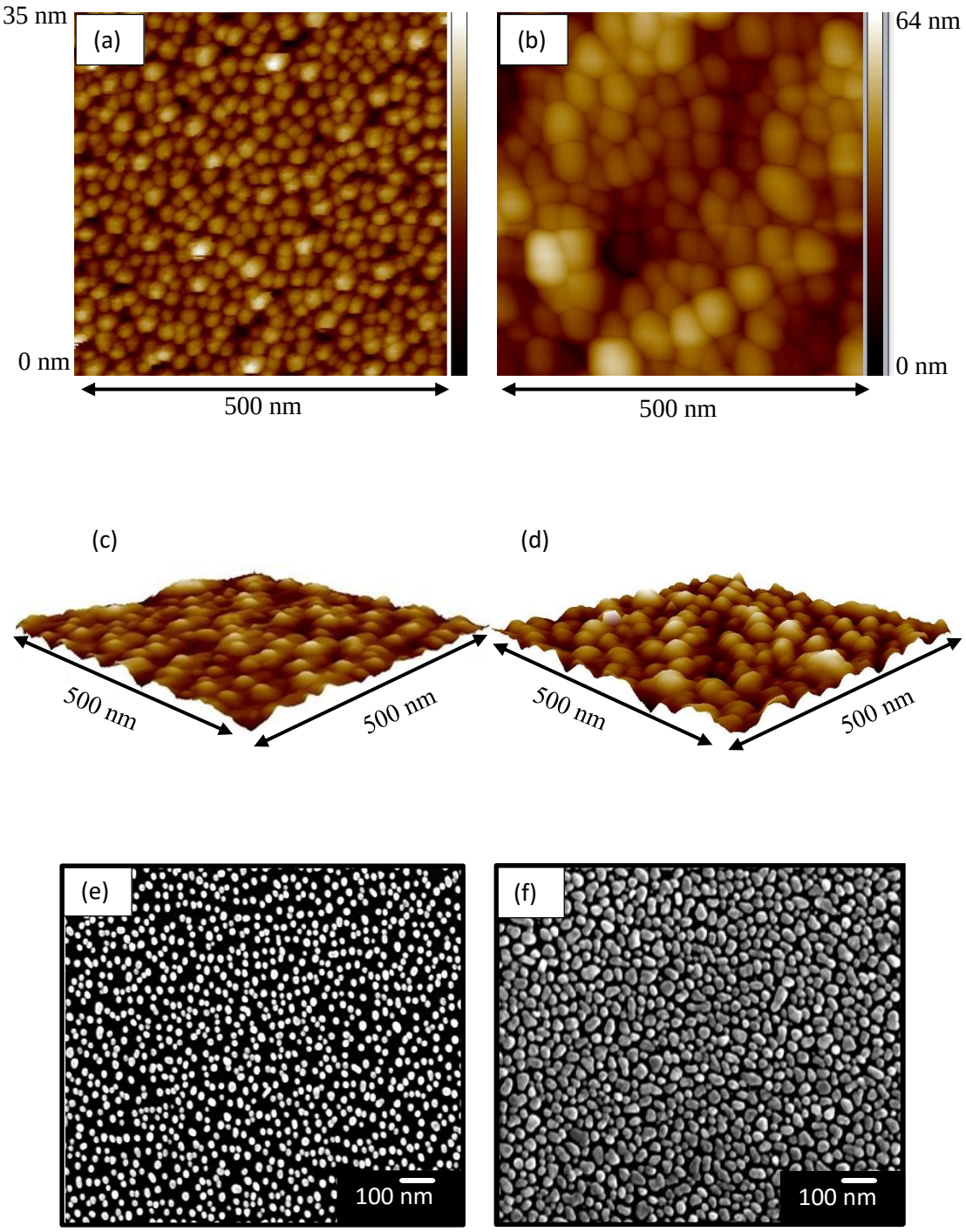

Figure 6.6: *High-resolution AFM and SEM images of ALD coated of silver nanoparticles on silicon substrate [(a), (c), (e)] and on titanium substrate [(b), (d), (f)] at 125 °C for 500 ALD cycles.*

To investigate the height and size distribution of silver nanoparticles on both substrates, AFM together with SEM were used respectively. The dispersion of silver nanoparticles height by AFM on silicon substrates reveals a relatively narrow Gaussian size distribution for 500 ALD cycles with an average height size of ~ 12.32 nm (Figure 6.7 (a)). Figure 6.7 (b) also shows that nanoparticles diameters achieved via SEM on the same sample follow a narrow Gaussian trend with controlled quasi-3D symmetrical growth with an average particle size of ~ 25 nm and a standard deviation of 2.1 nm, which is in relation to the AFM height data as the particle diameter obtained via SEM is approximately doubled the mean height of the particle obtained via AFM. This shows that the formation of homogenous hemispherical shapes nanoparticles was achieved on the silicon substrate for 500 cycles.

On the other hand, the dispersion of height distribution on titanium coated substrates by AFM shows wider range distribution and the density of the particles reduces for 500 ALD cycles with an average height size of ~ 27.69 nm (Figure 6.7 (c)). Also, the histogram of SEM image in Figure 6.7 (d) for the same sample demonstrates that silver nanoparticles follow a wider range of diameter size distributions which tend to be non-symmetrical and vary in size between ~ 40 nm and ~ 60 nm with an average particle size of ~ 48.3 nm and a standard deviation of 5.7 nm. Therefore, the formation of heterogeneous nanoparticles was obtained on titanium substrate including random shapes nanoparticles and spherical nanoparticles for the same number of cycles due to the faster growth on titanium substrates.

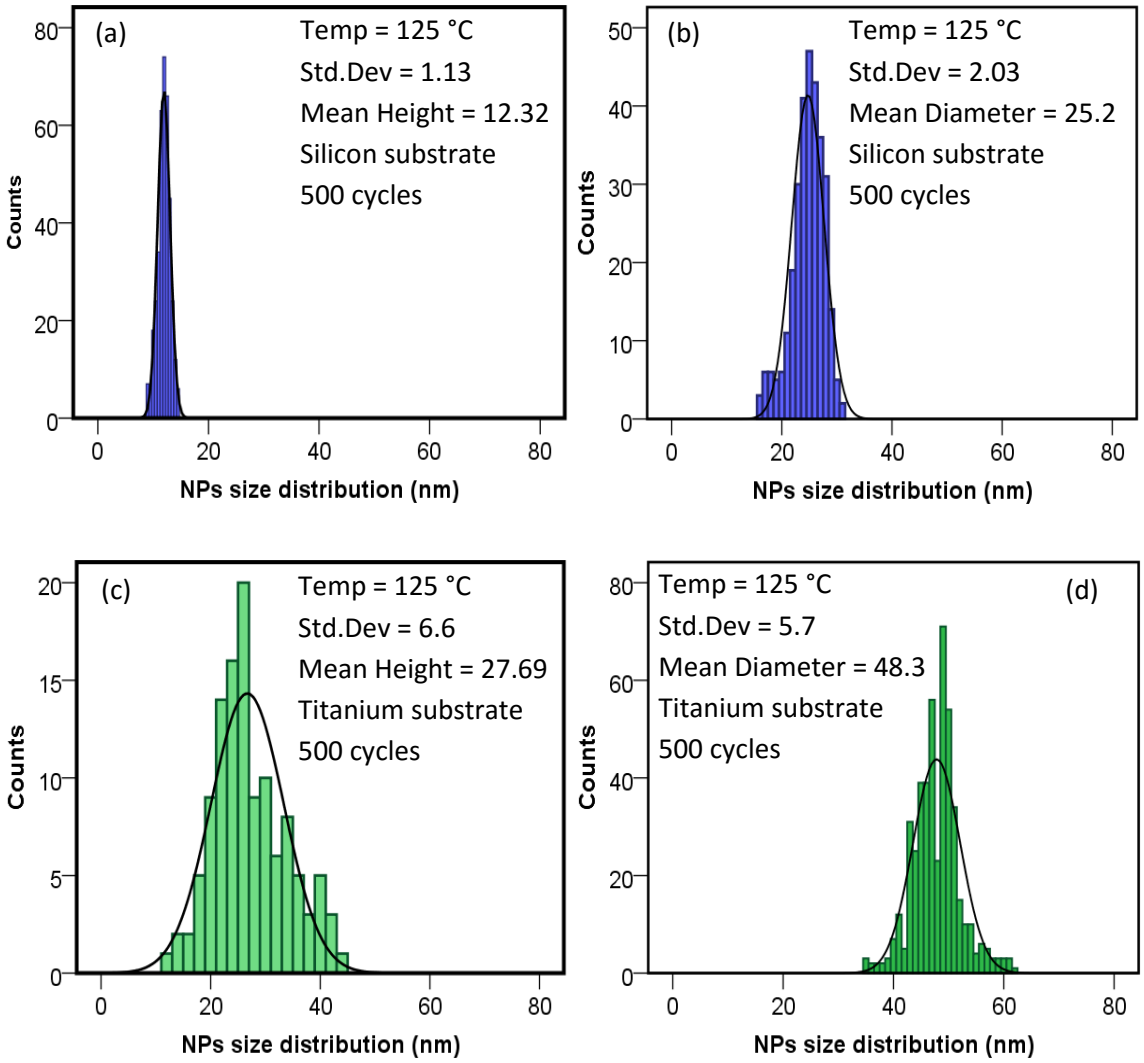

Figure 6.7: *Dispersion of silver nanoparticle height and radius by AFM and SEM respectively grown on a-b) silicon substrate, c-d) titanium substrate for 500 cycles*

To do the further investigation on the effect of increasing the number of ALD cycles on the growth of silver nanoparticles on silicon and titanium, SEM was carried out on films deposited for 1500 ALD cycles (Figure 6.8). The average particle size is 117.6 nm with a standard deviation of 13.5 nm on silicon (Figure 6.8 (a)) whereas on titanium, large island size and interconnected nanoparticles start growing to form a film (Figure 6.8 (b)). Therefore, the SEM analysis is in a good agreement with mass deposition data (Figure 6.2) where the total mass depositions achieved on titanium was more than the deposited mass on silicon 1500 ALD cycles.

As nanoparticles grow with increasing numbers of ALD cycles, individual nanoparticles begin to merge together to form irregular nano-structures, via a process of Ostwald ripening on both substrates. Therefore, the surface coverage of both titanium and silicon will reach to the point that is fully covered by silver thin layer and hence the effect of the surface itself on the growth will be eliminated.

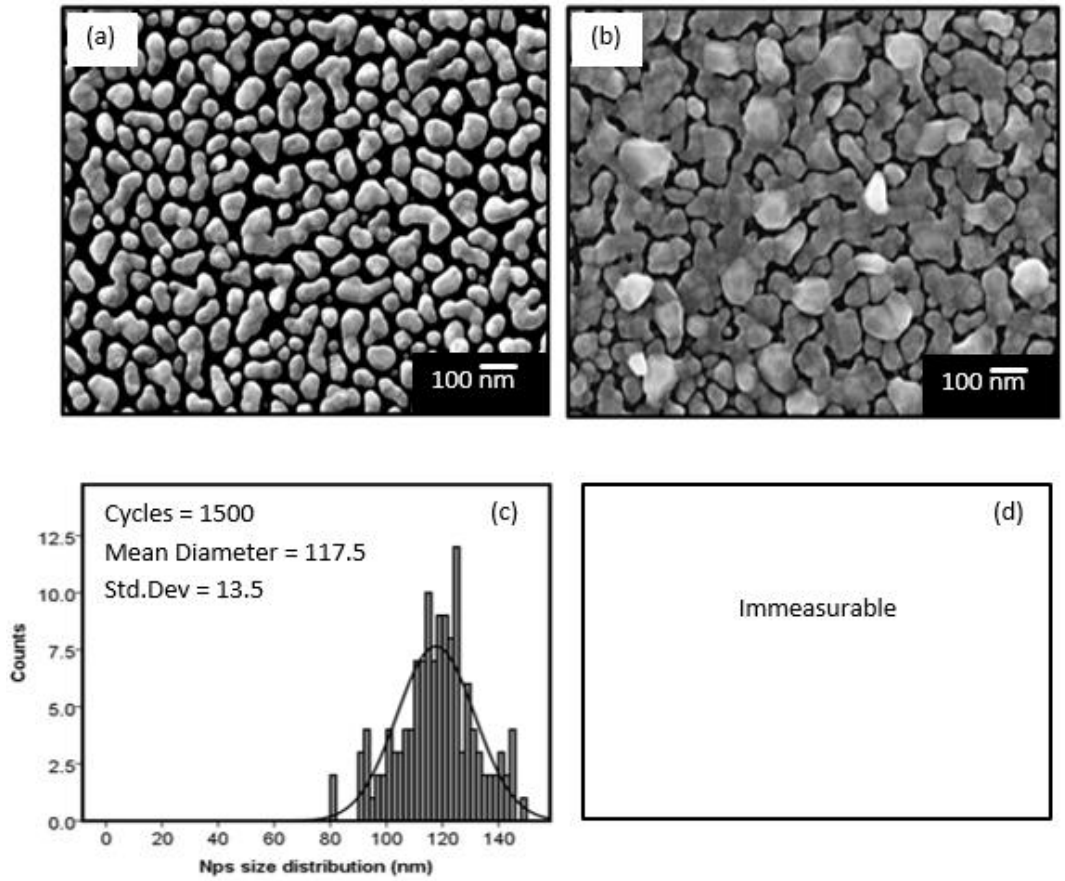

Figure 6.8: *High-resolution SEM images of ALD of silver nanoparticles for 1500 ALD cycles on a) silicon substrate, b) on titanium substrate, c) & d) the size distribution histograms*

6.3. Chemical composition of the silver NPs

6.3.1. XPS spectra on titanium flat substrate

As described in chapter 3, achieving accurate quantitative composition analysis of non-ideal surface topography (such as differences in Ag NPs size) and rough surface films (like the current study) is not possible due to photoelectron scattering effects. The surface roughness influences the number of electron signals and thus produces systematic errors and artifacts in quantitative analysis by assuming the surface an ideally flat substrate[384, 385] . Because of having silver nanoparticles film rather than having an ideal flat silver film in this study, obtaining an accurate composition map was difficult. However, these errors only influence the XPS peak intensities, rather than binding energy (BE)[386]. Therefore, XPS can be used to prove the existence of silver and any other elements from the precursor in this study. XPS information can provide only the surface property and not the bulk property, as the information on the depth of photoelectrons on only about 10 nm is achievable[387].

Figure 6.9 shows a full survey scans (200-700 eV) alongside high resolution scans of the Ag peak from islands deposited by ALD on Si (100) and titanium substrate at 125 °C with the same nominal thickness of 10 nm. The XPS of the silver on silicon substrate is in close agreement with the titanium substrate and in both spectra the main core-level peaks are related to Ag (3d), C (1s) and O (1s). Energy shifts produced by chemical bonding can have an effect on the peak positions and hence supply valuable information on bonding conditions. Peaks at binding energies of 368.0 and 374.0 eV are resolved, which correspond to the two spin-orbit components, $Ag3d_{5/2}$ and $Ag3d_{3/2}$ respectively with a spin orbit splitting of 6.0 eV on titanium substrate (Figure 6.10). These closely match the Ag3d features for the bulk silver reference sample and are attributed to metallic silver[340].

Compared with other noble metals, silver core levels show a shift to lower binding energies as its oxidases. Therefore, these silver peaks with reasonably high binding energies show pure silver peak rather than silver oxides[388, 389]. No extra peaks were observed above 374 eV, which clearly confirmed the absence of an oxidized form of silver[390] (Figure 6.10). Besides, XRD was taken in conjunction with the XPS data in further approval of existing of metallic silver[340] at 125 ºC and will be shown in the following section (Figure 6.12).

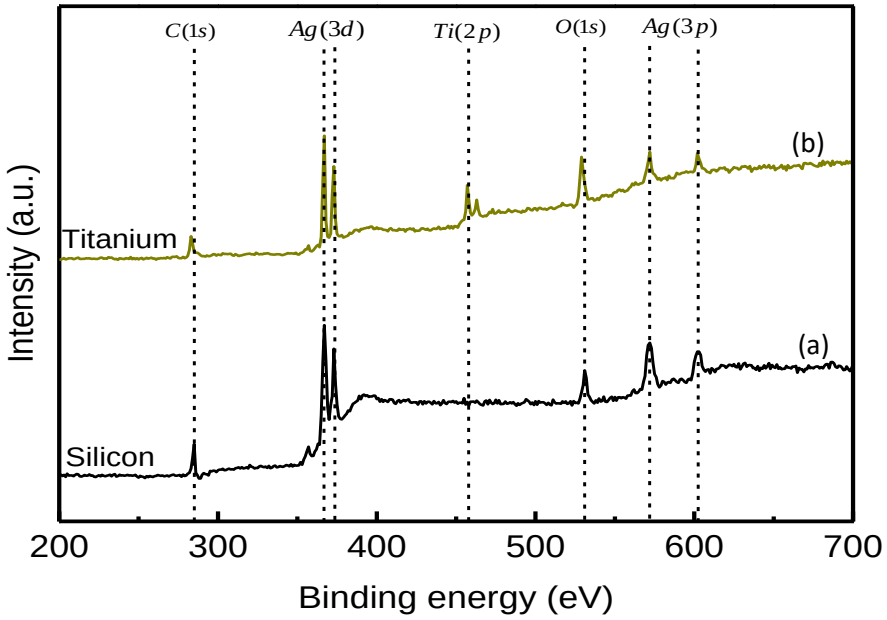

Figure 6.9: *XPS spectrum of a) Ag films deposited by ALD on silicon and b) Ag films deposited by ALD on titanium at 125 °C for the nominal thickness of 10 nm*

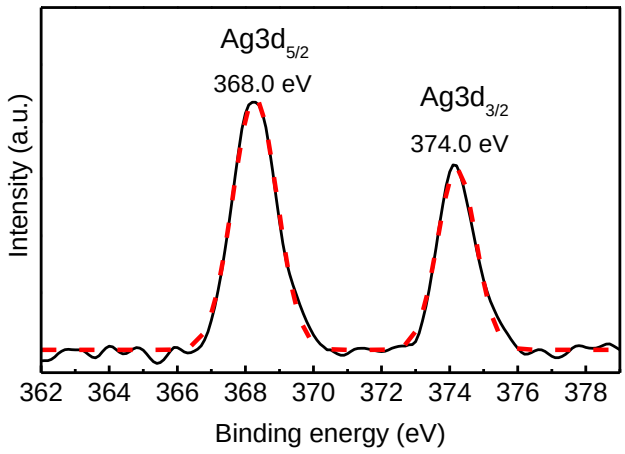

Figure 6.10: *High resolution Ag3d XPS spectrum of silver on titanium. The thin solid lines indicate the original data of XPS and the dashed curves indicate theoretically fitted curves by assuming Gaussian distribution.*

Figure 6.11 shows the region covering the carbon binding energy for the C1s peaks for both the ALD films on silicon and titanium substrates. The dotted line on Figure 6.11 (a) and (b) shows single Gaussian peak at 284.8 eV with no shoulder which is associated with C-C or C-H bonds and is attributed to surface contamination rather than bulk incorporation[391] which is inherently exist in all samples that have been exposed to air. The carbon peak was used to calibrate any energy shifts by the sample's surface induced by surface charging.

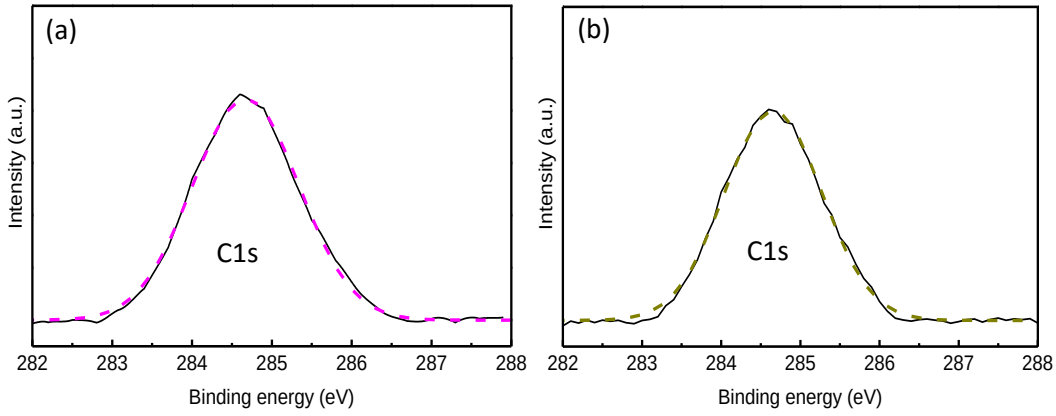

Figure 6.11: *High resolution of XPS of C1s peaks on a) silicon and b) titanium substrates at 284.8 eV*

Because of high intensity (002) plane of titanium substrate related diffraction peak at 38.5º, which particularly obscures the (111) silver peak at 38.2º, the peak at 44.4º was used to investigate the existence of metallic silver on titanium. As it is clear from Figure 6.12, at 125 °C, the peak is observed on titanium at 44.4° which is in agreement with (200) reflection of face centred cubic (fcc) metallic silver (Fm-3m) (JCPDS 04-0783). This is also in a good agreement with metallic silver shown by XPS at 125 °C (Figure 6.10).

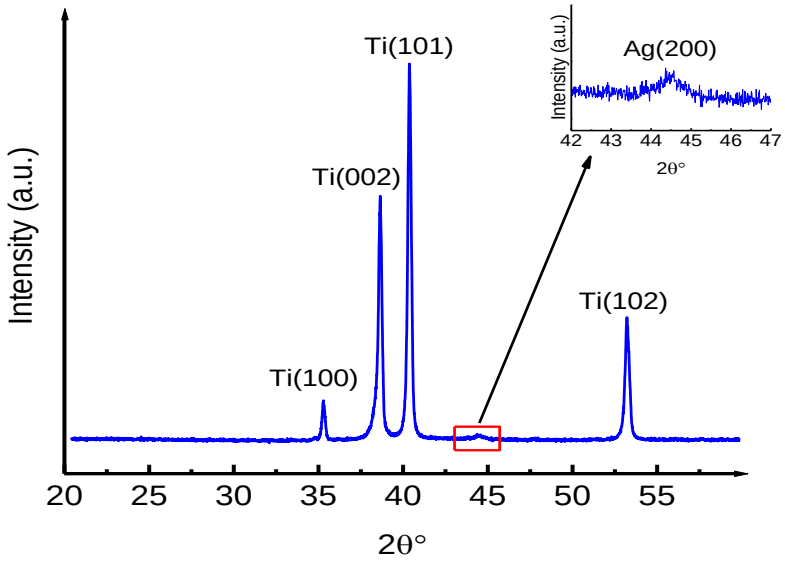

Figure 6.12: *X-ray diffraction pattern of silver on titanium at 125 ºC*

6.4. Microstructure study on bone-like SLM structures

6.4.1. SEM study of Ag NPs on the foam structures

This section investigates the microstructure of the coatings on SLM cylindrical implants structures. High resolution SEM images were taken from the samples before and after ALD coatings of silver. Figure 6.13 illustrates some high resolution SEM images on titanium porous structures before and after ALD under saturative growth conditions using 100 cycles. High resolution images on non-coated SLM structures (Figure 6.13 (a – b)) show featureless titanium surfaces even at highest magnification (50 nm scale bar). Figure 6.13 (c – d) on the other hand, shows high resolution SEM images taken from coated SLM structures where silver nanoparticles at the highest resolution (50 nm scale bar) on 3D SLM structures are observable with no agglomeration.

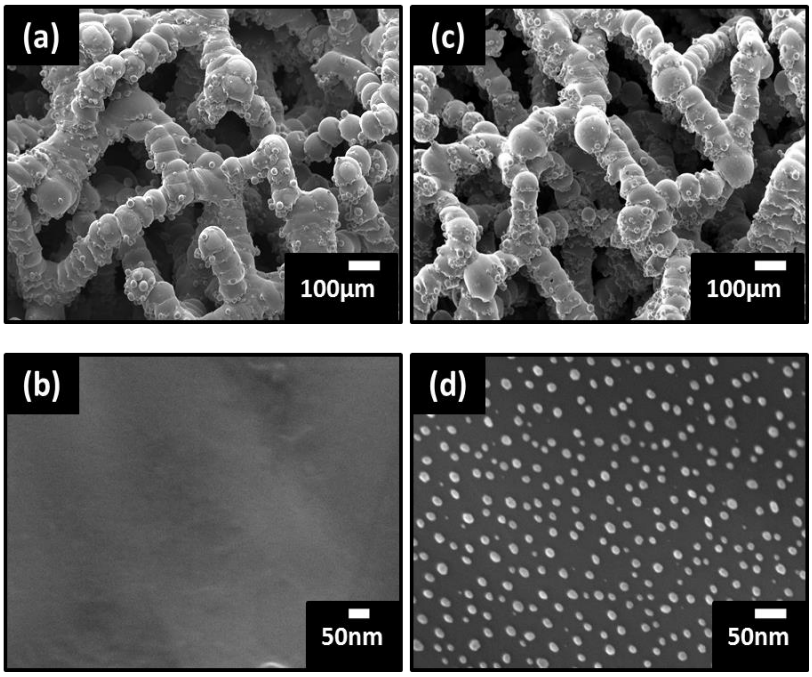

Figure 6.13: *High-resolution SEM images of a-c) non-coated titanium porous SLM structure, d-f) ALD of silver NPs coated titanium porous SLM structure for 100 ALD cycles*

6.4.2. Conformal coating of porous foam structures assessed by SEM

The conformity of the coating on three-dimensional structures was assessed using SEM of the 'split cube' samples for 2 s and 4 s silver precursor doses and 9 s purges for 500 ALD cycles. Each sample was made up of two 2.5 × 5 × 5 mm foam blokes tightly wired together to form 5 × 5 × 5 mm cubes (Figure 6.14). The more details of the experiment can be found in chapter 3.

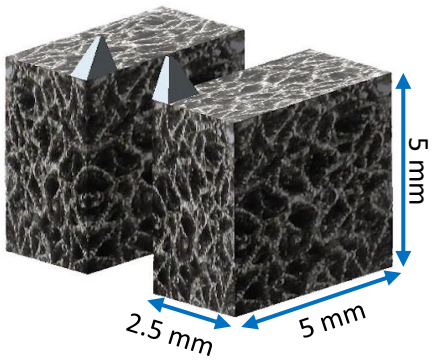

Figure 6.14: *A schematic of the two halves of the cubes*

With 2 s precursor doses dense silver nanoparticles were observed close to the sample edges (Figure 6.15 (b) and (d)), but considerably smaller nanoparticles were observed towards the middle of the sample (Figure 6.15 (c)). This is indicative of sub saturative growth in the central part of the structure, while 2 s doses resulted in conformal coating on the flat titanium substrates, they are insufficient for the 3D cube structure. The central part of the sample do not receive sufficient precursor dose to reach saturation. Increasing the precursor dose to 4 s produced much more consistent nanoparticles throughout the structure. Figure 6.16 (a), shows a low magnification SEM image of the whole sample and indicates the locations of high magnification images taken at the front (Fig 6.16, b & e), middle (Fig 6.16 (c) & (f)) and back (Fig 6.16 (d) & (g)) of the sample with respect to the gas flow direction in the ALD reactor. The high magnification images show that the size and density of the nanoparticles is very similar at each of the locations and supports the conclusion that the growth is controlled by saturative surface reactions.

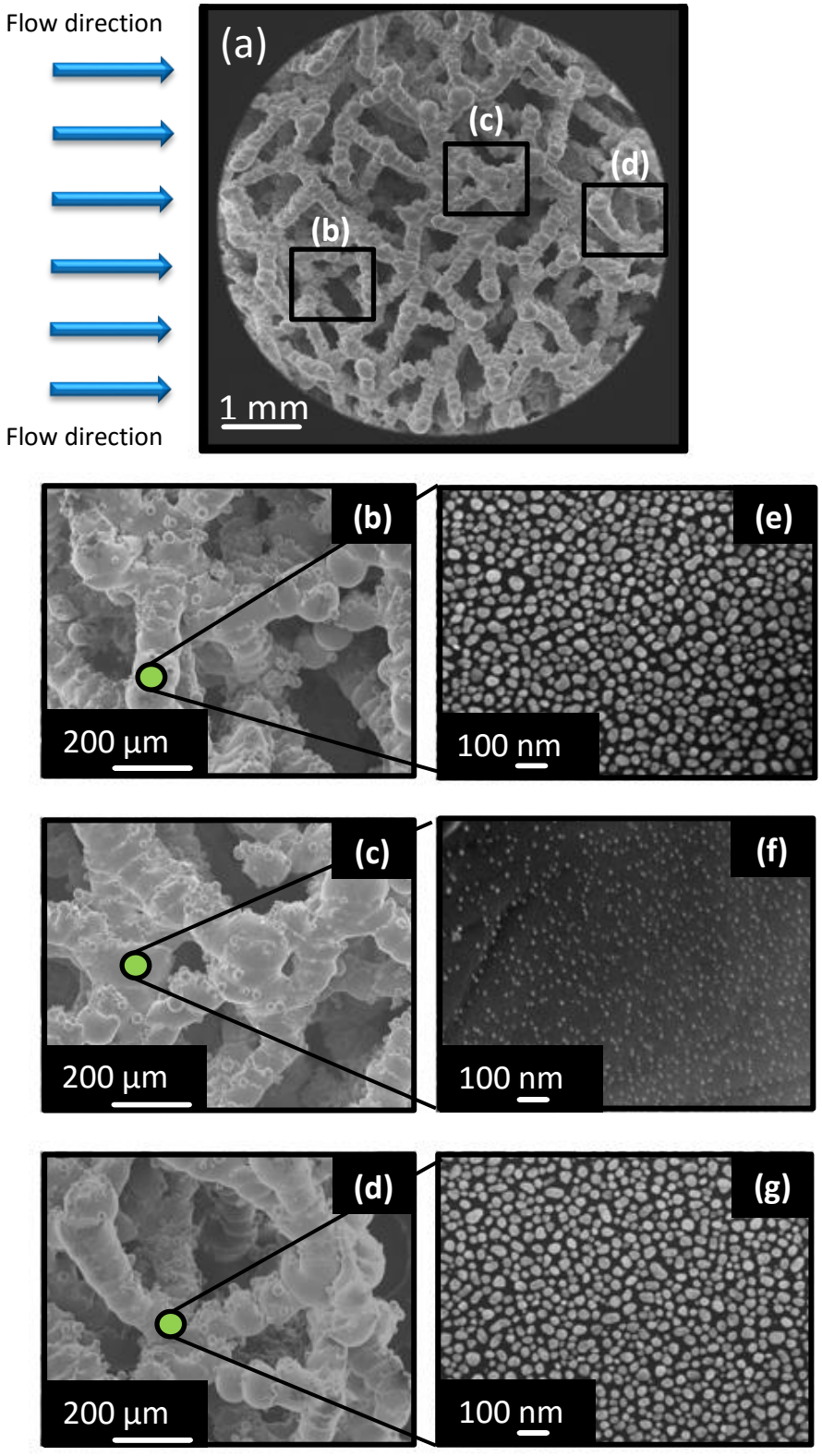

Figure 6.15: *(a) SEM of inner surface of one half of the split cube, and detailed high magnification SEM images of silver nanoparticles on the titanium structure at the front (b & e), middle (c & f) and back (d & g) of the sample for 2 s precursor doses*

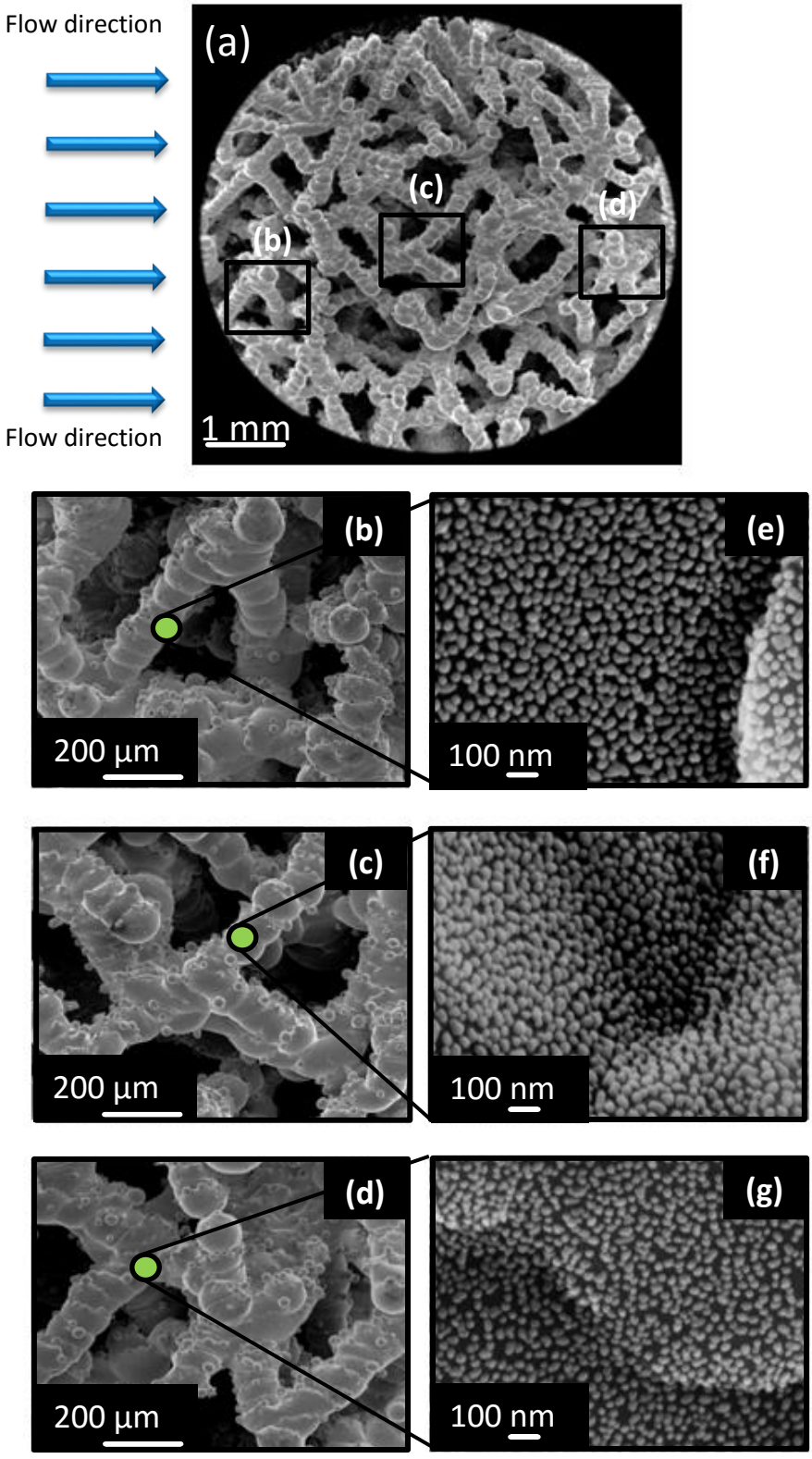

Figure 6.16: *(a) SEM of inner surface of one half of the split cube, and detailed high magnification SEM images of silver nanoparticles on the titanium structure at the front (b & e), middle (c & f) and back (d & g) of the sample for 4 s precursor doses*

As it was clear from Figure 6.15, front and back of the structure show similar size for silver nanoparticles even with insufficient precursor dose. With respect to the gas flow from left to right, it might be expected smaller nanoparticles at the back of the structure compared with the front. Figure 6.17 shows a schematic of the possible gas flow around the sample in the reactor. The gas comes in a laminar flow and as it hits the front edge gets turbulent towards the end edge[392].

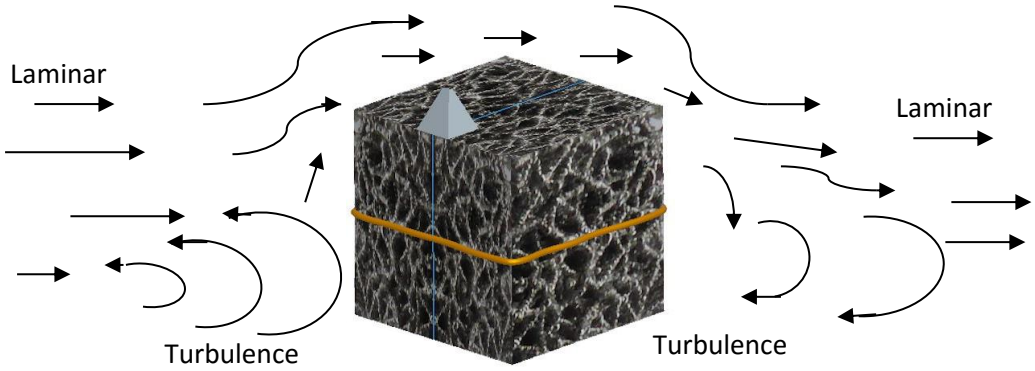

Figure 6.17: *Schematic of the laminar and turbulent flow towards the cube in the reactor*

The size and distribution of the silver NPs on the front, middle and end of the surface structure were analyzed using Image J software. It can be seen from Figure 6.18 the density and size distribution of the NPs is not significantly influenced by position. The size of the NPs was measured with an average size of 48.7 nm (standard deviation of 3.6), 47.6 nm (standard deviation of 2.62) and 48.5 nm (standard deviation of 3.1) on the front, middle and back respectively. Although this deposition process does not produce planar films, it is evident that the quasi-3D growth is still very much controlled in a self-limiting manner. It is important to mention that there is an extra error associated with the nanoparticles size and distribution measurement on these scaffolds due to the fact that the surfaces are not entirely flat within the field of view. However, these errors found to be less than ± 3 nm for NPs size as compared directly with titanium flat substrates.

(b)

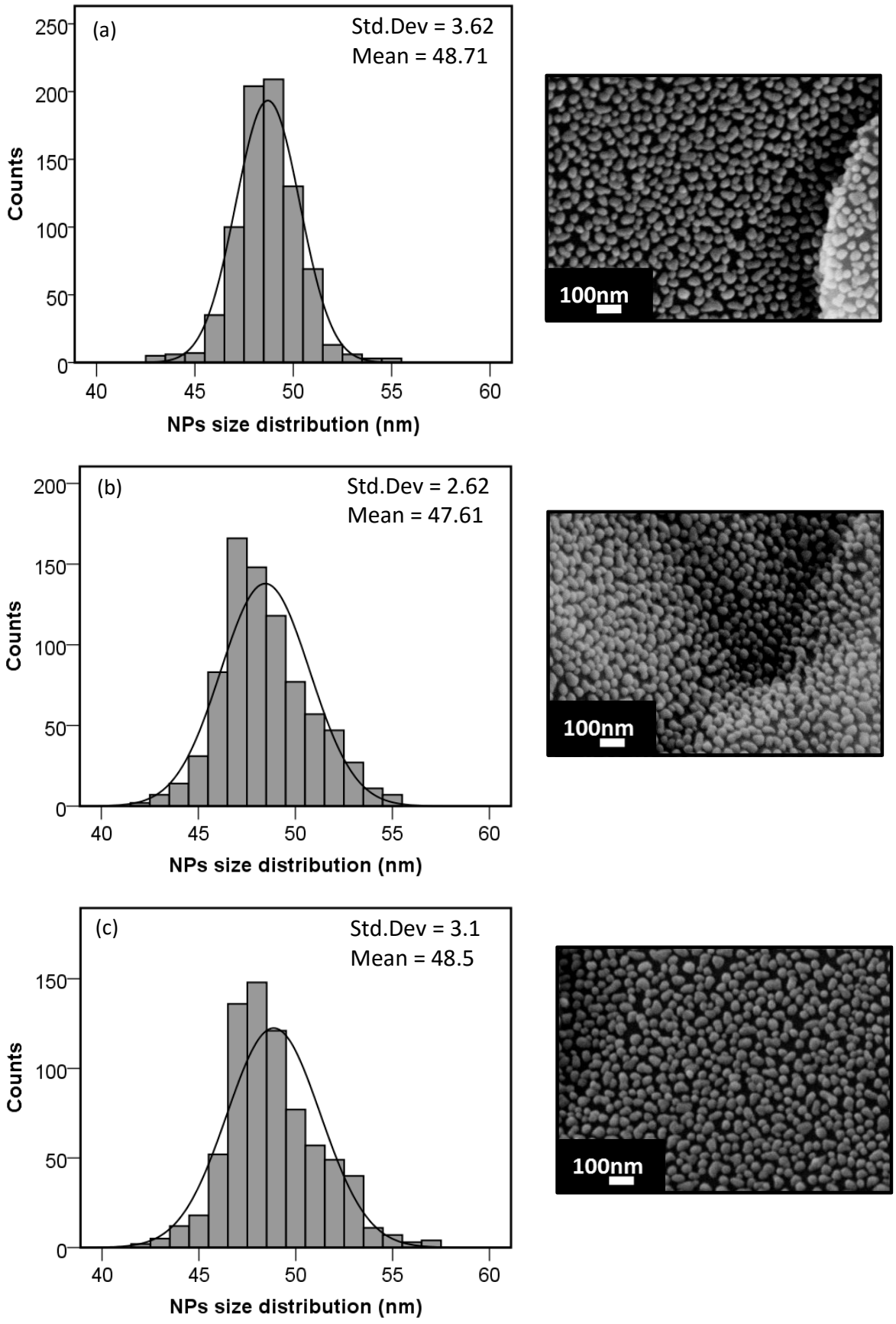

Figure 6.18: *SEM images of the surfaces at different parts of the 'split cube', a) front, b) middle and c) end along with the size distribution histograms.*

In addition to the SEM analysis across the 'split cube' structure, energy dispersive X-ray (EDX) mapping analysis was also applied on the cross sectional surface of the cube and illustrates silver nanoparticles are homogeneously dispersed on the surface through the entire structure, as it is shown in the Figure 6.19. Therefore, it can be concluded that silver is uniformly deposited via ALD on scaffold and the growth is controlled by saturative surface reactions.

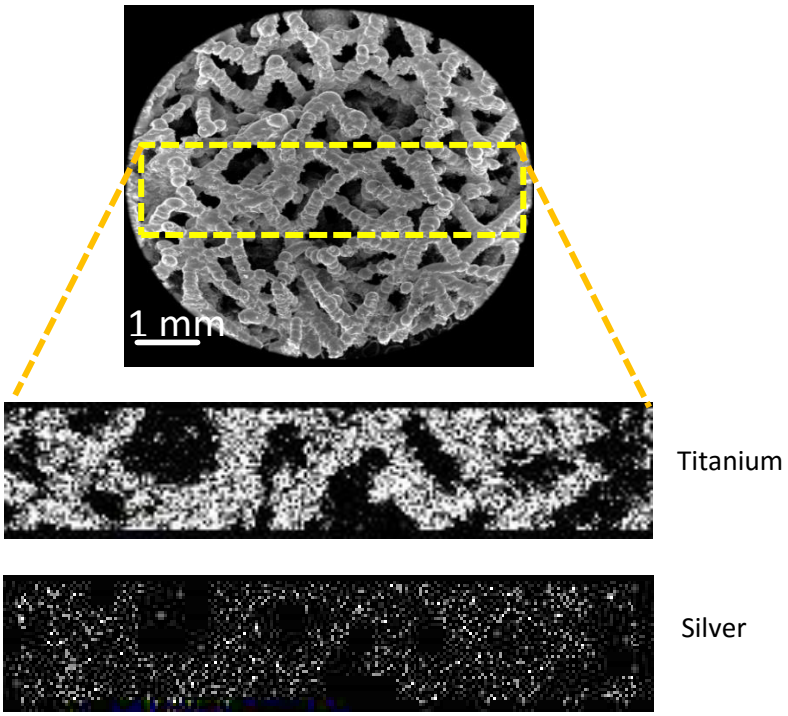

Figure 6.19: *Energy dispersive X-ray (EDX) mapping analysis of cross sectional split cube structure*

6.5. Titanium implants coated with a nano-layer of silver

The development of orthopaedic implants structures using SLM and the high priority of preventing implant related infections have been explained broadly in chapter 2. In this research, titanium implants structures coated with a nano-layer of metallic silver nanoparticles film using ALD method were utilised for the first time to reduce perioperative infections caused by *Staphylococcus epidermidis* as one of the major pathogens related with joint replacement infections. The aims of this study were as follows:

1. *In-vitro* study on titanium implants coated with a nano-layer of silver bacterial reduction and inhibit colonization by *s. epidermidis* compared with uncoated titanium implants.

2. *In-vitro* study on titanium implants coated with a nano-layer of silver to investigate the support of cell growth compared with uncoated titanium implants.

3. *In-vivo* study on titanium implants coated with a nano-layer of silver to investigate the bone and microvascular ingrowth compared with uncoated titanium implants.

To coat the SLM titanium implants in this study, the ALD cycle was repeated 500 times for each growth run with 4 s of silver dose and 8 s of purge and also 4 s of propan-1-ol with 8 s of purge at 125 °C. Figure 6.20 (a) and (b) show SEM images of uncoated titanium solid and foam structures and clearly show the size and shape of the actual implant samples. The detailed experimental procedures of making the SLM samples in this study are briefly mentioned in chapter 3. All of the SLM samples were made at the University of Liverpool by Samuel Evans and Dr. Joseph Robinson. Also, all *in-vivo* and *in-vitro* studies were conducted by Professor Christopher Mitchell, Aine Devlin and Naomi Todd at the University of Ulster.

Prior to microbiological assessment for both *in vitro* and *in vivo* analysis, all the samples were sterilized for 2 hours in 200 µl of 100% ethanol (Fisher Scientific UK Ltd, Loughborough, UK). The experimental procedures for antimicrobial study are briefly mentioned in chapter 3 and more specific details can be found in the reference[98]. Some examples of the actual implant samples coated with silver are shown in Appendix N.

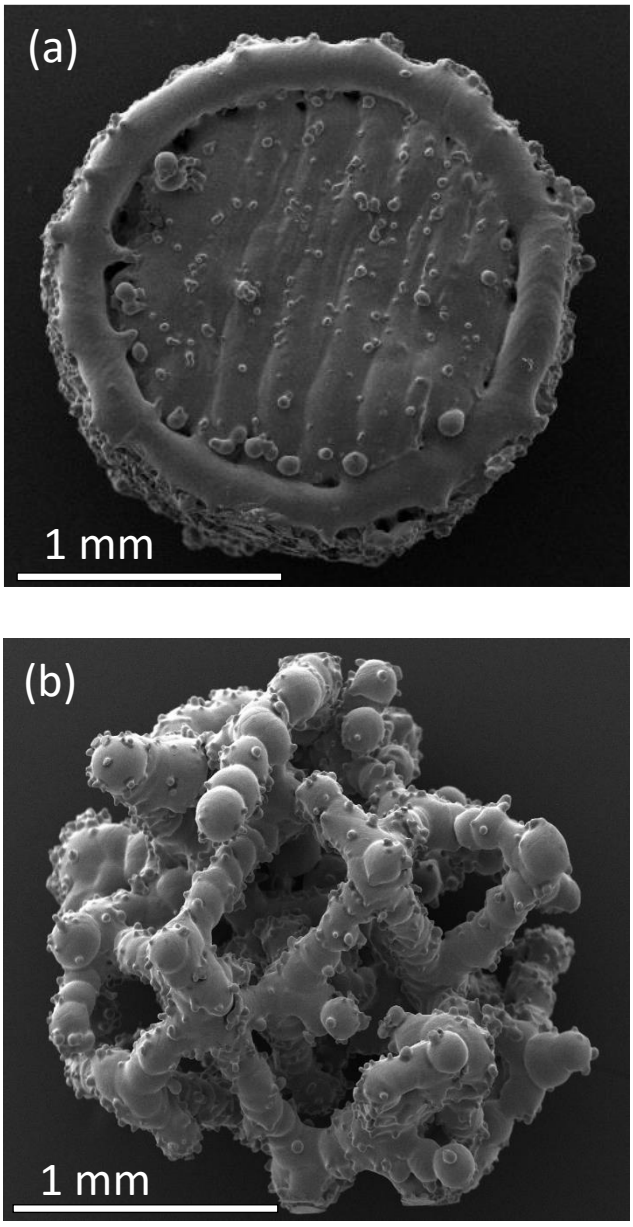

Figure 6.20: *SEM images of a) solid sample (titanium only), b) porous sample (titanium only)*

6.6. Growing *S. epidermidis* on Ti and Ti/Ag Solid samples

In this research, the microbicidal study was carried out in the presence of *Staphylococcus epidermidis* (ATCC 35983 Methicillin Resistant) onto titanium implant structures. Figure 6.21 shows the bacterial recovery (a) and biofilm formation (b) on both uncoated and silver coated titanium structures after 96 hours of incubation by culturing 10^3 organisms of *S. epidermidis*. As Figure 6.21 (a) shows, there was a 2-log fold reduction in the total number of bacteria on silver coated titanium structures as compared to uncoated titanium structures after 96 hours incubation. This graph clearly shows that silver has major negative effect on killing *S. epidermidis*. To explain this effect, one likely cause can be the availability of silver coating to react with water and release silver ions[393,394]. Silver ions have the ability to bind to different elements within the proteins and change the bacterial cell wall structure[394]. In addition, there are some reports on the ability of silver ions in interaction with DNA and hence, resulted in cell partake in protein synthesis and other vital metabolic processes[98].

Following the bacterial recovery investigation, spectrophotometric analysis of solutions shows that a considerably lower optical density is achieved on titanium structure with a nano-layer of silver coated in comparison with uncoated samples after 96 hours incubation with *S. epidermidis* and this is a significant reduction on biofilm formation ($p < 0.001$) (Figure 6.21 (b)). To investigate the difference in biofilm formation further on both coated and uncoated implants, some SEM images have been taken. SEM of uncoated titanium solid surface in Figure 6.22 (a) and (b) revealed a fibrous multi-layered structure adhered to the surface of uncoated titanium structures after 96 hours, consistent with the morphology of a bio-film[395,396]. SEM of titanium silver coated implants on the other hand, revealed very low numbers of organisms and limited indication of cell division after 96 hours incubation (Figure 6.22 (c) and (d)).

Therefore, it can be concluded that silver clearly shows negative effect against biofilm formation caused by *S. epidermidis*.

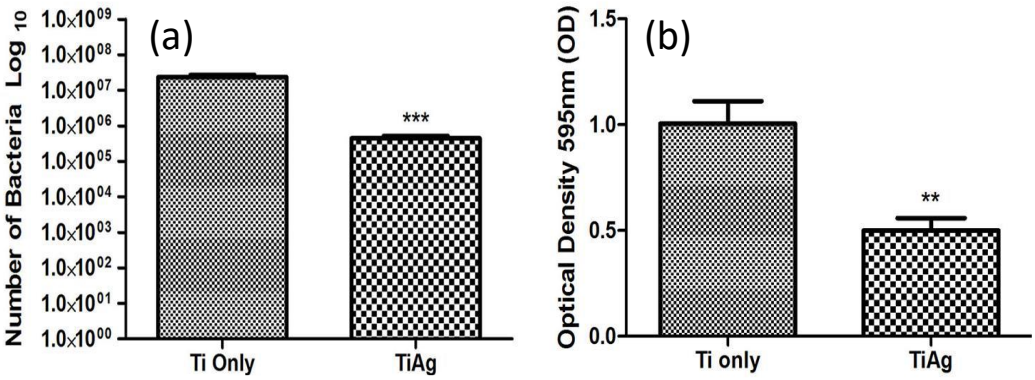

Figure 6.21: *(a) Antimicrobial potential of silver coated solid implants was evaluated using the bacterial recovery technique after 96 hours incubation with 10^3 S. epidermidis compared with uncoated samples, (b) Crystal violet staining assay comparison between silver coated and uncoated implants following 96 hours incubation with S. epidermidis*

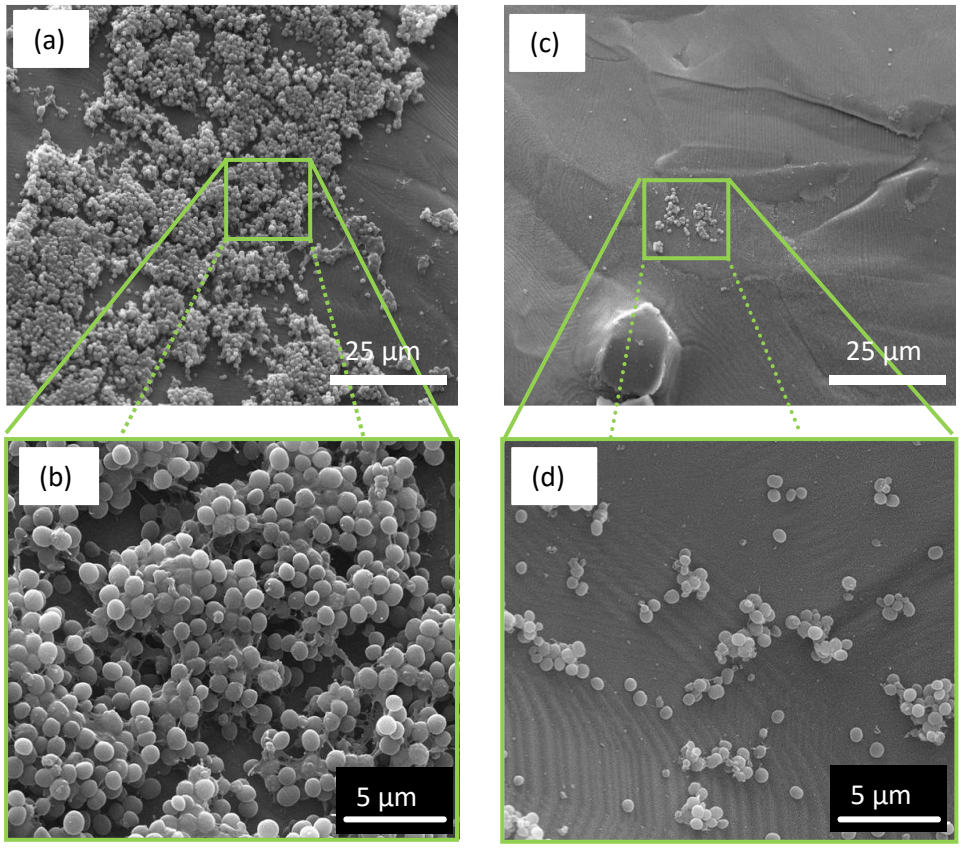

Figure 6.22: *SEM images of S. epidermidis bacterial cells formed after 96 hours of incubation on uncoated titanium solid implants (a and b), and on silver coated titanium solid implants (c and d)*

6.7. Human cell line adhesion on silver coated titanium structures

To investigate the support of silver coated titanium surface on the adhesion and growth of cell lines without altering the morphology or topography of the cell, different SEM images were taken at different incubation time with several human cell lines including; osteoblast-like SAOS-2 (osteosarcoma), HDMEC (endothelium), Hs27 (fibroblasts) and HaCaT (keratinocytes) on the surface of silver coated solid implants and uncoated ones. Cell lines are clearly attached to the surface of both titanium and silver coated titanium surfaces after 6 hours of incubation with flattened cluster of cells evident by 24 hours (Hs27 is shown in Appendix O after 6 of incubation on solid structure).

After 48 hours of incubation time, large clusters of cells with flattened morphology are clearly evident for all four cell lines (Figure 6.23). Hs27 shows a distinctive spindle shape morphology and HaCaT reveals a fully confluent monolayer. So, in this study, silver coated surface has been shown to support the adhesion and growth of analysis cell lines without altering the morphology or topography of them and hence, the *in vitro* cytocompatibility of these silver ALD coated surfaces is confirmed.

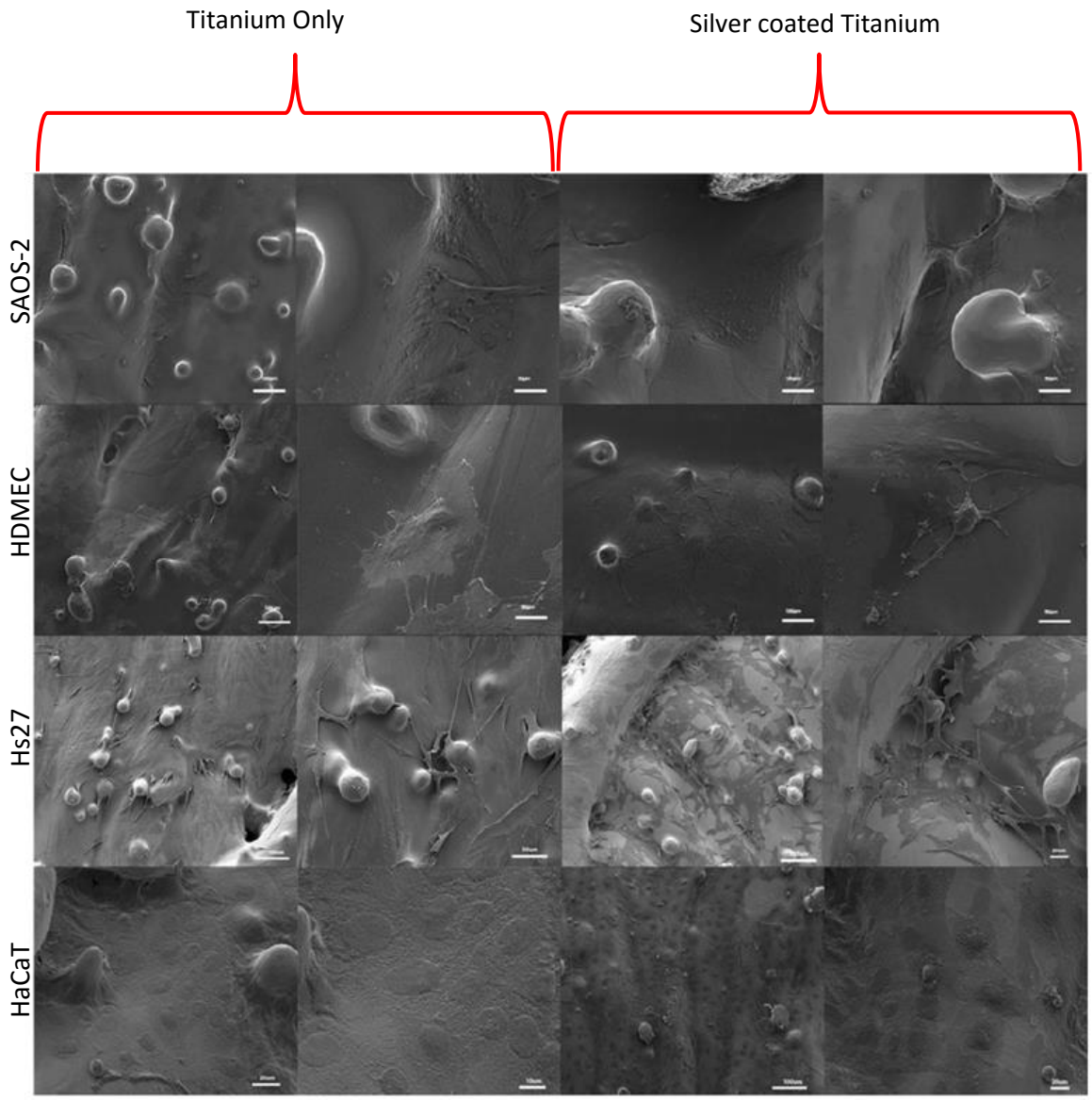

Figure 6.23: *SEM images after 48 hours of incubation of Saos-2, HDMECS, Hs27 and HaCatT on solids (Bar = 100 µm and 50 µm)*

6.8. Vascular Corrosion Casting

In-vivo study was done to investigate the effect of a nano-layer silver coated or uncoated titanium porous implants on the morphology and promotion of microvascular at 2, 6 and 12 weeks following surgery. In order to do the *in-vivo* tests, 24 male Wistar rats with 10-12 weeks old and between 300 to 400 g body weights were used. The detail of the surgical procedure used for *in-vivo* test in this study was previously described and is available in the reference[98]. Figure 6.24 shows the rat's leg which was shaved by mechanical clipper and cleared of all hair using depilatory cream (Veet®,Rickitt Benckiser Group Plc, Berkshire UK). Rats were chosen randomly into two groups of twelve rats for study with titanium implants and silver coated titanium implants. Press-fit technique was used to insert gently both coated and uncoated implants.

Figure 6.24: *Surgical procedure to implant the coated and uncoated sample in the rat tibia*

By the time of two weeks following surgery, the foam scaffolds were surrounded with a dense network of micro-vessels and infiltrated with a porous bone matrix. After 6 weeks, silver coated and uncoated foams were mostly filled with porous bone with several dense networks of vessels. SEM Figures after 2 and 6 weeks are shown in Appendix P and Q.

SEM analysis revealed robust bone and microvascular ingrowth in titanium control samples and silver coated titanium foams implanted in rat's tibia at 12 weeks following surgery (Figure

6.25). Around both titanium (Figure 6.25 (b)) and silver coated titanium implants (Figure 6.25 (e)), several dense networks of vessels are obvious, with no visible difference between the morphology of regenerated bone or micro-vessel structure between the groups (yellow arrows). Also, from vascular cast analysis it is clear that after 12 weeks following surgery, the implant pores are fully penetrated with new bone and continues to grow in and around the micro-vessels until eventually occupy the implant cavity. Regular and smooth micro-vessel morphology on both types of implant are observed with several micro-vessels branching into new canals within redeveloped bone areas in pores from the implant (purple arrows).

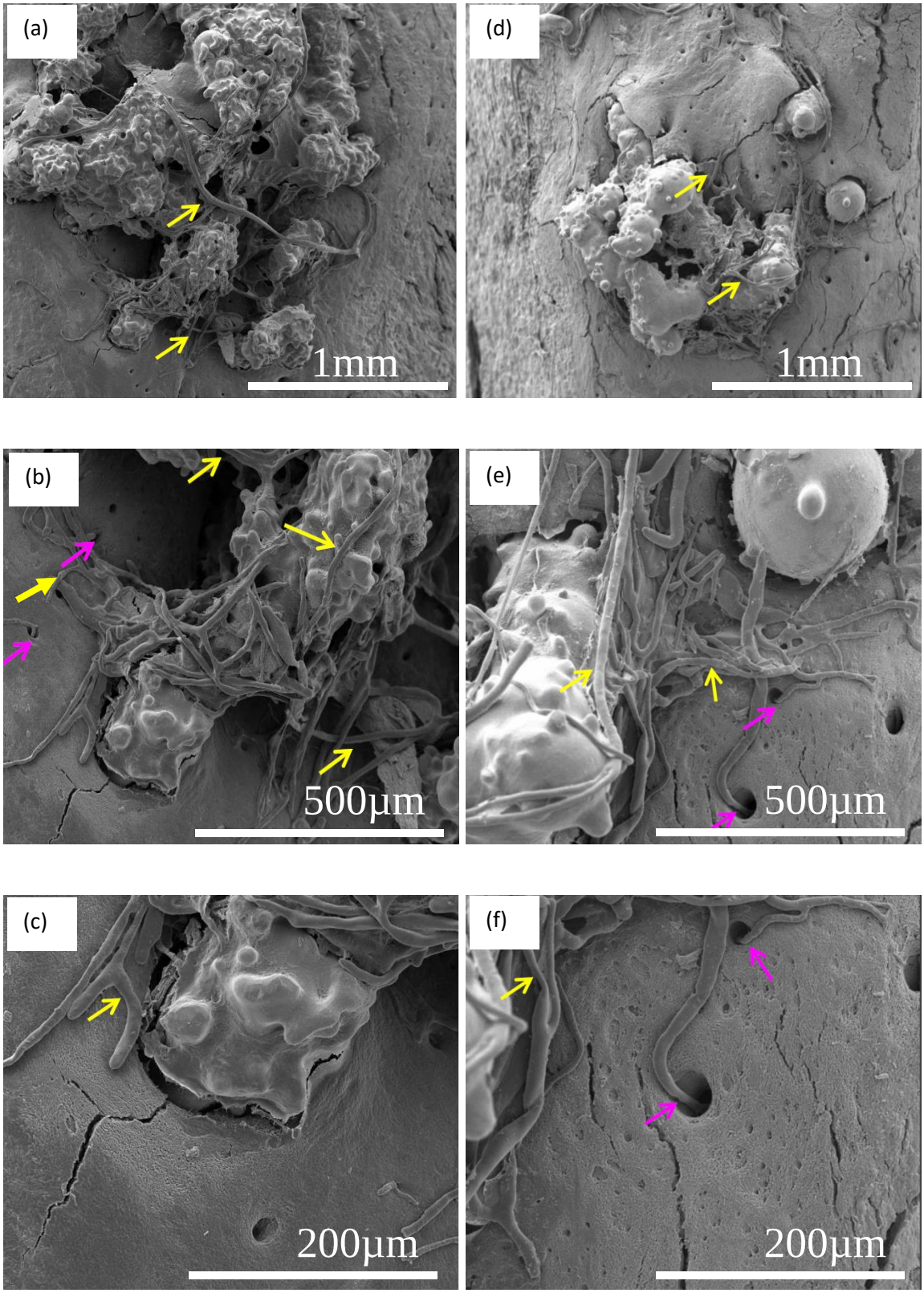

Figure 6.25: *Robust bone and microvascular ingrowth was observed in titanium control and silver coated titanium foams. Rat tibia sub-critical size defects were implanted with either uncoated (a-c) or silver coated (d-f) foams and animals recovered from surgery for 12 weeks.*

Chapter 7

Conclusions and Suggestions for Future Work

7.1. Conclusions

The contents of the work achieved during this thesis can be divided into three main parts. Firstly, a systematic study was carried out on the deposition of metallic silver nanoparticle films using thermal ALD and alcohol based co-reactants. Secondly, the deposition of silver with a hydrazine based co-reactant was characterised and developed. Lastly, a systematic study was performed on the conformality of thermal ALD of silver on high aspect ratio structures and was employed for the use in orthopaedic implants. The insights achieved during this research are provided below:

In the current study, the self-limiting deposition of metallic silver has been demonstrated using thermal ALD with (hfac)Ag(1,5-COD) and either propan-1-ol, butan-1-ol or TBH as a co-reactant. While previous studies have reported thermal ALD of silver, self-limiting growth has not been conclusively shown.

Self-limiting ALD of (hfac)Ag(1,5-COD) using alcohol based process is achievable, however, the ALD window is narrow as a result of thermal decomposition at elevated temperature above 128 °C and due to the incomplete reactions at temperature below 123 °C. The narrow window in principle enable conformal growth on complex high aspect ratio structures, however, the narrow width of the temperature window may cause practical limits for manufacturing in terms of thermal control of large, non-planar structures. At lower temperature, there is insufficient energy to complete the reaction and it is likely that the $Ag^{II}(hfac)_2$ intermediate species remains on the surface following the alcohol doses. This results in increased weight gain and high levels of F contamination which are observed experimentally using XPS. At higher temperature on the other hand, thermal decomposition of the (hfac)Ag(1,5-COD) is evident, resulting in increased weight gain due to a CVD-like contribution to the growth. Based on literature, this CVD growth is expected to progress via a catalytic dehydrogenation reaction of the alcohol co-reactant[320].

XPS and SEM confirms that within the ALD window, metallic silver is deposited in the form of silver nanoparticles, the growth of which is directly controlled by cycle numbers due to the saturative nature of the growth. The nanoparticles grow in diameter in a linear fashion with cycle numbers up until neighbouring particles start to interact and begin to merge together into irregular shape particles via a 'surface Ostwald ripening' like process. The formation of nanoparticles rather than films is due to the 'Volmer-Weber' growth mode which is believed to be promoted due to the poor wetting of silver on silicon, glass or titanium surfaces. The highly textured surface topography of silver ALD results in immeasurable electrical conductivity of films, which indicates that neighbouring particles are disconnected from each other at the micro-length scale. The poor wetting may also account for the relatively poor adhesion strength of silver nanoparticles, making it easy to damage films through handling.

With increasing doses of (hfac)Ag(1,5-COD), propan-1-ol and butan-1-ol, saturative growth rates are achievable, which is a clear indication that both halves of the ALD process are controlled by self-limiting surface reactions as long as the growth temperature is maintained within the ALD window. The envelope of the in-situ QCM data indicates a linear increase in mass with the number of ALD cycles. The detailed QCM mass gain/loss data supports the ALD reaction scheme where the chemisorption of Ag(hfac) is followed by the formation of metallic silver via heterogeneous catalytic dehydrogenation of the alcohol (chapter 4).

Replacing the alcohol with hydrazine significantly extend the ALD temperature window at low temperature end by up to 18 °C growing an ALD window between 105 °C and 128 °C (chapter 5). One potential hypothesis could be explained due to a significantly higher pKa value of hydrazine than propan-1-ol/butan-1-ol. This can lead to readily reduce Ag(hfac) via direct proton donation. Within the ALD temperature window, growth rates are saturative with (hfac)Ag(1,5-COD) and TBH doses.

The relatively large ALD temperature window achieved using TBH (23 °C) is potentially very advantageous compared to the narrow ALD temperature window obtained with the alcohol based process (5 °C) in terms of manufacturing. The wider temperature window makes thermal control less critical, which is especially useful for large, non-planar structures.

No visible F peaks are observed within this temperature window which indicates that the surface reactions are progressing cleanly. At lower temperature below the ALD window, there is insufficient thermal energy to fully reduce the precursor and hence, it is likely that organic ligands are not fully reduced, leading to incorporation of ligand by products and hence F contamination.

Another important insights achieved with TBH as a co-reactant compared with alcohol is the significant difference in growth habit of the silver films. The TBH promotes the 'Frank-van der Merwe' growth mode instead of 'Volmer-Weber' growth mode. Less textured, more film like metallic silver coatings are produced using TBH and these films are electrically conductive. The film also show better adhesion strength compared to films grow using the alcohol based process. One possible reason that could explain this phenomenon during the early stages of the growth process, is that TBH has an effect on the substrate akin to 'self-cleaning' observed with TMA. Then modification of the surface enables better wetting of the silver on the surface, hence producing film like growth and improved adhesion.

For the first time, ALD of silver has been used as a coating method for antimicrobial coating of three dimensional orthopaedic implant structures. The coatings are ultra-thin and highly conformal which has been evaluated by the self-limiting surface reactions of the propan-1-ol based ALD process. The conformality within foam like titanium structures has been confirmed using 'split cube' test specimens assess by SEM.

For bio-implants as silver in high concentration is known to be toxic with the body, the sub-nanometre scale control over the coating thickness is considered to be helpful advantageous. A key objective of the current work was therefore to show that conformal ALD silver at thickness of ~ 10-12 nm would be effective as an anti-microbial coating, while being bio-compatible.

The ALD of silver films deposited by the propan-1-ol based process are very effective at killing *Staphylococcus epidermidis* and show a 2-log reduction in bacteria compared to control samples. The silver films are bio-compatible in terms of the growth and deposition of native body cells. *In vitro* cell culturing studies show good support to cell adhesion and robust growth of different cell lines including SAOS-2, HDMEC, Hs27 and HaCaT, without changing their morphology on both silver coated and control titanium implant surfaces and hence, confirm the cytocompatibility of the silver coated surface.

In vivo investigation also shows that silver coated implant structures as well as uncoated samples are incorporated into 2.5 mm defects in rat tibia, with robust bone ingrowth into the porous scaffold with vessels moving over the scaffolds and connecting with one another and therefore, supports the conclusion that a nano-layer of silver coated SLM structures by ALD does not impact bio-integration of the orthopaedic titanium implants.

In final conclusion, self-limiting thermal ALD is a promising route to the conformal coating of nano-layer silver. It shows initial signs of potential as an antimicrobial coating for orthopaedic implants giving good bacteria kills for *Staphylococcus epidermidis* and biocompatibility. Although further work is necessary to optimise the process, particularly in terms of adhesion and to see if bacteria such as MRSA can be targeted.

7.2. Suggestions for Future Work

The research carried out in this PhD thesis has raised more questions that would be valuable pursuing in the future, however, answering these questions were beyond the scope of this research.

It has been shown in chapter 5 that using TBH as a co-reactant has increased the ALD temperature window and produce more film like growth rather than a 3D growth with alcohol-based co-reactant. This explained due to the higher reactivity of hydrazine and its derivatives due to the lower dissociation energies and weak N-N bonding. However, using QCM in order to in-situ monitoring the actual chemical reaction happened in each ALD cycle with TBH would be a really interesting study. In-situ monitoring could identify surface reaction caused by TBH particularly for the initial cycles, gas phase composition and diagnose reaction by-products. This would hopefully provide further experimental evidence and therefore, the actual mechanism can be explained.

According to the literature, the release of bactericidal Ag (+) ions from smaller diameter silver nanoparticles showed better antimicrobial effects against both Gram-negative (i.e. Escherichia coli) and Gram-positive (i.e. Staphylococcus aureus bacteria)[397]. During the current study, due to the practicality and money involves in running the test, we were only able to try one coating condition (500 ALD cycles at 125 ºC) which produced particles with the roughly size of ~ 48 nm (chapter 6). According to the literature, the silver nanoparticles can be more effective as an antimicrobial agent for smaller nanoparticles size on certain bacteria[398]. Therefore, the future work plan would be to investigate the effect of smaller size range nanoparticles (i.e. 10 to 30 nm) coated with ALD and compare and contrast the effect of them on antimicrobial studies.

In order to produce smaller nanoparticles, lower number of cycles are needed. In this case, the distance between nanoparticles will increase due to their smaller size and leave larger uncoated area among silver nanoparticles. To overcome this challenge, we did briefly look at how using ZnO as a seeding nucleation layer might be effective in increasing the density of nanoparticles. The preliminary study of the particles show that adding in-situ 2 nm ZnO ALD layer in the AIXTRON reactor before starting the ALD cycles of silver, lead to an increase in the density of nanoparticles to twice with the same size (Figure 7.1).

Several parts of the study were inconclusive and we didn't have time and money to buy enough materials to do a detail study, however the SEM results on the preliminary study on density of particles have been shown in Figure 7.1. In Figure 7.1 (a), (hfac)Ag(1,5-COD) was deposited on silicon surface with no surface pre-treatment for 400 ALD cycles. In Figure 7.1 (b) on the other hand, 2 nm of ZnO layer was applied prior to 400 ALD cycles of (hfac)Ag(1,5-COD). The nanoparticle average size distribution was achieved roughly 21 nm for both growth, however, the density of particles per μm^2 was increased from 320 and 690 with the addition of the ZnO layer.

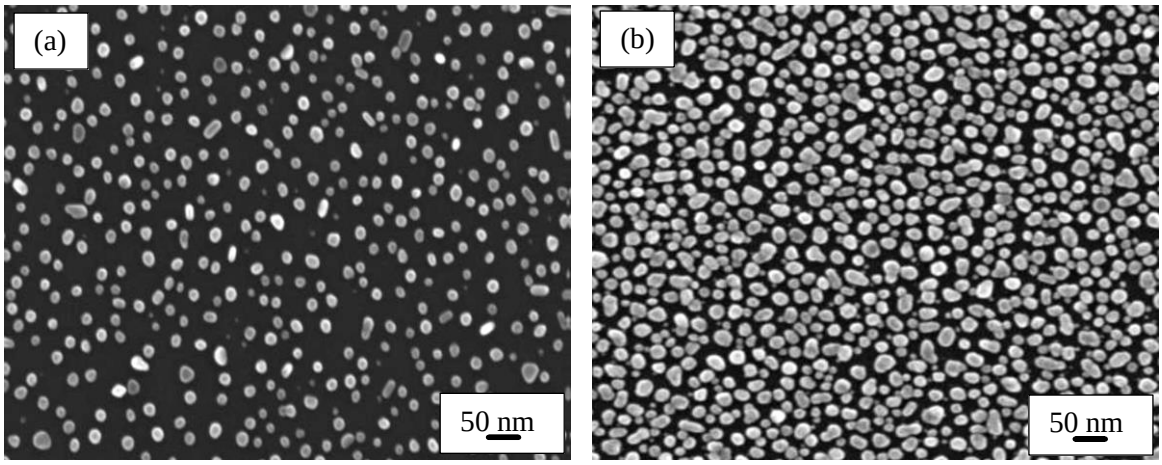

Figure 7.1: *SEM images of the surfaces at 400 ALD cycles, (a) No pre-growth layer, (b) 2 nm ZnO pre-growth layer*

Appendix A

Nano-layer silver coated Titanium inhibits colonization by *Staphylococcus epidermidis* and supports vascularized osseointegration *in vivo*

Aine Devlin-Mullin[1a], Naomi M. Todd[1a], Zahra Golrokhi[b], Hua Geng[c], Moritz A. Konerding[d,†], Nigel G. Ternan[a], John A. Hunt[e], Richard J. Potter[b], Chris Sutcliffe[b], Eric Jones[b], Peter D. Lee[c], Christopher A. Mitchell[a*]

[1]These authors contributed equally to this study

[a]Centre for Molecular Biosciences (CMB), School of Biomedical Sciences, Ulster University, Coleraine, Northern Ireland

[b]School of Engineering, University of Liverpool, Liverpool, L69 3GH, UK

[c]School of Materials, The University of Manchester, Oxford Rd., M13 9PL, UK

[d]Institute of Functional and Clinical Anatomy, Johannes Gutenberg University, Mainz, Germany

[e] Institute of Ageing and Chronic Disease, University of Liverpool, Liverpool L7 8TX, UK

*Corresponding author: Christopher A. Mitchell ca.mitchell@ulster.ac.uk

Abstract

The major microbial pathogens associated with significant joint replacement revision morbidity and mortality include Methicillin-resistant *Staphylococcus aureus* and *Staphylococcus epidermidis*; both of which have strong biofilm forming capabilities in deep wounds and on the surface of prostheses. As few as 103 – 104 of these organisms can result in an infection requiring hospitalization and surgical revision procedures, making prevention of prosthesis-associated osteolytic infections a high priority for orthopaedic research. In order to inhibit biofilm formation on surfaces of implants we developed 3D titanium structures using the selective laser melting technique and subsequently coated them with a layer of metallic silver nano-particles using atomic layer deposition (ALD). Bacterial recovery assays showed that growth of *S. epidermidis* was slow on bare Titanium scaffolds but was reduced by up to 2- log fold ($p < 0.0001$) on silver coated implants with biofilm formation also being significantly reduced ($p < 0.001$). MRSA growth was slow on bare Titanium scaffolds but was, however, unaffected by the silver coating. Ultrastructural examination and viability (MTT) assays of bone (SAOS2) and endothelial (HDMEC) cells demonstrated their strong adherence to and cell growth on, both silver coated and non-coated Titanium implant surfaces. In addition, histological, x-ray computed micro-tomographic and ultrastructural analyses revealed that nano-layer silver coated Titanium scaffolds implanted into 2.5mm defects in rat tibiae promote robust vascularization on the surface of struts as well as conspicuous bone ingrowth. Data from this study supports the conclusion that SLM manufactured Titanium implants coated with a nano-layer of silver significantly reduce pathogenic biofilm formation *in vitro*, while at the same time facilitating vascularization and osseointegrative properties, making these surface-modified implants promising candidates for clinical orthopaedic applications.

Key words:

Bone; Titanium; silver; implant; atomic layer deposition; biofilms, *Staphylococcus epidermidis*, Methicillin Resistant *Staphylococcus aureus*; cell culture; in vivo; rat; vascular casting; angiogenesis

Introduction

Total hip replacements (THR) generally have an excellent clinical outcome, however peri-operative infection rates following this procedure range from 0.5 - 2% [1] and with over 62,000 of these surgeries performed each year in the UK (National Joint

Registry, 2014) there is an urgent clinical need to reduce biofilm formation on the surface of materials used in these devices. THR infection usually results in two additional surgical procedures: one to remove the implant and eradicate the infection followed by an additional THR. This treatment puts a significant burden on the patient and health service resources, as revision surgery can be up to 3 - 4 times the cost of the initial THR [2]. There are several risk factors which can increase the possibility of implant related infection; including increased operative time [3], comorbidities and a prior history of a joint arthroplasty [4].

Infections following THR can be caused by very low numbers (10^3 – 10^4) of osteolytic microorganisms and are mainly attributable to coagulase negative staphylococci, Gram negative rod shaped bacteria and streptococci [1, 4]. Implant related infections are caused by microorganisms which colonise and form biofilms on the implant surface, and infection occurs in 3 main ways: microbial colonisation at the time of implantation; haematogenous spreading of the pathogen to the implant; or *via* direct spreading from an adjacent infection [5]. When microbial pathogens adhere to the implant they form a complex biofilm, which provides protection for the constituent organisms from both the host's immune system and from the penetration of antibiotics [6]. The process of colonisation of an implant is described as a "race for the surface" between the host cells, bone extra cellular matrix and the microbial pathogen [7]. With the onset of an osteolytic infection there are many problems for the patient: including primarily, pain, increased risk of hospitalisation, additional surgical procedures and poor functional outcome [8]. Treatment options will depend on the health of the patient, the extent of the infection, debridement of infected tissue around the joint and retention of a well fixed

prosthesis. The two main treatment options are: 1-stage revision surgery, consisting of the removal of the prosthesis, infected tissue and cement with re-implantation of a new prosthesis; or alternatively, 2-stage revision surgery, where re-implantation of the prosthesis is delayed for 6-8 weeks and antibiotic eluting cement spacers are used to combat infection. Bone cements loaded with antibiotics are still in use but the extensive use of Gentamicin as well as increasing antibiotic resistance means further infection prevention measures are required to lower the incidence of clinically relevant peri-operative hip infections [9, 10]. Two-stage revisions are the most common approach to treat chronic prosthetic joint infections in many hospitals, but in severe cases where the patient is unsuitable for surgery and antibiotics are not effective, hip disarticulation may be considered [11, 12].

The prevention of osteolytic infections is a high priority in the field of orthopaedic research and has been widely explored with approaches including the coating of implants with various metallic and organic compounds, and impregnation of bone cement with silver [13] or antibiotics [14] being considered. The use of silver as an antimicrobial agent is known from ancient Egypt (around 4000BC; [15]) and it is still used today as a microbicide as it kills a broad range of microorganisms [16], although *in vitro* resistance in *E. coli* and has been noted in organisms with metal ion-transport pump deficiencies [17]. Silver coatings have previously been used in the field of orthopaedics on a variety of implantable devices such as catheters, where they have been shown to reduce bacterial associated urinary tract infections [18, 19]. Metallic silver is inert in the body but has been demonstrated to ionize to the Ag^+ active form in the presence of moisture and body fluids, whereupon it binds to bacterial cell walls leading to cell death [17]. The mechanism of action of these Ag^+ ions has been linked to their interaction with thiol (sulfhydryl) groups, although other target sites principally on the bacterial cell wall may be involved in its' microbicidal activity [19]. In the past, poly-methyl methacrylate (PMMA) bone cement was loaded with silver but following human trials, this

was observed to cause serious side effects including neurological deficits and muscle paralysis due to the silver accumulation within the central nervous system [13]. However, nano-silver exhibits none of this cytotoxicity whilst at the same time maintaining a high effectiveness against multidrug resistant bacteria [9].

We have previously described the development of novel porous titanium structures for orthopaedic applications using the Selective Laser Melting (SLM) technique [20, 21]. This allows the production of intricate, porous, functionally graded parts compatible with human bone, having optimal pore sizes (100 – 700 µm) which permit osteoconductive in-growth [21]. The SLM process allows manufacture of orthopaedic implants that contain porous and solid structures that are required to encourage bone ingrowth into certain areas, and to provide greater strength for the bony attachment of the prosthesis, respectively. To determine if silver can be employed to reduce surface colonization by clinically relevant pathogens we coated our Titanium implants with a nano-layer of metallic silver using Atomic Layer Deposition (ALD). ALD, an adaptation of chemical vapour deposition, uses self-limiting surface reactions, which offers two main benefits. Firstly, the amount of material deposited during each reaction cycle is constant; secondly and critically, film coverage is highly conformal even on very high aspect ratio micro-structures. Overall therefore, the process yields a uniform deposition [22] of silver on complex structures such as the foams and solids described in this study [23]. The purpose of our investigation was to determine the microbicidal effect of a nanolayer of metallic silver deposited on Titanium implants in the presence of clinically relevant osteolytic bacterial strains (S*taphylococcus epidermidis* ATCC 35983 and methicillin-resistant *Staphylococcus aureus* ATCC 43300) and to confirm that the surface modification was compatible with cell growth *in vitro* as well as integration into bone defects *in vivo*.

Materials and Methods

Selective Laser Melting (SLM) of bespoke titanium solids and foams

All of the SLM parts in this work were fabricated on a SLM Realizer 2 - 250 (MCP, Germany), using Realizer software (Realizer, GmbH, Borchen, Germany) for the manipulation of CAD files. Before starting the SLM manufacturing process, the chamber was flushed with Argon gas until the oxygen level was below 250 ppm. The oxygen level was determined using a Rapidox 2100 gas analyser (Cambridge Sensotec Ltd., St Ives, UK). The flushing was stopped once the oxygen was below 250 ppm and the build process was then started. The feedstock for SLM was grade 1 commercially pure titanium (CpTi) powder, which was produced by a gas atomisation process (Sumitomo, Japan). The feedstock had a modal particle diameter of 28.5 μm, with 90% of the particles being under 45 μm.

For the porous structures, the powder layer thickness for SLM was set at 50 μm and the laser beam diameter was 80 μm, with the laser power and exposure set to produce melt spots of nominal diameter 180 μm in order to produce wire frame structures with a nominal porosity of 65%. For the solid structures, the scanning strategy involved was to create the outer profile first (circle) and then filling in with hatch lines which alternated in x direction (one layer) and y direction (next layer) repeated until required z height was attained. Laser beam diameter used was 80 μm and point distance (separation of hatch lines for in-fill section) of 70 μm. The laser power was 95W (profile) and 165W (hatch lines) and laser exposure time was 700 micro-seconds (profile) and 600 micro-seconds (hatch).

Following manufacture, scaffolds were cleaned (to remove residual organic solvents and un-sintered powder) by immersion in 5% micro-90 detergent (Decon, Sussex,

UK) in distilled water at 60 °C using a ultra-sonic bath (VWR, Radnor, USA) for 90 minutes, followed by rinsing in distilled water, sonication at 70 °C in distilled water for a further 90

minutes before a final rinse in distilled water. The structures were then dried at 80 °C in an oven before being sintered at 1400 °C for 3 h in a VFS HEQ 2624 vacuum furnace (Philadelphia, USA) at a pressure of 5 Torr to increase compressive strength and reduce the quantity of incipiently melted powder particles. Prior to ALD, sintered solid and porous structures were cleaned again by repeating the process described above. To ensure consistency in scaffolds used throughout the experiments described in this study, 2400 samples were fabricated in a single batch (1200 solid and 1200 foam structures) and used for all subsequent experiments described in this study. All the samples were sintered and cleaned prior to half their number being coated with nano-layer of silver as described below.

Atomic layer deposition of silver

Silver was deposited by direct liquid injection ALD using a customised Aixtron AIX200FE reactor [24], using the self-limited process previously reported [23]. A 0.1M solution of (hexafluoroacetylacetonato)silver(I)(1,5-cyclooctadiene) (hfac)Ag(1,5-COD) (SAFC Hitech, Bromborough, UK) in anhydrous toluene (Sigma- Aldrich, Germany) was used as the silver precursor. During each ALD cycle, silver precursor was introduced for four seconds at a rate of 17.5 µl/s. The solution was introduced into the reactor using direct liquid injection and was volatilised using a Jipelec vaporiser set to a nominal temperature of 130 °C. The vapour was carried into the reactor by 200 sccm of argon (99.999%; BOC, UK) carrier gas. Propan-1-ol (HPLC grade/Fisher, Leics, UK) was use as a co-reactant and was introduced into the reactor for 4 seconds via a Swagelok ALD valve using a conventional vapour draw source held at room temperature (~20 °C). The ALD cycle was defined by sequential pulses of the two reactants separated by eight second gas purges to prevent gas phase reactions. To coat the SLM titanium implants, samples were mounted in a custom made titanium holder and the ALD cycle was repeated 500 times for each growth run. To ensure that ALD growth on the implant structures

proceeded in a self-limiting fashion, the reactor temperature was adjusted slightly until a low mass thermocouple attached to the top of one of the implants read 125 °C (the midpoint of the self-limiting ALD temperature window) [23].

The microstructure and morphology of the ALD silver films was investigated using Xray diffraction (XRD) and scanning electron microscopy (SEM). XRD was carried out on silver films deposited on virgin test grade Si(100) wafers (Compart technology Ltd, Tamworth, UK) using a Bragg Brentano diffractometer with a Cu Kα source (Rigaku miniflex, Tokyo, Japan). Although titanium foils can be used for XRD, silicon was selected for this purpose as it avoids substrate related diffraction peaks in the region of interest, which partially obscures the silver diffraction peaks. SEM of silver deposited onto SLM titanium structures was carried out using a FEG-SEM (JEOL JSM-7001F, Tokyo, Japan). Film composition was investigated using Energy dispersive X-ray spectroscopy (EDX) on coated implants as well as X-ray photoelectron spectroscopy (XPS) on flat titanium witness samples. EDX was carried out using an INCA x-act detector (x-act-51-ADD0001, Oxford Instruments plc, Abingdon, UK) attached to the FEG-SEM. XPS measurements were carried using a FISONS VG Escalab MKII with an Al Kα x-ray source (1486.6 eV). Mass gain measurements were used to estimate the quantity of silver deposited during the ALD process. Mass gain per unit area was estimated by measuring the mass of flat titanium witness samples using a high precision analytical balance (Mettler Toledo XS-205-DU) before and after film deposition.

Sterilisation of solid and porous titanium implants

Before use in biological assays, all samples were sterilized by immersion in 200µl of 70% ethanol (Fisher Scientific UK Ltd, Loughborough, UK) for 2hours. The ethanol was then removed and the samples were exposed to UV radiation (30 min each side of implant) in a Class II biological safety cabinet; method adapted from [25]).

Microbiology

Bacterial strains and culturing

The provenance of osteolytic strains of both *S. epidermidis* (ATCC 35983 [26]) as well as MRSA (*S. aureus* ATCC 43300) was confirmed by a universal 16S rRNA PCR protocol [27], followed by DNA sequencing and confirmation of identity using the BLAST sequence algorithm [28] within the NCBI database. These organisms were grown at 37◦C under aerobic conditions on either tryptone soya agar or in tryptone soya broth (both from Oxoid Ltd,Hampshire,U.K.) with shaking at 150 rpm.

A calibration graph for both microorganisms was constructed by means of dilution series plating of cultures at regular points throughout growth and then plotting cfu/mL versus optical density (OD_{660}). This calibration was repeated in triplicate and for experimental purposes, a final loading of ~1 x 10^3 cells scaffold/was used *via* serial dilution of fresh cultures in TSB. Cell loadings in these experiments were confirmed and verified using dilution plate counts.

Assessing bacterial biofilm formation on solid titanium implants

To seed *S. epidermidis* onto solid titanium implants, an overnight culture was serially diluted to a final concentration of 5 ×10^5 cells/ml, and a 2 µl suspension of this solution was applied to the surfaces of either the control titanium (Ti-only) or ALD prepared nano-layer silver scaffolds (Ti/Ag; coating thickness: 9-15 nm) solid titanium scaffold which were located in a 96 well culture plate. The samples were then incubated overnight at 4 °C to allow bacterial attachment, and the following day 100 µl of fresh TSB broth was gently added to avoid shear stress on the organisms.

The samples (n= 6 replicates per group) were then further incubated at 37 °C for 96 h. Microbial biofilms were assessed by the widely employed crystal violet staining method. Briefly, Ti scaffolds were recovered and following washing in distilled water, the implants were then allowed to dry at room temperature overnight prior to being stained with 1% crystal violet (CV; Sigma-Aldrich, UK) in water for 45 minutes. The excess dye was removed by washing the implants with distilled water. Elution of crystal violet stain was performed by adding a 150 µl volume of 95% ethanol with shaking, to dislodge the attached cells. The implant was removed prior to measuring the absorbance of the solubilized crystal violet at OD_{595} in a spectrophotometric plate reader (Flurostar Omega: BMG Labtech). All experiments were repeated 3 times and a single representative data set presented.

Bacterial recovery from titanium scaffolds

Unless otherwise indicated, all materials were purchased from Sigma-Aldrich, UK. Total bacterial counts (TBC) were used to estimate the number of viable organisms remaining on the implants. After 96 hours, implants with adherent bacteria were gently washed in sterile PBS and transferred into a 1.5 mL microcentifuge tube. A 1 ml volume of sterile of Ringers' solution (Oxoid Ltd, Hampshire, UK) was added to the sample and the bacteria were recovered by vortex mixing for 5 min. Following bacterial recovery, the washed implants were then stained with 1% (w/v) crystal violet (as above) to assess the numbers of organisms remaining on implants. The recovered viable bacteria in Ringers' were enumerated by serial dilution on Tryptone soya agar plates. The plates were subsequently incubated for 24 h at 37 °C and the colonies counted.

Cell culture

Seeding cells on implants

Solid implants were immersed in 1ml of serum free DMEM media and subsequently vacuum processed at 10psi for 15 min to remove air bubbles and wet the entire implant surface. The implants were then incubated in a humidified incubator at 37 °C with 5% CO_2 for a further 3 days in DMEM media supplemented with 10% FBS (both from Gibco, UK).

Prior to seeding cells on the implants, SAOS-2 (osteoblast-like), HDMEC (endothelial), HaCaT (keratinocyte) and Hs27 (fibroblast) cells were cultured in media consisting of DMEM supplemented with 10% heat-inactivated FBS and maintained in a humidified incubator at 37 °C and 5% CO_2. A total of 2 µl of cell suspension containing 5 x 10^3 cells were pipetted onto the surface and the implants further incubated for 30 min to allow cells to adhere to the scaffold surface. To avoid shear stress on the adherent cells, 400 µl of pre-warmed media (DMEM with 10% FBS) was gently added to the culture plate. The implants were then incubated for either 6, 24 or 48 h (n =4/group) before preparation for ultrastructural analyses.

In vivo model of bone regeneration

All animal procedures were approved and conducted in accordance with the local institutional (Ulster University) animal care committee and national (UK Home Office) guidelines. A total of 24 male Wistar rats (10–12 weeks old, 300–400 g body weight) had a single 2.5 mm diameter sub-critical defect made in the medial aspect of the right tibia. Briefly, rats were anaesthetised with 0.5ml/100g bodyweight of an anaesthetic solution containing 2.0ml Ketaset (100 mg ml^{-1}) and 1.0 ml Xylapan (20 mg ml^{-1}) diluted in 5ml phosphate buffered saline (PBS, pH 7.4). A deep plane of anaesthesia was confirmed by the loss of pedal reflex, then the lower right leg was shaved with mechanical hair clippers. The area was cleared of all hair using depilatory

cream (Veet®, Rickitt Benckiser Group Plc, Berkshire UK), cleaned and sterilized using three consecutive washes of pre-warmed chlorhexidine (Hibiscrub®, Regent Medical Ltd, UK), followed by 70% isopropanol. A sub-cutaneous injection of 0.5 ml/100g bodyweight of analgesic solution containing 0.5 mg ml^{-1} Metacam (Boehringer-Ingelheim, Germany) prepared in water for injection (Norbrook; Cumbria, UK) was administered for palliative pain relief.

Throughout the duration of the surgical procedure, animals were kept warm on a heating mat (37 °C). A 1.5 cm full-thickness skin incision was made longitudinally above the middle third of the medial aspect of the tibia. The skin flap was opened using fine spreaders (Inter Focus Ltd, Cambridge, UK) exposing the underlying tibia.

The tibial surface was cleared of connective tissue and periosteum. A 2.5mm circular defect was created using a trephine burr, which extended into the level of the marrow cavity. The defect site was continuously cleared of blood and bone fragments with the aid of suction and the tissue kept moist by saline irrigation. All implants were gently inserted into the defects by the press-fit technique.

Following implantation, the muscle was replaced and secured in place by 3 closed sutures using 4-0 Ethicon Ethilon polyamide (Johnson & Johnson, New Brunswick, New Jersey, U.S), one directly over the implant and one above and below the defect area. A running suture was used to close the skin. Post-surgery, animals received topical application of (0.5% w/v) chloramphenicol eye drop solution (FDC

International Ltd, Fareham, UK) antibiotic solution to the sutured skin to prevent contamination of the operated site, followed by intra-peritoneal administration of 5 ml of Vetivex 18 (sodium chloride 0.18% w/v and glucose 4% w/v) intravenous infusion solution (Dechra, Shrewsbury, UK) to aid recovery. Rats were housed in well ventilated rooms with 12h light: dark cycles and were given access to food and water *ad libitum*. Rats were randomly

divided into two groups of twelve rats each, as follows; animals were implanted with either a single Ti or Ti-Ag scaffold (n = 2/time point) and were euthanized at 1, 2, 3, 4, 6 or 12 weeks after surgery.

In vivo detection of Ag using ICP-MS

The rats implanted with either Ti-only or Ti/Ag foams in the tibia (see above) were left for 12 weeks and following euthanasia, livers harvested to determine the quantity of accumulated silver by ICP-MS. In preparation for determination of free silver content, 250 mg of bovine liver (as a control) and 500 mg rat liver were freeze-dried and powdered prior to mixing in a final volume of 50 mL in double-distilled water. The tissues were then digested by microwaving; to each tube containing a sample of tissue, 4 mls of HNO_3 and 1 mls of H_2O_2 were added. These were then microwaved for 120 seconds and then to each tube 1 ml of concentrated HCl was added. The contents of the digest tubes were decanted into a 50 ml tubes. Samples were auto loaded and analysed for Ag concentration using an Elan 6100 ICP-MS equipment (Perkin-Elmer SCIEX, Norwalk, CT, USA). This was calibrated using Aristar ICP-MS multi-element standards and single element standards (Merck BDH), diluted in 3.5% v/v HNO3 and 0.5% v/v HF. Blanks, Ag spiked samples and bovine liver were used a reference points and standards in addition to the normal ICP-MS SOP standards.

X-ray computed micro-tomography

For the 2, 6 and 12 weeks post-surgical samples, the tibiae from rats with either Ti only or Ti/Ag implants were harvested, immersed in 10% buffered formal saline solution and dissected for micro-CT (μCT) scanning as previously described [29]. An 85 kV, 111 μA source current was employed in the experiment and a total of 1000 projections were acquired. X-rays were filtered using a 0.5mm thick copper filter to minimise beam-hardening effects. The scans were

reconstructed using commercial software (Datos|x rec, Phoenix|X-ray General Electric Company, Measurement and Control) according to the manufacturer's instructions. The reconstructed images were visualised using Avizo Image processing software (Visualisation Sciences Group, Merignac Cedex, France). Region of interest (ROI) was acquired by an in-house algorithm as described [30]. The percentage of bone ingrowth was calculated for the 12 week samples (n=6 for each group) to investigate the biological effect of silver coating at the end point of the experiment.

Histology

Following XMT, the tibial samples were decalcified in a solution of 14% EDTA (Sigma-Aldrich, Dorset, UK) in PBS (pH 7.4), with the EDTA being changed every 2-3 days for 3 weeks. The samples were then processed for embedding in LR white (TAAB Laboratories Equipment Ltd, Berks, UK); in brief, samples were successively dehydrated in two changes of 70% Ethanol (overnight), two changes of 80% Ethanol (1.5 hours each), 2 changes of 90% Ethanol (1.5 hours each) and 3 changes of 100% Ethanol (twice for 1.5 h each and one overnight). Samples were then infiltrated with a mixture of 50% Ethanol/50% LR white (TAAB Laboratories Equipment Ltd, Berks, UK) overnight, followed by infiltration with 100% LR white for 24 h. To initiate hardening of the resin, 20 µl of accelerator (TAAB Laboratories Equipment Ltd, Berks, UK) was added to 10ml LR white and the tibial sample was critically orientated in a clear base mold (Surgipath®, Leica, Milton Keynes, UK) prior to polymerization at 4 °C for 2 h. Excess resin was ground from the sample and the trimmed blocks were glued onto plastic microscope slides (EXAKT, Oklahoma City, USA) with Krazy Glue (Westerville, USA) and UV treated for 5 min using the EXAKT Vacuum Adhesive Press (EXAKT, Oklahoma City, Oklahoma, USA). Samples were cut approximately 1mm from the

centre of the Titanium scaffold using the EXAKT 310 Macro Band System with a diamond blade (EXAKT, Oklahoma City, USA).

Samples were then ground on an EXAKT 400CS grinding system (EXAKT, Oklahoma City, USA) using K800 and K1200 Grinding paper and P4000 and P2500 polishing paper (EXAKT, Oklahoma City, USA) to yield 50 – 100 µm thick sections. Sections were stained with Gill's hematoxylin as follows; sections were placed in 1% formic acid (Sigma-Aldrich, Dorset, UK) for 10 minutes, rinsed in absolute Ethanol for 5 minutes and rinsed in deionised water for 2 min. Hematoxylin solution (Sigma-Aldrich, Dorset, UK) was applied dropwise onto the section, allowed to stain for 30 min and then sections thoroughly rinsed in tap water. Multiple stain solution (Polysciences Inc. Warrington, USA) was added for 20 min followed by another rinse in tap water and the sections were air dried, prior to examination on a Zeiss Axiophot microscope (Zeiss; Wetzlar, Germany) at a range of objective magnifications.

Vascular Casting

To examine vascular ingrowth into the Titanium scaffolds, a number of rats were injected intraperitoneally with 2400U/kg bodyweight of porcine heparin (Sigma-Aldrich, UK) 30 minutes before the casting procedure to inhibit clotting in the microvasculature. Prior to perfusion, animals were anaesthetized with a mixture of Ketamine and Xylazine as described above. After confirmation of a deep plane of anaesthesia, an incision was made in the midline of the abdomen and the descending aorta exposed and tied off proximally. A catheter was inserted into the descending aorta secured using 4-0 Ethicon Ethilon polyamide (Johnson & Johnson, New Brunswick, New Jersey, U.S) and, the inferior vena cava severed. The vasculature was flushed with 25 ml saline (warmed to 37 °C) followed by 25 ml of 2.5% PBS (pH 7.4) buffered glutaraldehyde warmed to 37 °C. Finally, a volume of 25ml Pu4ii resin

(vasQtec, Zurich, Switzerland) was injected into the circulation and the resin allowed to harden at room temperature overnight prior to storage at -20 °C.

The tibiae were subsequently harvested from animals by careful dissection, immersed in tap water and subsequently stored at -20°C prior to maceration. Samples were macerated in 20ml 20% NaOH (Fisher Scientific UK Limited, Leicestershire, UK) for 24h with regular changes followed by extensive washing in dH_2O a total of 5 times. Samples were left to dry at room temperature prior to preparation for SEM.

Preparation of samples for SEM

Scaffolds either containing bacteria (following 96 h of incubation), those incubated with cells (6 – 48 h) or alternatively tibiae that had been appropriately macerated to remove all cellular material (2 -12 weeks post-surgery; see above) were washed in sterile PBS and fixed in glutaraldehyde 2.5% in 0.1M sodium-cacodylate buffer (pH7.4) either overnight or until processing for SEM. The samples were then washed gently three times (for 10 minutes each) in 1ml of 0.1M sodium-cacodylate buffer and dehydrated in ascending grades of ethanol (25, 50, 75, 95 and 100%; Sigma, UK).

Following dehydration, samples were then immersed in hexameythldisilazane (Sigma, UK) for 10 mins, before removal, air drying and subsequent mounting on Aluminium stubs. Prior to ultrastructural examination, samples were sputter coated with gold-palladium (Polar ES100; set at 18 mA for 240 seconds) and imaged with a scanning electron microscope (JEOL; Japan) at accelerating voltage of 10 kV and a spot size of 25 μm.

Statistical analyses

For each microbiological (n=6 replicates; experiment repeated 3 times) or cell culture assay (n = 4; no repeats); individual representative experiments are shown in the results section. All

data sets were analysed with the aid of GraphPad Prism6 software (Intuitive Software for Science, San Diego, USA). Results are expressed as mean ± standard error. Significance was determined using Independent two-tailed tests for group comparisons, with $p < 0.05$ considered significant.

Results

Production of Ti-only or Ti/Ag scaffolds for *in vitro* and *in vivo* studies Ultrastructural examination of the samples revealed uniform solid (Fig. 1a & c) and 30° randomised tetrahedral foam scaffolds (Fig. 1b & d) characterised by a roughened surface topology, with varying numbers of 30 – 50 μm diameter nodules (incipiently melted Ti powder) on their surfaces. Low magnification ultrastructural examination revealed that surface topology of the Ti samples is smooth (Fig. 1a & b), whereas the surface morphology of Ti-Ag scaffolds (Fig. 1c & d) exhibited a grainy texture.

Characterisation of nano-layer silver surface coating of Titanium

Self-limiting ALD growth conditions for the silver process were established prior to the current work and are reported elsewhere [23]. As with other ALD processes, under self-limiting conditions, the film deposition is found to increase in a linear fashion with the number of ALD cycles (Fig. 2a). There appears to be a small deviation from this linear dependence for low numbers of cycles, which is attributed to nucleation effects. If the films are initially assumed to be planar (which is not actually the case, as will be discussed below), then the mass deposition data would give a nominal film thickness of ~13 nm for the films grown using 500 ALD cycles (based on an assumed bulk silver density of 10.49 g/cm$_3$). The diffraction pattern

(Fig. 2b) of ALD silver deposited on Si(100) shows reflections at 2θ values or 38.19° and 44.38°, which are consistent with the (111) and (200) reflections of face centred cubic (fcc) metallic silver with the (Fm-3m) space group (JCPDS 04-0783).

SEM analysis of the silver films deposited on titanium (Fig. 2c) reveals that the films are textured at the nanoscale. For films deposited using 500 cycles of ALD, the nanoparticles tend to be non-symmetrical and vary in size between ~40 and ~90 nm.

More detailed studies, which will not be reported here, show that growth proceeds by a process of nucleation and growth of uniformly sized hemispherical nanoparticles. However, as the nanoparticles grow with increasing numbers of ALD cycles, individual nanoparticles begin to merge together to form irregular nano-structures, via a process of Ostwald ripening. EDX of the films (Fig. 2d) shows two clear peaks at ~3 keV and ~4.5 keV which correspond to the L_α-emission line of silver and k_α- emission line of titanium respectively. To confirm that the ALD does not leave behind precursor residue, XPS was carried out on a titanium witness sample (Fig. 2e). Features relating to silver, titanium, carbon and oxygen are visible, but no fluorine feature is observed (the F1s feature would be at ~688.8 eV). The binding energies of the carbon and oxygen features are consistent with surface absorbates such as H_2O, CO_2 and CO [23]. The absence of a fluorine feature in the XPS provided evidence that the ALD reaction is clean and proceeds to completion [23].

Growth of *S. epidermidis* and MRSA on silver coated titanium structures

Bacterial adhesion and biofilm formation on both uncoated and silver coated titanium structures were investigated by ultrastructural examination and determination of colony forming units of scaffolds seeded with ~1 x 10_3 cells of either *S. epidermidis* (Fig 3a - d) or MRSA (Fig. 3e - h) on their surfaces for 96 hours. Ultrastructural features of *S. epidermidis* biofilm formation on Titanium scaffolds, included multi-layered coccoid structures within a

mucoid-like matrix containing water pores (Fig. 3a), whereas Ti/Ag scaffolds had much fewer of these organisms on their surface and showed little evidence of biofilm formation at 96 hours (Fig. 3b). In addition, a 2 log reduction in the numbers of *S. epidermidis* organisms recovered from silver coated titanium solids ($p<0.001$) was consistently observed (Fig. 3c). Following solubilisation of crystal violet (a quantitative measure of biofilm formation), solutions obtained from silver-coated titanium structures seeded with *S. epidermidis* also had a significantly lower optical density when compared to uncoated samples (Fig. 3d; $p<0.001$). Growth of MRSA on either Ti-only samples (Fig. 3e, g & h) was slow in comparison to that observed by S. epidermidis (*c.f.* Fig 3a, c & d). However, early indications of biofilm formation by MRSA were observed on both Ti-only and Ti/Ag scaffolds at 96 hours (Fig. 3e & f); although neither *c.f.u.* counts (Fig. 3g) nor spectrophotometric measurements for O.D. of crystal violet staining of biofilms (Fig. 3h) were significantly different (NS; $p > 0.05$).

Human cell lines attach and grow on silver coated titanium scaffolds

Ultrastructural analysis of SAOS-2 cells grown for 48 hours on either Ti-only (Fig. 4a) or Ti/Ag (Fig. 4b) scaffolds, revealed both implant types contained clusters of adherent cells with typically squamous morphology. MTT assays also confirmed that from 6 – 48 hours SAOS-2 cell viability increased (Fig. 4c), although there were no statistically significant differences between growth on either Ti-only or Ti/Ag scaffolds (NS; $p > 0.05$). Following incubation for 48 hours, HDMEC cells with typical bipolar morphology and exhibiting filopodial and lamellipodial extensions were observed on either Ti (Fig. 4d) or Ti/Ag scaffolds (Fig. 4e). MTT assay analyses revealed that cell viability of surface associated HDMEC cells also increased from 6 – 48 hours (Fig. 4f), although there were no significant differences between the Ti and Ti/Ag groups (NS; $p > 0.05$).

Detection of free Ag by ICP-MS

ICP-MS reading from samples of liver taken from animals implanted with either Ti only or Ti/Ag coated implants, resulted in readings that were at or below the limit of detection (1 part per billion), indicating that there is no detectable Ag/Ag^{+} in these samples.

Vascular Corrosion Casting and Ultrastructural Analysis

Ultrastructural analyses of vascular corrosion casts from rat tibiae implanted with either Ti-only (Fig. 5a, c & e) or Ti/Ag (Fig. 5b, d & f) foam scaffolds revealed the relationship between pre-existing bone, as well as morphology of microvasculature at 2 (Fig. 5a & b), 6 (Fig. 5c & d) and 12 weeks (Fig. 5e & f) following surgery. At 2 weeks, the foam scaffolds were infiltrated at their edges with a highly porous bone matrix and a dense network of micro-vessels (particularly around the struts) that originated from pre-existing bone surrounding the site of the defect (Figure 5a & b).

Conspicuous mineralised material also encrusts the struts on the surface of Ti-only and Ti/Ag scaffolds at 2 weeks (Fig. 5a & b). Ultrastructural examination of the surface of a 2 week Ti/Ag implant, revealed hemi-tubular structures in various stages of development (Fig. 6) which were characterised by concentric lamellae and contained mineralised, parallel-orientated fibril bundles (Fig. 6; inset); features that are consistent with *de novo* Haversian system formation. In 6 week samples, the gaps within scaffolds of both Ti-only and Ti/Ag foams contained numerous blood vessels interspersed with porous bone or partially ossified fibrous material (Fig. 5c & d). Ultrastructural analyses of vascular casts from rat tibia harvested at 12 weeks following implantation with Ti-only or Ti/Ag foams showed that implants were infiltrated with bone containing Volkmann canals with attendant micro-vessels (Fig. 5e & f). Micro-vessel morphology from tibiae implanted with Ti-only or Ti/Ag scaffolds and harvested at 12 weeks

were more regular, smooth and had fewer anastomoses with neighbouring vessels than those observed in 2 week samples (*c.f.* Fig. 5e & f with Fig. 5a & b).

Histology

Light microscopic examination of thick (50 -100 µm) sections from rat tibiae sampled at 2 weeks post implantation, revealed infiltration of porous woven bone at the edges and core of both Ti-only (Fig. 7a) and Ti/Ag scaffolds (Fig. 7b). By 12 weeks, compact bone ingrowth was observed throughout the scaffolds in both Ti-only (Fig. 7c) and Ti/Ag (Fig. 7d) scaffolds in close apposition to the struts.

X-ray microtomographic analysis of scaffolds *in vivo*

The percentage of bone ingrowth (BI) at 12 weeks and statistical significances for these values are presented in Figure 8. Post implantation, Ti or Ti/Ag scaffolds appear well incorporated into 2.5 mm defects in rat tibiae at all time-points, demonstrating robust bone ingrowth. A conspicuous amount of bone ingrowth is observed between 2 and 12 weeks. At 12 weeks' post-implantation, Ti (Fig 8a i) and Ti/Ag groups (Fig 8a ii) have a similar amount of BI, as confirmed by micro CT quantification (Fig. 8b). These results demonstrate that the nano-layer silver coating does not cause a marked unfavourable response in the volume of newly regenerated bone.

Discussion

Titanium and titanium alloys are the most widely chosen biomaterial for orthopaedic implants due to their intrinsic properties; these include lightness, high compressive/tensile strength and biocompatibility. These materials are also compatible with rapid 3D manufacturing techniques such as SLM. Due to the large numbers of joint replacements carried out worldwide, implant

failure as a result of osteolytic infection, which constitutes around 2% of all procedures, poses a serious post-surgical issue [25, 31]. Consequently, there is an urgent need to find a translatable, reliable method of surface modification for titanium orthopaedic materials that can reduce surface colonization, while preserving their osteoconductive properties [25, 32, 33]. One approach explored to reduce bacterial colonisation and proliferation is the introduction of metallic elements to modify the surface of biomaterials. A variety of metals have been explored in this field; including zinc [34], strontium [35], gallium [25] and gold/palladium [36] although silver is the most widely employed metal coating on materials surfaces due to its antimicrobial properties and the susceptibility of multi-drug resistant bacterial strains to silver [9, 32]. In terms of antimicrobial coatings on bone implants, ALD offers the prospect of producing ultra-thin, highly conformal coatings on all wettable surfaces of the implant [23, 37]. One of the key advantages of using ALD to coat the implants is that under appropriate conditions, it proceeds *via* saturative steps, resulting in self-limiting film growth. This means that ALD can give truly atomic scale control of the deposition process and can produce ultra-thin films with excellent uniformity and conformity, even on complex high aspect ratio three dimensional structures [38]. The coating is so thin that the total quantity of active material is kept to a minimum (and systemic release of Ag detected from liver sample was below levels of detection by ICP-MS in our study), which helps to reduce concern relating to systemic toxicity of nano-layer silver coated orthopaedic implants [39, 40].

The majority of studies examining the antimicrobial potential of silver for dental/orthopaedic applications rely on dissolution of Ag particles from either cements [9, 41] or surface coatings [35, 40, 42, 43] for titanium. These studies generally report a > 2 log-fold increase in microbicidal activity, although silver particles are highly mobile and potentially toxic, with their tissue accumulation characteristics being largely unexplored [39, 40]. Investigation of silver nanoparticle films that are bonded to the titanium is therefore of great interest as a method

for reduction of post-surgical osteolytic infections, while preventing the release of potentially toxic quantities of silver. The ability of Ag^{+} to exert a microbicidal effect is reported as being dependent on the lability of the complexed silver, with the majority of approaches for dissolution being directed towards localized release *via* gradual solubilisation. Although localized release of Ag-nanoparticles *via* dissolution achieves excellent anti-microbial effects *in vitro* [9, 41] in addition to a reports of efficacy *in vivo* [40, 42, 44], this approach is associated with increased silver levels in both serum and systemic organs in addition to evidence of toxicity, making its' clinical orthopaedic application problematic.

In our study, conformal nano-textured silver films, which are bonded to the titanium have been shown to reduce the growth of the osteolytic pathogen *S. epidermidis* on the surface of Ti/Ag scaffolds, however this response was organism specific as MRSA growth, while generally slow on Ti-only scaffolds (and similar to growth of *S. epidermidis* on Ti/Ag scaffolds) was not further inhibited by incubation on Ti/Ag scaffolds. This observation is consistent with that reported for Ag-coatings of endotracheal tubes where MRSA growth is also not inhibited (in comparison to uncoated samples) over a period of 5 days [45].

For scaffold surfaces with nano-layer silver (such as in this study) or silver doped surface additives (e.g. hydroxyapatite) to be used as orthopaedic materials, it is also critical that these surface modifications support the growth and differentiation of cell types associated with the regenerative response of bone. In our study, we examined the growth of SAOS-2 cells (an osteoblasts-like cell line) on scaffolds between 6 – 48 hours following culture and show ultrastructural evidence of adherence and an MTT assay confirming cell viability on both Ti-only and Ti/Ag scaffolds; findings that are consistent with both human SAOS-2 cell and mouse osteoblast cells (MC3T3-E1) [42, 46, 47] grown on silver-nanoparticle coated titanium surfaces [25]. However, responses may be cell type specific as high concentrations of labile Ag-containing surface coatings are known to be toxic to human foetal osteoblasts [48]. We also

found that both attachment and growth of human microvascular endothelial cells (HDMEC) is well tolerated on Ag-coated surfaces, consistent with that described for human umbilical vein endothelial cells (HUVEC's) grown on silver-doped ceramic Nano-powder [49]. In a mouse model where higher concentrations of Ag nanoparticles are released into the microcirculation, significant toxicity on endothelium was reported [50]. We also observed that two other human cell lines (Hs27 and HaCaT; data not shown) show robust cell growth on Ti/Ag scaffolds, consistent with observations that growth of a variety of cell types [51-53] on titanium surfaces coated with various compositions of silver-doped matrices is supported.

Our *in vivo* studies are the first to document the relationship between pre-existing bone, neovascularization (new blood vessel growth), osteogenesis and remodelling during the 12 week time frame of solid implant incorporation. Our unique observations on SEM of vascular casts of tibial samples, show robust new capillary formation by 2 weeks post-implantation, particularly around the struts of the scaffolds, with numerous small calibre vessels emerging from the surrounding periosteum and forming irregular inter-connected networks. The presence of numerous highly branched capillaries emerging from pre-existing vessels is a well-recognised process in the cortical bone regeneration process [54, 55]. These capillary networks precede mature bone ingrowth into the scaffolds at 2 weeks and are most-likely associated with the significant increase in gene expression associated with implantation of roughened titanium surfaces [56]. We also report the first ultrastructural evidence for *de novo* formation of Haversian systems directly on the surface of a 2 week post-implantation Ti/Ag scaffold; this result is consistent with a previous report in which Sr/Ag doped nanotubules induce osteogenesis *in vivo* [35]. Porous scaffolds with roughened surfaces (similar to both Ti-only and Ti/Ag implants described in our study) provide morphology similar to trabecular bone, to which osteoblasts can attach *in vitro* and *in vivo*, differentiate and deposit matrix that will eventually mineralise and begin the formation of woven bone [57-59]. By 12 weeks' post-

implantation, there is clear evidence of bone and vascular remodelling within the porous structure of Ti-only and Ti/Ag scaffolds; including Volkmann's canals with attendant capillaries - features that are characteristic of mature bone growth [55, 60]. Consistent with our ultrastructural observations, 2D light microscopic examination of thick histological sections and 3D x-ray-computed micro-tomographic reconstructions revealed excellent bone in-growth in both Ti-only and Ti/Ag scaffolds, similar to that described for rats implanted with titanium coated with either Silver oxide doped Hydroxyapatite [42] or silver impregnated nanotubes [61].

Conclusion

The data from our study demonstrates that silver nanoparticle deposition onto SLM titanium scaffolds by atomic layer deposition not only reduces surface growth of a major osteolytic pathogen (*S. epidermidis*) but also supports growth and differentiation of human cell lines important for bone regeneration. These titanium scaffolds coated in a silver nanolayer induced robust osteogenesis and angiogenesis *in vivo*. A further benefit, was that the Ti/Ag scaffolds neither released nor accumulated detectable quantities of silver *in vivo*. These results highlight the benefits of non-labile silver coating of the surface of SLM manufactured Titanium scaffolds warranting its' further investigation for use in clinical orthopaedic applications.

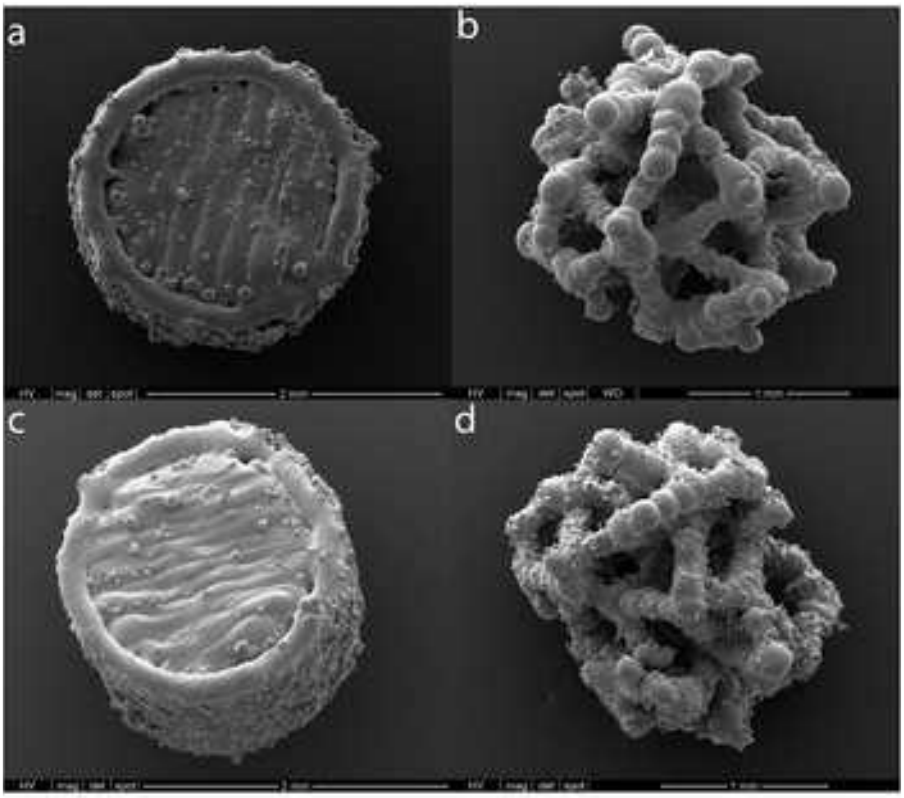

Figure 1: Two types of structures; solid (left panel) or 30° randomised tetrahedral foams (right panels) were generated by SLM followed by sintering. Approximately half the samples were used as Ti-only controls (top panel) or titanium coated with a nanolayer of silver (bottom panel). For microbiological and cell culture studies solid samples were used, whereas foam samples were used for in vivo studies to facilitate ingrowth of regenerating bone into the porous structure.

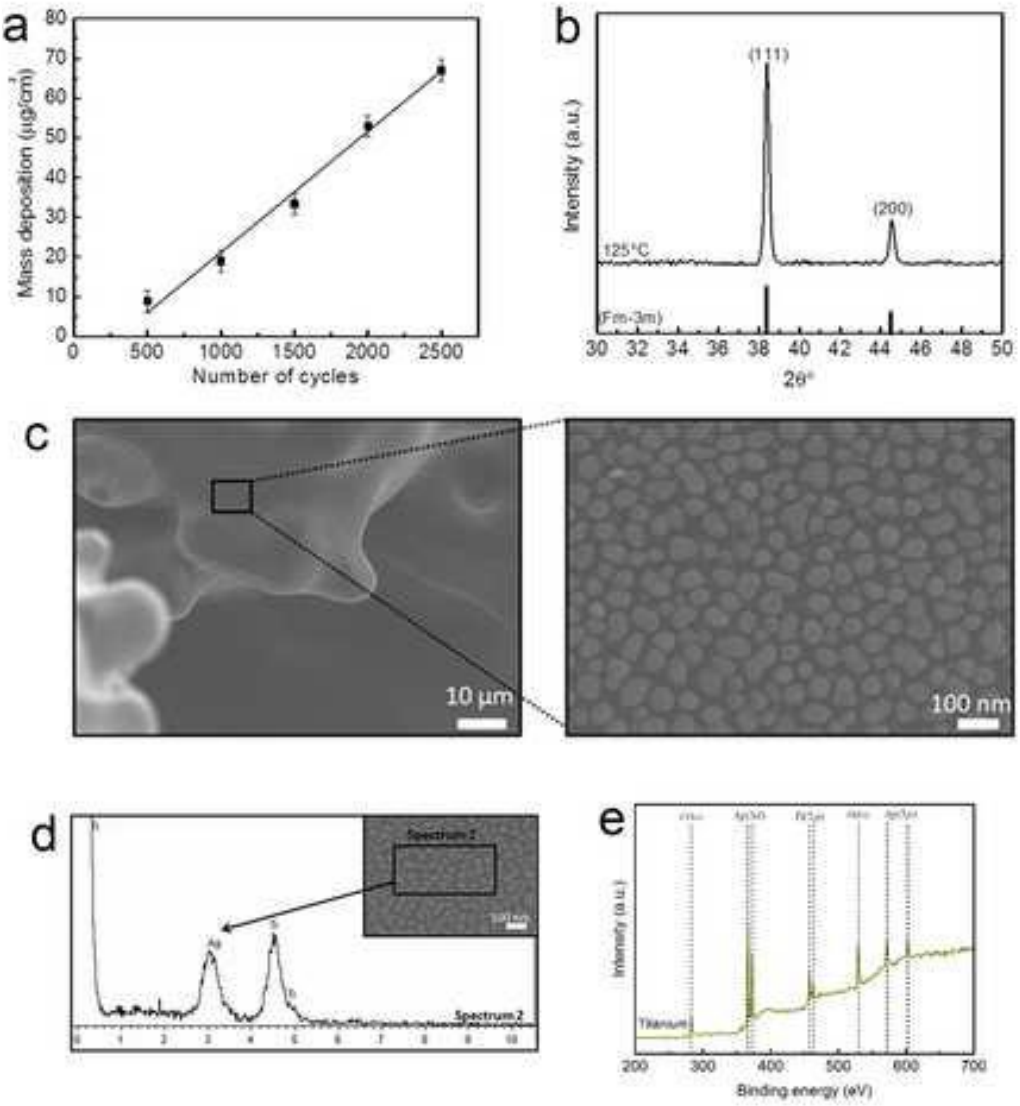

Figure 2: Growth and physico-chemical characterisation of ALD silver at 125 °C. Mass deposition per unit area as a function of ALD cycles (a) performed at 125 °C on flat titanium foil. X-ray diffraction of ALD silver deposited at 125 °C with 500 ALD cycles on silicon (b). High magnification SEM images reveals silver nano-particles deposited on a titanium porous substrate (c). Energy-dispersive x-ray spectroscopic characteristic spectrum obtained for silver nanoparticles deposited on titanium substrate (d); the observable peaks confirm the presence of silver and titanium in the sample. XPS spectrum of silver deposited on a flat titanium foil (e).

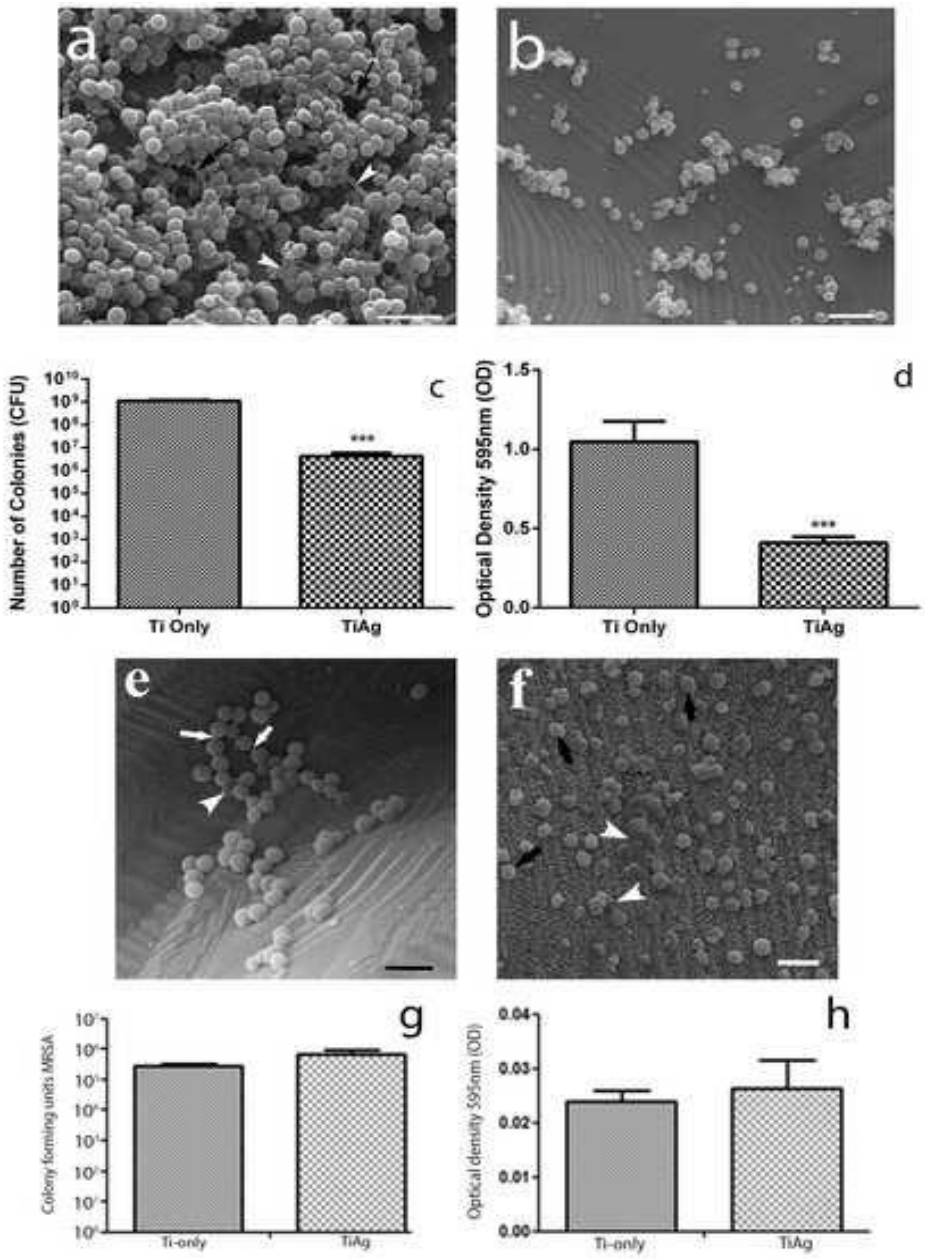

*Figure 3: Ultrastructural examination of a Ti-only sample, reveals a multi-layered S. epidermidis biofilm resulting from incubation of 103 organisms for 96 hours (a). Several water pores (black arrows) and threadlike appendages between organisms (arrowheads), both typical of biofilms are observed. On Ti/Ag solids (b) the surface density of organisms is markedly reduced compared to Ti-only samples. Bars = 5µm. Quantitative studies revealed a > 2-log reduction in c.f.u. numbers of S. epidermidis (c) as well as reduced crystal violet elution (d) in Ti/Ag samples when compared with Ti-only controls. Scanning electron microscopic examination of MRSA cultured for 96 hours on either Ti-control (e) or Ti/Ag scaffolds (f) revealed relatively few organisms on the materials' surfaces, although there is evidence of replication (arrows), in addition to deposition of mucoid-like matrix (arrowheads). No statistically significant differences in c.f.u. numbers were detected on either scaffold type (g), although there was a 2-3 log reduction in growth when compared to S. epidermidis cultures (c.f. Fig. 3c). There were also no differences in crystal violet quantitation (NS; $p > 0.05$) from MRSA cultures grown on either Ti-only or Ti/Ag scaffolds (h); although these values were much lower than those observed in S. epidermidis cultures (c.f. Fig. 3d). Graphs show a single representative data set (n=6) from 3 independent experiments, with columns indicating mean ± SEM. Statistical significance was assessed with a student's t-test; ***$p < 0.001$.*

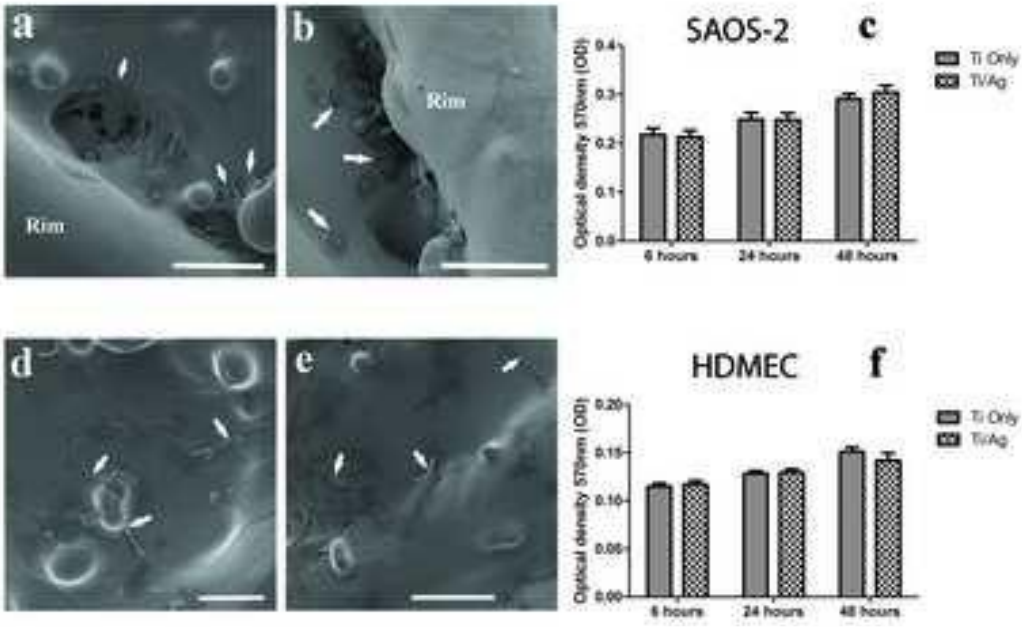

Figure 4: SAOS-2 osteosarcoma (a - c) and HDMEC-1 endothelial (d –f) cells grow on the surface of either Ti-only or Ti/Ag scaffolds. After 24 hours of culture, SAOS-2 cells with characteristic squamous morphology were observed to be tightly adherent, closely apposed and found in clusters, particularly near the rim of solid scaffolds of both Ti-only (a) and Ti/Ag samples (b). There was a gradual increase in cell viability of SAOS-2 cells (c) from 6 – 48 hours but no differences in viability between those seeded on either Ti or Ti/Ag scaffolds (NS; $p > 0.05$). HDMEC grown on the surface of either Ti-only (d) or Ti/Ag (e) scaffolds are typically found in small clusters, with some cells showing elongated lamellipodia spanning surface depressions (arrows). In HDMEC cultures, results from MTT assays indicated that there was a gradual increase in cell viability from 6 – 48 hours but no statistically significant difference between OD575 values from Ti-only or Ti/Ag scaffolds (NS; $p > 0.05$).

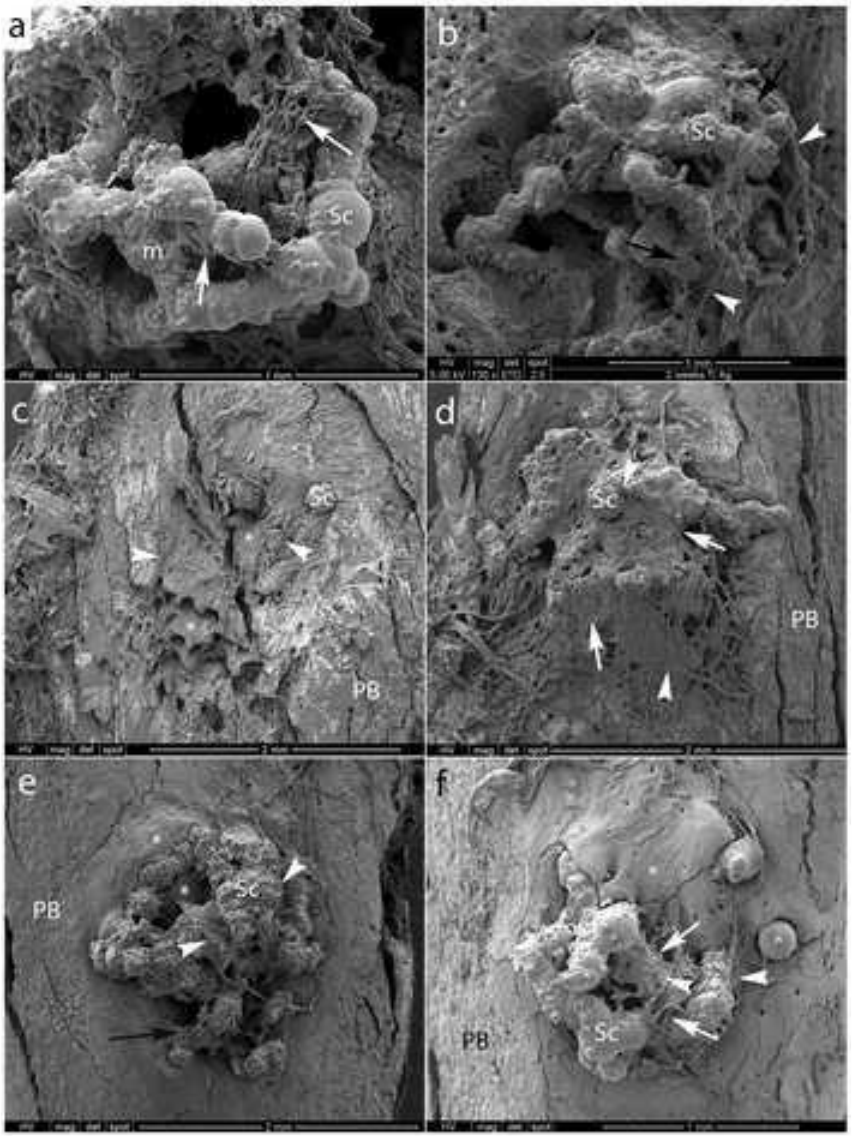

Figure 5: Robust bone and microvascular ingrowth is observed in both Ti-only and Ti/Ag foam scaffolds. Rat tibial sub-critical size defects were implanted with either un-coated (a, c & e) or Ti/Ag coated (b, d & f) foams and animals recovered from surgery for either 2 (a & b), 6 (c & d) or 12 (e & f) weeks. Animals were then perfused with vascular casting resin, the tibiae dissected, the soft-tissue removed by desiccation and samples prepared for imaging by scanning electron microscopy. At 2 weeks in both Ti (a) and Ti-Ag samples (b) there is new bone growth at the periphery and mineralised material on struts but relatively little new bone within the scaffold pores; robust ingrowth of larger calibre vessels (arrowheads) as well as capillaries is conspicuous around the struts (arrows). At the edge of the foams early bone ingrowth is evident (asterisk), while around the struts copious filamentous material and mineral deposition is seen. After 6 weeks in vivo, the foams were infiltrated with porous bone (asterisks) covered by a fibro-matrix with dispersed crystalline mineral deposits. After 12 weeks in vivo (e & f), there was evidence of compact bone ingrowth (asterisks) into the pores of both Ti-only (e) and Ti/Ag (f) implants and microvascular architecture around the struts was more organised with fewer anastomoses (c.f. 2 weeks). Volkmann canals (many with attending capillaries), were observed both at the edges of the implants as well as within the pore structures. Cracks on the specimens and separation of regenerated bone (particularly around struts) is an artefact of processing for SEM. PB = pre-existing bone; Sc = scaffold; asterisk = new bone growth; m = mineralised matrix.

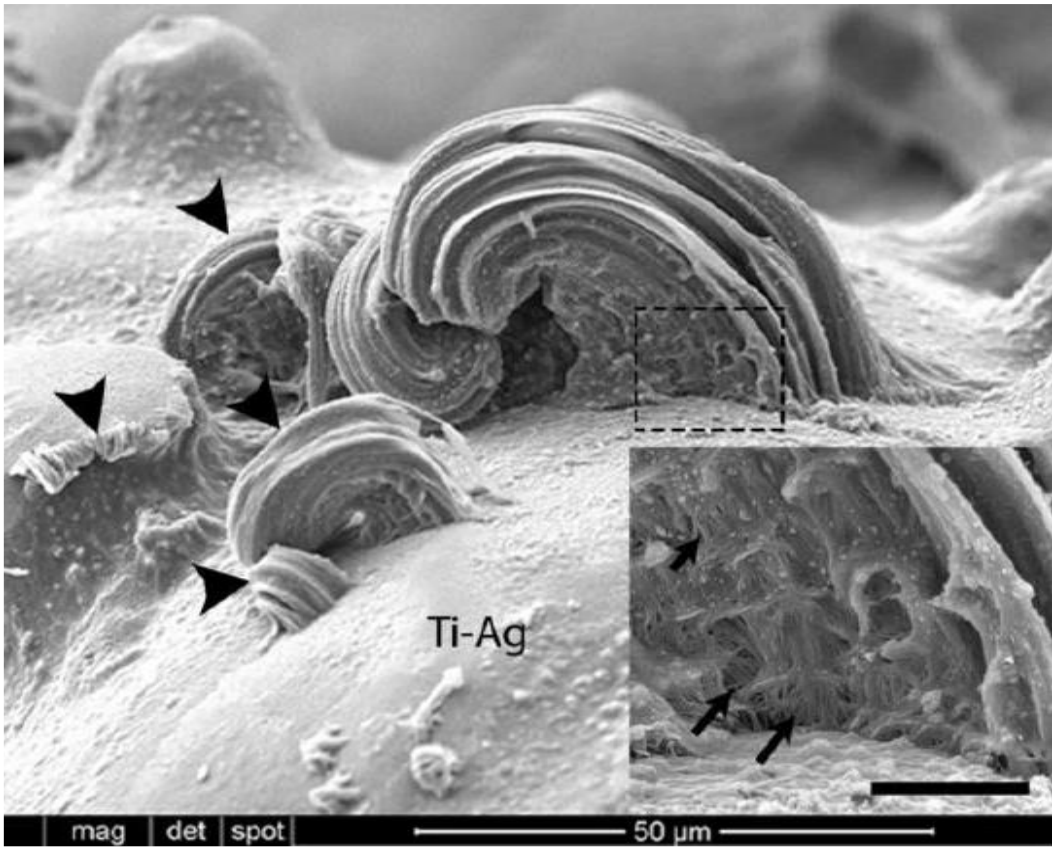

Figure 6: Scanning electron microscopy revealed conspicuous mineralized, hemi-tubular structures (arrowheads) attached to the surface of a Ti/Ag coated foam scaffold implanted for 2 weeks in a rat tibia. At higher magnification (inset from boxed area; bar = 5 µm), one of these structures exhibits aligned and mineralized fibre bundles (arrows) within concentric lamellae; structures that are consistent with formation of an early Haversian system directly on the material.

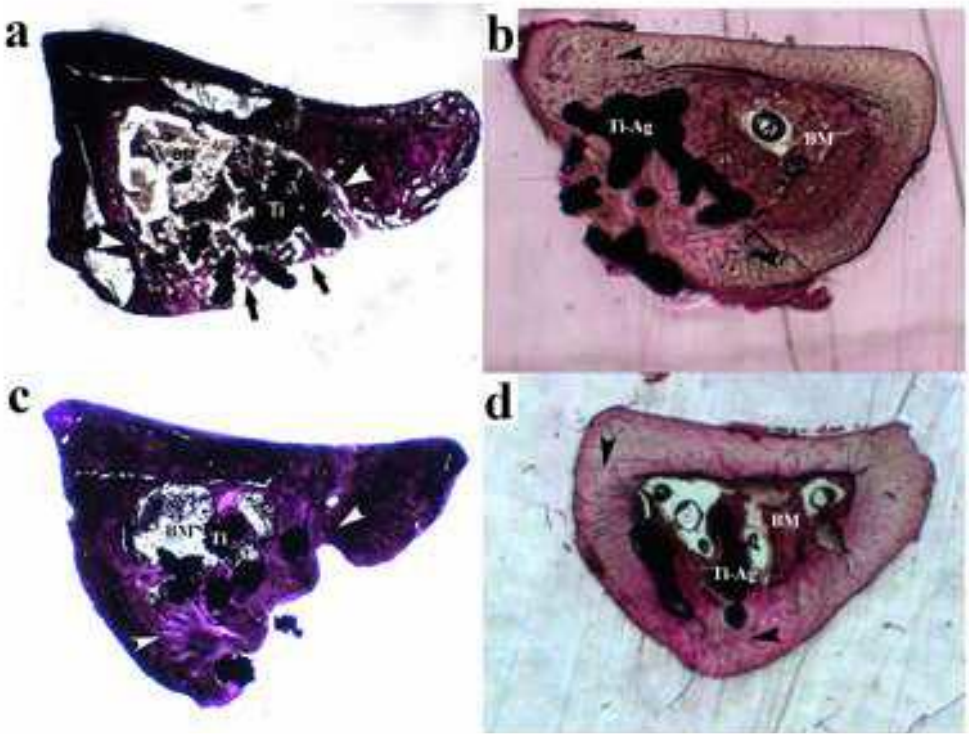

Figure 7: Light microscopic images of Haematoxylin and Eosin stained (50 – 100 µm thick) transverse sections from rat tibiae sampled at 2 (a & b) or 12 (b & d) weeks after implantation with either titanium (a & c) or nano-layer silver coated titanium (b & d). At 2 weeks, clear evidence of early bone deposition and dense connective tissue is seen surrounding the implants (between the black arrowheads). By 12 weeks there is a high proportion of bone within the lesion and it is in close apposition to the struts in both types of implant. Ti = titanium only; Ti/Ag = nano-layer coated titanium; BM = bone marrow. Monofilament suture used to secure muscle layers over implant (white arrows in a).

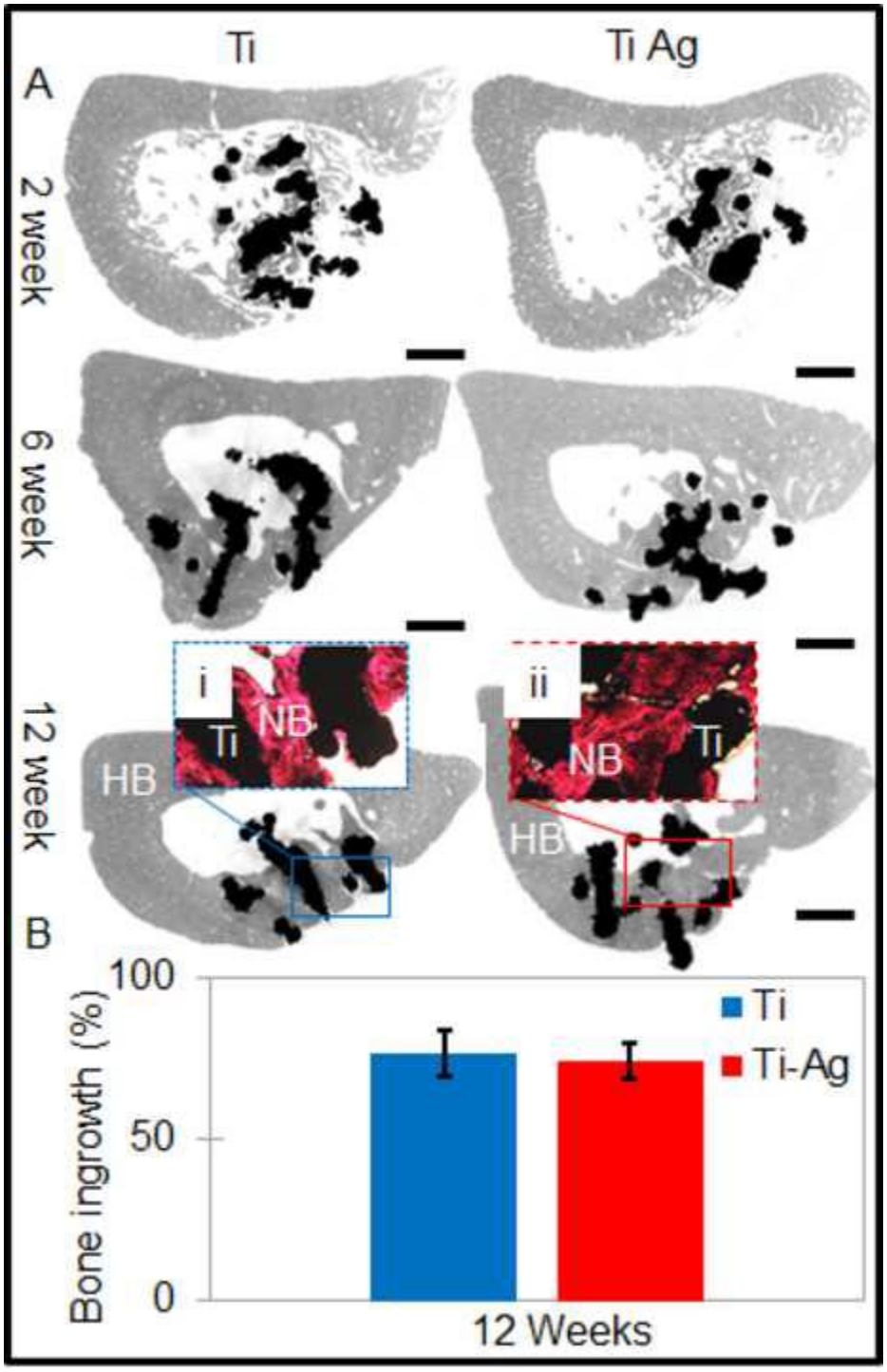

Figure 8: Representative microCT images of uncoated (Ti) and silver coated titanium scaffold (TiAg) at 2, 6 and 12 weeks post-implantation (a). At 12 weeks post-implantation, inset histology image (i. ii) shows comparable amount of newly formed bone in-growth in both groups, as confirmed by quantitative study of microCT data (b). Ti = Titanium insert, NB = new bone; HB = Host bone; Bar = 1mm.

References

[1] Geipel U, Herrmann M. [The infected implant. Part 1: bacteriology]. Orthopade. 2004;33:1411- 26; 27-8.
[2] Schwarzkopf R, Takemoto RC, Immerman I, Slover JD, Bosco JA. Prevalence of Staphylococcus aureus colonization in orthopaedic surgeons and their patients: a prospective cohort controlled study. The Journal of bone and joint surgery American volume. 2010;92:1815-9.
[3] Pedersen AB, Svendsson JE, Johnsen SP, Riis A, Overgaard S. Risk factors for revision due to infection after primary total hip arthroplasty. A population-based study of 80,756 primary procedures in the Danish Hip Arthroplasty Registry. Acta orthopaedica. 2010;81:542-7.
[4] Berbari EF, Hanssen AD, Duffy MC, Steckelberg JM, Ilstrup DM, Harmsen WS, et al. Risk factors for prosthetic joint infection: case-control study. Clinical infectious diseases : an official publication of the Infectious Diseases Society of America. 1998;27:1247-54.
[5] Zimmerli W, Ochsner PE. Management of infection associated with prosthetic joints. Infection. 2003;31:99-108.
[6] Nishimura S, Tsurumoto T, Yonekura A, Adachi K, Shindo H. Antimicrobial susceptibility of Staphylococcus aureus and Staphylococcus epidermidis biofilms isolated from infected total hip arthroplasty cases. J Orthop Sci. 2006;11:46-50.
[7] Gristina AG, Naylor P, Myrvik Q. Infections from biomaterials and implants: a race for the surface. Medical progress through technology. 1988;14:205-24.
[8] Hudetz D, Rod E, Radic A, Ivkovic A. Diagnosis and treatment of peri-prosthetic infections in total hip replacement. Medicinski glasnik : official publication of the Medical Association of Zenica- Doboj Canton, Bosnia and Herzegovina. 2012;9:152-9.
[9] Alt V, Bechert T, Steinrucke P, Wagener M, Seidel P, Dingeldein E, et al. An in vitro assessment of the antibacterial properties and cytotoxicity of nanoparticulate silver bone cement. Biomaterials. 2004;25:4383-91.
[10] Tunney MM, Ramage G, Patrick S, Nixon JR, Murphy PG, Gorman SP. Antimicrobial susceptibility of bacteria isolated from orthopedic implants following revision hip surgery. Antimicrobial agents and chemotherapy. 1998;42:3002-5.
[11] Schafroth M, Zimmerli W, Ochsner PE. The infected artificial hip joint: possibilities, follow-up and results of treatment. Praxis. 1999;88:2101-5.
[12] Schmalzried TP. The infected hip: Telltale signs and treatment options. J Arthroplasty. 2006;21:97-100.
[13] Sudmann E, Vik H, Rait M, Todnem K, Andersen KJ, Julsham K, et al. Systemic and Local Silver Accumulation after Total Hip-Replacement Using Silver-Impregnated Bone-Cement. Medical progress through technology. 1994;20:179-84.
[14] Josefsson G, Gudmundsson G, Kolmert L, Wijkstrom S. Prophylaxis with systemic antibiotics versus gentamicin bone cement in total hip arthroplasty. A five-year survey of 1688 hips. Clinical orthopaedics and related research. 1990:173-8.
[15] Alexander JW. History of the medical use of silver. Surgical infections. 2009;10:289-92.
[16] Russell AD, Hugo WB. Antimicrobial activity and action of silver. Progress in medicinal chemistry. 1994;31:351-70.
[17] Lansdown AB. Silver. I: Its antibacterial properties and mechanism of action. Journal of wound care. 2002;11:125-30.
[18] Liedberg H, Lundeberg T. Silver alloy coated catheters reduce catheter-associated bacteriuria. British journal of urology. 1990;65:379-81.
[19] Jung WK, Koo HC, Kim KW, Shin S, Kim SH, Park YH. Antibacterial activity and mechanism of action of the silver ion in Staphylococcus aureus and Escherichia coli. Appl Environ Microb. 2008;74:2171-8.
[20] Mullen L, Stamp RC, Brooks WK, Jones E, Sutcliffe CJ. Selective Laser Melting: a regular unit cell approach for the manufacture of porous, titanium, bone in-growth constructs, suitable for orthopedic applications. Journal of biomedical materials research Part B, Applied biomaterials. 2009;89:325-34.
[21] Mullen L, Stamp RC, Fox P, Jones E, Ngo C, Sutcliffe CJ. Selective laser melting: a unit cell approach for the manufacture of porous, titanium, bone in-growth constructs, suitable for orthopaedic applications. II. Randomized structures. Journal of biomedical materials research Part B, Applied biomaterials. 2010;92:178-88.
[22] Leskela M, Ritala M. Atomic layer deposition chemistry: Recent developments and future challenges. Angew Chem Int Edit. 2003;42:5548-54.
[23] Golrokhi Z, Chalker S, Sutcliffe CJ, Potter RJ. Self-limiting atomic layer deposition of conformal nanostructured silver films. Appl Surf Sci. 2016;364:789-97.
[24] Potter RJ, Chalker PR, Manning TD, Aspinall HC, Loo YF, Jones AC, et al. Deposition of HfO2, Gd2O3 and PrOx by Liquid Injection ALD Techniques. Chem Vap Deposition. 2005;11 159- 69.
[25] Della Valle C, Visai L, Santin M, Cigada A, Candiani G, Pezzoli D, et al. A novel antibacterial modification treatment of titanium capable to improve osseointegration. The International journal of artificial organs. 2012;35:864-75.

[26] Christensen GD, Simpson WA, Bisno AL, Beachey EH. Adherence of slime-producing strains of Staphylococcus epidermidis to smooth surfaces. Infection and immunity. 1982;37:318-26.
[27] Wagner J, Short K, Catto-Smith AG, Cameron DJ, Bishop RF, Kirkwood CD. Identification and characterisation of Pseudomonas 16S ribosomal DNA from ileal biopsies of children with Crohn's disease. PLoS One. 2008;3:e3578.
[28] Altschul SF, Madden TL, Schaffer AA, Zhang J, Zhang Z, Miller W, et al. Gapped BLAST and PSI-BLAST: a new generation of protein database search programs. Nucleic Acids Res. 1997;25:3389-402.
[29] Midha S, Kim TB, van den Bergh W, Lee PD, Jones JR, Mitchell CA. Preconditioned 70S30C bioactive glass foams promote osteogenesis in vivo. Acta biomaterialia. 2013;9:9169-82.
[30] Geng H, Todd NM, Devlin-Mullin A, Poologasundarampillai G, Kim TB, Madi K, et al. A correlative imaging based methodology for accurate quantitative assessment of bone formation in additive manufactured implants. J Mater Sci Mater Med. 2016;27:112.
[31] Smith BS, Yoriya S, Johnson T, Popat KC. Dermal fibroblast and epidermal keratinocyte functionality on titania nanotube arrays. Acta biomaterialia. 2011;7:2686-96.
[32] Besinis A, De Peralta T, Handy RD. Inhibition of biofilm formation and antibacterial properties of a silver nano-coating on human dentine. Nanotoxicology. 2014;8:745-54.
[33] Chen J, Bly RA, Saad MM, AlKhodary MA, El-Backly RM, Cohen DJ, et al. In-vivo study of adhesion and bone growth around implanted laser groove/RGD-functionalized Ti-6Al-4V pins in rabbit femurs. Materials Science and Engineering: C. 2011;31:826-32.
[34] Jin G, Qin H, Cao H, Qian S, Zhao Y, Peng X, et al. Synergistic effects of dual Zn/Ag ion implantation in osteogenic activity and antibacterial ability of titanium. Biomaterials. 2014;35:7699-713.
[35] Cheng H, Xiong W, Fang Z, Guan H, Wu W, Li Y, et al. Strontium (Sr) and silver (Ag) loaded nanotubular structures with combined osteoinductive and antimicrobial activities. Acta biomaterialia. 2016;31:388-400.
[36] Svensson S, Suska F, Emanuelsson L, Palmquist A, Norlindh B, Trobos M, et al. Osseointegration of titanium with an antimicrobial nanostructured noble metal coating. Nanomedicine. 2013;9:1048-56.
[37] Ritala M, Kukli K, Rahtu A, Raisanen PI, Leskela M, Sajavaara T, et al. Atomic layer deposition of oxide thin films with metal alkoxides as oxygen sources. Science. 2000;288:319-21.
[38] Ritala M, Leskela M, Dekker JP, Mutsaers C, Soininen PJ, Skarp J. Perfectly conformal TiN and Al2O3 films deposited by atomic layer deposition. Chem Vapor Depos. 1999;5:7-9.
[39] Qiao S, Cao H, Zhao X, Lo H, Zhuang L, Gu Y, et al. Ag-plasma modification enhances bone apposition around titanium dental implants: an animal study in Labrador dogs. Int J Nanomedicine. 2015;10:653-64.
[40] Tsukamoto M, Miyamoto H, Ando Y, Noda I, Eto S, Akiyama T, et al. Acute and subacute toxicity in vivo of thermal-sprayed silver containing hydroxyapatite coating in rat tibia. Biomed Res Int. 2014;2014:902343.
[41] Prokopovich P, Kobrick M, Brousseau E, Perni S. Potent antimicrobial activity of bone cement encapsulating silver nanoparticles capped with oleic acid. Journal of biomedical materials research Part B, Applied biomaterials. 2015;103:273-81.
[42] Eto S, Miyamoto H, Shobuike T, Noda I, Akiyama T, Tsukamoto M, et al. Silver oxidecontaining hydroxyapatite coating supports osteoblast function and enhances implant anchorage strength in rat femur. Journal of orthopaedic research: official publication of the Orthopaedic Research Society. 2015;33:1391-7.
[43] Khalilpour P, Lampe K, Wagener M, Stigler B, Heiss C, Ullrich MS, et al. Ag/SiO(x)C(y) plasma polymer coating for antimicrobial protection of fracture fixation devices. Journal of biomedical materials research Part B, Applied biomaterials. 2010;94:196-202.
[44] Akiyama T, Miyamoto H, Yonekura Y, Tsukamoto M, Ando Y, Noda I, et al. Silver oxide containing hydroxyapatite coating has in vivo antibacterial activity in the rat tibia. Journal of orthopaedic research : official publication of the Orthopaedic Research Society. 2013;31:1195-200.
[45] Tarquinio KM, Kothurkar NK, Goswami DY, Sanders RC, Jr., Zaritsky AL, LeVine AM. Bactericidal effects of silver plus titanium dioxide-coated endotracheal tubes on Pseudomonas aeruginosa and Staphylococcus aureus. Int J Nanomedicine. 2010;5:177-83.
[46] Liu Y, Zheng Z, Zara JN, Hsu C, Soofer DE, Lee KS, et al. The antimicrobial and osteoinductive properties of silver nanoparticle/poly (DL-lactic-co-glycolic acid)-coated stainless steel. Biomaterials. 2012;33:8745-56.
[47] Uhm SH, Song DH, Kwon JS, Lee SB, Han JG, Kim KN. Tailoring of antibacterial Ag nanostructures on TiO2 nanotube layers by magnetron sputtering. Journal of biomedical materials research Part B, Applied biomaterials. 2014;102:592-603.
[48] Necula BS, van Leeuwen JP, Fratila-Apachitei LE, Zaat SA, Apachitei I, Duszczyk J. In vitro cytotoxicity evaluation of porous TiO(2)-Ag antibacterial coatings for human fetal osteoblasts. Acta biomaterialia. 2012;8:4191-7.

[49] Bostancioglu RB, Peksen C, Genc H, Gurbuz M, Karel FB, Koparal AS, et al. Analyses of the modulatory effects of antibacterial silver doped calcium phosphate-based ceramic nano-powder on proliferation, survival, and angiogenic capacity of different mammalian cells in vitro. Biomed Mater.
2015;10:045024.
[50] Guo H, Zhang J, Boudreau M, Meng J, Yin JJ, Liu J, et al. Intravenous administration of silver nanoparticles causes organ toxicity through intracellular ROS-related loss of inter-endothelial junction. Part Fibre Toxicol. 2016;13:21.
[51] Cochis A, Azzimonti B, Della Valle C, Chiesa R, Arciola CR, Rimondini L. Biofilm formation on titanium implants counteracted by grafting gallium and silver ions. Journal of biomedical materials research Part A. 2015;103:1176-87.
[52] Nath S, Kalmodia S, Basu B. Densification, phase stability and in vitro biocompatibility property of hydroxyapatite-10 wt% silver composites. J Mater Sci Mater Med. 2010;21:1273-87.
[53] Verne E, Miola M, Vitale Brovarone C, Cannas M, Gatti S, Fucale G, et al. Surface silver doping of biocompatible glass to induce antibacterial properties. Part I: Massive glass. J Mater Sci Mater Med. 2009;20:733-40.
[54] Choi IH, Ahn JH, Chung CY, Cho TJ. Vascular proliferation and blood supply during distraction osteogenesis: a scanning electron microscopic observation. Journal of orthopaedic research: official publication of the Orthopaedic Research Society. 2000;18:698-705.
[55] Pazzaglia UE, Congiu T, Ranchetti F, Salari M, Dell'Orbo C. Scanning electron microscopy study of bone intracortical vessels using an injection and fractured surfaces technique. Anatomical science international. 2010;85:31-7.
[56] Donos N, Retzepi M, Wall I, Hamlet S, Ivanovski S. In vivo gene expression profile of guided bone regeneration associated with a microrough titanium surface. Clin Oral Implants Res. 2011;22:390-8.
[57] Chang CS, Su CY, Lin TC. Scanning electron microscopy observation of vascularization around hydroxyapatite using vascular corrosion casts. Journal of biomedical materials research. 1999;48:411-6.
[58] Gung YW, Cheng CK, Su CY. A stereomorphologic study of bone matrix apposition in HAimplanted cavities observed with SEM, being prepared by a microvascular cast and freeze-fracture method. Medical engineering & physics. 2003;25:565-71.
[59] Morini S, Continenza MA, Ricciardi G, Gaudio E, Pannarale L. Development of the microcirculation of the secondary ossification center in rat humeral head. The anatomical record Part A, Discoveries in molecular, cellular, and evolutionary biology. 2004;278:419-27.
[60] Pazzaglia UE, Bonaspetti G, Ranchetti F, Bettinsoli P. A model of the intracortical vascular system of long bones and of its organization: an experimental study in rabbit femur and tibia. Journal of anatomy. 2008;213:183-93. [61] Cheng H, Li Y, Huo K, Gao B, Xiong W. Long-lasting in vivo and in vitro antibacterial ability of nanostructured titania coating incorporated with silver nanoparticles. Journal of biomedical materials research Part A. 2014;102:3488-99.

Appendix B

SLM Background information

In order to explain the SLM sample preparation, a general introduction about this manufacturing technique is initially provided. Selective Laser Melting (SLM) is a layer by layer manufacturing technique which utilise a high energy laser beam (up to 400 W which melt the powder in place and bond it into the prior layer)[399] and is mainly used to generate complex and relatively small components which can be designed based on CAD files. Therefore, SLM can almost produce any complex geometry with reduced manufacturing times and cost in the pre-production stage[400]. Using 3D CAD model allows designers more freedom in producing various designs (both dense and highly porous geometries) and choosing a wide range of materials including titanium, aluminium, nickel-based alloys, stainless steel, etc[401]. A laser source, a sealed building chamber, a platform for making the part, a scanning system, a powder container and a scraper are the most important elements of an SLM machine[402]. Figure A represents a schematic of a SLM machine.

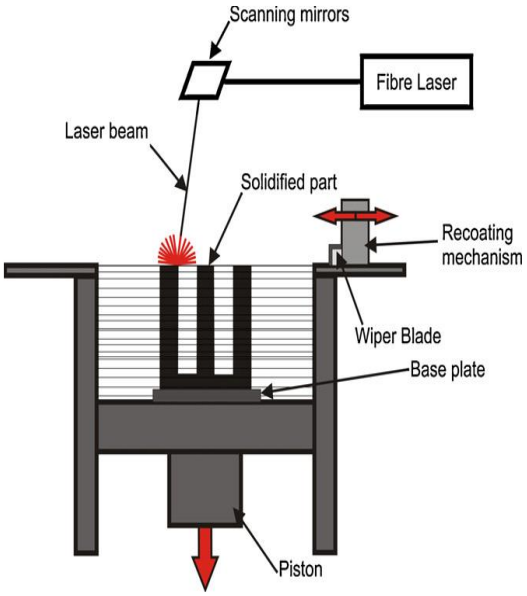

Figure A: *Principle of SLM machine*[403]

Pogson et al[404] was the first person who utilized an in house SLM machine (famous as Direct Metal Laser Re-Melting (DMLR)) at the University of Liverpool in 1996. The machine was able to construct both solid and porous structures via a 90W Nd: YAG laser. The ability to build porous structures allows this manufacturing technology to produce structures with similar mechanical and physical properties to human bones which can help the promotion of bone-in-growth[87].

Appendix C

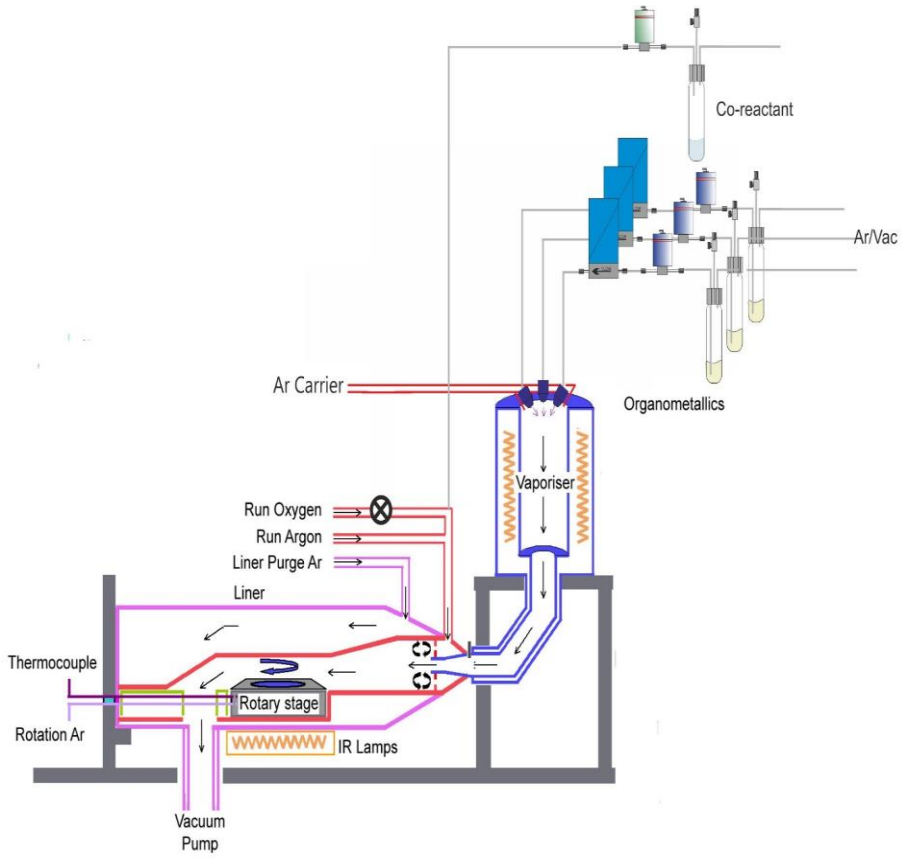

Figure B: *Schematic illustration of Aixtron AIX 200 FE system*[307]

Appendix D

QCM Background information

Quartz Crystal Microbalance (QCM) has been widely adapted for in-situ monitoring of ALD processes as it is highly sensitive to mass deposition on the crystal surface. It is sensitive enough to detect the mass gain and mass losses associated with individual ALD 'half cycles' and can therefore provide useful information on the surface reaction mechanisms[405]. QCM depends on piezoelectric resonance effect, by applying AC voltage the crystal start into mechanical oscillation at a frequency which is relevant to the crystal mass per unit area[181]. Any mass loss or gain on the crystal surface is measurable by the QCM due to high sensitivity of the QCM frequency. Shear mode is the most common oscillation or resonance mode in mass sensing applications (moving along the thickness direction of the disk surface)[406]. The change into the frequency by absorbing molecules onto the crystal surface can be explained by the Sauerbrey equation[407], which is proportional to reducing the resonance frequency by absorbing of the molecules onto the sensor.

$$\Delta f = - C_r . \Delta m \qquad \text{(Eq.1)}$$

Where Δf is the observed frequency change (HZ), Δm is the change in mass per unit area (g/cm²), and C_r is the sensitive factor for the crystal which used.

$$C_r = 2f_0^2 / (\rho_c \times \mu_c)^{1/2} \qquad \text{(Eq.2)}$$

Where f_0 is the crystal natural resonant frequency (Hz), ρ_c is the density of the crystal (g/cm³), and μ_c is the crystal shear modulus (g/cm s²).

Appendix E

Details of repeats of weight gain measurements have been shown in the table below.

Weights	Ref wafer		Start			End		
Gain	Start	End	1	2	3	1	2	3
0.00043	1.36668	1.36667	11.41487	11.41487	11.41488	11.41527	11.41528	11.41532
0.00032	1.36668	1.36667	10.61291	10.61291	10.61290	10.61321	10.61322	10.61323
0.00012	1.36668	1.36667	10.96029	10.96026	10.96028	10.96038	10.96038	10.96039
0.00046	1.36668	1.36666	10.83490	10.83488	10.83486	10.83532	10.83531	10.83534
0.00040	1.36668	1.36666	10.76653	10.76652	10.76654	10.76693	10.76690	10.76690
0.00032	1.36668	1.36666	11.00989	11.00988	11.00989	11.01020	11.01019	11.01018
-0.00008	1.36667	1.36666	11.65589	11.65590	11.65591	11.65581	11.65581	11.65582
-0.00003	1.36667	1.36666	10.98411	10.98411	10.98412	10.98408	10.98407	10.98407
-0.00038	1.36667	1.36666	11.26662	11.26661	11.26660	11.26622	11.26622	11.26622
0.00009	1.36665	1.36667	11.28006	11.28007	11.28007	11.28017	11.28019	11.28018
0.00005	1.36665	1.36667	10.81677	10.81676	10.81675	10.81683	10.81683	10.81683
0.00014	1.36665	1.36667	10.61781	10.61781	10.61780	10.61795	10.61798	10.61796
0.00020	1.36666	1.36666	11.56475	11.56478	11.56477	11.56497	11.56497	11.56497
0.00021	1.36666	1.36666	10.83869	10.83870	10.83868	10.83890	10.83889	10.83890
0.00023	1.36666	1.36666	11.27848	11.27849	11.27847	11.27871	11.27871	11.27870
0.00013	1.36668	1.36668	10.83899	10.83902	10.83899	10.83914	10.83913	10.83912
0.00003	1.36668	1.36668	0.36628	0.36628	0.36628	0.36632	0.36630	0.36631
0.00015	1.36668	1.36668	10.25383	10.25382	10.25380	10.25397	10.25397	10.25397
0.00014	1.36668	1.36668	11.14729	11.14729	11.14727	11.14741	11.14743	11.14742
0.00014	1.36666	1.36665	11.19351	11.19350	11.19347	11.19362	11.19362	11.19362

0.00007	1.36666	1.36665	11.43316	11.43315	11.43314	11.43323	11.43320	11.43320
0.00014	1.36666	1.36665	11.06874	11.06875	11.06876	11.06888	11.06888	11.06887
-0.00001	1.36667	1.36666	10.99564	10.99566	10.99563	10.99564	10.99563	10.99561
0.00003	1.36667	1.36666	11.14910	11.14912	11.14908	11.14910	11.14912	11.14913
0.00005	1.36667	1.36666	11.73746	11.73747	11.73745	11.73750	11.73750	11.73749
0.00026	1.36667	1.36666	10.66773	10.66772	10.66772	10.66796	10.66797	10.66798
0.00031	1.36667	1.36666	10.88514	10.88513	10.88512	10.88542	10.88543	10.88544
0.00044	1.36667	1.36666	10.85903	10.85905	10.85904	10.85944	10.85948	10.85949
0.00019	1.36666	1.36666	11.37897	11.37895	11.37898	11.37916	11.37916	11.37916
0.00000	1.36666	1.36666	11.13387	11.13384	11.13385	11.13385	11.13385	11.13385
-0.00001	1.36666	1.36666	11.23313	11.23311	11.23311	11.23311	11.23311	11.23311
0.00050	1.36667	1.36664	11.59670	11.59669	11.59670	11.59717	11.59717	11.59715
0.00050	1.36667	1.36664	10.86078	10.86077	10.86079	10.86124	10.86126	10.86125
0.00029	1.36667	1.36664	11.00849	11.00851	11.00852	11.00878	11.00876	11.00875
0.00002	1.36666	1.36663	11.01642	11.01640	11.01640	11.01638	11.01640	11.01640
0.00006	1.36666	1.36663	10.33041	10.33039	10.33039	10.33042	10.33042	10.33044
0.00005	1.36666	1.36663	11.16235	11.16234	11.16232	11.16236	11.16236	11.16236
0.00020	1.36667	1.36668	10.77117	10.77116	10.77116	10.77136	10.77139	10.77137
0.00014	1.36667	1.36668	10.89833	10.89833	10.89831	10.89847	10.89847	10.89847
0.00016	1.36667	1.36668	11.28784	11.28786	11.28786	11.28802	11.28803	11.28803
0.00019	1.36666	1.36666	11.33756	11.33755	11.33757	11.33775	11.33774	11.33775
0.00014	1.36666	1.36666	10.47378	10.47376	10.47375	10.47390	10.47390	10.47391
0.00011	1.36666	1.36666	11.00159	11.00158	11.00158	11.00170	11.00169	11.00169
0.00007	1.36666	1.36668	10.91832	10.91833	10.91834	10.91841	10.91842	10.91844
0.00002	1.36666	1.36668	11.11823	11.11823	11.11822	11.11828	11.11823	11.11829

0.00006	1.36666	1.36668	11.05169	11.05172	11.05170	11.05178	11.05177	11.05179
0.00040	1.36667	1.36670	11.01958	11.01962	11.01960	11.02003	11.02003	11.02003
0.00028	1.36667	1.36670	10.85411	10.85409	10.85410	10.85443	10.85441	10.85440
0.00023	1.36667	1.36670	11.06351	11.06351	11.06350	11.06377	11.06375	11.06377

Appendix F

XRD Background information

X-ray diffraction (XRD) was employed to provide information about the microstructure of samples. This technique has been widely used in this study to examine the crystal structures and the phase compositions of the deposited films. In 1895, Wilhelm Rontgen was a first person who discovered X-rays and was awarded the very first Nobel Prize in Physics in 1901[408,409]. In 1912 Max Laue proposed the first diffraction experiment from a single crystal[410]. Since 1901, more than 24 researchers have won Nobel Prizes connected with X-ray diffraction studies[411].

X-rays are electromagnetic radiation with wavelengths between 0.01 and 10 nm. X-rays can be generated when electrons accelerated from a high voltage source collide with the target (the most broadly used target for XRD is copper with a Kα wavelength of λ=1.5405 Å[309]) to ionise electrons in K and L shells (core-shell electrons). Electrons exited to higher energy levels and then, x-ray photons are emitted as they return back to their original energy levels. X-rays are also emitted by backscattering[412] (backscattering radiation) giving a broad band spectra. X-rays from Kα and Kβ are formed by transition from 2p-1s and 3p-1s respectively[413]. Figure C shows a schematic of XRD detection process where the constructive interference of x-rays reflecting

off crystallographic planes[181]. The angle of incidence of the two parallel x-rays is θ[414]. When the lattice planes are parallel to each other, the diffracted beams will create constructive interference and this is known as the Bragg condition (Bragg's Law)[415].

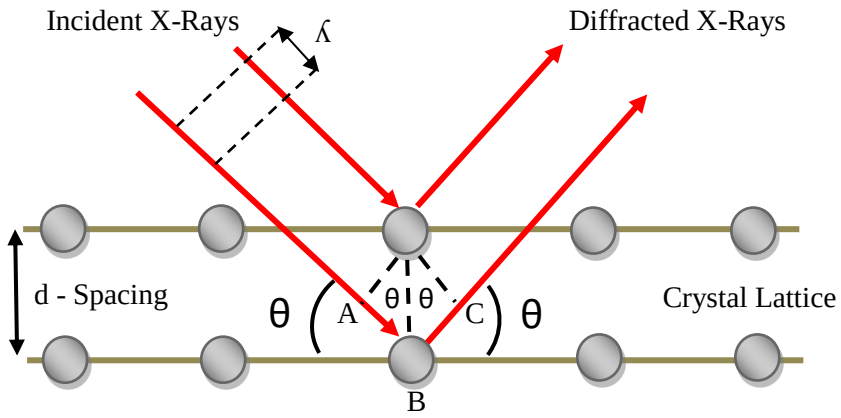

Figure C: *A schematic of diffraction geometry by Bragg's Law*

The d-spacing (the distance between the parallel (hkl) crystallographic planes) can be calculated by Braggs' law in Equation 3.

$$2d_{hkl} \sin \theta = n \lambda \qquad \text{(Eq. 3)}$$

where n is an integer, d is the atomic spacing of the planes (Å), λ is the x-rays wavelength (Å) and θ is the diffraction angle (°). By plotting the diffraction data (Equation. 3) and analysing the peak position via peak fitting of Gaussian function, some information such as the crystal structure, the lattice spacing, the crystalline size, phase and preferred orientation can be obtained. Experimental diffraction data can be compared with reference spectra from source samples as the Cambridge Structure Database (CSD) and International Centre for Diffraction Data (ICDD) which are the two mostly familiar sources of references of inorganic and organic spectra.

Figure D illustrates the main parts of the equipment. Scans between 5° and 150° with minimum speed down to 0.01° per minute were achievable based on the XRD arrangement. The measurement optimisation conditions was modified by Paul Marshal (University of Liverpool) for thin film characterization using the Rigaku Miniflex and has been used in this study[309]. XRD is a non-contact and non-destructive measurement technique with no need of sample preparation. Therefore, samples were used after ALD deposition with no additional preparation with surface area of 5 to 10 mm^2 for each experiment. In order to setup the diffraction measurements, the sample should be located in the centre part of the sample holder and horizontally aligned. The quality of the data is strongly dependent on the scan speed.

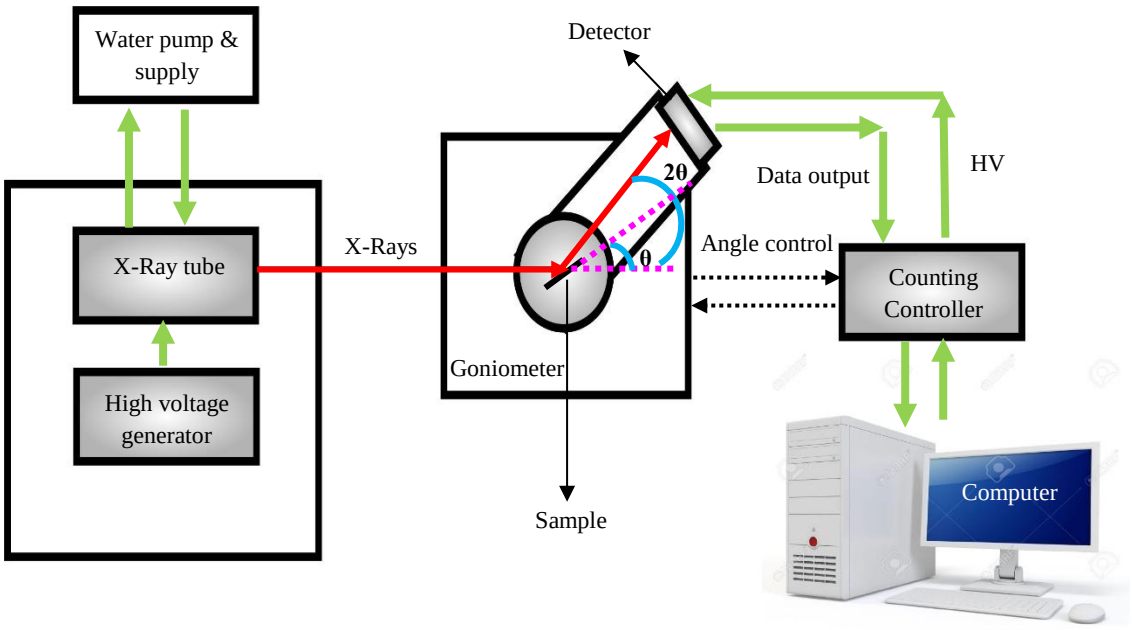

Figure D: *Main elements of Rigaku Miniflex*[309]

Appendix G

SEM Background information

Scanning Electron Microscope (SEM) was used to characterize the film microstructure and morphology in which used a primary electron beam scans to gather signals generated from electron beam interactions with the specimen (limited by the wavelength of electrons)[416] and therefore produce two-dimensional images[417]. An SEM requires an electron source, a series of EM lenses and apertures, specimen stage, vacuum chamber and observation system and recording. An electron gun is placed at the top of the SEM to produce an electron beam where the beam diameter is controlled by EM condenser lenses and focused on the sample which is mounted and secured on the specimen stage[418]. The beam then passes through apertures which are used to decrease and eliminate extraneous electrons in the lenses[419]. Finally, the images are produced via scanning system under high vacuum system (pressure ~ 5×10^{-5})[419,420,419]. Both secondary electrons (SE's) and back scattered electrons (BSE's) were used in this research.

Appendix H

AFM Background information

Atomic Force Microscopy (AFM) was first introduced by Binning, Quate and Gerber in 1986[421] and was utilized to investigate the surface topography of films at the atomic scale. This technique is a well-known method of surface scanning due to ease of specimen preparation and sub-nanometre vertical resolution. It is able to measure sub-nanometre average roughness (Ra) and the root mean square roughness (RMS) of the deposited films by ALD. Both RMS and Ra are extensively used in order to show the roughness of the surface with the only difference in

their calculations formulas[422]. AFM consists of a flexible cantilever connected to a sharp tip (<10 nm) which probe a specified area of the surface with a driven constant force controlled by applying voltage to a piezoelectric transducers (PZT) typically located under the sample holder. Tips are usually made from Si_3N_4 or Si[423] with tip-sample separations of 0.2-10 nm[424]. Figure E illustrates a configuration of a typical AFM.

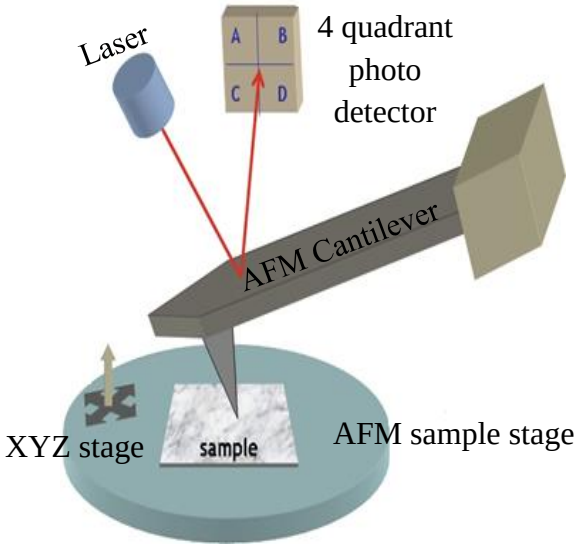

Figure E: *schematic illustration of AFM main components*[425]

AFMs can be used in the XYZ directions with the magnification ranging from 10^3 to 10^9 in order to obtain high resolution images in any types of environment including liquids, vacuum, ambient air, etc[426]. The ability to probe insulator and conductor samples by AFM is one of the most important advantages that this technique has over other techniques such as Scanning Tunnelling Microscope (STM), which can only scan conductive samples[427].

AFM operates in three imaging modes known as contact mode, tapping mode and non-contact mode (Figure F). Contact mode is the most common mode with fast scanning and it happens when the deflection of the cantilever is kept constant. Tapping mode is also referred to as dynamic force microscopy is usually used for soft surfaces (biological materials) to decrease the effects of friction with a very sharp tip. The tip is deflected by Van der Waals forces in a

constant distance from the specimen's surface (40-50 Å)[428,238]. In Non-contact mode on the other hand, the tip does not contact the specimen's surface and is oscillated with the constant amplitude at the resonance frequency. This mode usually use in ultra-high vacuum environment to have good quality images. For all modes, to image the topography, the cantilever deflection is monitored usually by at least a 4 quadrant photodiode which has the ability to detect the movement of the cantilever using a laser beam reflected from the tip[309]. Hence, this process ultimately provides an image of the specimen's surface.

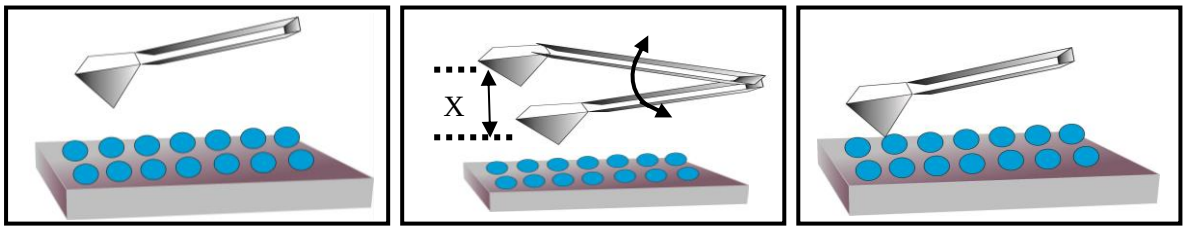

Figure F: *Three imaging modes in AFM: Left: Non-contact mode, Middle: Tapping mode, Right: Contact mode* [428]

Appendix I

XPS Background information

X-ray Photoelectron Spectroscopy (XPS), also known as Electron Spectroscopy for Chemical Analysis (ESCA) has become a widely used technique to explore the near surface chemical composition and bonding states. It is typically sensitive to concentrations as low as 0.1 at % except for H and He[429]. Kai Siegbahn and his co-workers developed the observation of peak intensities that corresponded to specific electron shell and could be used for quantitative analysis of composition and evaluating chemical bonding (in early 1960 at the University of Uppsala, Sweden)[430,431]. Figure G represents a schematic of the typical experimental arrangement for X-ray photoelectron spectrometer which consists of an X-ray source, an electron energy analyser joined with a detection system, a sample stage within an ultra-high vacuum system (< 10^{-9} Torr), and a computer to control and operate the equipment[432]. The ultra-high vacuum system is needed for two reasons: one is that electrons loss energy if they interact with residual gas molecules. Another reason is that scanning under high vacuum (< 10^{-9} Torr) avoids the formation of a monolayer of air contamination absorbed on the surface[433].

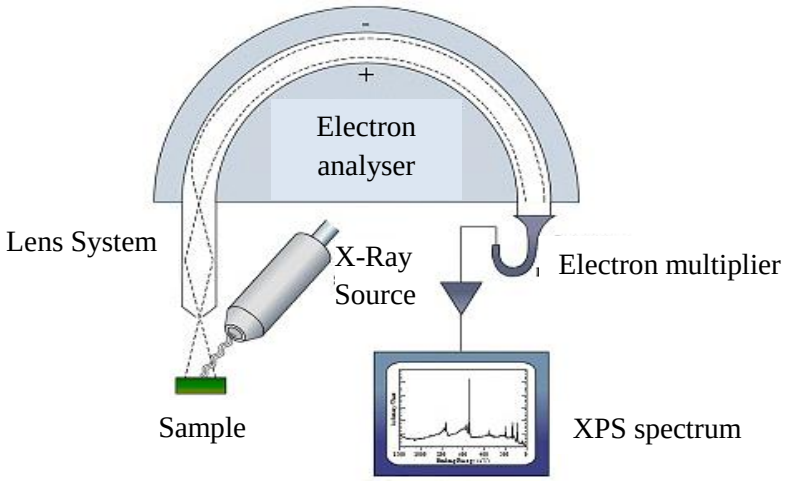

Figure G: *Diagram of the typical experimental arrangement for X-ray photoelectron spectrometer*[434]

In the XPS operation process, the specimen is bombarded by the x-rays and electrons absorb energy and irradiate, resulting in ejecting photoelectrons. The ejected photoelectrons from atomic energy levels can be identified by their relevant kinetic energies. X-rays can penetrate up to 1 µm depth, however electrons cannot escape as they are inelastic scattered and the ejected electrons are only the ones closer to the surface (up to 10 nm)[238].

Appendix J

FPP Background information

Four Point Probe is a simple technique to measure the sheet resistance resistivity of conductive thin films or bulk specimen to establish the electrical resistivity by using four in line equally spaced metal probes at the surface. Figure H represents a schematic of the setup. A constant current is applied through the two outer tips while the voltage is measured between the inners two probes.

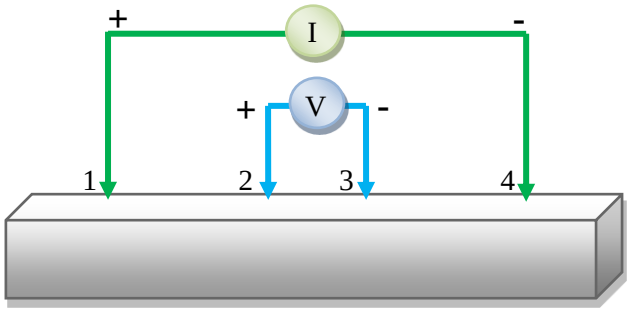

Figure H: *A schematic of a four point probe configuration (4 tips on the deposited film)*

The sheet resistance (R) can be calculated using the Equation 4, if the film thickness (t) is considerably smaller than the spacing of the tips (< 0.4)[435]. This is due to the fact that in thin films, the current forms as rings and therefore, the affected area is $A = 2\pi xt$.

$$R = 4.532 \times V/I \ (\Omega/cm) \qquad \text{(Eq.4)}$$

The electrical resistivity, ρ (Ω.cm) is then obtained by multiplying the film thickness (t) as it is shown in Equation 5.

$$\rho = R \times t \qquad \text{(Eq.5)}$$

Appendix K

XRD for Butan-1-ol for Chapter 4:

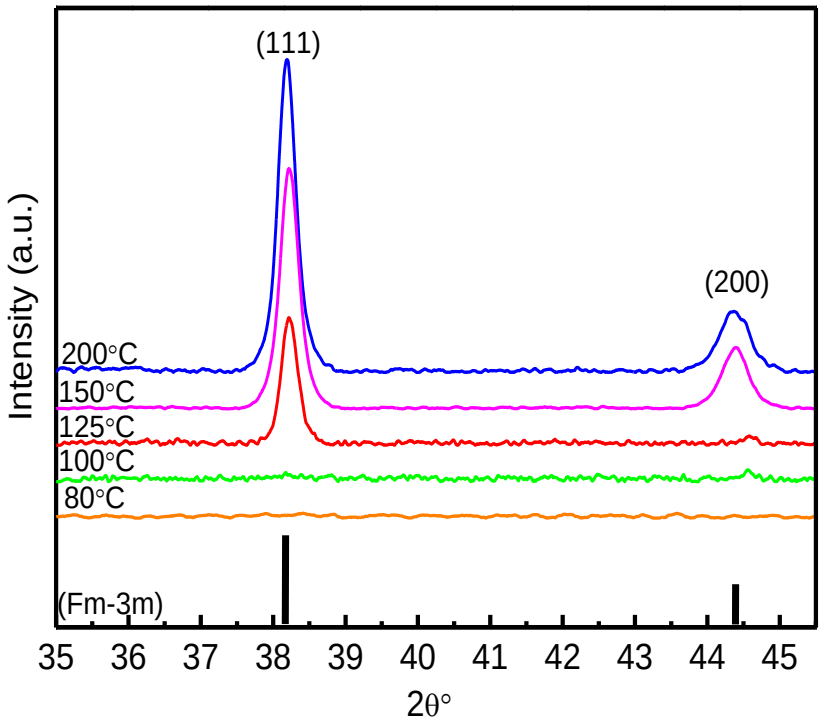

X-ray diffraction patterns of Ag NPs deposited at various temperatures for 500 ALD cycles using 4 s butan-1-ol doses as a co-reactant

Appendix L

AFM for Butan-1-ol for Chapter 4

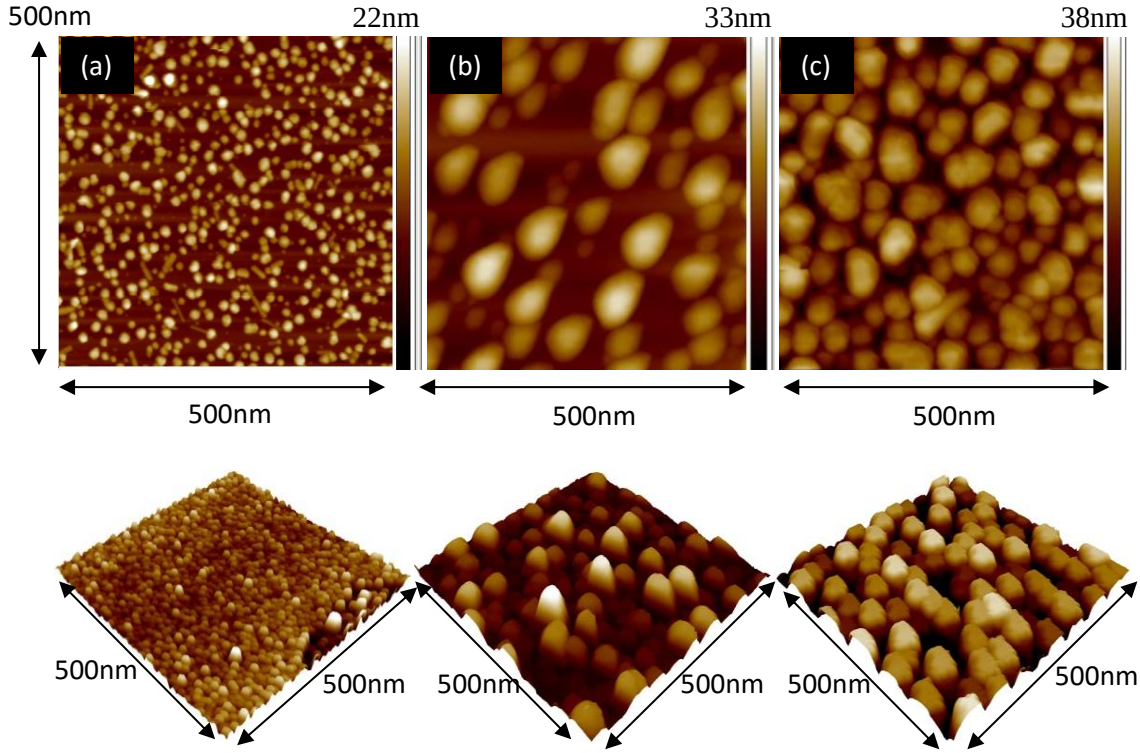

AFM images of silver coated samples using 4 s butan-1-ol doses grown at a) 125 °C, b) 150 °C, and c) 200 °C for same ALD cycles. The top images are 2D images and the bottom images are 3D images of the same samples

Appendix M

SEM for Butan-1-ol for Chapter 4

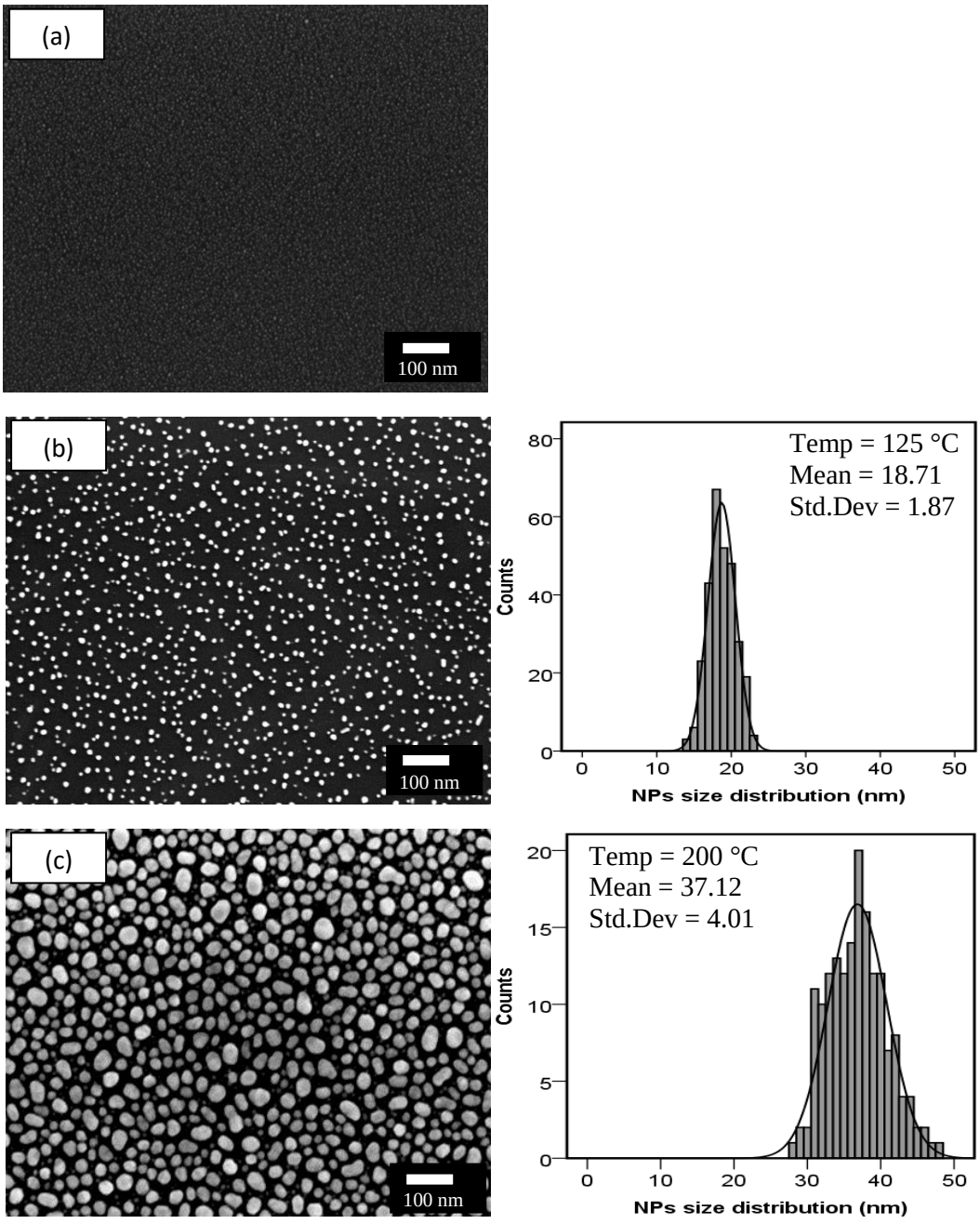

High-resolution SEM images of ALD of silver nanoparticles as a function of temperature at a) 80 °C, b) 125 °C and c) 200 °C with 4 s butan-1-ol dose for 500 cycle

Appendix N

Figure below shows two random selections of SEM images from internal surface of the porous sample. It is clear that silver goes down uniformly on internal sections of the sample. These tests have been applied to more than 30 different coated samples by randomly sampling at least four areas to ensure that the resulting data was representative of the whole.

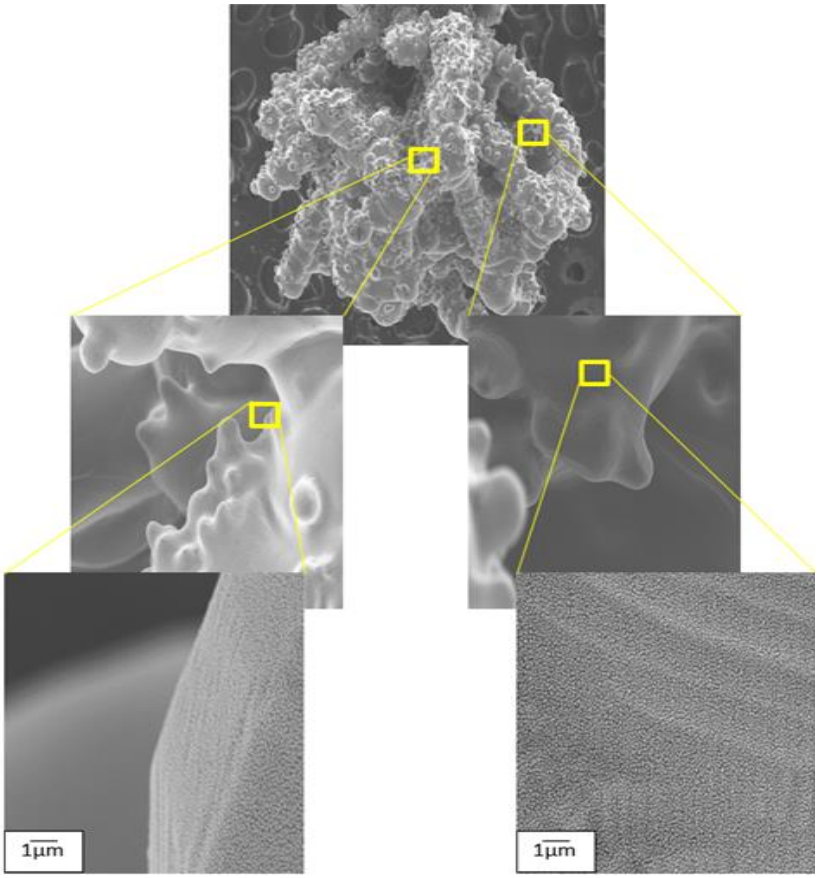

SEM images showing uniform coating of Ag NPs on internal surface of porous samples

Appendix O

SEM for Hs27 cell line on Titanium and Titanium silver coated solid implants for Chapter 6

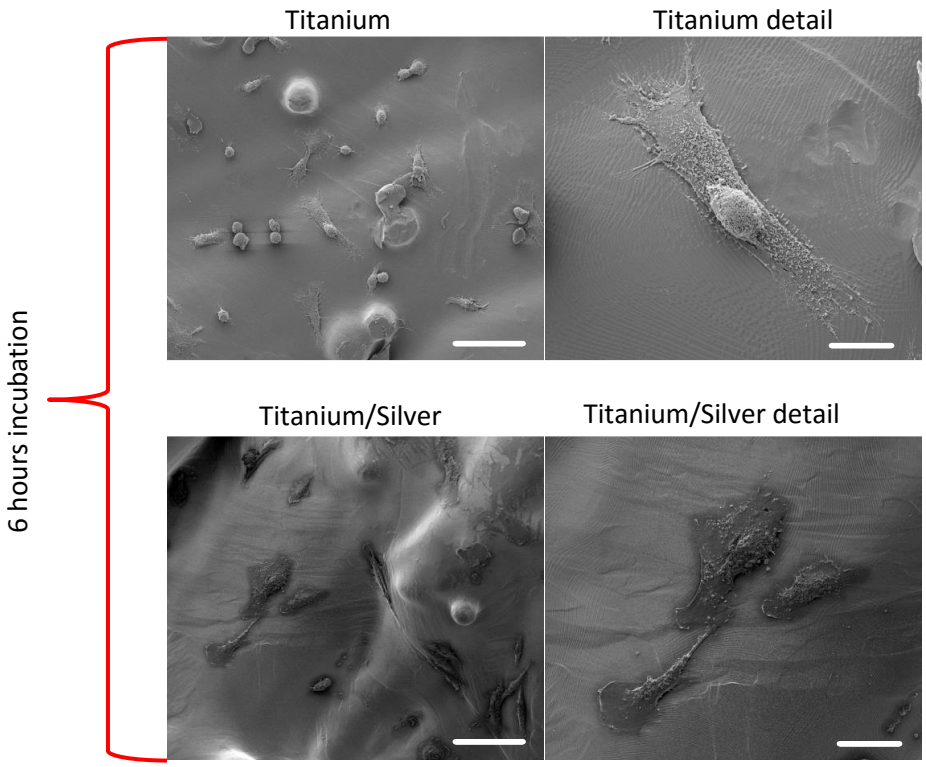

SEM images after 6 hours of incubation of Hs27 on un-coated titanium solid structure and silver coated titanium solid structure. (Bar = 100 µm and 50 µm)

Appendix P

Vascular casting for Chapter 6

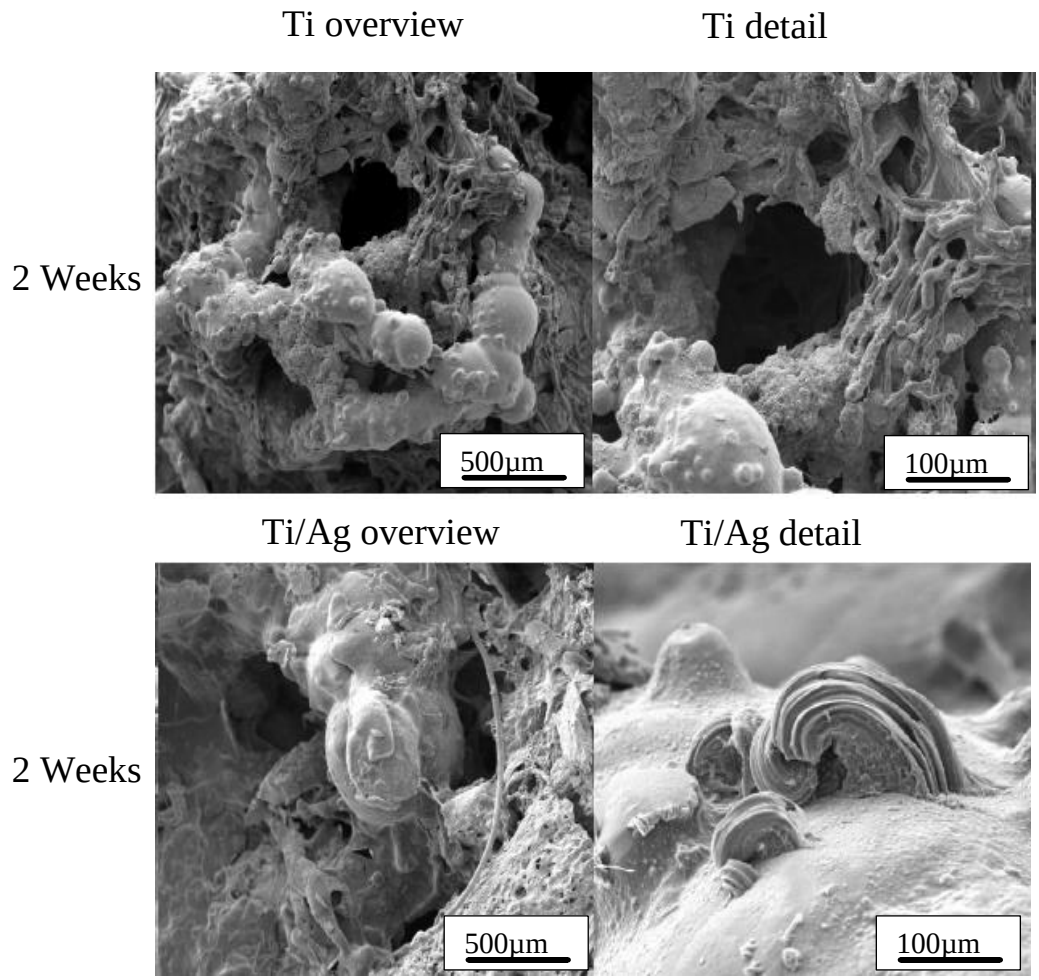

Appendix Q

Vascular casting for Chapter 6

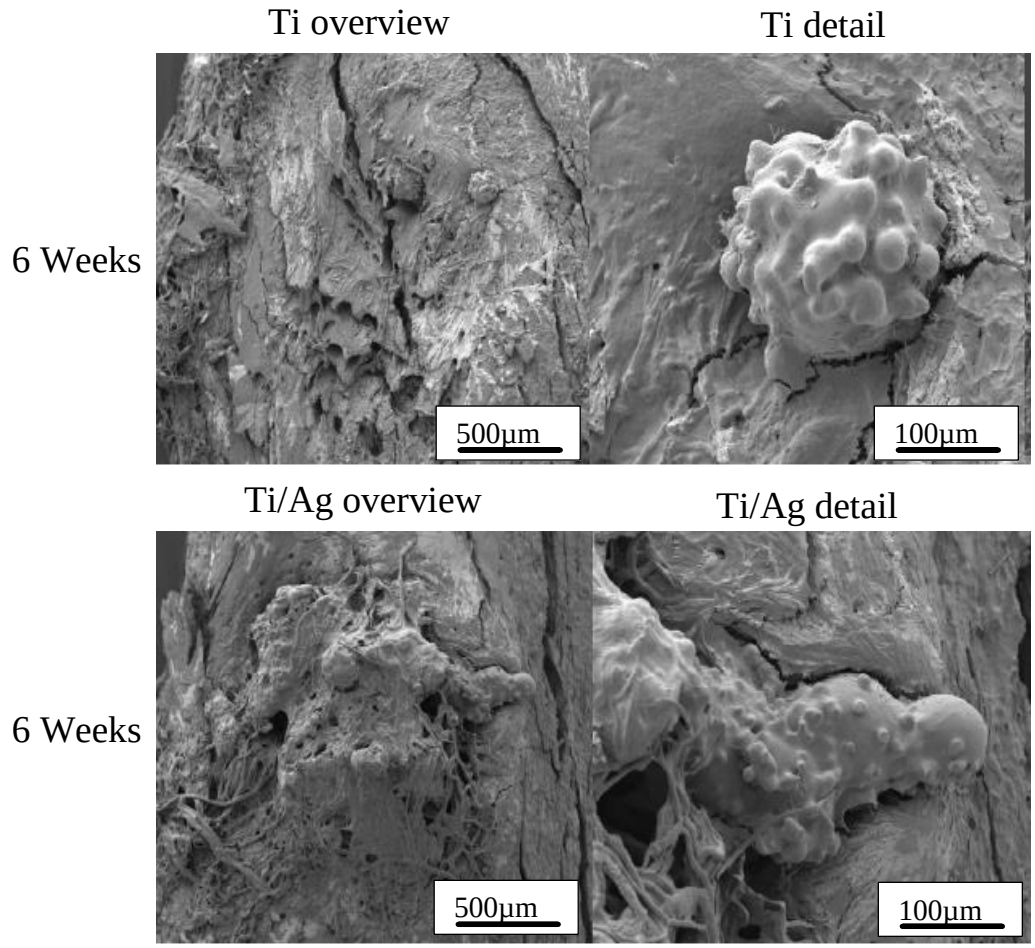

References

[1]. Johnson, R. W., Hultqvist, A., & Bent, S. F. (2014). A brief review of atomic layer deposition: from fundamentals to applications. Materials Today, 17(5), 236-246.

[2]. Longrie, D. (2013). Atomic layer deposition for surface engineering of powders (Doctoral thesis, University of Ghent, Ghent, Belgium). Retrieved from https://biblio.ugent.be/publication/4170707

[3]. Hausmann, D. M., Kim, E., Becker, J., & Gordon, R. G. (2002). Atomic layer deposition of hafnium and zirconium oxides using metal amide precursors. Chemistry of Materials, 14(10), 4350-4358.

[4]. Senzaki, Y., Park, S., Chatham, H., Bartholomew, L., & Nieveen, W. (2004). Atomic layer deposition of hafnium oxide and hafnium silicate thin films using liquid precursors and ozone. Journal of Vacuum Science & Technology A, 22(4), 1175-1181.

[5]. Senzaki, Y., Choi, K., Kirsch, P. D., Majhi, P., & Lee, B. H. (2005). Atomic layer deposition of high k dielectric and metal gate stacks for MOS devices. In Characterization and Metrology for ULSI Technology 2005 (Vol. 788, No. 1, pp. 69-72). AIP Publishing.

[6]. Jones, A. C., Aspinall, H. C., Chalker, P. R., Potter, R. J., Manning, T. D., Loo, Y. F., ... & Smith, L. M. (2006). MOCVD and ALD of high-k dielectric oxides using Alkoxide precursors. Chemical Vapour Deposition, 12(2-3), 83-98.

[7]. Becker, J. S., Kim, E., & Gordon, R. G. (2004). Atomic layer deposition of insulating hafnium and zirconium nitrides. Chemistry of Materials, 16(18), 3497-3501.

[8]. Fang, Z., Aspinall, H. C., Odedra, R., & Potter, R. J. (2011). Atomic layer deposition of TaN and Ta_3N_5 using pentakis (dimethylamino) tantalum and either ammonia or monomethyl hydrazine. Journal of Crystal Growth, 331(1), 33-39.

[9]. Wang, H., Gordon, R. G., Alvis, R., &Ulfig, R. M. (2009). Atomic layer deposition of ruthenium thin films from an Amidinate precursor. Chemical Vapour Deposition, 15(10-12), 312-319.

[10]. Short, A., Jewell, L., Doshay, S., Church, C., Keiber, T., Bridges, F. ...& Alers, G. (2013). Atomic layer deposition of zinc sulfide with $Zn(TMHD)_2$. Journal of Vacuum Science & Technology A, 31(1), 01A138.

[11]. George, S. M. (2009). Atomic layer deposition: an overview. Chemical Reviews, 110(1), 111-131.

[12]. Putkonen, M., & Niinistö, L. (2005). Organometallic precursors for atomic layer deposition. In Precursor Chemistry of Advanced Materials, 125-145.

[13]. Lu, J., & Stair, P. C. (2010). Low-temperature ABC-type atomic layer deposition: Synthesis of highly uniform ultrafine supported metal nanoparticles. Angewandte Chemie International Edition, 49(14), 2547-2551.

[14]. Kim, W. H., Heo, K., Lee, Y. K., Chung, T. M., Kim, C. G., Hong, S. ...& Kim, H. (2011). Atomic layer deposition of Ni thin films and application to area-selective deposition. Journal of the Electrochemical Society, 158(1), 1-5.

[15]. Dendooven, J. (2012). Modelling and in situ characterization of the conformality of atomic layer deposition in high aspect ratio structures and nano-porous materials (Doctoral thesis, University of Ghent, Ghent, Belgium). Retrieved from http://www.cocoon.ugent.be/sites/default/files//phdtheses/phd%20Jolien%20dendooven.pdf

[16]. Rowland, J. C. (2010). Atomic layer deposition of the AL_2O_3-Y_2O_3 pseudo-binary system (Doctoral thesis, University of Florida, Florida, United States). Retrieved from http://ufdc.ufl.edu/UFE0024884/00001.

[17]. Biercuk, M. J., Monsma, D. J., Marcus, C. M., Becker, J. S., & Gordon, R. G. (2003). Low-temperature atomic-layer-deposition lift-off method for microelectronic and nano-electronic applications. Applied Physics Letters, 83(12), 2405-2407.

[18]. Niu, W., Li, X., Karuturi, S. K., Fam, D. W., Fan, H., Shrestha, S., ... & Tok, A. I. Y. (2015). Applications of atomic layer deposition in solar cells. Nanotechnology, 26(6), 064001.

[19]. Elam, J. W., Dasgupta, N. P., &Prinz, F. B. (2011). ALD for clean energy conversion, utilization, and storage. MRS bulletin, 36(11), 899-906.

[20]. Vartiainen, J., Vähä-Nissi, M., &Harlin, A. (2014). Biopolymer films and coatings in packaging applications—A review of recent developments. Materials Sciences and Applications, 5(10), 708-718.

[21]. Finch, D. S., Oreskovic, T., Ramadurai, K., Herrmann, C. F., George, S. M., & Mahajan, R. L. (2008). Biocompatibility of atomic layer-deposited alumina thin films. Journal of Biomedical Materials Research Part A, 87(1), 100-106.

[22]. Gaillot, D. P., Deparis, O., Welch, V., Wagner, B. K., Vigneron, J. P., & Summers, C. J. (2008). Composite organic-inorganic butterfly scales: Production of photonic structures with atomic layer deposition. Physical Review E, 78(3), 031922.

[23]. Masango, S. S., Peng, L., Marks, L. D., Van Duyne, R. P., & Stair, P. C. (2014). Nucleation and growth of silver nanoparticles by AB and ABC-type atomic layer deposition. The Journal of Physical Chemistry C, 118(31), 17655-17661.

[24]. Chalker, P. R., Romani, S., Marshall, P. A., Rosseinsky, M. J., Rushworth, S., & Williams, P. A. (2010). Liquid injection atomic layer deposition of silver nanoparticles. Nanotechnology, 21(40), 405602.

[25]. Niskanen, A., Hatanpää, T., Arstila, K., Leskelä, M., & Ritala, M. (2007). Radical-enhanced atomic layer deposition of silver thin films using phosphine-adducted silver carboxylates. Chemical Vapour Deposition, 13(8), 408-413.

[26]. Kariniemi, M., Niinistö, J., Hatanpää, T., Kemell, M., Sajavaara, T., Ritala, M., & Leskelä, M. (2011). Plasma-enhanced atomic layer deposition of silver thin films. Chemistry of Materials, 23(11), 2901-2907.

[27]. Van den Bruele, F. J., Smets, M., Illiberi, A., Creyghton, Y., Buskens, P., Roozeboom, F., & Poodt, P. (2015). Atmospheric pressure plasma enhanced spatial ALD of silver. Journal of Vacuum Science & Technology A, 33(1), 01A131.

[28]. Amusan, A. A., Kalkofen, B., Gargouri, H., Wandel, K., Pinnow, C., Lisker, M., & Burte, E. P. (2016). Ag films grown by remote plasma enhanced atomic layer deposition on different substrates. Journal of Vacuum Science & Technology A, 34(1), 01A126.

[29]. Chi, K. M., & Lu, Y. H. (2001). MOCVD of Silver Thin Films from the (1, 1, 1, 5, 5, 5-Hexafluoro-2, 4-pentanedionato)-silver [bis (trimethylsilyl) acetylene] Complex. Chemical Vapour Deposition, 7(3), 117-120.

[30]. Zanotto, L., Benetollo, F., Natali, M., Rossetto, G., Zanella, P., Kaciulis, S., & Mezzi, A. (2004). Facile synthesis and characterization of new β-Diketonate silver complexes. Chemical Vapour Deposition, 10(4), 207-213.

[31]. Piszczek, P., Szłyk, E., Chaberski, M., Taeschner, C., Leonhardt, A., Bała, W., & Bartkiewicz, K. (2005). Characterization of silver trimethylacetate complexes with tertiary phosphines as CVD precursors of thin silver films. Chemical Vapour Deposition, 11(1), 53-59.

[32]. Ewald, A., Glückermann, S. K., Thull, R., & Gbureck, U. (2006). Antimicrobial titanium/silver PVD coatings on titanium. Biomedical Engineering Online, 5(1), 22.

[33]. Tran, Q. H., & Le, A. T. (2013). Silver nanoparticles: synthesis, properties, toxicology, applications and perspectives. Advances in Natural Sciences: Nanoscience and Nanotechnology, 4(3), 033001.

[34]. Gupta, R., Dyer, M. J., & Weimer, W. A. (2002). Preparation and characterization of surface plasmon resonance tunable gold and silver films. Journal of Applied Physics, 92(9), 5264-5271.

[35]. Guo, S., & Wang, E. (2011). Noble metal nanomaterials: controllable synthesis and application in fuel cells and analytical sensors. Nano Today, 6(3), 240-264.

[36]. Diggins, F. (2003). The true history of the discovery of penicillin by Alexander Fleming. Biomedical Scientist, 246-9.

[37]. Wallinga, D., & Burch, D. G. (2013). Does adding routine antibiotics to animal feed pose a serious risk to human health. British Medical Journal, 347.

[38]. Ecdc, E. (2009). The bacterial challenge: time to react. Technical report. Stockholm, Sweden, ECDC.

[39]. Hart, C. A., & Kariuki, S. (1998). Antimicrobial resistance in developing countries. British Medical Journal, 317(7159), 647.

[40]. Gilbert, P., McBain, A. and Lindsay, S. (2007). Biofilms, multi-resistance, and persistence. In Amabile-Cuevas, C. F. (Ed.) Antimicrobial resistance in bacteria, Wymondham, UK, Horizon Bioscience.

[41]. Garrett, T. R., Bhakoo, M., & Zhang, Z. (2008).Bacterial adhesion and biofilms on surfaces. Progress in Natural Science, 18(9), 1049-1056.

[42]. Hall-Stoodley, L. Costerton, J.W. & Stoodley, P. (2004). Bacterial Biofilms: from the natural environment to infectious diseases. Nature Reviews, 2(2), 95-108.

[43]. El Abed, S., Hamadi, F., Latrache, H., &Ibnsouda, S. K. (2012). Scanning electron microscopy (SEM) and environmental SEM: suitable tools for study of adhesion stage and biofilm formation. INTECH Open Access Publisher, 717-730.

[44]. Siedenbiedel, F., & Tiller, J. C. (2012). Antimicrobial polymers in solution and on surfaces: overview and functional principles. Polymers, 4(1), 46-71.

[45]. Klein, E., Smith, D. L., & Laxminarayan, R. (2007). Hospitalizations and deaths caused by methicillin-resistant Staphylococcus aureus. Emerging Infectious Diseases, 13(12), 1840.

[46]. Sansone, V., Pagani, D., &Melato, M. (2013). The effects on bone cells of metal ions released from orthopaedic implants. A review. Clinical Cases in Mineral and Bone Metabolism, 10(1), 34-40.

[47]. Gristina, A.G.; Naylor, P.; Myrvik, Q. (1988). Infections from biomaterials and implants: A race for the surface. Medical Progress through Technology, 14 (3-4), 205–224.

[48]. Lorenzetti, M., Dogša, I., Stošicki, T., Stopar, D., Kalin, M., Kobe, S., & Novak, S. (2015). The Influence of Surface Modification on Bacterial Adhesion to Titanium-Based Substrates. ACS Applied Materials & Interfaces, 7(3), 1644-1651.

[49]. Hetrick, E. M., & Schoenfisch, M. H. (2006). Reducing implant-related infections: active release strategies. Chemical Society Reviews, 35(9), 780-789.

[50]. Vejborg, R. M., & Klemm, P. (2008). Blocking of bacterial biofilm formation by a fish protein coating. Applied and Environmental Microbiology, 74(11), 3551-3558.

[51]. Goodman, S. B., Yao, Z., Keeney, M., & Yang, F. (2013).The future of biologic coatings for orthopaedic implants. Biomaterials, 34(13), 3174-3183.

[52]. Guran, C., Pica, A., Ficai, D., Ficai, A., & Comanescu, C. (2013).Antimicrobial coatings—obtaining and characterization. Bulletin of Materials Science, 36(2), 183-188.

[53]. Dastjerdi, R., & Montazer, M. (2010). A review on the application of inorganic nano-structured materials in the modification of textiles: focus on anti-microbial properties. Colloids and Surfaces B: Bio Interfaces, 79(1), 5-18.

[54]. Dastjerdi, R., Mojtahedi, M. R. M., Shoshtari, A. M., & Khosroshahi, A. (2010). Investigating the production and properties of Ag/TiO_2/PP antibacterial nanocomposite filament yarns. The Journal of the Textile Institute, 101(3), 204-213.

[55]. Panyala, NR, Pena-Mendez, EM, Havel, J. (2008). Silver or silver nanoparticles: a hazardous threat to the environment and human health. Journal of Applied Biomedical, 6, 117–129

[56]. Selezneva, A. (2012). Investing in the orthopaedic implant industry (Degree thesis, University of Arcada, Helsinki, Finland).
Retrieved from https://www.theseus.fi/bitstream/handle/10024/43536/Selezneva_Alina.pdf?sequence=1).

[57]. Stickles, B., Phillips, L., Brox, W. T., Owens, B., & Lanzer, W. L. (2001). Defining the relationship between obesity and total joint arthroplasty. Obesity Research, 9(3), 219-223.

[58]. Newton, J. N., Briggs, A. D., Murray, C. J., Dicker, D., Foreman, K. J., Wang, H., ... & Vos, T. (2015). Changes in health in England, with analysis by English regions and areas of deprivation, 1990–2013: a systematic analysis for the Global Burden of Disease Study 2013. The Lancet, 386(10010), 2257-2274.

[59]. Song, Z., Borgwardt, L., Høiby, N., Wu, H., Sørensen, T. S., & Borgwardt, A. (2013). Prosthesis infections after orthopaedic joint replacement: the possible role of bacterial biofilms. Orthopaedic Reviews, 5(2), 65-71.

[60]. Orthopaedic industry annual report®: Focus on join replacement. (2012). Retrieved from https://www.orthoworld.com/index.php/fileproc/index/knowentADJADJorthoknowADJADJ2012ADJADJorthoknow1206LXLXLXpdf

[61]. Kurtz, S., Ong, K., Lau, E., Mowat, F., & Halpern, M. (2007). Projections of primary and revision hip and knee arthroplasty in the United States from 2005 to 2030. The Journal of Bone & Joint Surgery, 89(4), 780-785.

[62]. Green, D., Walsh, D., Mann, S., & Oreffo, R. O. (2002). The potential of bio-mimesis in bone tissue engineering: lessons from the design and synthesis of invertebrate skeletons. Bone, 30(6), 810-815.

[63]. Navarro, M., Michiardi, A., Castano, O., & Planell, J. A. (2008). Biomaterials in orthopaedics. Journal of the Royal Society Interface, 5(27), 1137-1158.

[64]. Briggs, T. W. (2012). Getting it right first time. Improving the quality of orthopaedic care within the National Health Service in England. British Orthopaedic Association. 1-32.

[65]. Millar, W. J. (2002). Hip and knee replacement. Health Reports, 14(1), 37.

[66]. Rodgers, W. P. (2007). Characterization of osseointegrative phosphatidylserine and cholesterol orthopaedic implant coatings (Doctoral thesis, University of Colorado State, Colorado, US). Retrieved from https://dspace.library.colostate.edu/handle/10217/78867

[67]. Lonner, J. H. (2005). Prodromes of failure after revision total knee arthroplasty. In Revision Total Knee Arthroplasty, (265-268), New York.

[68]. Daines, B. K., & Dennis, D. A. (2012). Management of bone defects in revision total knee arthroplasty. Journal of Bone Joint Surgery, 94(12), 1131-1139.

[69]. Leordean, D., Dudescu, C., Marcu, T., Berce, P., Balc, N. (2015). Customized implants with specific properties, made by selective laser melting, Rapid Prototyping Journal, 21(2), 98-104.

[70]. Cosma, S. C., Balc, N., Leordean, D., Moldovan, M., Dudescu, M., & Borzan, C. (2015). Customized medical applications of selective laser melting manufacturing. Academic Journal of Manufacturing Engineering, 13(1).

[71]. Mandracci, P., Mussano, F., Rivolo, P., & Carossa, S. (2016). Surface Treatments and Functional Coatings for Biocompatibility Improvement and Bacterial Adhesion Reduction in Dental Implantology. Coatings, 6(1), 7.

[72]. Muller, M. P., MacDougall, C., & Lim, M. (2016). Antimicrobial surfaces to prevent healthcare-associated infections: a systematic review. Journal of Hospital Infection, 92(1), 7-13.

[73]. Paital, S. R., & Dahotre, N. B. (2009). Calcium phosphate coatings for bio-implant applications: materials, performance factors, and methodologies. Materials Science and Engineering: R: Reports, 66(1), 1-70.

[74]. Katti, K. S. (2004). Biomaterials in total joint replacement. Colloids and Surfaces B: Bio interfaces, 39(3), 133-142.

[75]. Ribeiro, M., Monteiro, F. J., & Ferraz, M. P. (2012). Infection of orthopaedic implants with emphasis on bacterial adhesion process and techniques used in studying bacterial-material interactions. Biomatter, 2(4), 176-194.

[76]. Dalby, M. J., Gadegaard, N., Tare, R., Andar, A., Riehle, M. O., Herzyk, P., & Oreffo, R. O. (2007). The control of human mesenchymal cell differentiation using nanoscale symmetry and disorder. *Nature materials*, *6*(12), 997-1003.

[77]. Peter, I., & Rosso, M. (2015). Study of Ti-enriched CoCrMo alloy for dental application. Access, IEEE, 3, 73-80.

[78]. Kulkarni, M., Mazare, A., Schmuki, P., Iglič, A., & Seifalian, A. (2014). Biomaterial surface modification of titanium and titanium alloys for medical applications. Nanomedicine, 111, 111.

[79]. Van Noort, R. (1987). Titanium: the implant material of today. Journal of Materials Science, 22(11), 3801-3811.

[80]. Rack, H. J., & Qazi, J. I. (2006). Titanium alloys for biomedical applications. Materials Science and Engineering: C, 26(8), 1269-1277.

[81]. Peters, M., & Leyens, C. (2003). Titanium and titanium alloys: Fundamentals and applications. New York, US, Wiley.

[82]. Bothe, R. T., Beaton, L. E., & Davenport, H. A. (1940). Reaction of bone to multiple metallic implants. Journal of the American College of Surgeons, 71(6), 598-602.

[83]. Ratner, B. D., Hoffman, A. S., Schoen, F. J., & Lemons, J. E. (2004). Biomaterials science: an introduction to materials in medicine. New York, US, Academic Press.

[84]. Larsson, C., Esposito, M., Liao, H., & Thomsen, P. (2001). The titanium-bone interface in vivo. In Titanium in Medicine, 587-648.

[85]. Li, Y., Yang, C., Zhao, H., Qu, S., Li, X., & Li, Y. (2014). New developments of Ti-based alloys for biomedical applications. Materials, 7(3), 1709-1800.

[86]. Total Hip Replacement. (2016). Retrieved from http://www.scottsdalejointcenter.com/patient-education/total-hip-replacement-faq/

[87]. Mullen, L. (2010). The Characterisation and structural optimisation of additively fabricated porous components specifically for use in orthopaedic applications (Unpublished doctoral thesis). University of Liverpool, Liverpool, UK.

[88]. Healy, K. E., Rezania, A., & Stile, R. A. (1999). Designing biomaterials to direct biological responses. Annals of the New York Academy of Sciences, 875(1), 24-35.

[89]. Greiner, C., Oppenheimer, S. M., & Dunand, D. C. (2005). High strength, low stiffness, porous NiTi with superelastic properties. Acta Biomaterialia, 1(6), 705-716.

[90]. Ridzwan, M. I. Z., Shuib, S., Hassan, A. Y., Shokri, A. A., & Ibrahim, M. M. (2007). Problem of stress shielding and improvement to the hip implant designs: a review. Journal of Medical Science, 7(3), 460-467.

[91]. Bobyn, J. D., Toh, K. K., Hacking, S. A., Tanzer, M., & Krygier, J. J. (1999). Tissue response to porous tantalum acetabular cups: a canine model. The Journal of arthroplasty, 14(3), 347-354.

[92]. Ryan, G., Pandit, A., & Apatsidis, D. P. (2006). Fabrication methods of porous metals for use in orthopaedic applications. Biomaterials, 27(13), 2651-2670.

[93]. Mullen, L., Stamp, R. C., Fox, P., Jones, E., Ngo, C., & Sutcliffe, C. J. (2010). Selective laser melting: A unit cell approach for the manufacture of porous, titanium, bone in-growth constructs, suitable for orthopaedic applications. II. Randomized structures. Journal of Biomedical Materials Research Part B: Applied Biomaterials, 92(1), 178-188.

[94]. Bobyn, J. D., Pilliar, R. M., Cameron, H. U., & Weatherly, G. C. (1980). The optimum pore size for the fixation of porous-surfaced metal implants by the ingrowth of bone. Clinical Orthopaedics and Related Research, 150, 263-270.

[95]. Schwarzkopf, R., Takemoto, R. C., Immerman, I., Slover, J. D., & Bosco, J. A. (2010). Prevalence of Staphylococcus aureus colonization in orthopaedic surgeons and their patients. Journal of Bone Joint Surgery, 92(9), 1815-1819.

[96]. Knetsch, M. L., & Koole, L. H. (2011). New strategies in the development of antimicrobial coatings: the example of increasing usage of silver and silver nanoparticles. Polymers, 3(1), 340-366.

[97]. Malchau, H., Herberts, P., & Ahnfelt, L. (1993). Prognosis of total hip replacement in Sweden: follow-up of 92,675 operations performed 1978–1990. Acta Orthopaedica Scandinavica, 64(5), 497-506.

[98]. Mullin,A., Todd,N.,Golrokhi,Z., Geng,H., Konerding,M., Potter, R., Sutcilffe, C., Jones, E., & Mitchell, C. (2016). Titanium implants coated with a nano-layer of silver inhibit colonization by S. epidermidis, support cell growth and promote vascularized osseo-integration in vivo. Biomaterials, Proceeding Journal.

[99]. Geipel, U., & Herrmann, M. (2004). The infected implant. Part 1: bacteriology. Der Orthopaedic, 33(12), 1411-26.

[100]. Pajkos, A., Vickery, K., & Cossart, Y. (2004). Is biofilm accumulation on endoscope tubing a contributor to the failure of cleaning and decontamination?, Journal of Hospital Infection, 58(3), 224-229.

[101]. An, Y. H., & Friedman, R. J. (1996). Prevention of sepsis in total joint arthroplasty. Journal of Hospital Infection, 33(2), 93-108.

[102]. Zilberman, M., & Elsner, J. J. (2008). Antibiotic-eluting medical devices for various applications. Journal of Controlled Release, 130(3), 202-215.

[103]. Starner, T. D., & McCray, P. B. (2005). Pathogenesis of early lung disease in cystic fibrosis: a window of opportunity to eradicate bacteria. Annals of Internal Medicine, 143(11), 816-822.

[104]. Gristina, A. G., Naylor, P., & Myrvik, Q. (1987). Infections from biomaterials and implants: a race for the surface. Medical Progress through Technology, 14(3-4), 205-224.

[105]. Gallo, J., Holinka, M., &Moucha, C. S. (2014).Antibacterial surface treatment for orthopaedic implants. International Journal of Molecular Sciences, 15(8), 13849-13880.

[106]. Antimicrobial/Ant-biofilm Therapeutics. Retrieved from http://www.microbioncorp.com/our-technology/health/

[107]. Moriarty, T. F., Zaat, S. A., & Busscher, H. (2012). Biomaterials associated infection: immunological aspects and antimicrobial strategies. Springer Science & Business Media.

[108]. Campoccia, D., Montanaro, L., & Arciola, C. R. (2006). The significance of infection related to orthopaedic devices and issues of antibiotic resistance.Biomaterials, 27(11), 2331-2339.

[109]. Centres for Disease Control and Prevention (US). (2013). Antibiotic resistance threats in the United States. Accessed at www.cdc.gov/drugresistance/threat-report-2013.

[110]. Tsourvakas, S. (2012). Local antibiotic therapy in the treatment of bone and soft tissue infections. InTech Open Access Publisher.

[111]. Ma, M., Kazemzadeh-Narbat, M., Hui, Y., Lu, S., Ding, C., Chen, D. D., ... & Wang, R. (2012). Local delivery of antimicrobial peptides using self-organized TiO_2 nanotube arrays for peri-implant infections. Journal of Biomedical Materials Research Part A, 100(2), 278-285.

[112]. Gomes, D., Pereira, M., & Bettencourt, A. F. (2013). Osteomyelitis: an overview of antimicrobial therapy. Brazilian Journal of Pharmaceutical Sciences, 49(1), 13-27.

[113]. Zimmerli, W., & Ochsner, P. E. (2003). Management of infection associated with prosthetic joints. Infection, 31(2), 99-108.

[114]. Deb, M., Gupte, S., Aggarwal, P., Kaur, M., Manhas, A., Bala, M., & Kant, R. (2014). Microbial Biofilms. SMU Medical Journal, 2(1), 116-127.

[115]. Costerton, W. (1999). Bacterial biofilms: a common cause of persistent infections. Retrieved from http://mpkb.org/home/pathogenesis/microbiota/biofilm#fn__25

[116]. Moojen, D. J. F., Fleer, A., Verbout, A. J., Castelein, R. M., & Dhert, W. J. A. (2006). Prophylaxis of infection using a tobramycin-periapatite coating on a titanium implant: An experimental study in the rabbit. In 52nd Annual Meeting of the Orthopaedic Research Society. No: 0714.

[117]. Lucke, M., Schmidmaier, G., Sadoni, S., Wildemann, B., Schiller, R., Haas, N. P., & Raschke, M. (2003). Gentamicin coating of metallic implants reduces implant-related osteomyelitis in rats. Bone, 32(5), 521-531.

[118]. Alt, V., Bitschnau, A., Österling, J., Sewing, A., Meyer, C., Kraus, R. ... & Schnettler, R. (2006). The effects of combined gentamicin–hydroxyapatite coating for cementless joint prostheses on the reduction of infection rates in a rabbit infection prophylaxis model. Biomaterials, 27(26), 4627-4634.

[119]. Collinge, C. A., Goll, G., Seligson, D., & Easley, K. J. (1994). Pin tract infections: silver vs uncoated pins. Orthopaedics, 17(5), 445-448.

[120]. Coathup, M., Ghani, Y., & Blunn, G. W. Controlled release of silver ions from an electrochemically deposited hydroxyapatite coating. Biomaterials. Retrieved from http://discovery.ucl.ac.uk/148755/

[121]. Romanò, C. L., Scarponi, S., Gallazzi, E., Romanò, D., &Drago, L. (2015). Antibacterial coating of implants in orthopaedics and trauma: a classification proposal in an evolving panorama. Journal of Orthopaedic Surgery and Research, 10(1), 1.

[122]. Del Curto, B., Brunella, M. F., Giordano, C., Pedeferri, M. P., Valtulina, V., Visai, L., & Cigada, A. (2005). Decreased bacterial adhesion to surface-treated titanium. International Journal of Artificial Organs, 28(7), 718-730.

[123]. Gallardo-Moreno, A. M., Pacha-Olivenza, M. A., Saldaña, L., Pérez-Giraldo, C., Bruque, J. M., Vilaboa, N., & González-Martín, M. L. (2009). In vitro biocompatibility and bacterial adhesion of physico-chemically modified Ti6Al4V surface by means of UV irradiation. Acta Biomaterialia, 5(1), 181-192.

[124]. Harris LG, Tosatti S, Wieland M, Textor M, Richards RG. (2004). Staphylococcus aureus adhesion to titanium oxide surfaces coated with non-functionalized and peptide-functionalized poly (L-lysine)-grafted-poly (ethylene glycol) copolymers. Biomaterials, 25:4135–48.

[125]. Singh, A. V., Vyas, V., Patil, R., Sharma, V., Scopelliti, P. E., Bongiorno, G., ... & Milani, P. (2011). Quantitative characterization of the influence of the nanoscale morphology of nanostructured surfaces on bacterial adhesion and biofilm formation. PLoS One, 6(9), 25029.

[126]. Darouiche, R. O. (2003). Antimicrobial approaches for preventing infections associated with surgical implants. Clinical Infectious Diseases, 36(10), 1284-1289.

[127]. Dayyoub, E. (2012). Anti-bacterial and Anti-adhesive Nanostructured Coatings for Improved Implant Biocompatibility. (Doctoral thesis, University of Marburg, Marburg, Germany). Retrieved from http://archiv.ub.uni-marburg.de/diss/z2014/0289/pdf/ded.pdf

[128]. Schierholz, J. M., Steinhauser, H., Rump, A. F. E., Berkels, R., & Pulverer, G. (1997). Controlled release of antibiotics from biomedical polyurethanes: morphological and structural features. Biomaterials, 18(12), 839-844.

[129]. Dibenedetto, A., & Aresta, M. (Eds.). (2013). Inorganic micro-and nanomaterials: synthesis and characterization. Ipswich, UK, Walter de Gruyter.

[130]. Moerman, F. (2014). Antimicrobial materials, coatings and biomimetic surfaces with modified microtography to control microbial fouling of product contact surfaces within food processing equipment: Legislation, requirements, effectiveness and challenges. Hygienic Eng. Design, 7, 8-29.

[131]. Kanematsu, H., Ikegai, H., & Yoshitake, M. (2013). Patents for Antibacterial Metallic Coating and Its Future Trend in Japan. Research Inventy. International Journal of Engineering Science, 3(6), 47-55.

[132]. Jung W. K., Koo H. C., Kim K. W., Shin S., Kim S. H., and Park Y. H. (2008). Antibacterial activity and mechanism of action of the silver ion in Staphylococcus aureus an Escherichia coli. Applied and Environmental Microbiology, 74 (7), 2171-2178.

[133]. Jesline, A., John, N. P., Narayanan, P. M., Vani, C., & Murugan, S. (2015). Antimicrobial activity of zinc and titanium dioxide nanoparticles against biofilm-producing methicillin-resistant Staphylococcus aureus. Applied Nanoscience, 5(2), 157-162.

[134]. Lee, S. (2009). Multifunctionality of layered fabric systems based on electrospun polyurethane/zinc oxide nanocomposite fibers. Journal of Applied Polymer Science, 114(6), 3652-3658.

[135]. Huang, Z., Zheng, X., Yan, D., Yin, G., Liao, X., Kang, Y. ...& Hao, B. (2008). Toxicological effect of ZnO nanoparticles based on bacteria. Langmuir, 24(8), 4140-4144.

[136]. Tariq Jan, J. I., Ismail, M., Zakaullah, M., Naqvi, S. H., & Badshah, N. (2013). Sn doping induced enhancement in the activity of ZnO nanostructures against antibiotic resistant S. aureus bacteria. International Journal of Nanomedicine, 8, 3679.

[137]. Jiang, W., Mashayekhi, H., & Xing, B. (2009). Bacterial toxicity comparison between nano-and micro-scaled oxide particles. Environmental Pollution, 157(5), 1619-1625.

[138]. Carvalho, P., Sampaio, P., Azevedo, S., Vaz, C., Espinós, J. P., Teixeira, V., & Carneiro, J. O. (2014). Influence of thickness and coatings morphology in the antimicrobial performance of zinc oxide coatings. Applied Surface Science, 307, 548-557.

[139]. Grass, G., Rensing, C., & Solioz, M. (2011). Metallic copper as an antimicrobial surface. Applied and Environmental Microbiology, 77(5), 1541-1547.

[140]. Polak, M., Ohl, A., Quaas, M., Lukowski, G., Lüthen, F., Weltmann, K. D., & Schröder, K. (2010). Oxygen and Water Plasma-Immersion Ion Implantation of Copper into Titanium for Antibacterial Surfaces of Medical Implants. Advanced Engineering Materials, 12(9), 511-518.

[141]. Finke, B., Polak, M., Hempel, F., Rebl, H., Zietz, C., Stranak, V., ... & Weltmann, K. D. (2012). Antimicrobial Potential of Copper-Containing Titanium Surfaces Generated by Ion Implantation and Dual High Power Impulse Magnetron Sputtering. Advanced Engineering Materials, 14(5), B224-B230.

[142]. Hempel, F., Finke, B., Zietz, C., Bader, R., Weltmann, K. D., & Polak, M. (2014). Antimicrobial surface modification of titanium substrates by means of plasma immersion ion implantation and deposition of copper. Surface and Coatings Technology, 256, 52-58.

[143]. Shirai, T., Tsuchiya, H., Shimizu, T., Ohtani, K., Zen, Y., & Tomita, K. (2009). Prevention of pin tract infection with titanium-copper alloys. Journal of Biomedical Materials Research Part B: Applied Biomaterials, 91(1), 373-380.

[144]. Williams, D. F. (1987). The biocompatibility of silver. In First International Conference on Gold and Silver in Medicine, 261-272.

[145]. Feied, C. (2004). Novel antimicrobial surface coatings andthe potential for reduced fomite transmission of SARS and other pathogens, 1-22.

[146]. Noda, I., Miyaji, F., Ando, Y., Miyamoto, H., Shimazaki, T., Yonekura, Y. ...& Hotokebuchi, T. (2009). Development of novel thermal sprayed antibacterial coating and evaluation of release properties of silver ions. Journal of Biomedical Materials Research Part B: Applied Biomaterials, 89(2), 456-465.

[147]. East, B. W., Boddy, K., Williams, E. D., Macintyre, D., &McLay, A. L. C. (1980). Silver retention, total body silver and tissue silver concentrations in argyria associated with exposure to an anti-smoking remedy containing silver acetate. Clinical and Experimental Dermatology, 5(3), 305-311.

[148]. Lansdown, A. B. (2010). A pharmacological and toxicological profile of silver as an antimicrobial agent in medical devices.Advances in Pharmacological Sciences, 2010:910686.

[149]. Vig Slenters, T. (2009). Novel silver containing antimicrobial coatings for implant materials. New applications of Ag (I) coordination networks (Doctoral thesis, University of Basel, Basel, Switzerland). Retrieved from http://edoc.unibas.ch/1011/1/TheseTVS_toPDF.pdf.

[150]. Vrček, I. V., Žuntar, I., Petlevski, R., Pavičić, I., Dutour Sikirić, M., Ćurlin, M., & Goessler, W. (2014). Comparison of in vitro toxicity of silver ions and silver nanoparticles on human hepatoma cells. Environmental Toxicology, 31(6), 679-692.

[151]. Drake, P. L., & Hazelwood, K. J. (2005). Exposure-related health effects of silver and silver compounds: a review. Annals of Occupational Hygiene, 49(7), 575-585.

[152]. Rosenman, K. D., Seixas, N., & Jacobs, I. (1987). Potential nephrotoxic effects of exposure to silver. British Journal of Industrial Medicine, 44(4), 267-272.

[153]. Chudobova, D., Nejdl, L., Gumulec, J., Krystofova, O., Rodrigo, M. A. M., Kynicky, J. ...&Kizek, R. (2013). Complexes of silver (I) ions and silver phosphate nanoparticles with hyaluronic acid and/or chitosan as promising antimicrobial agents for vascular grafts.International Journal of Molecular Sciences, 14(7), 13592-13614.

[154]. AEGIS Environments (2008). Understanding silver based antimicrobials: Mode of action, testing methods, environemental fate, and performance expectations. Retrieved from http://www.killgerms.co.nz/case-studies/safety/UnderstandingSilveBasedAntimicrobials.pdf

[155]. Chaloupka, K., Malam, Y., &Seifalian, A. M. (2010).Nanosilver as a new generation of nano-product in biomedical applications. Trends in biotechnology, 28(11), 580-588.

[156]. Unfried, K., Albrecht, C., Klotz, L. O., Von Mikecz, A., Grether-Beck, S., & Schins, R. P. (2007). Cellular responses to nanoparticles: target structures and mechanisms. Nanotoxicology, 1(1), 52-71.

[157]. AshaRani, P. V., Low KahMun, G., Hande, M. P., &Valiyaveettil, S. (2008). Cytotoxicity and genotoxicity of silver nanoparticles in human cells.American Chemical SocietyNano, 3(2), 279-290.

[158]. Alt, V, Bechert, T, Steinrücke, P, Wagener, M, Seidel, P, Dingeldein, E, Scheddin, D, Domann, E, Schnettler, R. (2004). Nanoparticulate silver. A new antimicrobial substance for bone cement. Orthopaedic. 33, 885–892.

[159]. Palza, H. (2015). Antimicrobial Polymers with Metal Nanoparticles. InternationalJournal of Molecular Sciences, 16(1), 2099-2116.

[160]. Prabhu, S., &Poulose, E. K. (2012). Silver nanoparticles: mechanism of antimicrobial action, synthesis, medical applications, and toxicity effects. International Nano Letters, 2(1), 1-10.

[161]. Johnston, H. J., Hutchison, G., Christensen, F. M., Peters, S., Hankin, S., & Stone, V. (2010). A review of the in vivo and in vitro toxicity of silver and gold particulates: particle attributes and biological mechanisms responsible for the observed toxicity. Critical Reviews in Toxicology, 40(4), 328-346.

[162]. Agnihotri, S., Mukherji, S., & Mukherji, S. (2013). Immobilized silver nanoparticles enhance contact killing and show highest efficacy: elucidation of the mechanism of bactericidal action of silver. Nanoscale, 5(16), 7328-7340.

[163]. Franci, G., Falanga, A., Galdiero, S., Palomba, L., Rai, M., Morelli, G., & Galdiero, M. (2015). Silver nanoparticles as potential antibacterial agents. Molecules, 20(5), 8856-8874.

[164]. Jain, J., Arora, S., Rajwade, J. M., Omray, P., Khandelwal, S., & Paknikar, K. M. (2009). Silver nanoparticles in therapeutics: development of an antimicrobial gel formulation for topical use. Molecular Pharmaceutics, 6(5), 1388-1401.

[165]. Zimmerli, W., Trampuz, A., & Ochsner, P. E. (2004). Prosthetic-joint infections. New England Journal of Medicine, 351(16), 1645-1654.

[166]. White, R. (2011). Silver in healthcare: its antimicrobial efficacy and safety in use. Journal of Wound Care, 20(1), 26-26.

[167]. Rosenman, K. D., Moss, A., & Kon, S. (1979). Argyria: clinical implications of exposure to silver nitrate and silver oxide. Journal of Occupational and Environmental Medicine, 21(6), 430-435.

[168]. Asharani, P. V., Hande, M. P., & Valiyaveettil, S. (2009). Anti-proliferative activity of silver nanoparticles. BMC Cell Biology, 10(1), 1.

[169]. Pal, S., Tak, Y. K., & Song, J. M. (2007). Does the antibacterial activity of silver nanoparticles depend on the shape of the nanoparticle? A study of the gram-negative bacterium Escherichia coli. Applied and Environmental Microbiology, 73(6), 1712-1720.

[170]. Hussain, S. M., Hess, K. L., Gearhart, J. M., Geiss, K. T., & Schlager, J. J. (2005). In vitro toxicity of nanoparticles in BRL 3A rat liver cells. Toxicology in Vitro, 19(7), 975-983.

[171]. Banerjee, I., Pangule, R. C., & Kane, R. S. (2011). Antifouling coatings: recent developments in the design of surfaces that prevent fouling by proteins, bacteria, and marine organisms. Advanced Materials, 23(6), 690-718.

[172]. Cloutier, M., Mantovani, D., & Rosei, F. (2015). Antibacterial Coatings: Challenges, Perspectives, and Opportunities. Trends in Biotechnology, 33(11), 637-652.

[173]. Copello, G. J., Teves, S., Degrossi, J., D'Aquino, M., Desimone, M. F., & Diaz, L. E. (2006). Antimicrobial activity on glass materials subject to disinfectant xerogel coating. Journal of Industrial Microbiology and Biotechnology, 33(5), 343-348.

[174]. Lichter, J. A., Van Vliet, K. J., & Rubner, M. F. (2009). Design of antibacterial surfaces and interfaces: polyelectrolyte multilayer as a multifunctional platform. Macromolecules, 42(22), 8573-8586.

[175]. Park, S. Y., Chung, J. W., Priestley, R. D., & Kwak, S. Y. (2012). Covalent assembly of metal nanoparticles on cellulose fabric and its antimicrobial activity. Cellulose, 19(6), 2141-2151.

[176]. Foster, H. A., Sheel, D. W., Sheel, P., Evans, P., Varghese, S., Rutschke, N., & Yates, H. M. (2010). Antimicrobial activity of titania/silver and titania/copper films prepared by CVD. Journal of Photochemistry and Photobiology A: Chemistry, 216(2), 283-289.

[177]. Phoenix, D. A., Harris, F., & Dennison, S. R. (Eds.). (2014). Novel antimicrobial agents and strategies. New Jersey, US, John Wiley & Sons.

[178]. Lewis, F., Cloutier, M., Chevallier, P., Turgeon, S., Pireaux, J. J., Tatoulian, M., &Mantovani, D. (2011). Influence of the 316 L stainless steel interface on the stability and barrier properties of plasma fluorocarbon films. ACS Applied Materials & Interfaces, 3(7), 2323-2331.

[179]. Wunderlich, W. (2014). The atomistic structure of metal/ceramic interfaces are the key issue for developing better properties. Metals, 4(3), 410-427.

[180]. Pellman, M. (2000). PVD coatings for medical device applications. Products Finishing-CIncinnati-, 64(10), 116-123.

[181]. Fang, Z. (2011). Atomic layer deposition of tantalum, hafnium and gadolinium nitrides (Doctoral thesis, University of Liverpool, Liverpool, UK).
Retrieved from http://ethos.bl.uk/OrderDetails.do?uin=uk.bl.ethos.570232

[182]. Wagendristel, A., & Wang, Y. (1994). An introduction to physics and technology of thin films. Singapore, World Scientific.

[183].Ghosh, D. S. (2013). Ultrathin Metal Capped Al-Doped ZnO as Transparent Electrode. In Ultrathin Metal Transparent Electrodes for the Optoelectronics Industry (69-78). Springer International Publishing.

[184]. Hauschild, G., Hardes, J., Gosheger, G., Stoeppeler, S., Ahrens, H., Blaske, F., ... & Höll, S. (2015). Evaluation of osseous integration of PVD-silver-coated hip prostheses in a canine model. Bio Medical Research International, 1-10.

[185]. Rossnagel, S. M., & Kim, H. (2001). From PVD to CVD to ALD for interconnects and related applications. In Interconnect Technology Conference, Proceedings of the IEEE 2001 International (3-5). IEEE.

[186]. Helmersson, U., Lattemann, M., Bohlmark, J., Ehiasarian, A. P., & Gudmundsson, J. T. (2006). Ionized physical vapour deposition (IPVD): A review of technology and applications. Thin Solid Films, 513(1), 1-24.

[187]. Edwards, D., Harker, R., Mahon, M., & Molloy, K. (1999). Aerosol-assisted chemical vapour deposition (AACVD) of silver films from triphenylphosphine adducts of silver β-diketonates and β-diketoiminates, including the structure of [Ag (hfac)(PPh_3)]. Journal of Materials Chemistry, 9(8), 1771-1780.

[188]. Lucovsky, G., Richard, P. D., Tsu, D. V., Lin, S. Y., & Markunas, R. J. (1986). Deposition of silicon dioxide and silicon nitride by remote plasma enhanced chemical vapour deposition. Journal of Vacuum Science & Technology A, 4(3), 681-688.

[189]. Sherman, A. (1987). Chemical vapour deposition for microelectronics: principles, technology, and applications. Park Ridge (NJ), Noyes.

[190]. Kamarudin, M. A., Sahamir, S. R., Datta, R. S., Long, B. D., Mohd Sabri, M. F., & Mohd Said, S. (2013). A review on the fabrication of polymer-based thermoelectric materials and fabrication methods. The Scientific World Journal, 2013 (10), 713640-713657.

[191]. Jones, A. C., & Hitchman, M. L. (2009). Overview of chemical vapour deposition. Chemical Vapour Deposition: Precursors, Processes and Applications, 1-36.

[192]. Choy, K. L. (2003). Chemical vapour deposition of coatings. Progress in Materials Science, 48(2), 57-170.

[193]. Creighton, J. R., & Ho, P. (2001). Introduction to chemical vapour deposition (CVD). Chemical Vapour Deposition, 2, 1-22.

[194]. Spear, K. E., & Dirkx, R. R. (1989). Role of high-temperature chemistry in CVD processing. High Temperature Science, 27,107.

[195]. Hoivik, N. D., Elam, J. W., Linderman, R. J., Bright, V. M., George, S. M., & Lee, Y. C. (2003). Atomic layer deposited protective coatings for micro-electromechanical systems. Sensors and Actuators A: Physical, 103(1), 100-108.

[196]. Saleem, M. R., Ali, R., Khan, M. B., Honkanen, S., & Turunen, J. (2014). Impact of atomic layer deposition to nanophotonic structures and devices. Frontiers in Materials, 1, 18.

[197]. Easton, C. D., Bullock, A. J., Gigliobianco, G., McArthur, S. L., & MacNeil, S. (2014). Application of layer-by-layer coatings to tissue scaffolds–development of an angiogenic biomaterial. Journal of Materials Chemistry B, 2(34), 5558-5568.

[198]. Di Ventra, M., Evoy, S., & Heflin, J. R. (2004). Introduction to nanoscale science and technology. Berlin, Germany, Springer Science & Business Media.

[199]. Wang, X., & Yushin, G. (2015). Chemical vapour deposition and atomic layer deposition for advanced lithium ion batteries and super capacitors. Energy & Environmental Science, 8(7), 1889-1904.

[200]. Parsons, G. N., George, S. M., & Knez, M. (2011). Progress and future directions for atomic layer deposition and ALD-based chemistry. MRS Bull, 36(11), 865-871.

[201]. Leskelä, M., & Ritala, M. (2002). Atomic layer deposition (ALD): from precursors to thin film structures. Thin Solid Films, 409(1), 138-146.

[202]. Ritala, M., & Niinistö, J. (2009). Industrial applications of atomic layer deposition. ECS Transactions, 25(8), 641-652.

[203]. Knez, M., Nielsch, K., & Niinistö, L. (2007). Synthesis and surface engineering of complex nanostructures by atomic layer deposition. Advanced Materials, 19(21), 3425-3438.

[204]. Elam, J. W., Routkevitch, D., Mardilovich, P. P., & George, S. M. (2003). Conformal coating on ultrahigh-aspect-ratio nanopores of anodic alumina by atomic layer deposition. Chemistry of Materials, 15(18), 3507-3517.

[205]. Riedl, T., Winkler, T., Schmidt, H., Meyer, J., Schneidenbach, D., Johannes, H. H. ... & Hinze, P. (2010, May). Reliability aspects of organic light emitting diodes. In Reliability Physics Symposium (IRPS), 2010 IEEE International, IEEE 327-333.

[206]. Cleveland, E. R., Henn-Lecordier, L., Perez, I., Banerjee, P., & Rubloff, G. W. (2009). ALD conformality and optimization in ultrahigh aspect ratio nanopores for electrical energy storage nanodevices. PowerMEMS, 1-4.

[207]. Leskelä, M., & Ritala, M. (2003). Atomic layer deposition chemistry: recent developments and future challenges. Angewandte Chemie International Edition, 42(45), 5548-5554.

[208]. Niinistö, L., Nieminen, M., Päiväsaari, J., Niinistö, J., & Putkonen, M. (2004). Advanced electronic and optoelectronic materials by Atomic Layer Deposition: An overview with special emphasis on recent progress in processing of high-k dielectrics and other oxide materials. Physica Status Solidi (a), 201(7), 1443-1452.

[209]. Liu, X., Ramanathan, S., & Seidel, T. E. (2003). Atomic layer deposition of hafnium oxide thin films from tetrakis (dimethylamino) hafnium (TDMAH) and ozone. In MRS Proceedings, 765, 3-8.

[210]. Rossnagel, S. M., Sherman, A., & Turner, F. (2000). Plasma-enhanced atomic layer deposition of Ta and Ti for interconnect diffusion barriers.Journal of Vacuum Science & Technology B, 18(4), 2016-2020.

[211]. Kim, H. (2003). Atomic layer deposition of metal and nitride thin films: Current research efforts and applications for semiconductor device processing. Journal of Vacuum Science & Technology B, 21(6), 2231-2261.

[212]. Van der Straten, O., Zhu, Y., Dunn, K., Eisenbraun, E. T., & Kaloyeros, A. E. (2004). Atomic layer deposition of tantalum nitride for ultrathin liner applications in advanced copper metallization schemes. Journal of Materials Research, 19(02), 447-453.

[213]. Morishita, S., Sugahara, S., & Matsumura, M. (1997). Atomic-layer chemical-vapor-deposition of silicon-nitride. Applied Surface Science, 112, 198-204.

[214]. Wojcik, H., Friedemann, M., Feustel, F., Albert, M., Ohsiek, S., Metzger, J. ... & Wenzel, C. (2007). A comparative study of thermal and plasma enhanced ALD Ta-NC films on SiO_2, SiCOH and Cu substrates. InInternational Interconnect Technology Conference, IEEE, 19-21.

[215]. D. P. Gaillot. (2007). Optical Properties of Complex Periodic Media Structurally Modified by Atomic Layer Deposition, (Doctoral Thesis, Georgia Institute of Technology, Atlanta, US). Retrieved from https://smartech.gatech.edu/handle/1853/14635?show=full

[216]. Wang, J. J., Nikolov, A., & Wu, Q. (2006). Nano-and microlens arrays grown using atomic-layer deposition. Photonics Technology Letters, IEEE, 18(24), 2650-2652.

[217]. Sneck, S., Soininen, P., Putkonen, M., & Norin, L. (2006). A new way to utilize atomic layer deposition-case study: optical fiber manu-facturing. InProc. AVS 6th International Conference on Atomic Layer Deposition.

[218]. Standridge, S. D., Schatz, G. C., & Hupp, J. T. (2009). Toward plasmonic solar cells: protection of silver nanoparticles via atomic layer deposition of TiO_2. Langmuir, 25(5), 2596-2600.

[219]. Lakomaa, E. L., Root, A., & Suntola, T. (1996). Surface reactions in Al_2O_3 growth from trimethylaluminium and water by atomic layer epitaxy. Applied Surface Science, 107, 107-115.

[220]. Koehler, F., Triyoso, D. H., Hussain, I., Mutas, S., & Bernhardt, H. (2012). Atomic layer deposition of SiN for spacer applications in high-end logic devices. In IOP Conference Series: Materials Science and Engineering, 41(1), 012006.

[221]. Tsai, C. H., Yang, C. W., Hsu, C. H., Lai, C. M., Lo, K. Y., Chen, C. G., ... & Hung, W. H. (2012). Characteristics of HfZrO x gate stack engineering for reliability improvement on 28nm HK/MG CMOS technology. In Proceedings of Technical Program of VLSI Technology, System and Application.

[222]. Hodson, C., & Kessels, E. (2009). Using ALD for improved efficiency crystalline silicon solar cells. Photovoltaics World, 4, 17-21.

[223]. Blauw, M. A., Van Anh, T. D., Calama, M. C., & Brongersma, S. H. (2013). Metal oxide ALD films for low power sensor applications. ECS Transactions, 50(13), 137-140.

[224]. Ritala, M., & Leskelä, M. (1999). Atomic layer epitaxy-a valuable tool for nanotechnology. Nanotechnology, 10(1), 19.

[225]. Leskelä, M., & Ritala, M. (1999). ALD precursor chemistry: Evolution and future challenges. Le Journal de Physique IV, 2(8), 837-852.

[226]. He, W. (2015). ALD: Atomic Layer Deposition–Precise and Conformal Coating for Better Performance. In Handbook of Manufacturing Engineering and Technology, 2959-2996. Springer London.

[227]. Grabow, M. H., & Gilmer, G. H. (1988). Thin film growth modes, wetting and cluster nucleation. Surface Science, 194(3), 333-346.

[228]. Mishra, D., Greving, D., Confalonieri, G. B., Perlich, J., Toperverg, B. P., Zabel, H., & Petracic, O. (2014). Growth modes of nanoparticle superlattice thin films. Nanotechnology, 25(20), 205602.

[229]. Venables, J. (2000). Introduction to surface and thin film processes. Cambridge, UK, Cambridge University Press.

[230]. Puurunen, R. L. (2004). Random deposition as a growth mode in atomic layer deposition. Chemical Vapor Deposition, 10(3), 159-170.

[231]. Wang, Y., Chen, W., Wang, B., & Zheng, Y. (2014). Ultrathin ferroelectric films: growth, characterization, Physics and Applications. Materials, 7(9), 6377-6485.

[232]. Suntola, T., & Hurle, D. T. J. (1994). Handbook of crystal growth. Thin Films and Epitaxy, 3, 601.

[233]. Profijt, H. B., Potts, S. E., Van de Sanden, M. C. M., & Kessels, W. M. M. (2011). Plasma-assisted atomic layer deposition: Basics, opportunities, and challenges. Journal of Vacuum Science & Technology A, 29(5), 050801.

[234]. Knisley, T. J., Kalutarage, L. C., & Winter, C. H. (2013). Precursors and chemistry for the atomic layer deposition of metallic first row transition metal films. Coordination Chemistry Reviews, 257(23), 3222-3231.

[235]. Suntola, T. (1989). Atomic layer epitaxy. Materials Science Reports, 4(5), 261-312.

[236]. Hashmi, S. (2014). Comprehensive materials processing. London, UK, Elsevier.

[237]. Steric effects In Wikipedia. Retrieved January 2016, from https://en.wikipedia.org/wiki/Steric_effects

[238]. Herodotou, S. (2015). Zirconium doped zinc oxide thin films deposited by atomic layer deposition (Doctoral thesis, University of Liverpool, Liverpool, UK). Retrieved from https://livrepository.liverpool.ac.uk/2013045/

[239]. Kim, H., Lavoie, C., Copel, M., Narayanan, V., Park, D. G., & Rossnagel, S. M. (2004). The physical properties of cubic plasma-enhanced atomic layer deposition TaN films. Journal of Applied Physics, 95(10), 5848-5855.

[240]. Lee, B. H., Cho, S., Hwang, J. K., Kim, S. H., & Sung, M. M. (2010). UV-enhanced atomic layer deposition of ZrO_2 thin films at room temperature.Thin Solid Films, 518(22), 6432-6436.

[241]. Lim, J. W., Yun, S. J., & Lee, J. H. (2005). Low-temperature growth of SiO2 films by plasma-enhanced atomic layer deposition. ETRI Journal, 27(1), 118-121.

[242]. Elers, K. E., Winkler, J., Weeks, K., & Marcus, S. (2005). TiCl4 as a Precursor in the TiN Deposition by ALD and PEALD. Journal of the Electrochemical Society, 152(8), 589-593.

[243]. Xie, Q., Musschoot, J., Deduytsche, D., Van Meirhaeghe, R. L., Detavernier, C., Van den Berghe, S., ... & Qu, X. P. (2008). Growth kinetics and crystallization behavior of TiO2 films prepared by plasma enhanced atomic layer deposition. Journal of the Electrochemical Society, 155(9), 688-692.

[244]. Choi, S. W., Jang, C. M., Kim, D. Y., Ha, J. S., Park, H. S., Koh, W. Y., & Lee, C. S. (2003). Plasma enhanced atomic layer deposition of Al_2O_3 and TiN. Journal of Korean Physics Society, 42, 975-979.

[245]. Sioncke, S., Delabie, A., Brammertz, G., Conard, T., Franquet, A., Caymax, M., ... & Keuning, W. (2009). Thermal and plasma enhanced atomic layer deposition of Al_2O_3 on GaAs substrates. Journal of the Electrochemical Society, 156(4), 255-262.

[246]. Maeng, W. J., Park, S., & Kim, H. (2006). Atomic layer deposition of Ta-based thin films: Reactions of alkylamide precursor with various reactants. Journal of Vacuum Science and Technology B Microelectronics and Nanometer Structures, 24(5), 2276.

[247]. Lay, N. E., Ten Eyck, G. A., Duquette, D. J., & Lu, T. M. (2007). Direct plating of Cu on Pd plasma enhanced atomic layer deposition coated TaN barrier. Electrochemical and Solid-state Letters, 10(1), 13-16.

[248]. Ten Eyck, G. A., Senkevich, J. J., Tang, F., Liu, D., Pimanpang, S., Karaback, T., ... & Lanford, W. A. (2005). Plasma-assisted atomic layer deposition of palladium. Chemical Vapour Deposition, 11(1), 60-66.

[249]. Park, D. J., Lim, J. W., & Park, B. O. (2010). Stabilization of Al_2O_3 gate oxide on plastic substrate for low temperature poly-silicon by in situ plasma treatment. Solid-State Electronics, 54(3), 323-326.

[250]. Knoops, H. C. M., Baggetto, L., Langereis, E., Van De Sanden, M. C. M., Klootwijk, J. H., Roozeboom, F. ... & Kessels, W. M. M. (2008). Deposition of TiN and TaN by remote plasma ALD for Cu and Li diffusion barrier applications. Journal of the Electrochemical Society, 155(12), 287-294.

[251]. Park, J. S., Park, H. S., & Kang, S. W. (2002). Plasma-enhanced atomic layer deposition of Ta-N thin films. Journal of the Electrochemical Society, 149(1), 28-32.

[252]. Choi, J. H., Mao, Y., & Chang, J. P. (2011). Development of hafnium based high-k materials—A review. Materials Science and Engineering: R: Reports, 72(6), 97-136.

[253]. Woo, S., Hong, H., Kim, S., Kim, H., Kim, J., Jeon, H. ... & Ishida, M. (2008). Characteristics of metal–oxide–semiconductor field-effect transistors with $HfO_2/SiO_2/Si$ and $HfO_2/SiOxNy/Si$ stack structures formed by remote plasma technique. Japanese Journal of Applied Physics, 47(8), 6196-6199.

[254]. Kim, W. S., Moon, D. Y., Kang, B. W., Park, J. W., & Park, J. G. (2009). Deposition of Al_ {2} O_ {3} by using ECR-ALD for organic substrate devices. Journal of Korean Physical Society, 55(1), 55-58.

[255]. Langereis, E., Creatore, M., Heil, S. B. S., Van de Sanden, M. C. M., & Kessels, W. M. M. (2006). Plasma-assisted atomic layer deposition of Al~ 2O~ 3 moisture permeation barriers on polymers. Applied physics letters, 89(8), 081915.

[256]. Beynet, J., Wong, P., Miller, A., Locorotondo, S., Vangoidsenhoven, D., Yoon, T. H. ... & Yoo, Y. M. (2009). Low temperature plasma-enhanced ALD enables cost-effective spacer defined double patterning (SDDP). In SPIE Lithography Asia (75201J-75201J). International Society for Optics and Photonics.

[257]. Niskanen, A., Rahtu, A., Sajavaara, T., Arstila, K., Ritala, M., & Leskelä, M. (2005). Radical-enhanced atomic layer deposition of metallic copper thin films. Journal of the Electrochemical Society, 152(1), 25-28.

[258]. Jeong, C. W., Lee, B. I., & Joo, S. K. (2001). Growth and characterization of aluminum oxide films by plasma-assisted atomic layer deposition. Materials Science and Engineering: C, 16(1), 59-64.

[259]. Lee, W. J., You, I. K., Ryu, S. O., Yu, B. G., Cho, K. I., Yoon, S. G., & Lee, C. S. (2001). SrTa2O6 thin films deposited by plasma-enhanced atomic layer deposition. Japanese Journal of Applied Physics, 40(12), 6941-6944.

[260]. De Keijser, M., & Van Opdorp, C. (1991). Atomic layer epitaxy of gallium arsenide with the use of atomic hydrogen. Applied Physics Letters, 58(11), 1187-1189.

[261]. Lee, E. J., Ko, M. G., Kim, B. Y., Park, S. K., Kim, H. D., & Park, J. W. (2006). Lanthanum-oxide thin films deposited by plasma-enhanced atomic layer deposition. Journal of Korean Physical Society, 49(3), 1243.

[262]. Lieberman, M. A., & Lichtenberg, A. J. (2005). Principles of plasma discharges and materials processing. John Wiley & Sons.

[263]. Grill, A. (1994). Cold plasma in materials fabrication. From fundamentals to applications. Piscataway, NJ, IEEE Press.

[264]. Niskanen, A. (2006). Radical enhanced atomic layer deposition of metals and oxides. (Doctoral thesis, University of Helsinki, Helsinki, Finland).
Retrieved from http://ethesis.helsinki.fi/julkaisut/mat/kemia/vk/niskanen/radicale.pdf

[265]. Heil, S. B. S. (2008). Plasma-assisted atomic layer deposition of metal oxides and nitrides (Doctoral thesis, University of Eindhoven, Eindhoven, Netherland).
Retrieved from https://pure.tue.nl/ws/files/2990148/200712446.pdf

[266]. Knoops, H. C. M., Langereis, E., Van De Sanden, M. C. M., & Kessels, W. M. M. (2010). Conformality of plasma-assisted ALD: physical processes and modeling. Journal of the Electrochemical Society, 157(12), 241-249.

[267]. Greaves, J. C., & Linnett, J. W. (1959). Recombination of atoms at surfaces. Part 5.—Oxygen atoms at oxide surfaces. Transactions of the Faraday Society, 55, 1346-1354.

[268]. Chalker, P. R., Marshall, P. A., Dawson, K., Brunell, I. F., Sutcliffe, C. J., & Potter, R. J. (2015). Vacuum ultraviolet photochemical selective area atomic layer deposition of Al_2O_3 dielectrics. AIP Advances, 5(1), 017115.

[269]. Kwak, J. C., Lee, Y. H., & Choi, B. H. (2004). Preparation of tantalum oxide thin films by photo-assisted atomic layer deposition. Applied Surface Science, 230(1), 249-253.

[270]. Kim, S. K., Hoffmann-Eifert, S., & Waser, R. (2011). High growth rate in atomic layer deposition of TiO_2 thin films by UV irradiation. Electrochemical and Solid-State Letters, 14(4), 146-148.

[271]. Kim, H. (2011). Characteristics and applications of plasma enhanced-atomic layer deposition. Thin Solid Films, 519(20), 6639-6644.

[272]. Jeong, W., Ko, Y., Bang, S., Lee, S., & Jeon, H. (2010). Characteristics of HfN films deposited by using remote plasma-enhanced atomic layer deposition. Journal of Korean Physical Society, 56(3), 905-910.

[273]. Burton, B. B., Lavoie, A. R., & George, S. M. (2008). Tantalum nitride atomic layer deposition using (tert-Butylimido) tris (diethylamido) tantalum and hydrazine. Journal of the Electrochemical Society, 155(7), 508-516.

[274]. Du, Y., & George, S. M. (2007). Molecular layer deposition of nylon 66 films examined using in situ FTIR spectroscopy. The Journal of Physical Chemistry C, 111(24), 8509-8517.

[275]. Niinistö, J., Petrova, N., Putkonen, M., Niinistö, L., Arstila, K., & Sajavaara, T. (2005). Gadolinium oxide thin films by atomic layer deposition. Journal of Crystal Growth, 285(1), 191-200.

[276]. Päiväsaari, J., Niinistö, J., Myllymäki, P., Dezelah IV, C., Winter, C. H., Putkonen, M. ... & Niinistö, L. (2007). Atomic layer deposition of rare earth oxides. In Rare earth oxide thin films (15-32). Springer Berlin Heidelberg.

[277].Wächtler, T. (2010). Thin films of copper oxide and copper grown by atomic layer deposition for applications in metallization systems of microelectronic devices. (Doctoral thesis, University of Chemnitz, Chemnitz, Germany). Retrieved from http://www.qucosa.de/fileadmin/data/qucosa/documents/5997/data/Waechtler_Thesis.pdf

[278]. Kim, S. K., Lee, S. Y., Lee, S. W., Hwang, G. W., Hwang, C. S., Lee, J. W., & Jeong, J. (2007). Atomic layer deposition of Ru thin films using 2, 4-(dimethylpentadienyl)(ethylcyclopentadienyl) Ru by a liquid injection system. Journal of the Electrochemical Society, 154(2), 95-101.

[279]. Hong, T. E., Choi, S. H., Yeo, S., Park, J. Y., Kim, S. H., Cheon, T. ... & Kim, H. (2013). Atomic layer deposition of Ru thin films using a Ru (0) metallorganic precursor and O_2. ECS Journal of Solid State Science and Technology, 2(3), 47-53.

[280]. Li, Z., Rahtu, A., & Gordon, R. G. (2006). Atomic layer deposition of ultrathin copper metal films from a liquid copper (I) amidinate precursor. Journal of the Electrochemical Society, 153(11), 787-794.

[281]. Nyns, L., Hall, L., Conard, T., Delabie, A., Deweerd, W., Heyns, M. ... & De Gendt, S. (2006). Nucleation and growth behaviour of atomic layer deposited HfO2 films on silicon oxide starting surfaces. Journal of the Electrochemical Society, 153(9), 205-209.

[282]. Tägtström, P., Maårtensson, P., Jansson, U., & Carlsson, J. O. (1999). Atomic layer epitaxy of tungsten oxide films using oxyfluorides as metal precursors. Journal of the Electrochemical Society, 146(8), 3139-3143.

[283]. Atomic Layer Deposition (n.d.). Retrieved from http://www.ipms.fraunhofer.de/en/applications/nanoelectronic/Front_End_of_Line/atomiclayerdeposition.html

[284]. Dasgupta, N. P., Mack, J. F., Langston, M. C., Bousetta, A., & Prinz, F. B. (2010). Design of an atomic layer deposition reactor for hydrogen sulfide compatibility. Review of Scientific Instruments, 81(4), 044102.

[285]. Su, P. C., Chao, C. C., Shim, J. H., Fasching, R., & Prinz, F. B. (2008). Solid oxide fuel cell with corrugated thin film electrolyte. Nano Letters, 8(8), 2289-2292.

[286]. Knez, M., Kadri, A., Wege, C., Gösele, U., Jeske, H., & Nielsch, K. (2006). Atomic layer deposition on biological macromolecules: metal oxide coating of tobacco mosaic virus and ferritin. Nano Letters, 6(6), 1172-1177.

[287]. King, J. S., Neff, C. W., Summers, C. J., Park, W., Blomquist, S., Forsythe, E., & Morton, D. (2003). High-filling-fraction inverted ZnS opals fabricated by atomic layer deposition. Applied Physics Letter, 83, 2566.

[288]. Sirviö, S. (2014). Characterization of Atomic Layer Deposited Thin Films: Conformality in High Aspect Ratio Pores and the Electrical Properties of Capacitors. (Doctoral dissertation, University of Aalto, Helsinki, Finland). Retrieved from https://aaltodoc.aalto.fi/bitstream/handle/123456789/14207/lic_sirvi%C3%B6_sari_2014.pdf?sequence=1

[289]. Raaijmakers, I. J. (2011). Current and Future Applications of ALD in Micro-Electronics. ECS Transactions, 41(2), 3-17.

[290]. Lakhtakia, A., & Martin-Palma, R. J. (Eds.). (2013). Engineered biomimicry. Waltham, Netherland, Elsevier.

[291]. Pinna, N., & Knez, M. (Eds.). (2012). Atomic layer deposition of nanostructured materials. New Jersey, US, John Wiley & Sons.

[292]. Ritala, M., & Leskela, M. (2001). Atomic layer deposition. Handbook of Thin Film Materials, 1, 103-159.

[293]. Leskelä, M., & Ritala, M. (2002). Atomic layer deposition (ALD): from precursors to thin film structures. Thin Solid Films, 409(1), 138-146.

[294]. Wang, H. (2009). Atomic layer deposition of oxides for microelectronics. Harvard, US, Harvard University Press.

[295]. Lee, S. W., Choi, B. J., Eom, T., Han, J. H., Kim, S. K., Song, S. J., ... & Hwang, C. S. (2013). Influences of metal, non-metal precursors, and substrates on atomic layer deposition processes for the growth of selected functional electronic materials. Coordination Chemistry Reviews, 257(23), 3154-3176.

[296]. Niinistö, L., Ritala, M., & Leskelä, M. (1996). Synthesis of oxide thin films and over layers by atomic layer epitaxy for advanced applications. Materials Science and Engineering: B, 41(1), 23-29.

[297]. Tiitta, M., & Niinistou, L. (1997). Volatile Metal β-Diketonates: ALE and CVD precursors for electroluminescent device thin films. Chemical Vapour Deposition, 3(4), 167-182.

[298]. Utriainen, M., Kröger-Laukkanen, M., Johansson, L. S., & Niinistö, L. (2000). Studies of metallic thin film growth in an atomic layer epitaxy reactor using M (acac) 2 (M= Ni, Cu, Pt) precursors. Applied Surface Science, 157(3), 151-158.

[299]. Juppo, M., Ritala, M., & Leskelä, M. (1997). Deposition of copper films by an alternate supply of CuCl and Zn. Journal of Vacuum Science & Technology A, 15(4), 2330-2333.

[300]. Huo, J., Solanki, R., & McAndrew, J. (2002). Characteristics of copper films produced via atomic layer deposition. Journal of Materials Research, 17(09), 2394-2398.

[301]. Consiglio, S. P. (2007). Metallorganic chemical vapor deposition and atomic layer deposition approaches for the growth of hafnium-based thin films from dialkylamide precursors for advanced CMOS gate stack

applications. (Doctoral thesis, State University of New York, New York, US). Retrieved from http://adsabs.harvard.edu/abs/2007PhDT.....232C

[302].Retrieved from https://www.sigmaaldrich.com/content/dam/sigma-aldrich/docs/SAFC/Bulletin/insight_july07.pdf

[303]. Paranjpe, A., Gopinath, S., Omstead, T., & Bubber, R. (2001). Atomic layer deposition of AlO_x for thin film head gap applications. Journal of the Electrochemical Society, 148(9), 465-471.

[304]. Riha, S. C., Racowski, J. M., Lanci, M. P., Klug, J. A., Hock, A. S., & Martinson, A. B. (2013). Phase discrimination through oxidant selection in low-temperature atomic layer deposition of crystalline iron oxides. Langmuir,29(10), 3439-3445.

[305]. Riedel, S. (2002). Untersuchungen zur Integration von MOCVD-Titannitridbarriere-und Kupferschichten in Leitbahnsysteme der Mikroelektronik. (Doctoral thesis, University of Chemnitz, Chemnitz, Germany). Retrieved from https://www.researchgate.net/publication/34202510_Untersuchungen_zur_Integration_von_MOCVD-Titannitridbarriere-_und_Kupferschichten_in_Leitbahnsysteme_der_Mikroelektronik

[306]. Hindley, S. (2014). Atomic layer deposition and metal organic chemical vapour deposition of materials for photovoltaic applications (Doctoral dissertation, University of Liverpool, Liverpool, UK). Retrieved from http://repository.liv.ac.uk/16313/

[307]. Potter, R. J., Chalker, P. R., Manning, T. D., Aspinall, H. C., Loo, Y. F., Jones, A. C., ... & Schumacher, M. (2005). Deposition of HfO_2, Gd_2O_3 and PrOx by liquid injection ALD techniques. Chemical Vapour Deposition, 11(3), 159-169.

[308]. Benson, S. (January 2012) Direct liquid injection vaporizers for high-efficiency, cost-effective photovoltaic manufacturing. Retrieved from http://www.processingmagazine.com/ext/resources/assets/whitepapers/archives/d/DLI-Photovoltaic-White-Paper.pdf

[309]. Pham, N. H. (2010). Liquid-injection atomic layer deposition of cerium-doped hafnium oxide dielectric films (Doctoral dissertation, University of Liverpool, Liverpool, UK). Retrieved from http://ethos.bl.uk/OrderDetails.do?uin=uk.bl.ethos.539745

[310]. Joint Laboratory InCVD (n.d.). Direct Liquid Injection. Retrieved from https://sites.google.com/site/labcomincvd/Direct-Liquid-Injection

[311].[311]. LAMP (n.d.) Chemical vapor deposition/Atomic layer: Metal gate electrodes deposition. Retrieved from http://phome.postech.ac.kr/user/indexSub.action?codyMenuSeq=69392&siteId=lamp&menuUIType=top

[312]. Henry, A. I., Courty, A., Pileni, M. P., Albouy, P. A., & Israelachvili, J. (2008). Tuning of solid phase in supracrystals made of silver nanocrystals. Nano Letters, 8(7), 2000-2005.

[313]. Piedade, A. P., Vieira, M. T., Martins, A., & Silva, F. (2007). In vitro behaviour of nanocrystalline silver-sputtered thin films. Nanotechnology, 18(10), 105103.

[314]. Butterman, W. C., & Hilliard, H. E. (2004). Silver. Reston, VA: US Geological Survey, 7, 18.

[315]. Butler, M. A., & Ricco, A. J. (1988). Chemisorption-induced reflectivity changes in optically thin silver films. Applied Physics Letters, 53(16), 1471-1473.

[316]. Boccas, M., Vucina, T., Araya, C., Vera, E., & Ahhee, C. (2006). Protected-silver coatings for the 8-m Gemini telescope mirrors. Thin Solid Films, 502(1), 275-280.

[317]. Dryden, N. H., Vittal, J. J., & Puddephatt, R. J. (1993). New precursors for chemical vapour deposition of silver. Chemistry of Materials, 5(6), 765-766.

[318]. Gao, L., Härter, P., Linsmeier, C., Gstöttner, J., Emling, R., & Schmitt-Landsiedel, D. (2004). Metalorganic chemical vapour deposition of silver thin films for future interconnects by direct liquid injection system. Materials Science in Semiconductor Processing, 7(4), 331-335.

[319]. Gao, L., Härter, P., Linsmeier, C., Wiltner, A., Emling, R., & Schmitt-Landsiedel, D. (2005). Silver metal organic chemical vapour deposition for advanced silver metallization. Microelectronic Engineering, 82(3), 296-300.

[320]. Bahlawane, N., Premkumar, P. A., Onwuka, K., Reiss, G., & Kohse-Höinghaus, K. (2007). Self-catalyzed chemical vapor deposition method for the growth of device-quality metal thin films. Microelectronic Engineering, 84(11), 2481-2485.

[321]. Kapaklis, V., Poulopoulos, P., Karoutsos, V., Manouras, T., & Politis, C. (2006). Growth of thin Ag films produced by radio frequency magnetron sputtering. Thin Solid Films, 510(1), 138-142.

[322]. Edwards, D. A., Harker, R. M., Mahon, M. F., & Molloy, K. C. (2002). Aerosol-assisted chemical vapour deposition (AACVD) of silver films from triorganophosphine adducts of silver carboxylates, including the structure of [Ag ($O_2CC_3F_7$)(PPh 3) 2]. Inorganica Chimica Acta, 328(1), 134-146.

[323]. Grodzicki, A., Łakomska, I., Piszczek, P., Szymańska, I., & Szłyk, E. (2005). Copper (I), silver (I) and gold (I) carboxylate complexes as precursors in chemical vapour deposition of thin metallic films. Coordination Chemistry Reviews, 249(21), 2232-2258.

[324]. Vasconcellos, L.M.R., Cairo, C.A.A., de Vasconcellos, L.G.O., de Alencastro Grac¸a, M.L., do Prado, R.F., Carvalho, Y.R. (2012). Porous titanium by powder metallurgy for biomedical Application: characterization, cell citotoxity and in vivo tests of osseointegration, INTECH Open Access Publisher, http://dx. doi.org/10.5772/47816.

[325]. Suntola, T. (1994). Handbook of crystal growth 3, thin films and epitaxy, Part B: Growth mechanisms and dynamics. Amsterdam, Netherland, Elsevier.

[326]. Palomba, M., Carotenuto, G., Cristino, L., Di Grazia, M. A., Nicolais, F., & De Nicola, S. (2012). Activity of antimicrobial silver polystyrene nanocomposites. Journal of Nanomaterials, 2012, 1-7.

[327]. King, P. J. (2013). Hafnium oxide-based dielectrics by atomic layer deposition (Doctoral dissertation, University of Liverpool, Liverpool, UK). Retrieved from http://repository.liv.ac.uk/9253/1/KingPet_Jan2013_9253.pdf

[328]. Elam, J. W., & Pellin, M. J. (2005). GaPO4 sensors for gravimetric monitoring during atomic layer deposition at high temperatures. Analytical Chemistry, 77(11), 3531-3535.

[329]. LabWrench (n.d.). METTLER TOLEDO Excellence XS Series Analytical http://www.labwrench.com/?equipment.view/equipmentNo/2553/METTLERTOLEDO/Excellence-XS-Series-Analytical/

[330]. Thin Film Technology/Physics of Thin Films (n.d.). Properties and Characterisation of Thin Films http://static.ifp.tuwien.ac.at/homepages/Personen/duenne_schichten/pdf/t_p_ds_chapter4.pdf

[331]. Pecharsky, V. K., & Zavalij, P. Y. (2009). Fundamentals of powder diffraction and structural characterization of materials. Berlin, Germany, Springer.

[332]. Agasti, N., & Kaushik, N. K. (2014). One Pot Synthesis of Crystalline Silver Nanoparticles. American Journal of Nanomaterials, 2(1), 4-7.

[333]. Rasband, W. (1997). National Institute of Health, USA. Software Available at http://rsb. info. nih. gov/ij/(accessed 20 March 2005). 500

[334]. R. Sperling (2010). Particle size analyzer. [Software]. InstitutCatalà de Nanotecnologia (ICN), Barcelona. [Online]. Available: http://code.google.com/p/psa-macro/downloads/detai l?name=PSA_r12.txt (accessed: 16/10/2011). _445

[335]. Sosa, E. D., Allada, R., Huffman, C. B., & Arepalli, S. (2009). XPS protocol for the characterization of pristine and functionalized single wall carbon nanotubes. NASA Technical Reports Server, 1-19.

[336]. Crist, B. V. (2007). A review of XPS data-banks. XPS Reports, 1(1), 10-21.

[337]. Britson, J. C. (2008). Pulsed laser deposition of aluminium magnesium borate thin films. ProQuest.

[338]. Jain, A., Chi, K. M., Hampden-Smith, M. J., Kodas, T. T., Farr, J. D., & Paffett, M. F. (1992). Chemical vapour deposition of copper via disproportionation of hexafluoroacetylacetonato (1, 5-cyclooctadiene) copper (I), (hfac) Cu (1, 5-COD). Journal of materials research, 7(02), 261-264.

[339]. Yanguas-Gil, A., Libera, J. A., & Elam, J. W. (2013). Modulation of the Growth Per Cycle in Atomic Layer Deposition Using Reversible Surface Functionalization. *Chemistry of Materials*, *25*(24), 4849-4860.

[340]. Kang, J. G., & Sohn, Y. (2012). Interfacial nature of Ag nanoparticles supported on TiO_2 photocatalysts. Journal of Materials Science, 47(2), 824-832.

[341]. Lopez-Salido, I., Lim, D. C., & Kim, Y. D. (2005). Ag nanoparticles on highly ordered pyrolytic graphite (HOPG) surfaces studied using STM and XPS. Surface Science, 588(1), 6-18.

[342]. P.Prieto, V.Nistor, K.Nouneh, M.Oyama, M.Abd-Lefdil, R.Díaz,XPS study of silver, nickel and bimetallic silver–nickel nanoparticles prepared by seed-mediated growth, Appl. Surf. Sci.258 (2012) 8807-8813.

[343]. D. M. Bastidas, E. Cano, A. G. Gonzalez, S. Fajardo, R. Lleras-Pérez, E. Campo-Montero, J. M. Bastidas, An XPS study of tarnishing of a gold mask from a pre-Columbian culture, Corros. Sci. 50 (2008) 1785-1788.

[344]. Baldan, A. (2002). Review progress in Ostwald ripening theories and their applications to nickel-base super alloys Part I: Ostwald ripening theories. Journal of materials science, 37(11), 2171-2202.

[345]. Tantra, R. (2016). Nanomaterial Characterization: An Introduction. John Wiley & Sons.

[346]. Butan-1-ol. (1984). Retrieved from http://www.fao.org/ag/agn/jecfa-additives/specs/Monograph1/Additive-064.pdf

[347]. 1-Propanol. Retrieved from http://www.chemspider.com/Chemical-Structure.1004.html

[348]. Ugur, I., Marion, A., Parant, S., Jensen, J. H., & Monard, G. (2014). Rationalization of the p K a Values of Alcohols and Thiols Using Atomic Charge Descriptors and Its Application to the Prediction of Amino Acid p K a's. Journal of Chemical Information and Modeling, 54(8), 2200-2213.

[349]. Properties and Uses of Alkanols. (2016) Retrieved from http://www.ausetute.com.au/alkanolp.html

[350]. Plasma or Radical? Enhanced or Assisted? Direct or Remote? Deposition or Epitaxy? (2016). Retrieved from http://www.plasma-ald.com/ald.php

[351]. Rushworth, S., & Williams, P. (2011). U.S. Patent Application No. 13/635,478.

[352]. 1-tert-butyl-hydrazine (2016). Retrieved from http://www.molbase.com/en/name-%201-tert-butyl-hydrazine.html

[353] Acharya, S., Neogi, G., Panda, R. K., & Ramaswamy, D. (1984). Kinetics of oxidation of hydrazine and of t-butylhydrazine using tris (dimethylglyoximato) nickelate (IV) in the presence of added Cu2+(aq). Journal of the Chemical Society, Dalton Transactions, (8), 1477-1484.

[354]. 1-Propanol (1998). Retrieved from http://pubchem.ncbi.nlm.nih.gov/compound/1-propanol#section=Information-Sources

[355]. Juppo, M., Ritala, M., & Leskelä, M. (2000). Use of 1, 1-Dimethylhydrazine in the Atomic Layer Deposition of Transition Metal Nitride Thin Films. Journal of the Electrochemical Society, 147(9), 3377-3381.

[356]. Kim, O. H., Kim, D., & Anderson, T. (2009). Atomic layer deposition of GaN using GaCl3 and NH3. Journal of Vacuum Science & Technology A, 27(4), 923-928.

[357]. Cheng, D., Xia, S., & Tong, J. (1996). The mechanism of directional oxidation of hydrazine by silver coordination compounds. Transition Metal Chemistry, 21(6), 503-506.

[358]. Kim, J. G., Ahn, J. Y., Kim, H. S., & Lim, J. W. (2005). U.S. Patent Application No. 11/031,611.

[359]. Gray, P., & Thynne, J. C. J. (1964). Kinetics of hydrogen abstraction from hydrazine, ammonia and trideuteroammonia. Transactions of the Faraday Society, 60, 1047-1052.

[360]. Retrieved from http://chemwiki.ucdavis.edu/Core/Organic_Chemistry/Fundamentals/Homolytic_CH_Bond_Dissociation_Energies_of_Organic_Molecules

[361]. D.M. Bastidas, E. Cano, A.G. Gonzalez, S. Fajardo, R. Lleras-Pérez, E.Campo-Montero, J.M. Bastidas, An XPS study of tarnishing of a gold mask from a pre-Columbian culture, Corros. Sci. 50 (2008) 1785–1788.

[362]. Z. Shi, J. Zhang, D. Gao, Z. Zhu, Z. Yang, Z. Zhang, D. Xue, Magnetic resonance of the NiFe2O4 nanoparticles in the gigahertz range, Nanoscale research letters, 8 (2013) 1-5.

[363]. J. Guo, H. Wu, X. Liao, B. Shi, Facile synthesis of size-controlled silver nanoparticles using plant tannin grafted collagen fiber as reductant and stabilizer for microwave absorption application in the whole Ku band, J. Phys. Chem. C, 115 (2011) 23688-23694.

[364]. X. Yang, A. Wolcott, G. Wang, A. Sobo, R.C. Fitzmorris, F. Qian, J.Z. Zhang, Y. Li, Nitrogen-doped ZnO nanowire arrays for photoelectrochemical water splitting. Nano Letters, 9 (2009) 2331-2336.

[365]. S. Thomas, S.K. Nair, E.M.A. Jamal, S.H. Al-Harthi, M.R. Varma, M.R. Anantharaman, Size-dependent surface plasmon resonance in silver silica nanocomposites, Nanotechnology 19 (2008) 075710.

[366]. M. Ferraris, S. Ferraris, M. Miola, S. Perero, C. Balagna, E. Vernè,G. Gautier, Ch. Manfredotti, A. Battiato, E. Vittone, G.Speranza, I. Bogdanovic, Effect of thermal treatments on sputtered silver nanocluster/silica composite coatings on soda-lime glasses: ionic exchange and antibacterial activity. J. Nanopart. Res. 14 (2012) 1-19.

[367]. P. Kumar, M.C. Mathpal, A.K. Tripathi, J. Prakash, A. Agarwal, M.M. Ahmad, H.C. Swart, Plasmonic resonance of Ag nanoclusters diffused in soda-lime glasses. Phys. Chem. Chem. Phys., 17 (2015) 8596-8603.

[368]. Sun, X., Hong, R., Hou, H., Fan, Z., & Shao, J. (2007). Thickness dependence of structure and optical properties of silver films deposited by magnetron sputtering. Thin Solid Films, 515(17), 6962-6966.

[369]. Z. Othaman, L.K. Boo, S. Sakrani, R. Muhammad, The Stranski–Krastanov three dimensional island growth predication on finite size model (Part I), J.Fiz.UTM., 3 (2008) 78-83.

[370]. D. Mishra, D. Greving, G.B. Confalonieri, J. Perlich, B.P. Toperverg, H. Zabel, O. Petracic, Growth modes of nanoparticle superlattice thin films. Nanotechnology, 25 (2014) 205602.

[371]. W. Jevasuwan, Y. Urabe, T. Maeda, N. Miyata, T. Yasuda, H. Yamada, M. Hata, N. Taoka, M. Takenaka, S. Takagi, Initial Processes of Atomic Layer Deposition of Al_2O_3 on InGaAs: Interface Formation Mechanisms and Impact on Metal-Insulator-Semiconductor Device Performance. Materials, 5 (2012) 404-414.

[372]. Choi, B. J., Choi, S., Eom, T., Ryu, S. W., Cho, D. Y., Heo, J. ... & Hong, S. K. (2009). Influence of substrates on the nucleation and growth behaviors of Ge2Sb2Te5 films by combined plasma-enhanced atomic layer and chemical vapor deposition. Chemistry of Materials, 21(12), 2386-2396.

[373]. Li, D., Liu, G. L., Yang, Y., Wu, J. H., & Huang, Z. R. (2013). Nucleation and Growth Mechanism of Si Amorphous Film Deposited by PIAD. Journal of Nanomaterials, 1-7.

[374]. Wenzel, R. N. (1936). Resistance of solid surfaces to wetting by water. Industrial & Engineering Chemistry, 28(8), 988-994.

[375]. Won, S. J., Suh, S., Lee, S. W., Choi, G. J., Hwang, C. S., & Kim, H. J. (2010). Substrate dependent growth rate of plasma-Enhanced atomic layer deposition of titanium oxide using N2O gas. Electrochemical and solid-state letters, 13(2), 13-16.

[376]. Ylilammi, M. (1996). Monolayer thickness in atomic layer deposition. Thin Solid Films, 279(1), 124-130.

[377]. Haukka, S., Tuominen, M., Vainonen-Ahlgren, E., Tois, E., Li, W. M., & Maes, J. W. (2003). Effect of starting surface in atomic layer deposition. In Proceedings-Electrochemical Society (405-416). Electrochemical Society.

[378]. Elliot, A. J., Malek, G., Wille, L., Lu, R., Han, S., Wu, J. Z. ... & Lewis, R. M. (2013). Probing the Nucleation of in Atomic Layer Deposition on Aluminum for Ultrathin Tunneling Barriers in Josephson Junctions. Applied Superconductivity, IEEE Transactions on, 23(3), 1101405-1101405.

[379]. Campbell, C. T. (1997). Ultrathin metal films and particles on oxide surfaces: structural, electronic and chemisorptive properties. Surface science reports, 27(1), 1-111.

[380]. Whitesides, G. M., & Laibinis, P. E. (1990). Wet chemical approaches to the characterization of organic surfaces: self-assembled monolayers, wetting, and the physical-organic chemistry of the solid-liquid interface. Langmuir, 6(1), 87-96.

[381]. Baker, L., Cavanagh, A. S., Seghete, D., George, S. M., Mackus, A. J. M., Kessels, W. M. M., ... & Wagner, F. T. (2011). Nucleation and growth of Pt atomic layer deposition on Al2O3 substrates using (methylcyclopentadienyl)-trimethyl platinum and O_2 plasma. Journal of Applied Physics, 109(8), 084333.

[382]. Goldstein, D. N., & George, S. M. (2011). Surface poisoning in the nucleation and growth of palladium atomic layer deposition with Pd $(hfac)_2$ and formalin. Thin Solid Films, 519(16), 5339-5347.

[383]. Sechrist, Z. A., Fabreguette, F. H., Heintz, O., Phung, T. M., Johnson, D. C., & George, S. M. (2005). Optimization and structural characterization of W/Al2O3 nanolaminates grown using atomic layer deposition techniques. Chemistry of Materials, 17(13), 3475-3485.

[384]. Zemek, J., Olejník, K., & Klapetek, P. (2008). Photoelectron spectroscopy from randomly corrugated surfaces. Surface Science, 602(7), 1440-1446.

[385]. Gunter P.L.J., Gijzeman O.L.J., Niemantsverdriet J.W. Surface roughness effects in quantitative XPS: magic angle for determining overlayer thickness. Applied Surface Science, 115, 342-346, 1997.

[386]. Geng, S., Zhang, S., & Onishi, H. (2002). XPS applications in thin films research. Materials Technology, 17(4), 234.

[387]. Yung, T. Y., Lee, J. Y., & Liu, L. K. (2013). Nanocomposite for methanol oxidation: synthesis and characterization of cubic Pt nanoparticles on graphene sheets. Science and Technology of Advanced Materials, 14(3), 035001.

[388]. Semaltianos, N. G., Perrie, W., Romani, S., Potter, R. J., Dearden, G., & Watkins, K. G. (2012). Polymer-nanoparticle composites composed of PEDOT: PSS and nanoparticles of Ag synthesised by laser ablation. Colloid and Polymer Science, 290(3), 213-220.

[389]. Waterhouse, G. I., Bowmaker, G. A., & Metson, J. B. (2001). The thermal decomposition of silver (I, III) oxide: a combined XRD, FT-IR and Raman spectroscopic study. Physical Chemistry Chemical Physics, 3(17), 3838-3845.

[390]. Balachandran, S., Praveen, S. G., Velmurugan, R., & Swaminathan, M. (2014). Facile fabrication of highly efficient, reusable heterostructured Ag–ZnO–CdO and its twin applications of dye degradation under natural sunlight and self-cleaning. RSC Advances, 4(9), 4353-4362.

[391]. Fu, Y., Du, H., Zhang, S., & Huang, W. (2005). XPS characterization of surface and interfacial structure of sputtered TiNi films on Si substrate. Materials Science and Engineering: A, 403(1), 25-31.

[392]. Bohr, T., Jensen, M. H., Paladin, G., & Vulpiani, A. (2005). Dynamical systems approach to turbulence. Cambridge, United Kingdom, Cambridge University Press.

[393]. Trujillo, N. A., Oldinski, R. A., Ma, H., Bryers, J. D., Williams, J. D., & Popat, K. C. (2012). Antibacterial effects of silver-doped hydroxyapatite thin films sputter deposited on titanium. Materials Science and Engineering: C, 32(8), 2135-2144.

[394]. Chimutengwende-Gordon, M., Pendegrass, C., Bayston, R., & Blunn, G. (2014). Preventing infection of osseointegrated transcutaneous implants: Incorporation of silver into preconditioned fibronectin-functionalized hydroxyapatite coatings suppresses Staphylococcus aureus colonization while promoting viable fibroblast growth in vitro. Biointerphases, 9(3), 031010.

[395]. Takahashi, C., Saito, S., Suda, A., Ogawa, N., Kawashima, Y., & Yamamoto, H. (2015). Antibacterial activities of polymeric poly (dl-lactide-co-glycolide) nanoparticles and Soluplus® micelles against Staphylococcus epidermidis biofilm and their characterization. RSC Advances, 5(88), 71709-71717.

[396]. Hou, W., Sun, X., Wang, Z., & Zhang, Y. (2012). Biofilm-Forming Capacity of Staphylococcus epidermidis, Staphylococcus aureus, and Pseudomonas aeruginosa from Ocular InfectionsBiofilm-Forming Capacity of Human Flora Bacteria. Investigative Ophthalmology & Visual Science, 53(9), 5624-5631.

[397]. Zille, A., Fernandes, M. M., Francesko, A., Tzanov, T., Fernandes, M., Oliveira, F. R. ... & Souto, A. P. (2015). Size and aging effects on antimicrobial efficiency of silver nanoparticles coated on polyamide fabrics activated by atmospheric DBD plasma. ACS Applied Materials & Interfaces, 7(25), 13731-13744.

[398]. Ayala-Núñez, N. V., Villegas, H. H. L., Turrent, L. D. C. I., & Padilla, C. R. (2009). Silver nanoparticles toxicity and bactericidal effect against methicillin-resistant Staphylococcus aureus: nanoscale does matter. Nanobiotechnology, 5(1-4), 2-9.

[399]. Realizer. Rapid Laser Manufacturing. (2009). Available from: http://www.realizer-gmbh.de.

[400]. Meiners, W. (1999). Direktes selektives Laser-Sintern einkomponentiger metallischer Werkstoffe. Shaker. (Doctoral dissertation, University of Hochschule Aachen).

[401]. Campanelli, S. L., Angelastro, A., Ludovico, A. D., & Contuzzi, N. (2010). Capabilities and performances of the selective laser melting process. Italy: INTECH Open Access Publisher. 233–252.

[402]. Stamp, R. C. (2007). The rapid manufacture of hierarchical structures for orthopaedic applications (Doctoral thesis, University of Liverpool, Liverpool, UK). Retrieved from http://ethos.bl.uk/OrderDetails.do?uin=uk.bl.ethos.486451

[403]. Louvis, E., Fox, P., & Sutcliffe, C. J. (2011). Selective laser melting of aluminium components. Journal of Materials Processing Technology, 211(2), 275-284.

[404]. Pogson, S. R., Fox, P., Sutcliffe, C. J., & O'neill, W. (2003). The production of copper parts using DMLR. Rapid Prototyping Journal, 9(5), 334-343.

[405]. Granstaff, V.E. and S.J. Martin. (1994). Characterization of a thickness-shear mode quartz resonator with multiple non piezoelectric layers. Journal of Applied Physics, 75, 1319-1329.

[406]. Lucklum, R., & Eichelbaum, F. (2006). Interface circuits for QCM sensors. In Piezoelectric Sensors (3-47). Springer Berlin Heidelberg.

[407]. Sauerbrey, G. (1959). Use of vibrating quartz for thin film weighing and microweighing. Zeitschrift für Physik, 155(2), 206-222.

[408]. Nobel Prizes (n.d.). Retrieved from http://www.nobelprize.org/nobel_prizes/physics/1. Laureates/.

[409]. Glasser, O. (1934). Wilhelm conrad rontgen and the early history of the roentgen rays. The American Journal of the Medical Sciences, 187(4), 566.

[410]. Eckert, M. (2012). Max von Laue and the discovery of X-ray diffraction in 1912. Annalen der Physik, 524(5), 83-85.

[411]. Krastev, V., & Exner, G. K. (2013). 100 years of X-ray diffraction: from Röntgen's discovery to top-of-the-art synchrotron source applications. Bulgarian Chemical Communications, 45(4), 411-417.

[412]. Liu, C., Uesaka, M., Fujiwara, T., Dobashi, K., & Kusano, J. (2014). Backscattering x-ray system by using 950 kev x-band linac x-ray source. Materials Analysis and Modification, 2209-2211.

[413]. Suryanarayana, C., & Norton, M. G. (2013). X-ray diffraction: a practical approach. Berlin, Germany, Springer Science & Business Media.

[414]. Fultz, B., & Howe, J. (2013). Diffraction and the X-ray powder diffractometer. In Transmission Electron Microscopy and Diffractometry of Materials (1-57). Springer Berlin Heidelberg.

[415]. Cole, H. (1970). Bragg's law and energy sensitive detectors. Journal of Applied Crystallography, 3(5), 405-406.

[416]. Schneider, R. (2008). Scanning electron microscopy studies of Nafion deformation into silicon micro-trenches for fuel cell applications (Doctoral dissertation, University of Princeton, NJ, US). Retrieved from http://pemfc.princeton.edu/Documents/Theses/Schneider_senior-thesis.pdf

[417]. Boegelein, T. (2014). Selective laser melting of a ferritic oxide dispersion strengthened steel (Doctoral dissertation, University of Liverpool, Liverpool, UK). Retrieved from http://repository.liv.ac.uk/2010620/

[418]. Goldstein, J., Newbury, D. E., Echlin, P., Joy, D. C., Romig Jr, A. D., Lyman, C. E., ... & Lifshin, E. (2012). Scanning electron microscopy and X-ray microanalysis: a text for biologists, materials scientists, and geologists. Springer Science & Business Media.

[419]. Postek, M. T., Howard, K. S., Johnson, A. H., & McMichael, K. L. (1980). Scanning Electron Microscopy: A Student's Handbook. Ladd Research Industries. Inc, Burlington, VT.

[420]. Cheney, B. (n.d.). Introduction to scanning electron microscopy, Materials Engineering department, San Jose State University.
Retrieved from http://www.sjsu.edu/people/anastasia.micheals/courses/MatE143/s1/SEM_GUIDE.pdf

[421]. Binnig, G., Quate, C. F., & Gerber, C. (1986). Atomic force microscope. Physical Review Letters, 56(9), 930.

[422]. Raposo, M., Ferreira, Q., & Ribeiro, P. A. (2007). A guide for atomic force microscopy analysis of soft-condensed matter. Modern research and educational topics in microscopy, 1, 758-769.

[423]. Nanosensors Homepage http://www.nanosensors.com (Accessed 11/06/06).

[424]. Wilson, R. A., & Bullen, H. A. (2006). Introduction to scanning probe microscopy (spm) basic theory atomic force microscopy (afm). Creative Commons Attribution-Noncommercial-Share Alike, 859-572-5411.

[425]. Schematic of AFM. Retrieved from http://scixchange.missouri.edu/blog-post/afm-an-introduction-part-iii/

[426]. Bhushan, B., & Marti, O. (2010). Scanning probe microscopy–principle of operation, instrumentation, and probes. Berlin, Germany, Springer.

[427]. Binnig, G., Gerber, C., Stoll, E., Albrecht, T. R., & Quate, C. F. (1987). Atomic resolution with atomic force microscope. Euro Physics Letters, 3(12), 1281.

[428]. Mourougou-Candoni, N. (2012). Tapping mode AFM imaging for functionalized surfaces. INTECH Open Access Publisher, 978-953-51-0114-7.

[429]. Vickerman, J. C. (Ed.). (2009). Surface analysis: the principal techniques. Chichester, UK, John Wiley & Sons Ltd.

[430]. Siegbahn, K. (1967). ESCA; atomic, molecular and solid state structure studied by means of electron spectroscopy. Almqvist & Wiksells, Vol. 20.

[431]. Steinhardt Jr, R. G., Granados, F. A., & Post, G. I. (1955). X-Ray Photoelectron Spectrometer with Electrostatic Deflection. Analytical Chemistry, 27(7), 1046-1050.

[432]. Pantano, C. G. (1993). X-Ray photoelectron spectroscopy of glass. Methods of Glass Research, 129-60.

[433]. Johnson, B. E. (2010). The Role of Cd and Ga in the Cu (In, Ga) S2/CdS Heterojunction Studied with X-Ray Spectroscopic Methods (Doctoral thesis, University of Berlin, Berlin, Germany). Retrieved from http://www.helmholtz-berlin.de/media/media/angebote/bibliothek/Examensarbeiten-Master/dissertation-johnson-hzb-b-10.pdf

[434]. Lahtonen, K. (2012). Electron spectroscopy (XPS, AES, UPS). Retrieved from http://www.tut.fi/en/about-tut/departments/optoelectronics-research-centre/research/surface-science/electron-spectroscopy/index.htm

[435]. Chan, J. (1994). Four-Point Probe Manual. http://microlab.berkeley.edu/ee143/Four-Point Probe.